

Design and Fabrication of Superhydrophobic and
Antimicrobial Surfaces on AISI 316L Stainless Steel

Yukui Cai

A thesis submitted for the degree of Doctor of Philosophy

Centre for Precision Manufacturing

Department of Design, Manufacture and Engineering Management

University of Strathclyde

July 2019

Declaration Statement

This thesis is the result of the author's original research. It has been composed by the author and has not been previously submitted for examination which has led to the award of a degree.

The copyright of this thesis belongs to the author under the terms of the United Kingdom Copyright Acts as qualified by University of Strathclyde Regulation 3.50. Due acknowledgement must always be made of the use of any material contained in, or derived from, this thesis.

Signed:

Date:

Abstract

In a surgical procedure, the medical devices come into contact with blood, which increases the risk of the formation of blood clots, also known as thrombi. Antimicrobial resistance is another pressing issue in the healthcare field. With the increasing consumption of antimicrobial drugs, the threat of antimicrobial resistance is rising, and the global dimensions of this trend have been increasingly recognised. Some new strategies that utilise superhydrophobicity or antimicrobial properties to medical devices have garnered more attention and interest.

Superhydrophobic surfaces have attracted extensive attention over the past decade, primarily due to their self-cleaning, corrosion resistance, anti-icing and drag reduction abilities. The ability to reduce blood adhesion is one of the critical benefits of these types of surfaces. Nanosecond pulsed laser ablation is considered to be a promising technique for the industrial fabrication of superhydrophobic structures due to its high efficiency and low-cost. In this PhD thesis, nanosecond pulsed laser-based ablation technology was developed to manufacture functional surfaces that have superhydrophobicity or antimicrobial properties on AISI 316L stainless steel.

To achieve that goal, a deterministic design method was developed to design the dimensions of the microstructures to be fabricated by laser ablation in order to maximise superhydrophobicity. Then computational fluid dynamics (CFD) simulation was conducted to explore the underlying mechanism of superhydrophobicity and predict the hydrophobicity of the designed structures. The simulation results proved that the substrates trapped a large volume of air with high pressure at the bottom of the structures, which is critical to achieving stable superhydrophobicity. Moreover, the superhydrophobic substrate has greater potential energy and kinetic energy in the

water droplet's impacting process, which helps explain its self-cleaning and low-adhesion properties.

In the next step, the process and the product fingerprints are proposed for the first time to identify the correlations among the machining parameters, surface topography and functional performance (i.e. the contact angle of the laser ablated superhydrophobic surface on AISI 316L stainless steel) of the specimen. The dimensionless surface functional characterisation parameter R_{hy} (i.e. the average ratio of R_z to R_{sm}) has maximum values of Spearman and Kendall rank correlation coefficients with contact angle, which can be regarded as the product fingerprint. The laser pulse energy per unit area on the specimen (I_s) represents the combined effect of the laser power, exposure time and pitch of the structure on the surface topography, and it is the best process fingerprint that can be used to control the product fingerprint R_{hy} . The threshold values of R_{hy} and I_s are 0.41 and 536 J/mm^2 , respectively, ensuring the specimen's superhydrophobicity (contact angle larger than 150°) in the laser ablation process.

Finally, two new hybrid processes based on laser ablation were developed to manufacture functional surfaces with anisotropic superhydrophobicity and antimicrobial properties. First, a sequential process of laser ablation and chemical etching (LA-CE) was proposed to produce ratchet-like microstructures on AISI 316L stainless steel. The experimental investigation concluded that the direction of the microstructures is the same as the direction of the laser beam feed. Moreover, the droplet easily rolls off the surface in the laser beam feed direction; however, it is pinned tightly in the opposite direction. This study was the first to use a single-step fabrication approach (StruCoat) to develop the antimicrobial surfaces based on laser

ablation technology in order to generate the antimicrobial microstructures coated with silver nanoparticles (AgNPs) on AISI 316L stainless steel. The experimental results showed that silver nitrate with a molarity of 50 mmol at the laser power of 14 W, which resulted in AgNPs with a mean size of 480 nm, was the best processing condition for the chemical decomposition of silver nitrate micro drops. Furthermore, StruCoat helped increase the cooling rate of the substrate in the laser ablation process, resulting in a significant decrease in the material grain size (by 81%). Furthermore, antimicrobial efficacy testing also demonstrated the enhanced antimicrobial properties of StruCoat, with an 86.2% antimicrobial rate against *Staphylococcus aureus*, in comparison to the unmodified specimens.

Acknowledgements

“Life was like a box of chocolates. You never know what you're gonna get.”

Doing a PhD is extremely challenging work. Fortunately, I have met a lot of wonderful people during this amazing journey.

Firstly, I would like to express the most profound appreciation to my advisor Prof Xichun Luo for the continuous support of my PhD study and related research, for his patience, motivation, and immense knowledge. His guidance helped me in all the time of research and writing of this thesis.

My sincere thanks go to the Dr King Hang Aaron Lau, Dr Ana M. L. Sousa and Dr Kunal Tewari from Department of Pure & Applied Chemistry, and Dr Michelle Maclean from the Department of Biomedical Engineering. Their knowledge and assistance helped me to accomplish chemical experiments and antimicrobial test.

I would like to acknowledge my second supervisor, Prof Yi Qin for the aid, guidance, and his support during my PhD life. I would also like to acknowledge Prof Zhanqiang Liu from Shandong University for his support during the academic exchange period and giving me access to their measurement instruments.

I would like to thank my friends and research colleagues Dr Wenlong Chang, Dr Quanren Zeng, Dr Wenbin Zhong, Mr Fei Ding, Mr Yankang Tian, Mr Zhengjian Wang as well as all members of the Centre for Precision Manufacturing. It's my pleasure and honour to work with those excellent people.

I would like to gratefully acknowledge the financial support from the MICROMAN project (ID: 674801) and the EPSRC (EP/K018345/1) project. I would also like to thanks all the supervisors and ESRs in the MICROMAN Project. I have

learned a lot of knowledge and skills from them during the workshops and project meetings.

Finally, I am grateful to my dear wife, Meijie Niu, for her encouragement and support. I need to thank my little boy, Hangqi Cai, for being such a bundle of joy and laughter. My love and appreciation go to my parents and sisters for their never-ending love and support during all stages of my study.

Table of Contents

Declaration Statement	II
Abstract.....	III
Acknowledgements.....	VI
Table of Contents	VIII
List of Tables	XIII
List of Figures.....	XV
Nomenclature.....	XXI
Abbreviations	XXV
List of Publications.....	XXVI
Journal papers	XXVI
Conference papers.....	XXVII
Book chapter	XXVII
Chapter 1 Introduction.....	1
1.1 Background	1
1.2 Aims and objectives	4
1.3 Chapter overviews.....	5
Chapter 2 Literature Review	8
2.1 Wettability.....	8
2.1.1 <i>Contact angle and sliding angle</i>	8
2.1.2 <i>Classification of wettability</i>	9
2.1.3 <i>Wettability of rough surfaces</i>	11
2.2 State-of-the-art of superhydrophobic surfaces	12

2.2.1	<i>Natural superhydrophobic surfaces</i>	12
2.2.2	<i>Artificial superhydrophobic surfaces: pattern design</i>	17
2.2.3	<i>Artificial superhydrophobic surfaces: numerical simulation</i>	21
2.2.4	<i>The manufacturing processes for superhydrophobic surfaces</i>	23
2.3	State-of-the-art of antimicrobial surface	46
2.3.1	<i>Introduction</i>	46
2.3.2	<i>Preparation of antimicrobial silver-containing surface</i>	46
2.4	Summary of knowledge gaps and research challenges	50
Chapter 3 Design Method for Laser Ablated Superhydrophobic Microstructures		
.....		52
3.1	Introduction	52
3.2	A deterministic design approach for superhydrophobic structures	52
3.2.1	<i>Geometrical model of microstructures</i>	53
3.2.2	<i>A nonlinear geometrical optimisation model</i>	56
3.3	CFD simulation: method and setup	60
3.3.1	<i>Mathematical model of the VOF method</i>	61
3.3.2	<i>Geometrical model and simulation parameter setup</i>	63
3.4	CFD simulation: results and discussions.....	67
3.4.1	<i>Dynamic behaviour of the water droplet on varied substrates at a Weber number of 0.026</i>	67
3.4.2	<i>Impacting behaviour of water droplet on varied substrates at Weber number of 7.26</i>	82
3.5	Summary	87
Chapter 4 Experimental Validation		89

4.1	Introduction	89
4.2	Laser processing experiment hardware	89
4.3	Laser processing parameters	91
4.3.1	<i>Laser power (P_{ave})</i>	91
4.3.2	<i>Exposure time (t_e)</i>	91
4.4	Surface preprocessing, post-processing and characterisation	92
4.5	Dynamic impacting test of water droplets by a high-speed camera... 94	
4.6	Experimental validation results	95
4.6.1	<i>Analysis of surface morphology</i>	96
4.6.2	<i>Analysis of surface hydrophobicity</i>	99
4.6.3	<i>Results comparison</i>	104
4.6.4	<i>High-speed camera test</i>	106
4.7	Summary	109
Chapter 5 Process and Product Fingerprints for a Laser Ablated Superhydrophobic Surface.....		111
5.1	Introduction	111
5.2	Definition of process and product fingerprints	112
5.2.1	<i>Analysis of process fingerprint candidates</i>	113
5.2.2	<i>Analysis of product fingerprint candidates</i>	114
5.2.3	<i>Laser ablation experiments</i>	116
5.3	Product fingerprint	117
5.4	Process fingerprints	123
5.5	Correlation between laser ablation parameters and contact angle ...	125
5.6	Summary	128

Chapter 6 A Sequential Process for Manufacturing Nature-inspired Anisotropic Superhydrophobic Structures.....	130
6.1 Introduction	130
6.2 Work principle of LA-CE and experimental setup	130
6.2.1 <i>Work principle of LA-CE</i>	130
6.2.2 <i>Materials and experimental setup</i>	132
6.3 Experimental results and discussion	133
6.3.1 <i>Surface morphologies and composition</i>	133
6.3.2 <i>Anisotropic superhydrophobicity of specimens</i>	138
6.4 Summary	142
Chapter 7 A Single-step Fabrication Approach for the Development of Antimicrobial Surfaces	143
7.1 Introduction	143
7.2 The working mechanism of StruCoat and experimental setup.....	144
7.2.1 <i>Working principle of StruCoat</i>	144
7.2.2 <i>Mechanism of decomposition and deposition of AgNPs</i>	145
7.2.3 <i>Materials and experimental setup</i>	147
7.2.4 <i>Post-processing and characterization</i>	148
7.3 Experiments with StruCoat technology.....	148
7.3.1 <i>The effect of laser power on the morphology of AgNPs and microstructures</i>	149
7.3.2 <i>The effect of silver nitrate molarity on the synthesis of AgNPs</i> . 153	
7.3.3 <i>Material microstructures of StruCoat processed substrates</i>	159
7.4 Antimicrobial test and results.....	161

7.4.1	<i>Antimicrobial activity testing</i>	161
7.4.2	<i>Antimicrobial evaluation of StruCoat</i>	162
7.5	Summary	164
Chapter 8 Conclusions and Future Works		166
8.1	Conclusions	166
8.2	Contributions to knowledge	170
8.3	Recommendations for future works	171
References		172

List of Tables

Table 2.1 Superhydrophobicity of nature plant surfaces.	13
Table 2.2 Superhydrophobicity of animal surfaces.....	15
Table 2.3 Geometric patterns of superhydrophobic substrates.	20
Table 2.4 Summary of the previous works on the impact of the drops on solid surfaces.	23
Table 2.5 Femtosecond pulsed laser ablated superhydrophobic surfaces.....	36
Table 2.6 Picosecond pulsed laser ablated superhydrophobic surfaces.	38
Table 2.7 Nanosecond pulsed laser ablated superhydrophobic surfaces.	42
Table 2.8 Advantages and disadvantages of different manufacturing process.	45
Table 3.1 Details of IPG 20w fiber laser YLP-1-100-20-20.....	54
Table 3.2 Initial conditions used in the optimisation process.	59
Table 3.3 Predicted dimensions of Gaussian hole and its contact angle.....	60
Table 3.4 Dimensions and initial conditions of Gaussian hole model for VOF simulation.....	65
Table 3.5 VOF simulation parameters.	65
Table 4.1 Conditions of high-speed camera test.	95
Table 4.2 The laser ablation parameters in the experiments.....	96
Table 5.1 Product fingerprint candidates.	116
Table 5.2 The laser ablation parameters with varied laser power and pitch.	116
Table 5.3 The laser ablation parameters with varied exposure time and pitch.	117
Table 5.4 Interpretation of the strength of the correlation coefficient.	118
Table 6.1 Operational conditions for experiments.....	132

Table 7.1 Operational conditions used to evaluate the effect of laser power on the synthesis of AgNPs.	147
Table 7.2 Operational conditions used to evaluate the effect of molarity of silver nitrate on the synthesis of AgNPs.	148
Table 8.1 The optimal technological parameters and key performance indicators for fabricating functional surfaces on AISI 316L stainless steel.	169

List of Figures

Figure 1.1 Number of published articles per year: (a) keywords ‘superhydrophobic’; (b) keywords ‘superhydrophobic’ and ‘laser’— matched on 11th March 2019 in the ISI Web of Knowledge database.	3
Figure 1.2 Structural outline of the thesis.	7
Figure 2.1 Conception of (a) contact angle and (b) sliding angle.	9
Figure 2.2 (a) low surface energy, (b) high surface energy, (c) superhydrophilic, (d) hydrophilic, (e) hydrophobic and (f) superhydrophobic.	10
Figure 2.3 Wetting state of water droplet: (a) Wenzel state; (b) Cassie-Baxter state.	12
Figure 2.4 The photos and SEM images: (a) lotus leaves; (b) rice leaves [19,21,28].	14
Figure 2.5 SEM images of the upper wing surfaces of insects: (a) <i>Papilio xuthus</i> ; (b) <i>Acrida cinerea</i> ; (c) <i>Meimuna opalifera</i> [30].....	15
Figure 2.6 Schematics of various rough surfaces [47].	19
Figure 2.7 Flow chart of soft-lithographic imprinting technology to prepare lotus leaf- like micro/nano structures [96].	25
Figure 2.8 Schematic presentation of the electrodeposition process on aluminium alloy [110].	27
Figure 2.9 Reaction route of fluorinated TiO ₂ sol preparation and coating procedure [117].	28
Figure 2.10 Schematic process of membrane preparation via simultaneous electrospraying and electrospinning [121].	30
Figure 2.11 The flow chart of combined wet chemical etching and anodic oxidation method [129].	31

Figure 2.12 (a) 3D printer, (b) An overview image of the 3D printer for direct writing of PDMS ink, (c) schematic of 3D printing process and (d) anisotropic porous PDMS film [136].	33
Figure 2.13 Experimental setup for the fabrication of superhydrophobic soda-lime glass surface. (a) Schematic diagram; (b) photograph [144].	35
Figure 2.14 Laser fabricated 2D array asperities (a) laser beam path, (b) overview photo, (c) SEM images, and (d) AFM measurement result [159].	38
Figure 2.15 Superhydrophobicity development after nanosecond pulsed laser ablation [166].	40
Figure 2.16 Schematic of UV nanosecond-pulsed laser ablation and heat treatment process [172].	41
Figure 2.17 The schematic diagram of fabricating laser ablated superhydrophobic steel [179].	42
Figure 2.18 Schematic of the implantation process and major components of the reactive low voltage ion plating equipment [190].	47
Figure 2.19 Schematic of MAO process followed by mussel-adhesive-inspired immobilization of AgNPs [196].	48
Figure 2.20 Schematic of the elaboration of multifunctional surfaces achieved via liquid-assisted plasma-enhanced chemical vapour deposition [197].	49
Figure 3.1 Intensity of the nanosecond laser beam and 2D profiles of machined micro holes: (a) Gaussian intensity profile of laser beam; (b) surface profile for P110 arrays.	54
Figure 3.2 (a) Gaussian curve; (b) 3D geometry model of laser ablated Gaussian holes.	55

Figure 3.3 Geometrical model of laser ablated Gaussian holes at Cassie-Baxter state: (a) 2D geometric model; (b) 3D topography.....	56
Figure 3.4 (a) 3D geometrical model of fluid domain based on Gaussian characters; (b) initial state of a water droplet.	67
Figure 3.5 A series of images of a water droplet impact on the specimen with a smooth surface at a low impact velocity of 0.03 m/s ($We = 0.026$, Case 1): (a) shape of the water droplet, (b) static pressure and velocity vector and (c) static pressure and velocity vector at 200 ms.	69
Figure 3.6 A series of images of a water droplet impact on a specimen with Gaussian hole arrays P150 (revised) at a low impact velocity of 0.03m/s ($We = 0.026$, Case 2): (a) shape of water droplet, (b) static pressure and velocity vector and (c) Cassie-Wenzel transition process and pressure distribution of Gaussian holes. 71	71
Figure 3.7. A series of images of a water droplet impact on the specimen with Gaussian hole arrays P150 (optimised) at a low impact velocity of 0.03m/s ($We = 0.026$, Case 3): (a) shape of water droplet, (b) static pressure and velocity vector and (c) Cassie-Wenzel transition process and pressure distribution of Gaussian holes. 73	73
Figure 3.8 A series of images of a water droplet impact on the specimen with Gaussian hole arrays P110 (optimised) at a low impact velocity of 0.03 m/s ($We = 0.026$, Case 4): (a) shape of water droplet, (b) static pressure and velocity vector and (c) Cassie-Wenzel transition process and pressure distribution of Gaussian holes. 75	75
Figure 3.9 (a) Time evolution of h^* of water drops ($We = 0.026$); (b) variations of average air pockets' pressure ($We = 0.026$).	77
Figure 3.10 The variations in the water droplet's (a) gravitational potential energy (E_g) and (b) kinetic energy (E_k).	80

Figure 3.11 Simulated contact angle of water droplet at 200 ms for (a) smooth surface, (b) P150 (revised), (c) P150 (optimised) and (d) P110 (optimised).	81
Figure 3.12 Comparison between simulation and the theoretical predicted value of contact angle.....	81
Figure 3.13 Time evolution of water drops with impacting velocity 0.5 m/s at (a) P150 (revised; $We = 7.26$, Case 5), (b) P150 (optimised; $We = 7.26$, Case 6) and (c) P110 (optimised; $We = 7.26$, Case 7).....	84
Figure 3.14 Time evolution of (a) D^* , (b) h^* and (c) average pressure of air pocket ($We 7.26$).....	87
Figure 4.1 Experimental setup for laser ablation trials: (a) hybrid ultra-precision machine; (b) IPG fibre laser.	90
Figure 4.2 Schematic of periodic Gaussian holes machined by laser ablation.	92
Figure 4.3 Schematic of preparation of laser ablated superhydrophobic surface.	94
Figure 4.4 Schematic of the silanization procedure.	94
Figure 4.5 Phantom v2012 high-speed camera.	95
Figure 4.6 Schematic for laser processing route.	96
Figure 4.7 SEM images of P110 specimens at different laser power: (a) 4 W, (b) 6 W, (c) 10 W and (d) 14 W.	97
Figure 4.8 SEM images of specimens ablated under laser power of 14 W with different pitches (a) 50 μm , (b) 70 μm , (c) 90 μm and (d) 150 μm	98
Figure 4.9 Surface morphologies under different laser powers for microstructures with a pitch of 130 μm (P130): (a) 4 W, (b) 6 W, (c) 10 W and (d) 14 W.	99
Figure 4.10 Water droplet on the smooth milled surface (a) before and after (b) silanization.	100

Figure 4.11 Water droplet shapes for different specimens: (a) P110-4 W, (b) P110-6 W, (c) P110-10 W, (d) P110-14 W, (e) P050-6 W and (f) P090-10 W.	101
Figure 4.12 Water droplet fall on specimen P110-14 W at a tilt angle of 3.5 °.....	101
Figure 4.13 Effect of laser power and pitch on the hydrophobicity of laser ablated specimens.	103
Figure 4.14 Influence of surface roughness on contact angles.	104
Figure 4.15 Comparison of design profile and experiments for specimens with pitches of (a) 150 μm and (b) 110 μm	105
Figure 4.16 Comparison between the predicted, simulated and measured contact angles.....	106
Figure 4.17 Time evolution of water drops with impacting velocity 0.5 m/s: (a) simulation results of P150 (revised) and (b) captured images of P150-14 W.	107
Figure 4.18 Time evolution of water drops with impacting velocity 0.5 m/s: (a) simulation results of P110 (optimised) and (b) captured images of P110-14 W.	108
Figure 4.19 High-speed camera captured images under impacting velocity 1 m/s of (a) P150-14 W and (b) P110-14 W.....	109
Figure 5.1 Concept of the process and product fingerprints in the laser ablation of the superhydrophobic surface.	113
Figure 5.2 Influences of the product fingerprint candidates on the contact angle for Gaussian hole pattern: (a) Sa, (b) Sz, (c) Sku, (d) Sdr, (e) Sdq and (f) R _{hy}	119
Figure 5.3 Spearman and Kendall rank correlation coefficient between the contact angle and six candidates of product fingerprint.	120

Figure 5.4 (a) Fitted line by exponential function between R_{hy} and contact angle; (b) surface morphology and shape of water drops on specimens with a different value of R_{hy}	122
Figure 5.5 3D colourmap of the product fingerprint (R_{hy}) as a function of laser power and pitch of Gaussian hole.	123
Figure 5.6 3D colourmap of the product fingerprint (R_{hy}) as a function of exposure time and pitch of Gaussian holes.	124
Figure 5.7 Scatter plots and fitted curve of R_{hy} and I_s	125
Figure 5.8 (a) 3D colourmap of the contact angle as a function of laser power and pitch of microstructures; (b) 3D colourmap of the contact angle as a function of exposure time and pitch of microstructures.	126
Figure 5.9 (a) Scatter plot and fitted curve between contact angle and I_s ; (b) surface morphology and shape of water drops on specimens with a different value of I_s	128
Figure 6.1 Schematic illustration of the manufacturing process (LA-CE) of superhydrophobic ratchet structures.	131
Figure 6.2 Schematic of feed directions: (a) unidirectional and (b) bidirectional. ..	132
Figure 6.3 SEM images (left) and high-magnification images (right) of Specimens: (a) Specimen 1 with a pitch of 25 μm after laser ablation; (b),(c),(d),(e),(f),(g),(h) surface morphologies of specimens 1 to 7 manufactured by LA-CE process.	136
Figure 6.4 X-ray diffraction pattern of AISI 316L stainless steel at different process: (a) smooth surface, (b) laser ablation and (c) LA-CE process.	137
Figure 6.5 (a) Captured images of water droplets; (b) variations of contact angle versus pitches for different laser power.	139

Figure 6.6 Anisotropic superhydrophobicity of specimen 3 (pitch 25 μ m at laser power of 20W).	140
Figure 6.7 (a) Wetting states of a water droplet at different dip directions; (b) retention force of asymmetric feature with rising angles of ω_1 and ω_2	142
Figure 7.1 Schematic illustration of StruCoat approach.	144
Figure 7.2 Schematic of chemical reaction process of AgNPs.	146
Figure 7.3 Ultrasonic atomiser used to generate micro drops.....	147
Figure 7.4 SEM image (left) and high-magnification image (right) of Specimens manufactured by StruCoat under different laser powers: (a) smooth and machined at laser powers of (b) 2 W; (c) 8 W; (d) 14 W; (e) 20 W.....	151
Figure 7.5 X-ray diffraction pattern of AISI 316L stainless steel: (a) smooth surface, (b) laser-machined surface and (c) StruCoat surface.	152
Figure 7.6 Low and high magnification SEM images of StruCoat processed microstructured surfaces with different molarities of silver nitrate: (a) 25 mmol; (b) 50 mmol; (c) 100 mmol; (d) 200 mmol. Images labelled (1) were low magnification ($\times 500$), and (2)-(4) were high magnification ($\times 1.5$ -6.0 k). Arrows on images indicate the silver particles.	155
Figure 7.7 Histogram and probability density function of AgNPs.	157
Figure 7.8 Comparison between predicted and measured particles size.....	158
Figure 7.9 Whole image of FIB processed areas (Left) and magnified image of the cross-section (Right).	158
Figure 7.10 SEM images ($\times 1.0$ k) of cross-sections of stainless steel surfaces: (a) unprocessed, (b) processed by laser machining and (c) processed by StruCoat.	161

Figure 7.11 Bacterial attachment and biofilm formation on StruCoat modified stainless steel surfaces. Results on smooth and laser ablated surfaces are included as a comparison (n=3 ± standard deviation)..... 163

Figure 7.12 Antimicrobial mechanism of structured specimens coated with AgNPs. 164

Nomenclature

θ	Contact angle
γ_{LG}	Surface tensions coefficient at liquid/gas interface
γ_{SG}	Surface tensions coefficient at solid/gas interface
γ_{SL}	Surface tensions coefficient at liquid/solid interface
θ_{ADV}	Advancing angle
θ_{REC}	Receding angle
θ_W	Contact angle in Wenzel state
r	Roughness factor (i.e. the ratio of the actual area of the solid surface to the planar area)
θ_{CB}	Contact angle in Cassie-Baxter state
f	The fraction of solid-liquid contact area to planar area
a	The depth of the Gaussian hole
b	The width of micropillar
$6c$	The width of micro Gaussian hole
h	The height of sag of water droplet between pillars
R	The radius of water droplet
P	Pitch of microstructures
W	Weight of water droplet
F_{LP}	Laplace pressure
E_{CB}	Surface free energy of water droplet in the Cassie-Baxter state
E_W	Surface free energy of water droplet in the Wenzel state
S_z	Maximum height

Sp	Maximum peak height
Sv	Maximum valley depth
ρ	Density
t	Time
\vec{v}	Fluid velocity.
S_m	Source item
p	Static pressure
$\bar{\tau}$	Stress tensor
g	Acceleration of gravity
\vec{F}	External body force
μ	Molecular viscosity
I	Unit tensor
F_{vol}	Volume force
k_1	The curvature of first phase
\hat{n}_1	Unit normal
γ_{12}	Surface tension coefficient between two phases
α_1	Volume fraction of first phase
\hat{n}_{wall}	Unit vectors normal to the wall
\hat{t}_{wall}	Unit vectors tangential to the wall
l	Characteristic length
We	Weber number
D^*	Dimensionless diameter
h^*	Dimensionless height
D_0	Initial diameter of water droplet

D	Instantaneous maximum diameter of the water droplet
h	Instantaneous maximum height of water droplet
E_k	Kinetic energy
E_g	Gravitational potential energy
ρ_w	Density of water
n	Total number of the element which contains the water phase
V_{element}	Volume of element
h_{element}	Height of every element
\vec{v}	Velocity of water in every element
P_{ave}	Laser average power
f_p	Pulse repetition rate
E_p	Energy of a single pulse
P_{peak}	Peak power of laser
$\Delta\tau$	Pulse duration
N	Number of irradiated pulses
t_e	Exposure time
T	Pulse period
I_s	Average laser pulse energy irradiated on a unit area of the specimen
L	Length of the specimen
S_a	Arithmetical mean height
S_{ku}	Kurtosis
S_{dr}	Developed interfacial area ratio
S_{dq}	Root mean square gradient
R_{hy}	Average ratio of Rz to Rsm

X_1, X_2, X_3	Coefficients
and X_4	
F_d	Downslope gravitational force
F_1	Retention force when the downslope gravitational force F_d opposite with laser beam feed direction
F_2	Retention force when the downslope gravitational force F_d same with the laser beam feed direction
ω_1, ω_2	Rising angles of ratchet structures
λ	Wavelength
ρ_L	Density of liquid
f_{atomiser}	Frequency of atomiser
D_L	Most probable diameter of drops
D_{Ag}	Most probable diameter of silver particle
C_{Ag}	Molarity of silver ions
M_{Ag}	Molar mass of silver
ρ_{Ag}	Density of silver

Abbreviations

3D	Three dimensional
AgNPs	Silver nanoparticles
CFD	Computational fluid dynamics
CFU	Colony-forming unit
CSF	Continuum surface force
DFM	Design-for-manufacture
FIB	Focused Ion Beam
GLASS	Global Antimicrobial Surveillance System
HAZ	Heat-affected zone
LBM	Lattice Boltzmann method
LA-CE	Laser ablation and chemical etching
MDS	Molecular dynamics simulation
PBS	Phosphate buffered saline
PDMS	Polydimethylsiloxane
POTS	1H, 1H, 2H, 2H-perfluorodecyltriethoxysilane
RF	Radio frequency
SEM	Scanning electron microscope
VOF	Volume of fluid
WHO	World Health Organization
XRD	X-ray diffraction patterns

List of Publications

The following papers are related to the research work presented in this dissertation.

Journal papers

1. Cai, Y., Chang, W., Luo, X., Sousa, A. M., Lau, K. H. A., & Qin, Y. (2018). Superhydrophobic structures on 316L stainless steel surfaces machined by nanosecond pulsed laser. *Precision Engineering*, 52, 266-275.
2. Cai, Y., Chang, W., Luo, X., & Qin, Y. (2018). Superhydrophobicity of microstructured surfaces on zirconia by nanosecond pulsed laser. *Journal of Micromanufacturing*, 2516598418799933.
3. Cai, Y., Luo, X., Liu, Z., Qin, Y., Chang, W., & Sun, Y. (2019). Product and process fingerprint for nanosecond pulsed laser ablated superhydrophobic surface. *Micromachines*, 10(3), 177.
4. Cai, Y., Luo, X., Maclean, M., Qin, Y., Duxbury, M., & Ding, F. (2019). A single-step fabrication approach for development of antimicrobial surfaces. *Journal of Materials Processing Technology*, 271, 249-260.
5. Cai, Y., Luo, X., The spreading dynamics of water droplet on surfaces at low Weber number: simulation and theoretical analysis. (Ready to submit).
6. Davoudinejad, A., Cai, Y., Pedersen, D. B., Luo, X., & Tosello, G. (2019). Fabrication of micro-structured surfaces by additive manufacturing, with simulation of dynamic contact angle. *Materials & Design*, 107839.

Conference papers

1. Cai, Y., et al. Fabrication of Hydrophobic Structures by Nanosecond Pulse Laser. 15th International Conference on Manufacturing Research, 2017.
2. Cai, Y., et al. Hydrophobicity of pyramid structures fabricated by micro milling. 2017 World Congress on Micro and Nano Manufacturing, 2017.
3. Cai, Y., et al. Simulation study of dynamic behaviour of water droplet on laser machined surface. 2018 World Congress on Micro and Nano Manufacturing, 2018.
4. Cai, Y., et al. A hybrid laser ablation and chemical etching process for manufacturing nature-inspired anisotropic superhydrophobic structures. Euspen's 19th International Conference & Exhibition, 2019.

Book chapter

Luo, X., Cai, Y., SZ Chavoshi. Hybrid Machining: Theory, Methods, and Case Studies: Chapter 1 "Introduction to hybrid machining technology", ELSEVIER.

Chapter 1 Introduction

1.1 Background

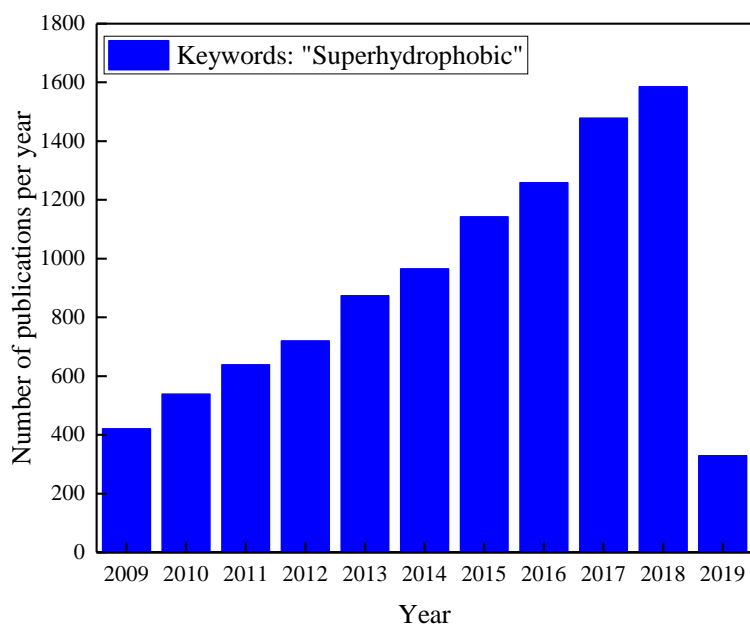
In a surgical procedure, the contact between surgical devices and blood increases the risk of forming blood clots or thrombi [1]. Similar problems exist in the operation of medical implants, like stents, catheters and tubing, due to platelet adhesion and activation [2]. Even worse, thrombosis formed after implantation can obstruct blood flow at the site of the implant and restrict downstream circulation. Furthermore, clots released from thrombi will flow with the bloodstream and occlude vessels. These problems will eventually lead to inflammation, ischemia, infarction, and irreversible tissue damage [1]. Hence, how to reduce the adhesion between blood and surgical tools or implants becomes an important research question. Many kinds of research have proven that blood platelet adhesion and activation can be controlled by modifying surface chemistry and texture [2,3]. Recently, a new strategy that employs superhydrophobicity on medical materials has attracted increased interest, particularly for its ability to reduce blood adhesion.

The second pressing issue in the healthcare field is antimicrobial resistance. With the increased consumption of antimicrobial drugs, the threat of antimicrobial resistance has become an ever-increasing trend, and its global dimensions have been increasingly recognised. According to a report from the World Health Organization's (WHO) new Global Antimicrobial Surveillance System (GLASS, <https://www.who.int/glass/en/>) in January 2018, widespread antimicrobial resistance occurs among 500,000 people with suspected bacterial infections across 22 countries [4]. Antimicrobial resistance is defined as a property of bacteria that confers the

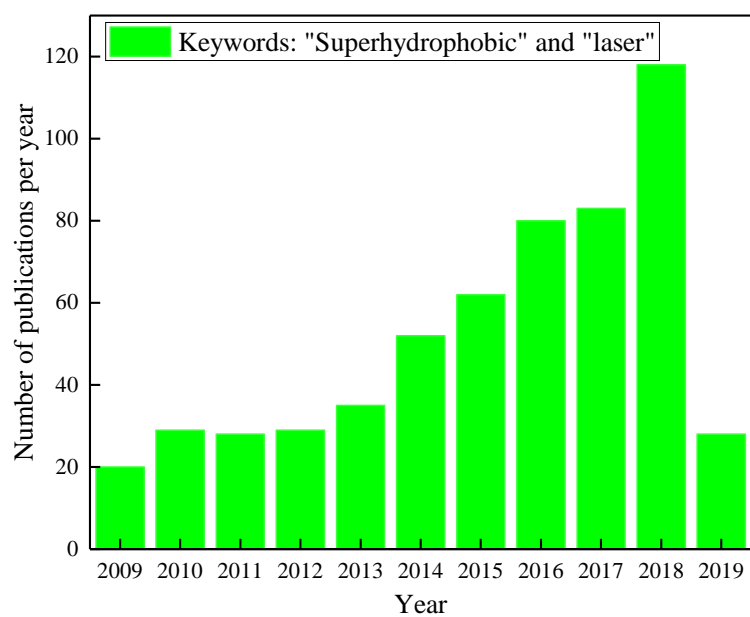
capacity to inactivate or exclude antibiotics or as a mechanism that blocks the inhibitory or killing effects of antibiotics, leading to survival despite exposure to antimicrobials [5]. Thus, the overuse of antibiotics must be prevented. In addition, surgical site infection is another serious issue, and this refers to an infection that occurs after surgery in the part of the body where the operation took place [6]. Millions of people globally become infected after a surgical procedure in low- and middle-income nations [7]. Therefore, the increasing incidence of healthcare-associated infections and antibiotics overuse has demanded alternative strategies to reduce antibiotics consumption, such as developing medical devices that possess antimicrobial properties.

Surfaces with a water contact angle higher than 150° are generally classified as superhydrophobic surfaces, and they have the ability to repel liquids, such as water and blood, due to low surface energy coatings and hierarchical micro/nano surface structures. Through evolution and natural selection, many kinds of plants and animals have developed superhydrophobicity, as seen in lotus leaves [8], rice leaves [9], butterfly wings [10] and water-strider legs [11]. Inspired by these natural surfaces, many kinds of artificial surfaces possess superhydrophobicity or antimicrobial properties that are fabricated by using numerous manufacturing processes. Furthermore, superhydrophobic surfaces have tremendous applications for self-cleaning, corrosion protection, anti-icing and drag reduction, drug delivery and microfluidic devices. As shown in Figure 1.1 (a), the past decade has witnessed a significantly increased interest in the topic of superhydrophobic. In 2018, more than 1,500 articles were published in the superhydrophobic area. Among them, publications

in the field of laser-ablated superhydrophobic surfaces showed a significant increasing trend, and more than 100 articles were published in 2018 (Figure 1.1 (b)).



(a)



(b)

Figure 1.1 Number of published articles per year: (a) keywords ‘superhydrophobic’; (b) keywords ‘superhydrophobic’ and ‘laser’— matched on 11th March 2019 in the ISI Web of Knowledge database.

AISI 316L stainless steel has been widely used for biomedical implants and surgical instruments, such as haemostat, surgical knives and dental devices. Therefore, it is meaningful to explore how to manufacture functional surfaces with superhydrophobicity and antimicrobial properties on AISI 316L stainless steel.

Laser ablation is gradually becoming a common manufacturing technique in the industry due to its high productivity, low cost and contactless process for a variety of materials, including metals, ceramics and polymers. Usually, laser ablation refers to removing material with a pulsed laser. It utilizes laser beam energy to removing material from a solid surface. At low laser flux, the material is heated by the absorbed laser energy and evaporates or sublimates; At high laser flux, the material is typically converted to a plasma [12]. Specifically, nanosecond pulsed fibre lasers are ideal for industrial applications, such as ablation, marking and micro-machining. The global fibre lasers market will increase from \$1.782 billion to \$4.403 billion between 2017 and 2025, with a compound average growth rate of 11.9% [13]. Therefore, nanosecond pulsed laser ablation has become an excellent candidate for the industrial-scale production of superhydrophobic and antimicrobial engineering surfaces on stainless steel.

1.2 Aims and objectives

This thesis aims to establish a deterministic design approach for superhydrophobic microstructures and cost-effective manufacturing processes to obtain functional surfaces possessing superhydrophobicity and antimicrobial properties on AISI 316L stainless steel. The thesis also aims to reveal the underlying mechanism of the superhydrophobic phenomenon for laser-structured surfaces. The principal objectives are:

1. To review the state-of-the-art design and manufacturing approaches for superhydrophobic and antimicrobial surfaces. Thus, knowledge gaps and research challenges can be determined.

2. To develop a deterministic design method for laser-ablated microstructures to address the crucial design-for-manufacture (DFM) issue and to explore the underlying mechanism of the superhydrophobic phenomenon.

3. To establish process and product fingerprints as critical measurable characteristics in determining the required surface topography and process parameters for superhydrophobic surfaces.

4. To advance a new process for manufacturing nature-inspired anisotropic superhydrophobic structures.

5. To develop a new innovative laser-based fabrication process for obtaining antimicrobial surfaces and for reducing the use of chemical agents.

1.3 Chapter overviews

The thesis is organised in eight chapters, as outlined in Figure 1.2.

Chapter 1 explains the background of the thesis and the quantitative analysis of the published statistics based on bibliometrics to determine the aim and objectives of this research.

Chapter 2 reviews the basic theory of wettability for different surfaces and state-of-the-art research on superhydrophobic and antimicrobial surfaces.

Chapter 3 develops a deterministic design method for laser-ablated superhydrophobic structured surfaces. The chapter also explores the underlying mechanism of the superhydrophobic phenomenon by analysing the simulation results.

Chapter 4 presents the experimental setup and methodology for laser processing and the characterisation of superhydrophobic surfaces. This chapter also presents experimental validation results.

Chapter 5 proposes the concepts of product and process fingerprints to determine the most effective process parameter and surface characterisation parameter that are sensitive to the hydrophobicity of the microstructured surface for the laser ablation process.

Chapter 6 develops a sequential process of laser ablation and chemical etching (LA-CE) for manufacturing nature-inspired anisotropic superhydrophobic structures.

Chapter 7 proposes an innovative StruCoat approach for the preparation of antimicrobial microstructures with AgNPs coatings in a single-step process. The hybrid fabrication approach combines laser ablation technology for micro-structuring, laser-assisted thermal decomposition and deposition for synthesising and coating AgNPs from silver nitrate (AgNO_3) solution simultaneously.

Chapter 8 summarises the study's conclusions, contributions to the knowledge and recommendations for future works.

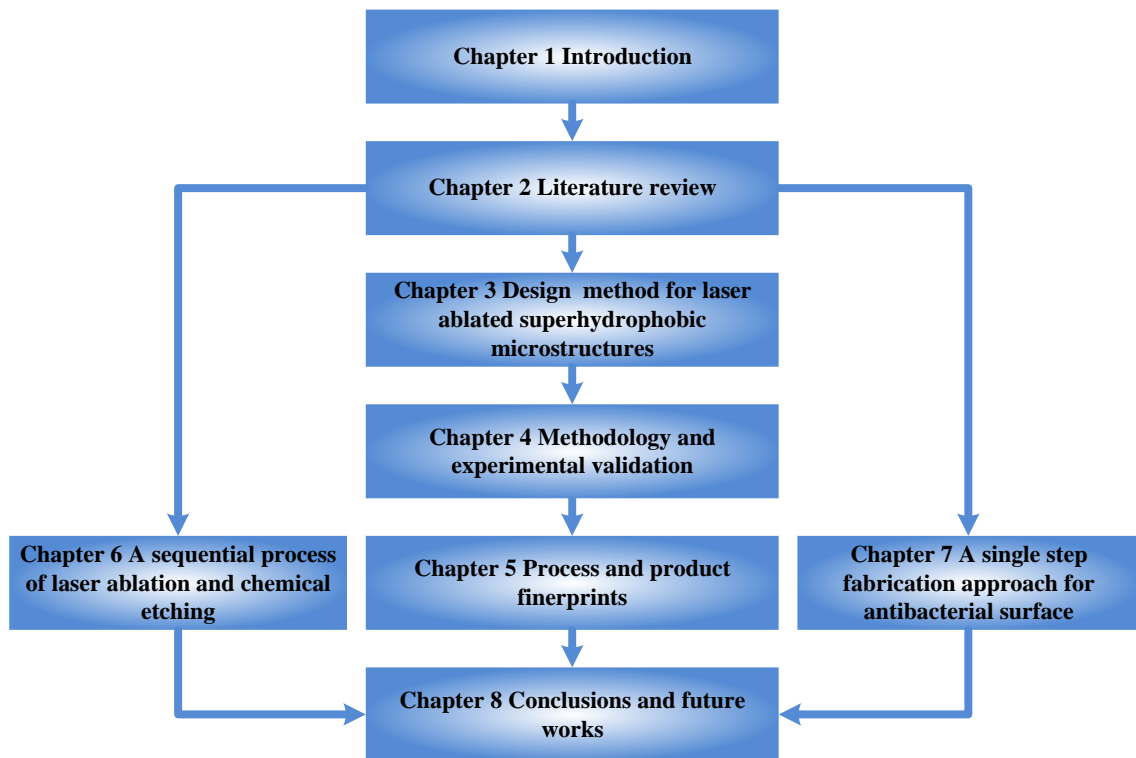


Figure 1.2 Structural outline of the thesis.

Chapter 2 Literature Review

This chapter summarises the fundamental conception of wettability and state-of-the-art superhydrophobic and antimicrobial surfaces. The chapter includes four sections: 1) wettability, 2) state-of-the-art superhydrophobic surface, 3) state-of-the-art antimicrobial surface, 4) summary of the knowledge gaps and research challenges.

2.1 Wettability

Wettability of water is the capability of a water droplet to maintain contact with a solid substrate. It is affected by surface tension, surface topography and chemistry.

2.1.1 Contact angle and sliding angle

The contact angle is commonly employed to quantify the wettability of a solid substrate (i.e. how the water droplet will spread on it). As shown in Figure 2.1 (a), the contact angle θ is defined as the angle formed by a liquid at the three-phase boundary where a liquid, gas, and solid intersect [14]. For a smooth surface, the contact angle can be expressed by Young's equation using surface tensions between among solid, liquid and gas. Young's Equation is expressed as [15]. The inward attraction of molecules causes net attractive force pointing toward the liquid. And surface tension coefficient γ is the force per unit length at a boundary.

$$\cos \theta = \frac{\gamma_{SG} - \gamma_{SL}}{\gamma_{LG}} \quad (2-1)$$

where γ_{LG} , γ_{SG} , γ_{SL} are the surface tensions coefficient at liquid/gas, solid/gas, and liquid/solid interfaces, respectively. For a determined material, its intrinsic contact angle can be calculated using Young's equation and measured by the contact angle on a smooth surface.

As shown in Figure 2.1 (b), sliding angle α is defined as the tilt angle between the substrate and the horizontal plane at which the liquid drop starts to slide off the solid surface. The advancing angle θ_{ADV} and receding angle θ_{REC} can be determined in the measurement of sliding angle. θ_{ADV} is measured at the front of the liquid droplet just before the droplet starts to slide. At the same time, θ_{REC} is measured at the back of the droplet.

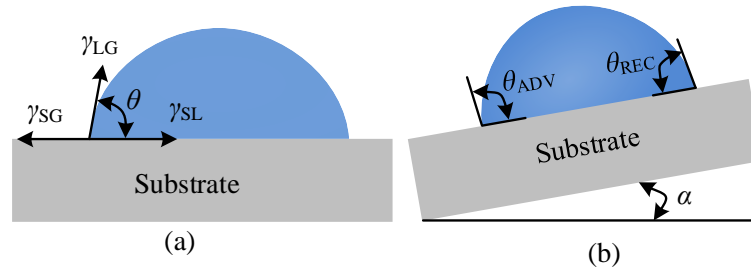


Figure 2.1 Conception of (a) contact angle and (b) sliding angle.

2.1.2 Classification of wettability

For a smooth surface, surface energy determines its contact angle. The water will not be able to wet the surface, and the surface tension will result in a high contact angle on a low energy surface as shown in Figure 2.2 (a). However, when the surface energy is high, the water droplet will tend to spread with a low contact angle, to create more interfacial surface hence to reduce surface energy as shown in Figure 2.2 (b).

Four different types of wetting state are defined according to their water droplet's contact angles. The superhydrophilic surface has a huge attraction to water, and its contact angle of water is smaller than 10° (Figure 2.2 (c)). The surface has a contact angle between 10° and 90° is classified as hydrophilic surface (Figure 2.2 (d)). Furthermore, the hydrophobic surface is defined as the surface with a contact angle higher than 90° but smaller than 150° (Figure 2.2 (e)). Typically, surfaces with a water

contact angle higher than 150° are classified as superhydrophobic surfaces (Figure 2.2

(f)).

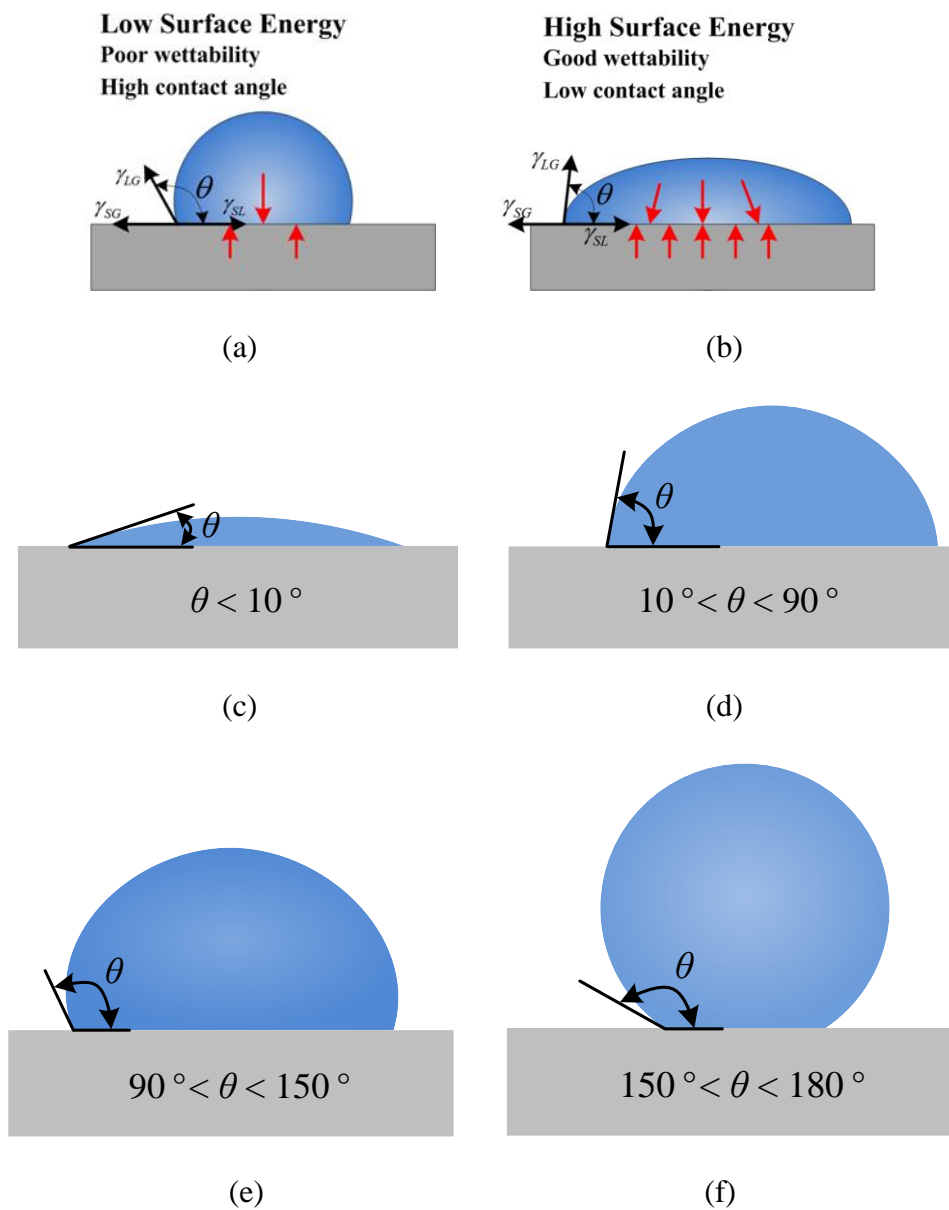


Figure 2.2 (a) low surface energy, (b) high surface energy, (c) superhydrophilic, (d) hydrophilic, (e) hydrophobic and (f) superhydrophobic.

2.1.3 Wettability of rough surfaces

In literature, two theoretical models have been developed to describe the wetting state of a droplet on a rough surface (i.e. the Wenzel and Cassie-Baxter models) [16,17].

According to the Wenzel model, the droplet maintains contact with the structures and penetrates the asperities, and the solid-liquid contact area is increased as shown in Figure 2.3 (a). The contact angle θ_w is expressed as follows:

$$\cos\theta_w = r\cos\theta \quad (2-2)$$

$$r = \frac{\text{actual surface area}}{\text{planar area}} \quad (2-3)$$

where, r is the roughness factor, which defined as the ratio of the actual area of the solid surface to the planar area and is always greater than 1. θ is the intrinsic contact angle of the material.

According to Equation 2-2, for the water droplet that has a Wenzel state on a rough surface, the contact angle will further decrease for hydrophilic materials, but increasing for hydrophobic materials.

Alternatively, according to the Cassie-Baxter model, the droplet is not able to penetrate the microstructure spaces as shown in Figure 2.3 (b). Its static contact angle θ_{CB} is expressed as:

$$\cos\theta_{CB} = -1 + f(1 + \cos\theta) \quad (2-4)$$

$$f = \frac{\text{actual solid and liquid contact area}}{\text{planar area}} \quad (2-5)$$

where f is the fraction of solid-liquid contact area to planar area.

According to Equation 2-4, for the water droplet that has a Cassie-Baxter state on a rough surface, smaller solid-liquid contact area will result in increased contact angle.

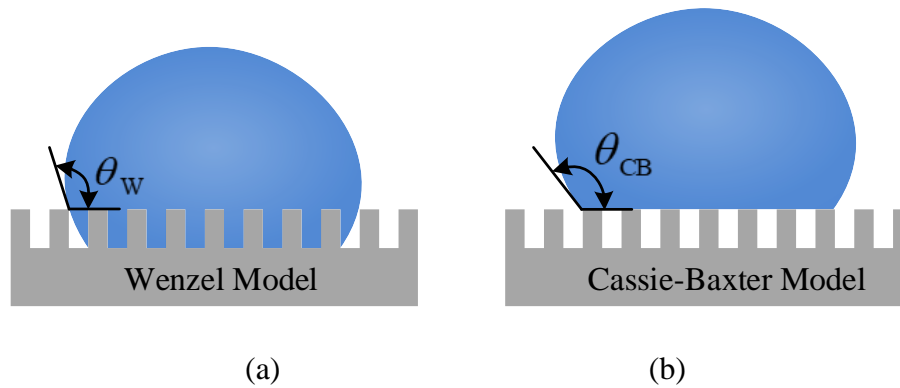


Figure 2.3 Wetting state of water droplet: (a) Wenzel state; (b) Cassie-Baxter state.

2.2 State-of-the-art of superhydrophobic surfaces

2.2.1 Natural superhydrophobic surfaces

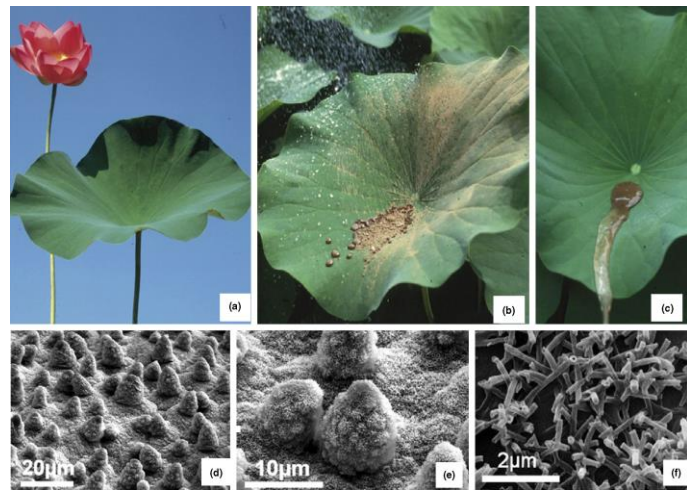
Natural biological surfaces, such as lotus leaf, rice leaf, rose petal, dragonfly and butterfly wings have attracted so much attention over the last few decades. It is mainly due to their hydrophobicity that formed during long-time evolution and natural selection [18,19].

The hydrophobicity of typical plant surfaces is listed in Table 2.1 [20–25]. For instance, the lotus leaves exhibit the unusual wetting characteristics of superhydrophobicity and self-cleaning property due to the hierarchical structures and the epicuticular wax on the surface. As shown in Figure 2.4 (a), the lotus leaves are textured with protrusions and valleys (3–10 μm) and wax tubules (70–100 nm) [19–21]. The hierarchical structure of taro leaves is composed of elliptic protrusions of 10 μm and nano-scale pins [21,22]. However, the contact angle significantly decreased

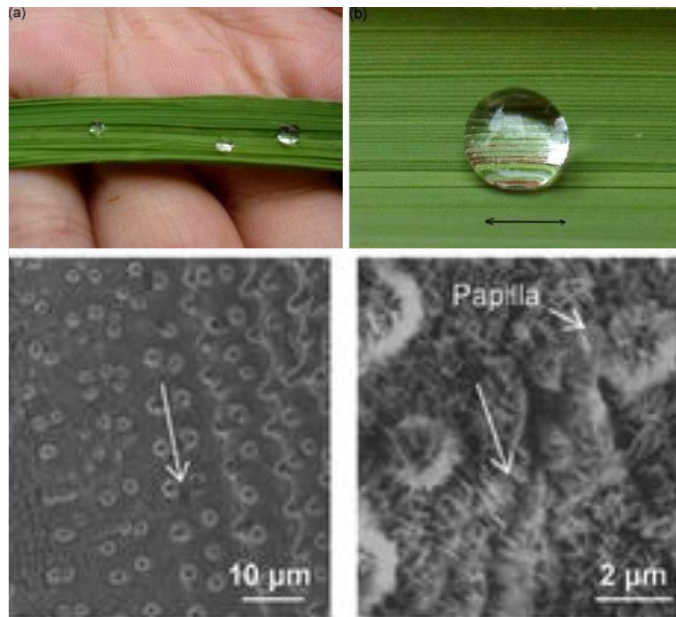
when the wax melt. Hence, the nanoscopic wax on lotus leaves also plays an important role in hydrophobicity [26,27]. Like the lotus leaves, the rice leaves also possess hierarchical structures on its surface as shown in Figure 2.4 (b). The average diameter of protrusions is around 5–8 μm but distributed along the direction that parallels to the edge [20,21,24,28]. In addition, rice leaves are also covered with epicuticular wax and longitudinal grooves. As a result, the sliding angles are different in two directions as shown in Table 2.1. Thus, the collective effect of surface chemistry and hierarchical structures is crucial for the realisation of superhydrophobicity. Besides, purple setcreasea, plant leaves of perfoliate knotweed both have a water contact angle larger than 150° and a smaller sliding angle [21]. However, rose petal has a larger contact angle but a high adhesive force for water droplet [25].

Table 2.1 Superhydrophobicity of nature plant surfaces.

Name	Contact angle ($^\circ$)	Sliding angle ($^\circ$)
India canna leaves	165°	4°
Lotus leaves	161°	3°
Taro leaves	159°	3°
Rice leaves	157°	4° (along the direction that parallels to the edge), 12° (along the direction that perpendicular to the edge)
Rose petal	152°	Adhesion



(a)



(b)

Figure 2.4 The photos and SEM images: (a) lotus leaves; (b) rice leaves [19,21,28].

The superhydrophobicity also helps animals survive from the extreme natural environment. For instance, superhydrophobicity of insect wings helps to reduce the dust adhesion and to enhance their flight capability [18,24]. Wagner et al. investigated the surface structures and wettability of 97 insect wings and found that most of them possess superhydrophobic micro/nano structures (e.g. mayflies, dragonflies, stoneflies, lacewings, scorpionflies, alderflies, caddisflies, butterflies, moths and flies et al.) [29]. The hydrophobicity of typical insect wings or legs is listed in Table 2.2

[11,29,30]. The *Papilio xuthus* is a kind of butterfly, which has greater superhydrophobicity due to the layered cuticle on the wings as shown in Figure 2.5 (a) [30]. Micro/nano hierarchical architectures on the wings of *Acrida cinerea* help improve its superhydrophobicity, while the wing of *Meimuna* shows superhydrophobicity only due to its nano-scale denticles (Figure 2.5 (b) and (c)) [30]. Furthermore, *Pantala flavescens* and *Orthetrum albistylum speciosum* possess fractal structures on the wings. However, water strider's legs rely on microseta and nanoscale grooved structures on the seta to realise its superhydrophobicity [11].

Table 2.2 Superhydrophobicity of animal surfaces.

Name	Contact angle (°)	Microstructures
<i>Papilio xuthus</i>	168 °	Layered cuticle
<i>Acrida cinerea</i>	151 °	Micro/nano
<i>Meimuna opalifera</i>	165 °	Nano-scale denticles
<i>Pantala flavescens</i>	160 °	Fractal structures
<i>Orthetrum albistylum speciosum</i>	162 °	Fractal structures
Water strider's legs	167 °	Microseta

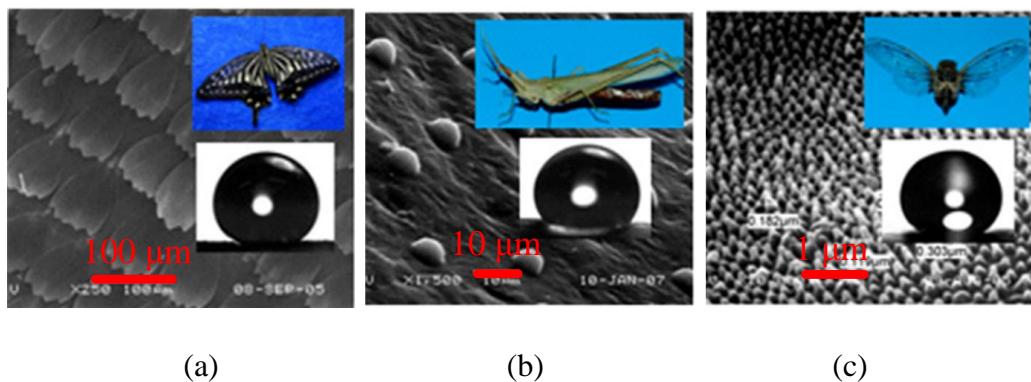


Figure 2.5 SEM images of the upper wing surfaces of insects: (a) *Papilio xuthus*; (b) *Acrida cinerea*; (c) *Meimuna opalifera* [30].

Additionally, some natural surfaces with anisotropic hydrophobicity can realise unidirectional droplet transportation, which has tremendous applications for drag reduction, drug delivery, and microfluidic devices [10,31–34]. The natural surface that possesses capabilities of transporting liquid directionally exists in rice leaves, spider silk, shorebird’s beak, butterfly wing, desert beetle, nepenthes peristome and cactus spine [35]. For example, on a butterfly wing, a water droplet will roll off along one direction with a small rolling angle while shows a pinned state along the opposite direction. The results show that the asymmetric microstructures of butterfly wings led to the unstable state of the water droplet and made it easily roll off along the radial direction away from the body [36]. Bixler et al. reported that butterfly wings possess unique surface properties that combine the anisotropic flow, superhydrophobicity and low adhesion force with water [28,31]. The author also found that aligned shingle-like scales in butterfly wings provide anisotropic flow leading to low drag, while microgrooves on its top offered superhydrophobicity and low adhesion properties [28]. The ryegrass leaf is another typical surface with the property of directional shedding-off of water, primarily due to their taper-ratchets in a periodic stripe-style array. Guo found that the reversible release and pinning of liquids at solid-liquid interfaces in the process of drop moving is the underlying mechanism to achieve characteristic directional water shedding-off [36]. All the above phenomena rely on taper-ratchets that have an open apex angle and tilt up slightly, resulting in a gradient of retention at solid-liquid interfaces along the orientation of tips [36]. Therefore, directional microstructures are indispensable to realise anisotropic superhydrophobicity.

2.2.2 Artificial superhydrophobic surfaces: pattern design

Artificial superhydrophobic surfaces, usually created by surface structuring or coating technology, have received tremendous attention in recent years [37–42]. Surface chemical composition and morphology are two critical factors in determining their hydrophobicity [43–45]. The surface chemical composition affects the intrinsic contact angle, which can be measured by a liquid droplet deposited on a smooth surface. However, in artificial or natural materials, the maximum intrinsic contact angle on a smooth surface is only approximately 120° [44,45]. For this reason, more and more structuring technologies have been developed for the fabrication of superhydrophobic surfaces. However, microstructure design is essential and critical to ensure the hydrophobicity of the specimen before the manufacturing process. Moreover, explore the underlying mechanism of the superhydrophobic phenomenon will help design the microstructures that can realise a higher contact angle ($>150^\circ$).

It was generally thought that water droplet should have a Cassie-Baxter state on the superhydrophobic substrate with microstructures. Michael and Bharat reviewed the theory of roughness-induced superhydrophobicity related with wetting transition, contact angle hysteresis and concluded that it is necessary to control microstructures at different scale levels to obtain superhydrophobicity like biological superhydrophobic surfaces [46]. Bharat's research group also analysed the relationship between different patterns (e.g. periodic and surfaces with rectangular, hemispherically topped cylindrical, conical and pyramidal asperities and the random Gaussian height distribution as shown in Figure 2.6) and contact angle [47]. The following principles are beneficial for superhydrophobicity of substrate: (1) asperities should have a high aspect ratio to provide larger surface area; (2) sharp edges may

result in pinning of the triple line, and it should be avoided in the design of microstructures; (3) smaller separation distance will help improve the stabilization of the solid-liquid-air composite interface; (4) scale of asperities should be small enough compared to water droplet size; (5) hydrophobic coating to ensure the surface has an initial contact angle larger than 90° is essential for a hydrophilic material [47]. Herminghaus et al. found that self-affine profiles of microstructures result in a superhydrophobic state [48]. Liu et al. investigated the geometric condition and energy requirement of Cassie-Baxter state on the substrate with different patterns (e.g. open to air and air proof sinusoidal microstructures, periodic array of trapezoids, mushroom-like microstructure) for achieving stable superhydrophobicity [49]. The authors reported that the approach to realise the superhydrophobic state on hydrophilic materials is not only limited to some particular topologies of the pillars or hairs on solid substrates like lotus leaves and lady's mantle. Besides, another mechanism is that the air pockets were trapped in the airproof microstructures due to a negative Laplace pressure difference [49]. Anjishnu et al. reported the design of square pillars for the robust superhydrophobic surface for applications involving quasi-static liquid transfer [50]. The above theoretical analysis laid a good foundation for the design of superhydrophobic microstructures.

Sawtooth periodic profile



Periodic profile

$$z(x) = \sum_{n=1}^{\infty} A_n \sin \frac{2\pi nx}{\lambda} + B_n \cos \frac{2\pi nx}{\lambda}$$



A surface with rectangular asperities



A surface with hemispherically topped cylindrical asperities

(a)

A surface with hemispherically topped cylindrical asperities



A surface with conical or pyramidal asperities



Random Gaussian surface

σ, β^*

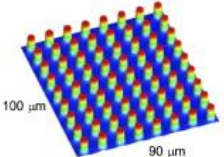
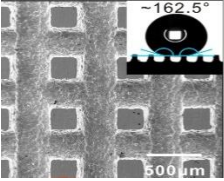
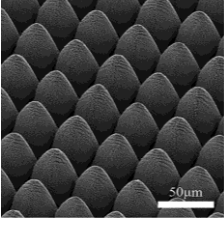
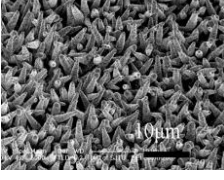
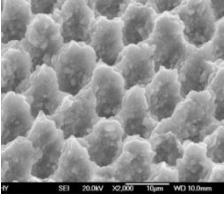


(b)

Figure 2.6 Schematics of various rough surfaces [47].

In general, the constraints in the manufacturing process often narrow the design choices and hence drive design. Apart from the geometric condition and surface energy requirements, the possible manufacturing process for microstructures with the specific shapes should be considered. Accordingly, the typical geometries in the artificial textured superhydrophobic surface as listed in Table 2.3. The regular geometric patterns include cylindrical pillars [51–58], square pillars [59–64], conical pillars [65–69], hierarchical structures [70–74] and porous structures [75–79].

Table 2.3 Geometric patterns of superhydrophobic substrates.

Researcher name	Material	Patterns	Scale	Contact angle (°)	Picture
Bhushan [51]	Silicon	Cylindrical pillars	Diameter: 5 μm ; height: 10 μm ; Pitch: 45 μm	165°	
Liu [64]	304 stainless steels	Square pillars	Length: 200 μm ; pitch: 600 μm ; height: 400 μm	162.5°	
Han [65]	Copper	Conical pillars	Diameter: around 50 μm	163°	
Wang [71]	Cu/Ni-C alloy	Hierarchical structures	Height: around 4 μm	165.5°	
Yong [75]	Single crystal n-type Si	Porous structures	Diameter of holes: 6 μm Depth of holes: 3 μm	158°	

2.2.3 Artificial superhydrophobic surfaces: numerical simulation

Section 2.2.2 shows that the research about superhydrophobic structure design is mostly limited to theoretical analysis, relatively few studies employed simulation approach to predict the hydrophobicity of designed microstructures, hence to optimise its dimensions. Furthermore, the dynamic behaviour of the water droplet impacting on a superhydrophobic surface is critical to understand the underlying mechanism of formation of the superhydrophobic phenomenon. However, it is challenging to observe the details of solid-liquid contact area through experiments due to unfavourable optical measurement condition and short impacting time [80]. Specifically, it is complicated to measure the dynamic velocity and pressure of water drops in the impacting process on the superhydrophobic surface. Hence, various numerical approaches have been put forward to explore the underlying mechanism and dynamic process of a water droplet impacting on the surface with different wettability. Molecular dynamics simulation (MDS), Lattice Boltzmann method (LBM) and volume of fluid (VOF) method are three primary numerical methods currently.

Using molecular dynamics simulation (MDS), Yan et al. investigated the impact phenomenon of a nano-sized water droplet on a pillared graphite surface [81]. The simulation results showed that the decrease of the gaps leads to a higher contact angle, and the increase of the height of pillars help increase the critical velocity of the wetting transition. In their research, the simulation was conducted for 1 ns with a time interval of 2 fs. Khan et al. used MDS to study the transfer behaviour between the Wenzel state and Cassie-Baxter state with varying pillar height [82]. Their numerical

analysis showed that it takes 500-600 ps to reach the equilibrium state. Xu et al. explored the heterogeneous nucleation of the water droplet on surfaces with different surface free energies [83]. The time step of 2 fs was chosen in their research, and each simulation was carried out for 2 ns. Thus, MDS is capable at nano-scale and ns level, but not suitable to simulate the case with a real scale such as length at millimetre level or time at the ms level.

LBM is a mesoscale modelling method, which is also developed to model the superhydrophobic phenomenon. Kevin et al. calculated forced wetting under the gravity of a water droplet on the pillared superhydrophobic surface by LBM [84]. The authors reproduced boundary conditions of the experimental contact angles of drops on a superhydrophobic surface. Li et al. also utilised LBM to investigate the dynamic behaviour of coalesced droplet jumping on the superhydrophobic surface with randomly distributed rough structures [85]. The timescale used in their simulation varied from μs to 20 ms. However, the high-speed camera recorded results confirmed that the impacting process of water droplet does not reach a stable state after 20 ms [86]. Besides, there has been very little research reported on simulation of the contact angle of the structured surface in an equilibrium state to make a comparison between simulated and experimental results.

In recent years, some researchers have resorted to VOF method, a fixed-mesh method, in which the interface between immiscible fluids is modelled as the discontinuity in characteristic function (such as volume fraction) to simulate water droplet impacted on a structured surface [87,88]. The computational studies and parameters considered in these studies are summarised in Table 2.4. Most of these studies focused on bouncing behaviour of a droplet with a very limited prediction for

static contact angle at equilibrium state. On the other hand, numerical geometries used in most of the simulations are limited to a smooth surface or simple pillar patterns. Zhang et al. investigated the shapes of water drops in the quasi-static and impacting process. The wetting and spreading characteristics of a water drop on a surface were proven to be highly dependent on the geometric parameters of the micro-texture of the surface [89]. Although they provide useful information for the droplet impacting process, these studies have still not completely revealed the dynamic behaviour of water droplet impact. The dynamic water droplet impacting process includes air pockets pressure, kinetic energy and potential energy, but they are absent in most of the research up to now.

Table 2.4 Summary of the previous works on the impact of the drops on solid surfaces.

Authors	Weber number	Impact velocity (m/s)	Contact angle (°)	Water droplet diameter (mm)	Computational time (ms)	Pattern
Liu [90]	93	1.505	154	3	13.1	Smooth surface and square pillars
Tembely [88]	27.3	1.0	154	2	60	Smooth surface
Yun [91]	27	1.0	155	1.97	8	Smooth surface
Quan [92]	0.5-6.2	0.7-3.2	110	0.045	0.052	Square pillars
Murugadoss [93]	0.93-6.2	1.17-3	114,128	0.05	0.016	Square and circular pillars
Zhang [89]	3.4-6, 3.4	0.001,1	110	0.25	30	Square Pillars

2.2.4 The manufacturing processes for superhydrophobic surfaces

Recently, tremendous attention has been devoted to the fabrication process of the superhydrophobic surface. Surface chemical composition and morphology are two

critical factors in determining the hydrophobicity. However, in artificial or natural materials, the maximum intrinsic contact angle is only approximately 120° [44,45]. For this reason, more and more approaches were developed to prepare the superhydrophobic surface on various materials, including lithography, electrochemical deposition, sol-gel processing, electrospinning, chemical etching method, 3D printing and laser ablation process.

2.2.4.1 Lithography

Lithography is a well-established technique to fabricate superhydrophobic surfaces. This process can control the microstructures precisely and with the capability of fabricating nanostructures with high resolution [94]. Many different patterns with nanospheres, nanotubes, microchannels, circular pillars, cone pillars, squared pillars, lotus-leaf-like structures have been prepared [95–103]. The substrate materials mostly include silicon, silox, titanium, polystyrene etc.

Natural surfaces (e.g. lotus leaves and insect wings) can be regarded as the moulds for the lithography process. Wang et al. employed soft-lithographic imprinting technology to prepare lotus leaf-like micro/nano structures with a maximum contact angle of 154.6° under a water droplet of $5\ \mu\text{L}$ on polymer as shown in Figure 2.7 [96]. Kang et al. fabricated a polydimethylsiloxane replica of the multi-layered scales on the wings of a Morpho butterfly by soft lithography technology [103]. Besides, some research proved that a combination of lithography and etching is also a potential technology to prepare the superhydrophobic surface. For instance, superhydrophobic micro/nano structures have been fabricated by coupling nanoimprint lithography and wet chemical etching. Pozzato et al. fabricated microchannels with width of $6\text{--}20\ \mu\text{m}$ on silox and silicon wafers by the above sequential process. Its maximum contact angle

can reach 169° [104]. Cheung et al. combined the nanosphere lithography and reactive ion etching process to fabricate nanospheres on silicon [99]. Photocatalytic lithography is another practical technique because of its capability to accurately transfer structures from photomask pattern to substrate [98,105]. Lai et al. prepared nanotube structured TiO_2 films with a contact angle of 156° using self-assembly and photocatalytic lithography technology [105]. Feng et al. introduced electron-beam lithography to obtain the superhydrophobic surface with regular primary and secondary structures [95]. Kothary and Li et al. developed colloidal lithography technology to fabricate periodic polymer nanostructures, polystyrene microspheres with contact angle larger than 150° for a water droplet of $3 \mu\text{L}$ [97,106]. However, lithography is a high-cost multistep process, requiring unique masks and can be only applied to a limited number of materials.

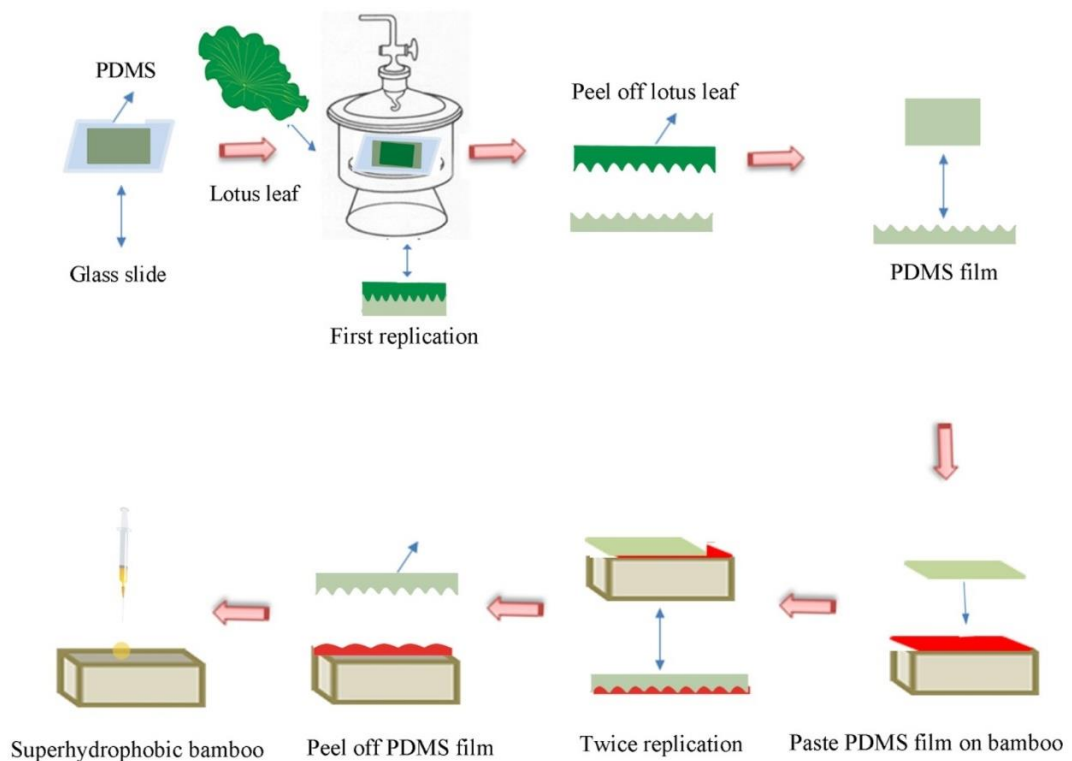


Figure 2.7 Flow chart of soft-lithographic imprinting technology to prepare lotus leaf-like micro/nano structures [96].

2.2.4.2 Electrochemical deposition

Electrochemical deposition is a widely used technique to fabricate superhydrophobic hierarchical structures or films for conductive materials (e.g. metals and its alloys), and the various electrochemical parameters can precisely control the features of the micro/nanostructure.

Liu et al. fabricated micro/nano structures on cathodic copper by an electrochemical deposition technique. The ethanol electrolyte solution contained cerium chloride and myristic acid. The obtained specimen exhibited excellent superhydrophobicity with a contact angle of 161.5° under a water droplet of $2\ \mu\text{L}$ and better corrosion inhibitive properties in comparison with smooth Cu substrate [107]. Liu et al. prepared superhydrophobic micro/nanostructured metal surfaces (e.g. copper, nickel, cadmium, zinc, gold and palladium) by electrodeposition approach, in which the sulfuric acid is essential. Then the modified specimen is heat-treated for 12 hours at $65\ ^\circ\text{C}$ to realise a maximum contact angle of 159° under a water droplet of $2\ \mu\text{L}$ [108]. Liu et al. reduced the conversion period to one minute and applied it to a magnesium alloy [109]. The reason is that the ethanol solution used in electrodeposition process contains low surface energy composition (i.e. cerium nitrate hexahydrate and myristic acid) [109]. As shown in Figure 2.8, Xu et al. employed electrodeposition method to fabricate superhydrophobic cauliflower-like micro/nano structures of nickel stearate on aluminium alloy with the maximum contact angle of $160 \pm 1^\circ$ in the solution containing ethanoic stearic acid and nickel nitrate hexahydrate [110]. However, the electrolytic solution includes more than one harmful chemical reagent, which is essential for the electrochemical deposition process. Therefore, it is not an environmental-friendly process.

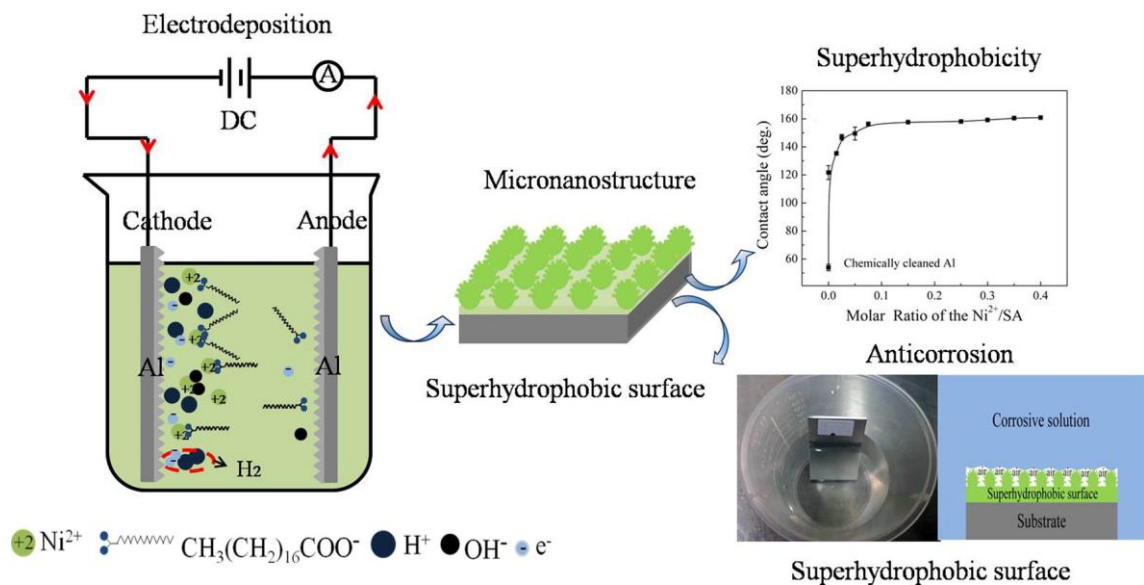


Figure 2.8 Schematic presentation of the electrodeposition process on aluminium alloy [110].

2.2.4.3 Sol-gel processing

Sol-gel processing is a typical wet-chemical technique used for the superhydrophobic coating on various materials including metal, silicon, glass and cotton fabric et al. The advantage of this approach is that the formula can be easily adjusted to control the mechanical properties and superhydrophobicity of the coating [111–119].

Liu et al. used long-chain fluoroalkylsilane to prepare transparent superhydrophobic coatings on glass via the sol-gel technology. The prepared coating exhibited a contact angle of 169° and a sliding angle of less than 5° for a water droplet of $5 \mu\text{L}$ [112]. Jiang et al. reported a sol-gel and high-temperature treatment process followed by addition of nano-silica (SiO_2) sol and organ siloxane to fabricate polyorganosiloxane superhydrophobic surfaces with a contact angle of 156.7° for a water droplet of $3 \mu\text{L}$ [113]. However, Lee et al. proposed an innovative method, which employed the Si content of the alloy to fabricate a superhydrophobic surface on

an Al/Si alloy without high-temperature processing [114]. Furthermore, for the metallic surface, Raimondo et al. reported another sol-gel route to prepare a hybrid organic-inorganic superhydrophobic coating on the copper surface with contact angle above 170° and sliding angle below 5° for a water droplet of $10\ \mu\text{L}$, which consists of alumina nanoparticles and fluoroalkylsilane film [115]. However, most of the above research requires multiple steps to prepare the superhydrophobic surface. Chen et al. synthesised superhydrophobic coatings with contact angle 158° and sliding angle of 1.8° under a water droplet of $5\ \mu\text{L}$ via a one-pot sol-gel method on glass, metal, and polymer [116]. As shown in Figure 2.9, Yang incorporated fluorinated TiO_2 nanoparticles into cotton fabric, and the contact angle reached 152.5° under a water droplet of $4\ \mu\text{L}$ [117]. Similarly, Jiang et al. also reported a one-step sol-gel process to prepared a superhydrophobic surface on soft material (i.e. cotton textile) [118]. However, the sol-gel process has some limitations too, for instance, the precursors are generally costly, and the preparation process involves several chemical ingredients in the solution.

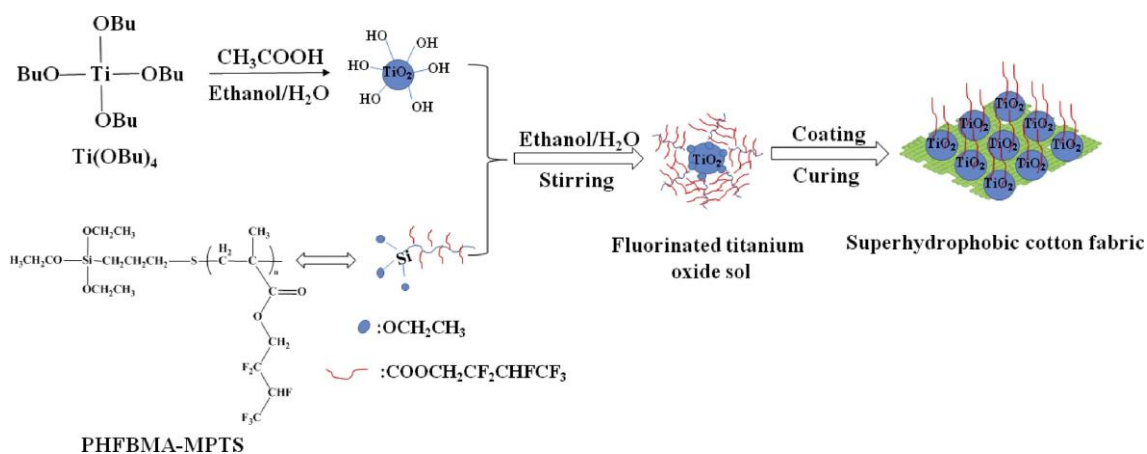


Figure 2.9 Reaction route of fluorinated TiO_2 sol preparation and coating procedure [117].

2.2.4.4 Electrospinning

Electrospinning is a method used for the production of micro/nano fibre from polymer solutions and is driven by electrostatic forces. Electrospinning has been shown that to fabricate superhydrophobic nanofiber membranes by coating micro/nano fibres on substrates [120–125].

Ma et al. reported a flexible method by combination of electrospinning and chemical vapour deposition to produce superhydrophobic poly (caprolactone) fabrics, which have diameters ranging from 600 to 2200 nm and exhibited a contact angle of 175° and a sliding angle less than 2.5° for a 20 mg droplet [120]. As shown in Figure 2.10, Su et al. demonstrated another hybrid process to fabricate highly superhydrophobic porous membranes with a contact angle of 163° and sliding angle of 3° for a water droplet of 10 μL by the combination of electrospaying of silica colloids and electrospinning of poly (vinylidene fluoride) solutions [121]. Then the poly (vinylidene fluoride) membranes with controllable structure and adjustable wettability from hydrophobic to superhydrophobic or superoleophilic were prepared by adjusting the weight percentage of ZnO nanoparticles, ammonia or 1H, 1H, 2H, 2H-perfluorodecyltriethoxysilane (POTS) ammonia treatment [122]. Except for polymer materials, some electrospinning processes can also be applied to metal material. For instance, Radwan et al. fabricated electrospun nanocomposite coatings on Al substrates using polystyrene and aluminium oxide [124]. The authors found that the addition of Al_2O_3 nanoparticles results in the increase of surface roughness. The specimen with the highest surface roughness R_a possesses a maximum value of contact angle of 155° under a water droplet of 4 μL [124]. However, electrospinning can only be used with a limited number of polymers.

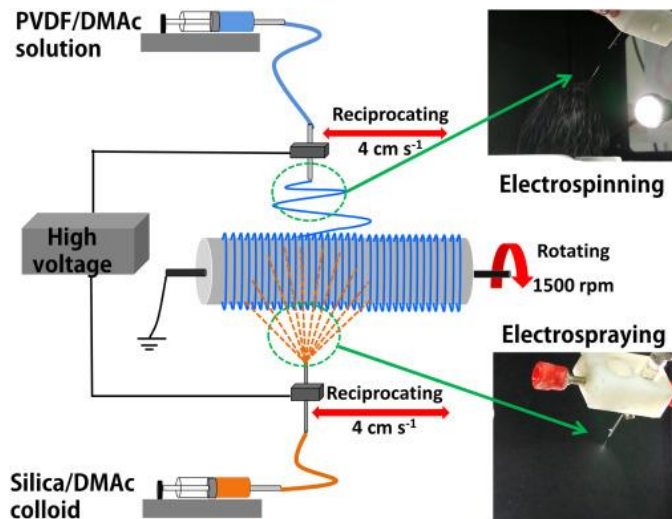


Figure 2.10 Schematic process of membrane preparation via simultaneous electrospaying and electrospinning [121].

2.2.4.5 Chemical etching

Chemical etching is a common method for manufacturing hierarchical structures by chemical ion replacement reaction. Usually, the obtained micro/nano structures require modifications by chemical reagents to reduce the surface free energy [126–135].

Some researchers employed acid solution in the chemical etching process to prepare superhydrophobic surfaces [126–131]. Kumar et al. employed a chemical etching process to synthesized superhydrophobic aluminium surfaces with a mixture of hydrochloric and nitric acids, followed by treatment with hexadecyltrimethoxysilane [126]. Li et al. reported a chemical etching process on the iron plate to obtain micro/nano structures and then modified with stearic acid [127]. The contact angle of specimens employed hydrochloric acid (HCl) solution and silver nitrate (AgNO_3) solution are 152° and 156° respectively under a water droplet of $5 \mu\text{L}$ [127]. Gao et al. etched Farmland-like textures on the titanium substrate (with a water

contact angle of 164° and a sliding angle of 2° for a water droplet of $10\ \mu\text{L}$ by a chemical etching method with an aqueous solution containing 72% H_2SO_4 [128]. As shown in Figure 2.11, Ganne et al. prepared the superhydrophobic surface with maximum contact angle of 168° for a water droplet of $15\ \mu\text{L}$ on aluminium alloy by wet chemical etching in a solution of HCl and HF , then anodic oxidation in phosphoric acid solution, and modified by fluorooxysilane lastly [129]. Han et al. demonstrated a combined chemical etching and heat treatment process to manufacture a superhydrophobic brass surface. A contact angle of up to 153.6° was attained after modification with stearic acid [130]. Kim et al. used HF solution to etch the stainless steel plates first, then followed by a fluorination process. The obtained sample had a contact angle of 166° and a sliding angle of 5° for a water droplet of $5\ \mu\text{L}$ [131].

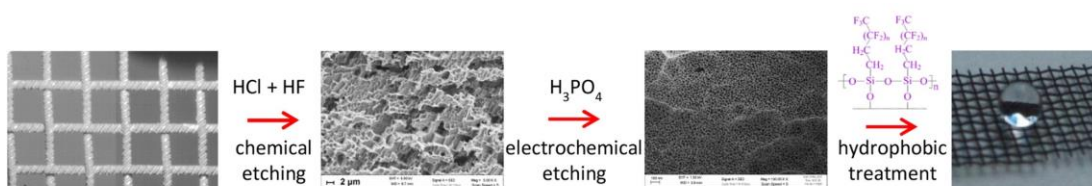


Figure 2.11 The flow chart of combined wet chemical etching and anodic oxidation method [129].

In addition, some other researchers utilised the alkaline solution in the chemical etching process to prepare superhydrophobic surfaces [132–135]. Huang et al. employed a chemical etching process by NaOH solution to obtain flake-like micro-nanostructure morphology, and then used passivation by ethanolic stearic acid to realise the contact angle of 156° [132]. Choi et al. investigated surface morphology and superhydrophobicity by three different chemical etching solutions: NaOH solution, Ni -containing solution and Zn containing solution [134]. The experimental results indicated that all these three methods could be used to prepare

superhydrophobic specimens. Varshney et al. employed two-step and one-step chemical etching processes using potassium hydroxide and lauric acid solutions to prepare superhydrophobic coatings on aluminium substrates [135]. Thus, it can be concluded that the chemical reagents of acid or alkaline solutions are essential in chemical etching, which is not an environmental-friendly process.

2.2.4.6 3D printing

Recently, additive manufacturing (3D printing) has created new opportunities for the manufacture of superhydrophobic structures, as it does not require complicated processing steps, templates or moulds. He et al. prepared microporous Polydimethylsiloxane structures with a contact angle of 155° (water droplet of $5\ \mu\text{L}$) by 3D printing technology, as shown in Figure 2.12 [136]. Lv et al. reported a similar 3D printing process to fabricate ordered porous structure with a contact angle of 160° for oil-water separation by nanosilica-filled polydimethylsiloxane (PDMS) ink [137]. Yang et al. employed immersed surface accumulation 3D printing process to construct microscale artificial hairs with eggbeater heads with a maximum contact angle of 170° for a water droplet with a diameter of about 2.6 mm. Simultaneously, carbon nanotubes were mixed to the photocurable resins to enhance the surface roughness and mechanical strength of the microstructures [138]. Yuan et al. developed selective laser sintering technology to manufacture superhydrophobic surfaces with a contact angle of 161° on polysulfone membranes [139]. Graeber et al. generated alternating, protruding, and indented truncated cones with a scale of 0.1 mm by 3D printing technology on the photocurable polymer, then employed soft lithography and spray coating to fabricate superhydrophobic surfaces with a maximum contact angle of 167° for a pure water droplet with a diameter of 2.2 mm [140]. In addition, except liquid

based 3D printing technology, fused deposition 3D printers also can be used for fabrication of superhydrophobic surfaces. Lee et al. printed line and grid patterns by the polylactic acid filament, then silica nanoparticles and 2-Butanone are used for dip coating to reduce surface energy to obtain the superhydrophobic surface with contact angle of 158° for a water droplet of $11 \mu\text{L}$ [141]. However, most of the printed materials for superhydrophobic structures are still limited to plastic or polymer materials.

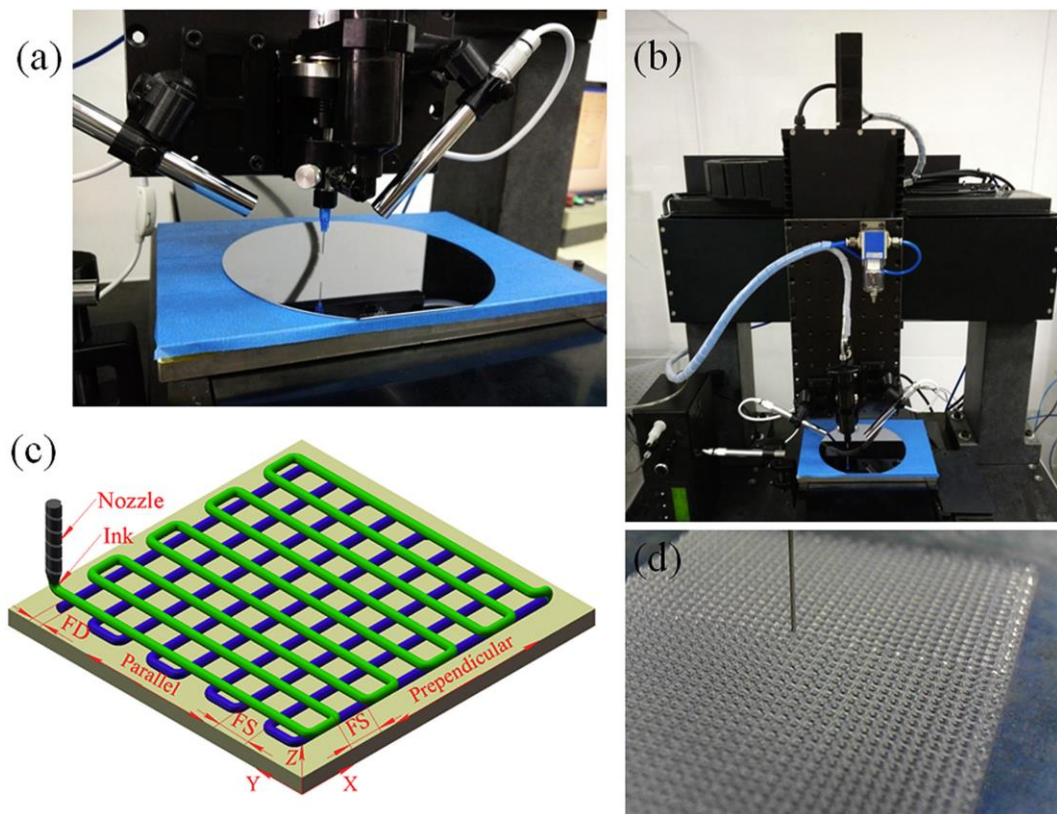


Figure 2.12 (a) 3D printer, (b) An overview image of the 3D printer for direct writing of PDMS ink, (c) schematic of 3D printing process and (d) anisotropic porous PDMS film [136].

2.2.4.7 Laser ablation

The primary challenges for industrial application of superhydrophobic surface are achieving high production efficiency with low production cost. The laser ablation process is a reliable manufacturing method due to its high-efficiency and contactless characteristics. Most of the research reported that hierarchical structures, which consist of micron and nanoscale level patterns, could be generated using the laser ablation to improve surface hydrophobicity. Femtosecond, picosecond and nanosecond pulsed laser are three major types used for the laser ablation process of the superhydrophobic surface.

Femtosecond pulsed laser ablation process

A femtosecond pulsed laser is a laser which emits pulses with a duration of lower than 1 ps (10^{-12} s). It has been demonstrated as a promising technique to fabricate superhydrophobic structures on various materials, such as silicon, glass, polydimethylsiloxane, stainless steel, platinum, brass and titanium. The state of the art of femtosecond pulsed laser ablated superhydrophobic surfaces is listed as Table 2.5. The laser fluence is a critical parameter that determines the hydrophobicity of specimens. The femtosecond laser ablation process was employed to fabricate micro/nano structures on silicon substrate [75,142,143]. Superhydrophobic surfaces with a maximum contact angle of 160° were obtained after coating a layer of fluoroalkylsilane molecules [142]. The authors found that the contact angle increases rapidly when the laser fluence varies between 0.26 to 0.4 J/cm^2 . Then the contact angle remains constant with the laser fluence further increased to 0.9 J/cm^2 [142]. As shown in Figure 2.13, femtosecond laser ablation also has the potential to manufacture periodic micro-gratings with superhydrophobicity on transparent glass surfaces with

only a minor effect on transparency [144]. The microstructured surface possesses a contact angle ranges from 152° to 155° after silanization process [144].

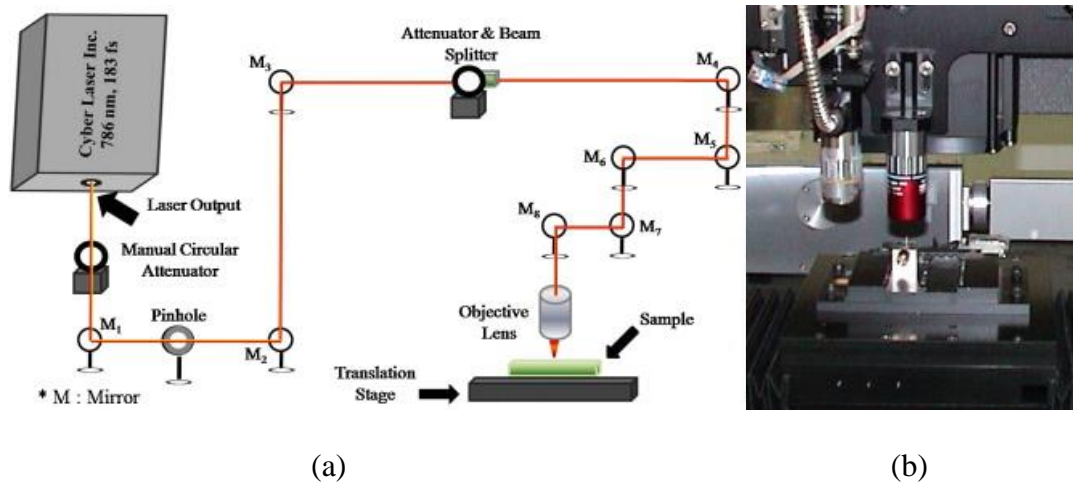


Figure 2.13 Experimental setup for the fabrication of superhydrophobic soda-lime glass surface. (a) Schematic diagram; (b) photograph [144].

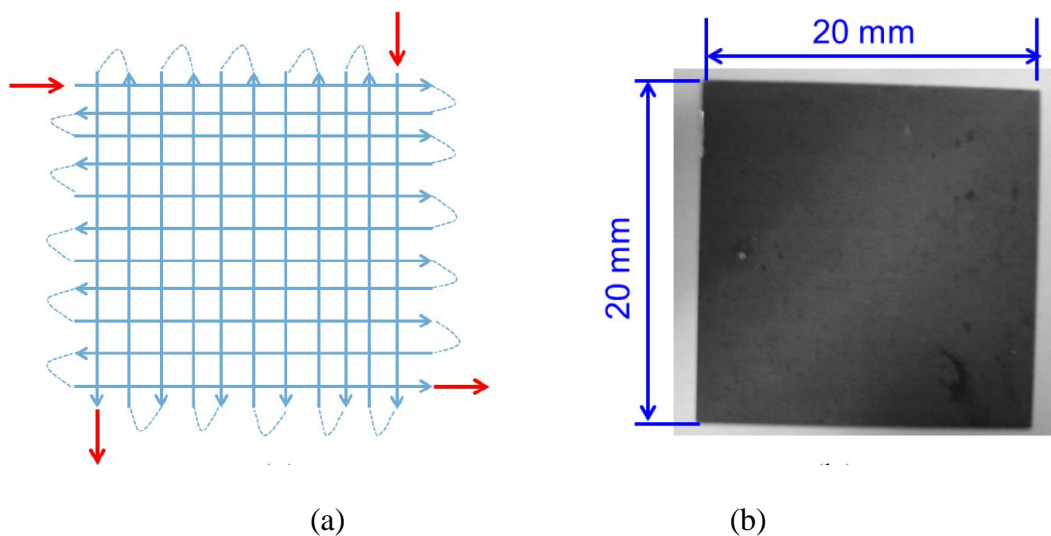
The studies discussed above all required follow-on silanization post process to reduce the surface energy after developing micro/nano structures on the surface because silicon and glass are intrinsic hydrophilic materials. PDMS surface also has high transparency, but there is no requirement of silanization process to realise superhydrophobicity after femtosecond laser ablation, because its intrinsic contact angle is 110° [145,146]. For superhydrophobic surfaces on metallic materials, Wu et al. fabricated periodic ripples and periodic cone-shaped spikes on AISI 316L stainless steel, and realised a maximal contact angle of 166° and a sliding angle of 4° [147]; Fadeeva et al. fabricated structures mimicking lotus leaf by femtosecond laser ablation process [148].

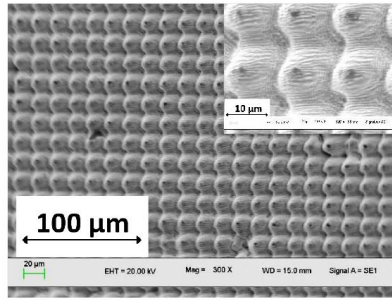
Table 2.5 Femtosecond pulsed laser ablated superhydrophobic surfaces.

Authors	Laser pulse duration (fs)	Laser fluence (J/cm ²)	Post-process	Volume of water droplet (μL)	Contact angle (°)	Sliding angle (°)	Materials
Baldacchini [142]	100	0.22-0.9	Silanization	5	160	N/A	Silicon
Zhang [143]	30	N/A	Silanization	9	164	5	Silicon
Yong [75]	30	N/A	Silanization	9	158	4	Silicon
Ahsan [144]	183	N/A	Silanization	4	155	N/A	Glass
Boinovich [149]	200	5	Silanization	15	166	8	Glass
Gong [145]	700	4.68	No	4 and 9	154.5	6	Polydimethylsiloxane
Yong [146]	50	N/A	No	7	162	N/A	Polydimethylsiloxane
Wu [147]	130	0.08-0.2	Silanization	1	166.3	4.2	AISI 316L stainless steel
Rukosuyev [150]	120	N/A	No	8	165.8	N/A	AISI 316L stainless steel
Kam [151]	490	0.1-1	Silanization	7	150	N/A	AISI 316L stainless steel
Moradi [152]	150	1.5-480	Silanization	4	164	4	AISI 316L stainless steel
Vorobyev [153]	65	3.9-9.8	No	N/A	158	4	Platinum, titanium, and brass
Fadeeva [148]	30	20-100	No	10	166	N/A	Titanium
Yong [154]	50	N/A	No	N/A	159.5	8	Zinc
Long [155]	800	N/A	Silanization	4.5	158	4	Copper

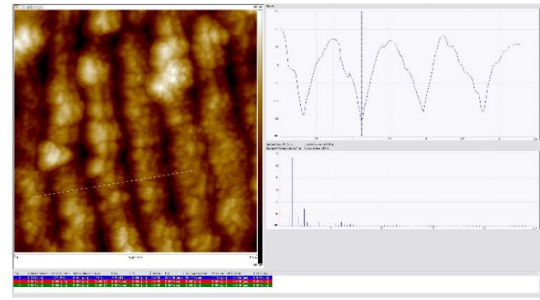
Picosecond pulsed laser ablation process

A picosecond pulsed laser has a duration between 1 ps and some tens of picoseconds, it also belongs to one of the ultrashort pulse lasers. The research recently employed picosecond pulsed laser to prepare superhydrophobic surface is summarized in Table 2.6. Jagdheesh et al. found that an increase in the number of pulses per irradiated spot increased the surface roughness, and the nanoscale structures tend to transform into hierarchical structures [156]. Jiang et al. reported fabrication of micro/nano structures on titanium substrate as a mould insert by picosecond laser ablation process, and then soft lithography technology was used to replicate the structures on a plastic polymer material [157]. Long et al. fabricated surfaces with structural colouration and superhydrophobicity by picosecond laser on copper [158]. As shown in Figure 2.14, Wang et al. manufactured hierarchical surface structure of regular micro-bumps with nano-ripples on nickel surface [159]. Faas et al. found that heat accumulation has a strong effect on surface structuring rates and a maximum contact angle of 173° has been realised on AISI 316L stainless steel by picosecond laser ablation process [160].





(c)



(d)

Figure 2.14 Laser fabricated 2D array asperities (a) laser beam path, (b) overview photo, (c) SEM images, and (d) AFM measurement result [159].

Table 2.6 Picosecond pulsed laser ablated superhydrophobic surfaces.

Authors	Laser pulse duration (ps)	Laser fluence (J/cm ²)	Post-process	Volume of water droplet (μL)	Contact angle (°)	Sliding angle (°)	Materials
Jiang [157]	8.1	0.1-2	No	2	158	N/A	Titanium
Long [158,161]	10	0.43, 22.4	Silanization	3	154	11	Copper, aluminium
Wang [159]	10.3	1.43	No	1	159	5	Nickel
Zheng [162]	10		Silanization	N/A	159	N/A	Ti-6Al-4V
Jagdheesh [156,163]	6.7	0.098	Silanization	2	152	N/A	304L stainless steel, Ti-6Al-4V, alumina
Faas [160]	8	0.71	No	N/A	173	N/A	AISI 316L stainless steel
Sun [164]	10	4,9	Silanization	3	152	3	AISI 304L stainless steel
Rajab [165]	N/A	0.625	Silanization	6	160	N/A	AISI 316L stainless steel

Nanosecond pulsed laser ablation process

Nanosecond pulsed lasers are lasers emitting pulses with nanosecond durations. Compared with femtosecond or picosecond pulse lasers, the nanosecond pulsed laser has the advantages of low-cost and high-efficiency. Examples of research that recently employed nanosecond pulsed lasers to prepare superhydrophobic surfaces are summarised in Table 2.7.

Combining laser ablated micro/nano structures and surface energy reduction is crucial to fabricate superhydrophobic surface. Currently, three different processes are put forward to realise the superhydrophobicity of laser ablated specimens and can be summarised as follows:

First of all, the hydrophobicity of nanosecond pulsed laser ablated surface will change with time in ambient air due to modification of the surface chemistry [42,119,166–169]. As shown in Figure 2.15, Gregorčič et al. reported that the transition from superhydrophilic to superhydrophobic surface with a contact angle of 153° happened after 30 days by laser ablation [166]. Yang et al. prepared nanosecond laser ablated superhydrophobic surface on aluminium and Inconel 718 material after exposure to ambient air of 30 days [167,170]. The author found that the gradual increase of contact angle was attributed to the absorbed organic matter (i.e. nonpolar C–C(H) bond) onto the laser ablated surfaces from the ambient environment, which helps reduce surface free energy slowly [167,170]. Duong et al. fabricated superhydrophobic patterns on 304 stainless steel copper and brass surfaces by nanosecond laser and investigated the time effects on superhydrophobicity of specimen [168,169]. The author found that the laser ablated 304 stainless surfaces require 13 days to realise superhydrophobic transition under ambient conditions [168].

For copper, the superhydrophobic transition finished after 11 days in ambient air due to partial deoxidization of CuO into Cu₂O [171]. Trdan et al. investigated the superhydrophobicity transition process of laser ablated AISI 316L stainless steel [42]. The author concluded that superhydrophobic state with a contact angle of 168 ° and a sliding angle below 3 ° was achieved in 1 month [42]. Hence, the transition time from hydrophilic to superhydrophobic in ambient air depends on material types.

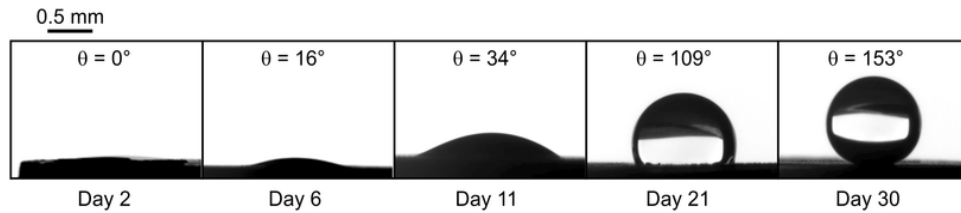


Figure 2.15 Superhydrophobicity development after nanosecond pulsed laser ablation [166].

Secondly, some other researchers reported that additional heat treatment can reduce the time of wettability change from hydrophilicity to superhydrophobicity. Ngo's research group used nanosecond pulsed laser ablation process and heat treatment approach to manufacture superhydrophobic patterns on titanium, aluminium, copper and 304 stainless steel substrates [172–175]. As shown in Figure 2.16, the laser ablated titanium specimens can attain contact angles larger than 160 ° and a sliding angle smaller than 10 ° after heat treatment in an oven at 200 °C for six hours [172]. More importantly, the authors found that the superhydrophobic transition time was reduced for titanium and aluminium with increasing heating temperature as the heat treatment accelerated the organic adsorption process of hydrophobic groups (e.g. -CH₃ and -CH₂) [173]. For 304 stainless steel, the grid patterns were fabricated by a nanosecond pulsed laser; then heat treatment was conducted at 100 °C for 20 hours to prepare the surface with a contact angle of 175 ° and sliding angle smaller than

5° [175]. Wan et al. fabricated microchannels on stainless steel through the combination of nanosecond laser ablation and 150 °C heat treatment in an oven for 24 hours, which realised a contact angle of 152° [176]. Patil et al. employed nanosecond pulsed laser to prepare microstructures on Ti-6Al-4V substrate first, then a 300 °C annealing treatment was used to realise the rapid wettability transition from hydrophilic to the superhydrophobic surface [177]. He et al. prepared superhydrophobic surfaces on copper by nanosecond laser ablation and ethanol assisted 150 °C annealing treatment; the underlying mechanism is that the ethanol can help transition from CuO to hydrophobic materials Cu₂O [178].

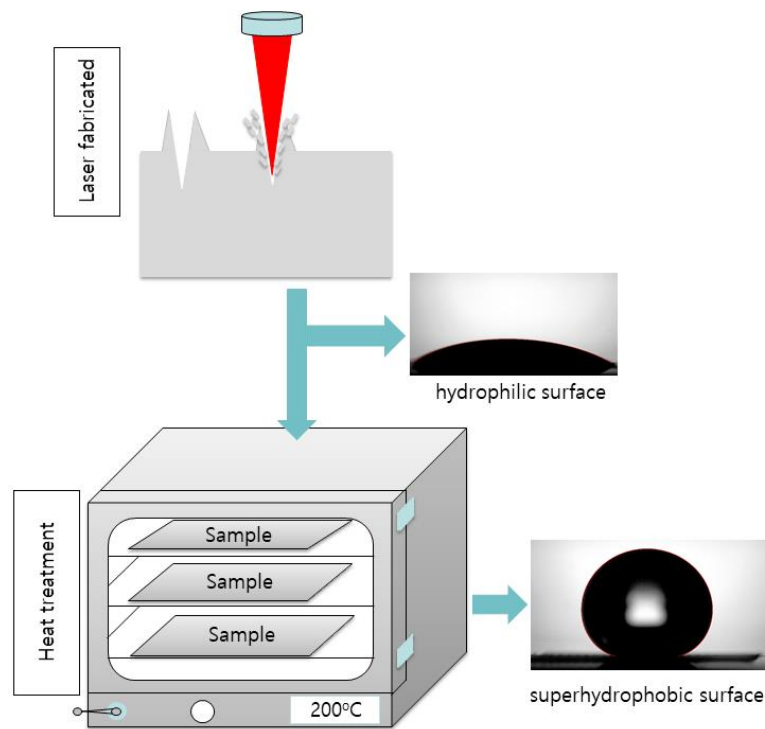


Figure 2.16 Schematic of UV nanosecond-pulsed laser ablation and heat treatment process [172].

Finally, silanization by a chemical reagent is the most effective approach to reduce the surface energy of laser ablated specimens, and the superhydrophobicity of

specimens can be realised in a very short time. As shown in Figure 2.17, Ma et al. proposed nanosecond laser ablation and chemical silanization process to construct a superhydrophobic surface on carbon steel [179]. Wang’s research group presented a combination technology of nanosecond laser ablation and organic polysilazane or perhydropolysilazan coating to prepare superhydrophobic Ti-6Al-4V and carbon steel surface [180,181]. Besides, a similar process is successful in preparing the superhydrophobic surface on copper, aluminium alloy [182,183]. Conradi et al. presented a new method to fabricate AISI 316L stainless steel superhydrophobic surfaces, which combined laser texturing and coating of fluoroalkylsilane functionalized 30 nm silica nanoparticles [184].

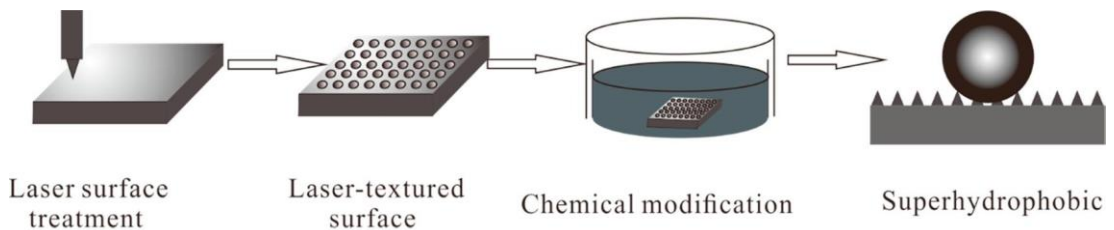


Figure 2.17 The schematic diagram of fabricating laser ablated superhydrophobic steel [179].

Table 2.7 Nanosecond pulsed laser ablated superhydrophobic surfaces.

Authors	Laser pulse duration (ns)	Laser fluence (J/cm^2)	Post-process	Volume of water droplet (μL)	Contact angle ($^\circ$)	Sliding angle ($^\circ$)	Materials
Gregorčič [166]	95	31	Exposed to ambient air	5	153	N/A	AISI 316L stainless steel
Yang [167,170]	50	25.46	Exposed to	8	153	5	1060 aluminium, Inconel 718

			ambient air				
Duong [168,169]	220	55-93	Exposed to ambient air	5	153	3-4	AISI 304 stainless steel, copper, brass
Trdan [42]	40	N/A	Exposed to ambient air	5	168	3	AISI 316L stainless steel
Ngo [172– 175]	20	N/A	Heat treatment	11	169	5	Titanium, aluminium, copper, AISI 304 stainless steel
Wan [176]	100	N/A	Heat treatment	4	152	N/A	AISI 304 stainless steel
Patil [177]	20	N/A	Heat treatment	3	162	N/A	Ti-6Al-4V textured
He [178]	25	N/A	Heat treatment	4	161	N/A	Copper
Ma [179]	220	19	Silanizati on	3	162	N/A	Carbon steel
Hu [180,181]	100	N/A	Silanizati on	4	164	3.5	Ti-6Al-4V, Carbon steel
Long [182]	20-200	N/A	Silanizati on	5	160	3	Copper
Lei [183]	30	5.52	Silanizati on	10	154	N/A	Aluminium alloy
Conradi [184]	95	31	FAS- SiO2 nanoparti cles.	5	153	N/A	AISI 316L stainless steel

Besides the above post processes, some researchers also investigated the effect of laser ablated micro/nanostructures, the pitch of microstructures and laser pulse energy on hydrophobicity. Yang et al. investigated the wettability transition

mechanism of laser ablated aluminium substrate, and the results indicated that laser-ablated microstructures had amplified effects on the hydrophobicity of the specimen as the water droplet is easier to form Cassie-Baxter state on laser ablated specimen [167]. Long et al. reported the effect of the laser pulse energy and width on the morphology of micro/nanostructures on a copper surface. They found that the morphology of the laser ablated structures is more sensitive to the laser pulse energy when nanosecond lasers with long pulse widths are used. Slightly decreasing the laser pulse energy results in the non-formation of hierarchical micro/nano-structures [182,185]. Gregorcic et al. fabricated an AISI 316L stainless steel specimen with a pitch of 50 μm at average pulse power of 0.6 W and 97% pulse overlapping rate and achieved a static contact angle of 153° [166]. Long and Gregorcic both reported that variations of the pitch of channels resulted in entirely different surface morphologies- from the highly porous surface to well-separated microchannels, whose width and depth depend on laser fluence [166]. Duong et al. concluded that surface roughness could be well controlled by laser power. The arithmetical mean height S_a increased linearly when laser fluence was higher than 33 J/cm^2 . The roughness was around 2 and 7 times larger than that of the untextured surface under fluences of 36 and 48 J/cm^2 , respectively [168].

Furthermore, the effect of laser fluence and line separation on the contact angle of laser structured surfaces were investigated. Experimental results showed that the specimens possessing superhydrophobicity have pitches of 50–150 μm and are machined at the laser fluence of 36 J/cm^2 [168]. Conradi et al. discovered that higher line density resulted in a higher contact angle. However, the average surface roughness S_a increased first then further decreased gradually with the increase of line density

[184]. Thus, these studies have indicated that the laser machining parameters significantly affect the hydrophobicity of the specimens while surface topography is a crucial factor to determine the superhydrophobicity of the specimen.

The advantages and disadvantages of different manufacturing processes for superhydrophobic surface are summarised in Table 2.8. It can conclude that nanosecond pulsed laser ablation is a good candidate for industrial scale production of superhydrophobic surface. Hence, nanosecond pulsed laser ablation is choosing as the process for manufacturing functional surfaces on stainless steel in this study.

Table 2.8 Advantages and disadvantages of different manufacturing process.

Manufacturing process	Advantages	Disadvantages
Lithography	High precise; high resolution.	High-cost multistep process; require masks; limited types of materials used.
Electrochemical deposition	High precise; high throughput.	Require templates; Limitation in use of electrical conductive materials.
Sol-gel processing	Formula can be easily adjusted.	Limited types of materials used; difficult to apply on large scale area.
Electrospinning	Continues process; easy to control the size of micro/nano fibres.	Limited on polymer solutions; toxic solutions.
Chemical etching	Low cost and simple process; controllable etching rate.	Chemical contamination;
3D printing	Flexible process; easy to print complex structures.	Limited choice of materials; low feature resolution.
Femtosecond pulsed laser ablation	High precision; non-contact machining.	High-cost; low efficiency.
Picosecond pulsed laser ablation	Precision machining; non-contact machining.	High-cost; low efficiency.
Nanosecond pulsed laser ablation	High efficiency and low cost; non-contact machining.	Heat-affected zone

2.3 State-of-the-art of antimicrobial surface

2.3.1 Introduction

Surgical site infections are one of the most devastating complications after surgical procedures. More importantly, with the increased use of antimicrobial drugs, the threat of antimicrobial resistance is significant and is increasingly being recognised as a global problem [186]. Thus, the increasing incidence of healthcare-associated infections and overuse of antibiotics leads to the need for alternative strategies which can decrease antibiotic consumption, such as the development of antimicrobial medical devices.

Surface treatment of medical devices by coating with antimicrobial agents is a promising solution. Currently, silver and its compounds are the most commonly used antimicrobial materials, due to their strong, broad-spectrum antimicrobial effects against bacteria, fungi, and viruses [187]. Recently, silver nanoparticles (AgNPs) have received interest for antimicrobial applications as they can enter bacterial membranes and deactivate respiratory chain dehydrogenases to inhibit respiration and growth of microorganisms [187]. Due to this, AgNPs are believed to have good potential for application in silver-based dressings and silver-coated medical devices without promoting microbial resistance [188].

2.3.2 Preparation of antimicrobial silver-containing surface

A variety of physical and chemical methods have been developed to prepare AgNPs on biomaterial substrates. For physical approaches, Cao et al. employed silver plasma immersion ion implantation process to embed AgNPs on titanium substrates [189]. The prepared specimens were extremely effective in inhibiting both *Escherichia*

coli and *Staphylococcus aureus* strains while exhibiting noticeable activity in promoting the propagation of the osteoblast-like cells (MG63) [189]. Echeverrigaray et al. prepared stainless steel specimens with silver atoms by ion implantation process at low energy (4 keV) on a reactive low voltage ion plating equipment as shown in Figure 2.18 [190]. Ferraris et al. deposited silver nanocluster/silica composites onto AISI 304L stainless steel via a radio frequency (RF) co-sputtering deposition method [191]. After one month of immersing in diverse food relevant fluids, these coated specimens showed an excellent property for the reduction of bacterial adhesion [191]. However, the high cost and low efficiency of the above physical methods limited the industrial application of AgNPs.

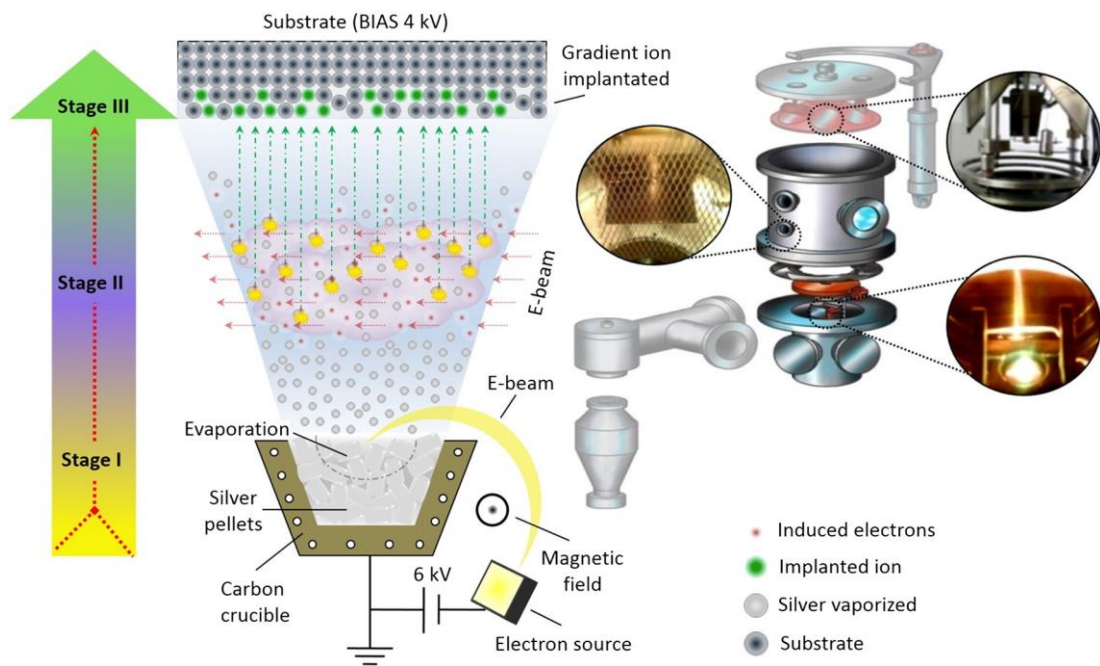


Figure 2.18 Schematic of the implantation process and major components of the reactive low voltage ion plating equipment [190].

Researchers have also resorted to wet chemical procedures to synthesise AgNPs on biomaterials. Inoue et al. prepared sodium titanate thin films with a porous

network structure through the reaction of titanium samples with NaOH solutions, then immersed in $\text{CH}_3\text{CO}_2\text{Ag}$ solution for 3 hours to conduct silver ion exchange treatment [192]. Soloviev et al. employed ultrasound irradiation to deposit AgNPs on stainless steel from AgNO_3 solution, which comprised aqueous ammonia and ethylene glycol [193]. Diantoro et al. used sodium borohydride, mercaptosuccinic acid and methanol to finish the reduction reaction of AgNPs from silver nitrate solution [194]. Heinonen et al. applied sodium hydroxide, ammonia and glucose to prepare the superhydrophobic surface with AgNPs by sol-gel technology [195]. As shown in Figure 2.19, Jia et al. presented a strategy of mussel-adhesive-inspired immobilisation of AgNPs [196]. Moreno-Couranjou et al. employed catechols to realise the reduction of silver nitrate to obtain AgNPs as shown in Figure 2.20 [197]. Cao et al. used dopamine as a reducing reagent to manufacture AgNPs on 304 stainless steel in a weak alkaline aqueous solution [198]. All the testing results illustrated that the existence of silver nanoparticles is essential for the antimicrobial activity of silver-containing surfaces.

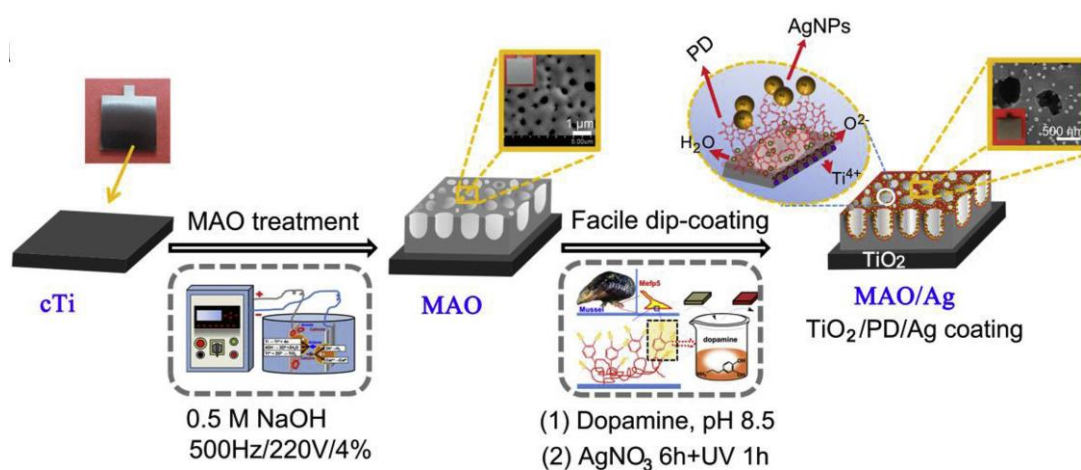


Figure 2.19 Schematic of MAO process followed by mussel-adhesive-inspired immobilization of AgNPs [196].



Figure 2.20 Schematic of the elaboration of multifunctional surfaces achieved via liquid-assisted plasma-enhanced chemical vapour deposition [197].

The current chemical synthesis methods are not environmentally friendly as they involved at least two different toxic reagents as reducing and stabiliser agents in the chemical reaction [188]. Thus, the reduction of the participant chemical reagents, even only using silver nitrates, is another challenge for the chemical synthesis method from the viewpoint of sustainable chemistry.

In addition to the coating approach, research has also demonstrated that microstructures of certain geometries can reduce surface adhesion of bacteria. Ferraris et al. proved that microgrooves on titanium surfaces prepared by electron beam surface structuring technology help reduce adhesion of bacteria [199]. For instance, in surgical tools, ultra-sharp knife-edges in combination with textured surfaces in the knife-tissue contact region could lead to significant reductions in forces and resulting tissue damage. The microstructures act as stores to realise immobilisation and release of silver ions into the surgical point. Besides, microstructures will protect the AgNPs from detachment and wear when subjected to external forces. Thus, the synergistic effect of AgNPs and micro-structures will lead to even better antimicrobial results [196].

2.4 Summary of knowledge gaps and research challenges

Designing appropriate microstructures and choosing a low-cost, high-efficiency manufacturing process are crucial for the industrial-scale production of superhydrophobic surfaces on AISI 316L stainless steel. Many preparation methods for superhydrophobic surfaces have been successfully applied to various materials. However, there are still some limitations due to the complicated preparation process, low efficiency and high cost. At present, the nanosecond laser ablation process has been proven to be a promising method for manufacturing superhydrophobic structures on AISI 316L stainless steel. However, most of the theoretical research concerning superhydrophobicity is independent of the manufacturing process. There is still a lack of systematic study of pattern design, the prediction of superhydrophobicity and the control and optimisation of the nanosecond pulsed laser ablation process. The knowledge gaps and research challenges are summarised in the following paragraphs.

First, the current microstructure design methods do not consider the manufacturing process. Thus, a deterministic design method that aims to predict surface contact angle and to optimise structure geometries for maximising hydrophobicity for laser-ablated microstructures is required.

Second, the current theoretical designs for superhydrophobic structures are not combined with computational fluid dynamic (CFD) simulation to predict the hydrophobicity of different structures. Furthermore, the underlying mechanism of the superhydrophobic phenomenon requires further exploration according to the experimental and simulation results.

Third, a research gap exists regarding the correlation between a specimen's surface topography and hydrophobicity. The challenge is determining the most

effective process parameter and surface characterisation parameter for these microstructures that are sensitive to the hydrophobicity of the microstructured surface.

Finally, a research gap exists in developing new hybrid processes based on laser ablation that can be used to manufacture functional surfaces with a specific property (e.g. anisotropic superhydrophobicity and antimicrobial properties). The challenge is how to combine the laser ablation process with other methods to cost-effectively produce functional surfaces.

Chapter 3 Design Method for Laser Ablated Superhydrophobic Microstructures

3.1 Introduction

As concluded in Chapter 2, the current microstructure design method for superhydrophobic surfaces does not consider manufacturability. Most of the research of laser ablated superhydrophobic structures employed line and grid patterns without considering structure design and dimension optimisation. However, the shape, dimensions of the microstructure and the laser ablation process are inextricably intertwined.

The purpose of Chapter 3 is to address the crucial design-for-manufacture (DFM) issue. First, a deterministic design approach, including a geometrical model for laser machined Gaussian micro holes, together with the theoretical constraints for a stable Cassie-Baxter state, will be advanced to design the necessary microstructure dimensions for maximising surface hydrophobicity. Then, a 3D CFD numerical simulation is used to predict the contact angle of design structures and to explore the underlying mechanism of the superhydrophobic phenomenon.

3.2 A deterministic design approach for superhydrophobic structures

In current research, laser ablated superhydrophobic surface mostly possessed pillars or channels patterns. Yong fabricated mesh-porous structure with a contact angle of 158° by a femtosecond laser ablation process and found that the superhydrophobicity is stable even if the PH of the solution changes from 1 to 14 [75]. Park manufactured surface with a durable dual hole pattern through imprinting techniques. As high aspect ratio pillars were not used the manufactured surface has

stable superhydrophobic properties and is robust against physical damage [200]. As stability of superhydrophobicity is a critical design requirement for practical application, the enclosure hole pattern is used in this study.

3.2.1 Geometrical model of microstructures

The nanosecond pulsed laser beam has a Gaussian intensity profile as shown in Figure 3.1 (a), so the profile of laser ablated micro hole also has a cross section like a Gaussian curve. Thus, some micro holes with a pitch of 110 μm (P110) are machined at different laser powers on AISI 316L stainless steel specimens to help develop a geometrical model of laser ablated microstructures. The detail of the IPG fibre laser are shown in Table 3.1. The surface morphologies of laser ablated specimens were measured by an optical microscope (Alicona G4) under 50X magnification objective lens. This instrument has a vertical resolution of 20 nm. The 2D profiles extracted along the diagonal direction of the machined holes under different laser powers for P110 are shown in Figure 3.1 (b). The depth and the width of the micro holes are observed to increase in proportion to the laser power. Especially when the laser power varies from 4 W to 14 W, the average depth of the micro holes gradually increases from 9.2 μm to 68.3 μm . Besides, the increased laser power also results in the increasing height of pillars due to the formation of recast layers in the laser ablation process. However, the increased laser power results in the decrease of the width of the pillars from 90 μm to 30 μm . The depths of the micro Gaussian holes are almost the same at 10 W and 14 W, but the pillar width further decreases as the increase of laser power leads to more material removed from the specimen surface.

Table 3.1 Details of IPG 20w fiber laser YLP-1-100-20-20.

Characteristic	Test condition	Minimum	Typical	Maximum	Unit
Mode of operation		Pulsed			
Nominal average output power		19	20	21	W
Output power adjustment range		10		100	%
Central emission wavelength	20W	1055	1064	1070	nm
Pulse repetition rate		20		200	KHz
Pulse duration	20 W, 20 kHz	90	100	120	ns
Pulse energy	20 W, 20 kHz		1		mJ

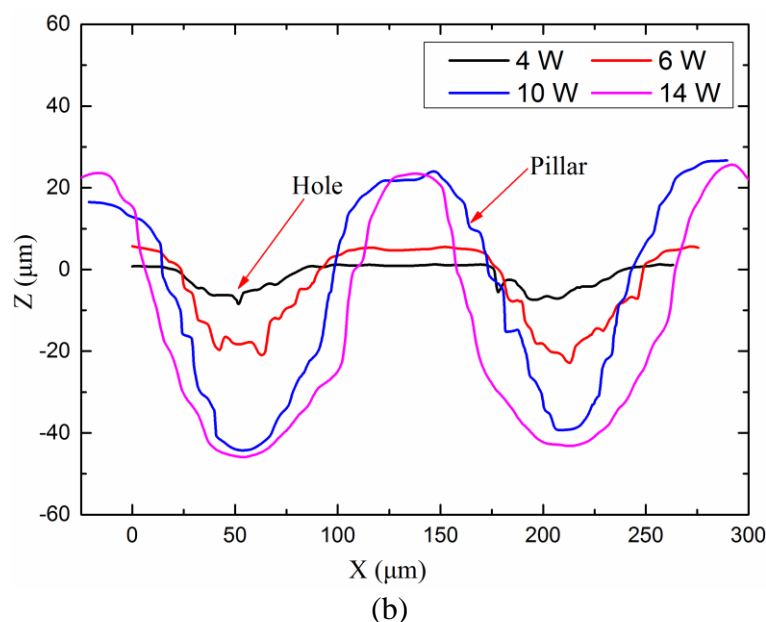
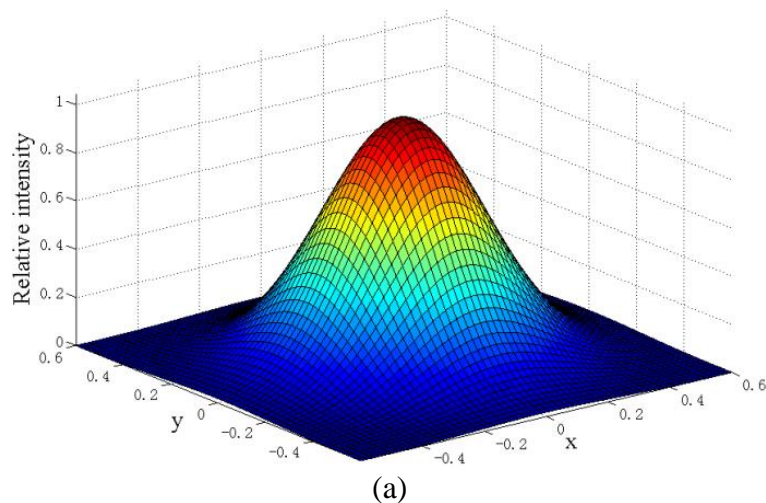


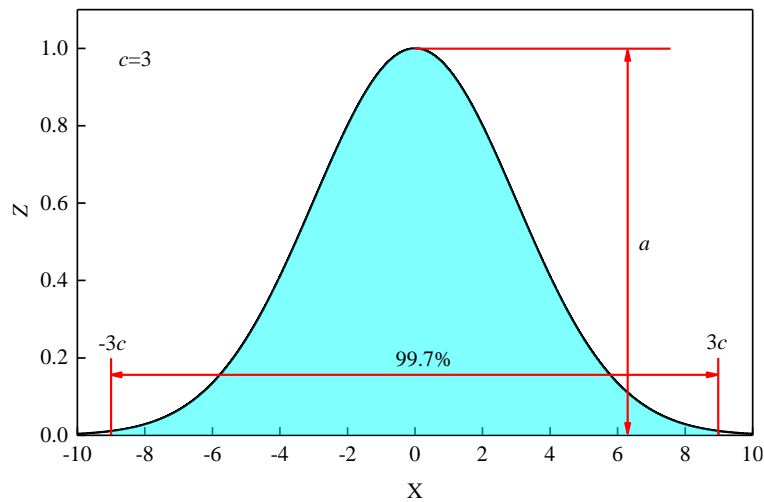
Figure 3.1 Intensity of the nanosecond laser beam and 2D profiles of machined micro holes: (a) Gaussian intensity profile of laser beam; (b) surface profile for P110 arrays.

From the above analysis results, the geometry model of laser ablated Gaussian holes can be developed. The 2D profile and 3D morphology of the microholes can be described by a Gaussian function as shown in Equations 3-1 and 3-2. For the Gaussian curve, the area proportion between $-3c$ and $+3c$ is about 99.7%, so the curve between $\pm 3c$ was chosen to represent the Gaussian hole machined by the pulsed laser as shown in Figure 3.2 (a). The developed 3D geometrical model of laser ablated Gaussian holes is shown in Figure 3.2 (b).

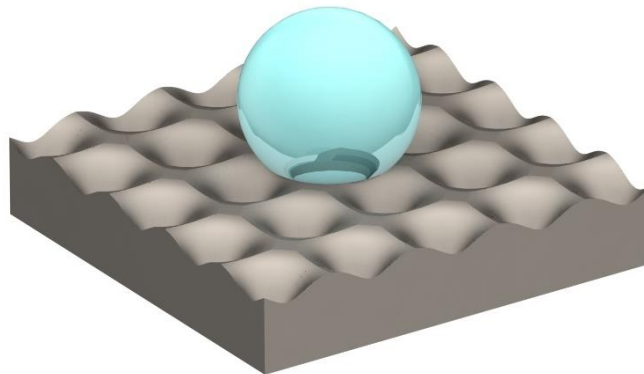
$$z = -a \times e^{-\frac{x^2}{2c^2}} \quad (3-1)$$

$$z = -a \times e^{-\frac{x^2+y^2}{2c^2}} \quad (3-2)$$

where a and c are arbitrary real constants.



(a)



(b)

Figure 3.2 (a) Gaussian curve; (b) 3D geometry model of laser ablated Gaussian holes.

3.2.2 A nonlinear geometrical optimisation model

The 2D and 3D geometrical models of laser ablated Gaussian holes can be plotted based on Equations 3-1 and 3-2, as shown in Figure 3.3. For superhydrophobic AISI 316L stainless steel specimen, the water droplet should have a stable Cassie-Baxter state on the specimen. Due to the effect of gravity, the water droplet sags downward between micropillars but will not touch the bottom of micro holes. In Figure 3.3 (a), a is the depth of the Gaussian hole, b is the width of micropillar, $6c$ is the width of microhole, h is the height of sag of water droplet between pillars, θ is the intrinsic contact angle of AISI 316L stainless steel, and R is the radius of water droplet. We suppose that the interface of sag of the droplet is part of a ball surface and r is the ball radius. Furthermore, the pitch P , b and c form a right-angled triangle as shown in Figure 3.3 (b).

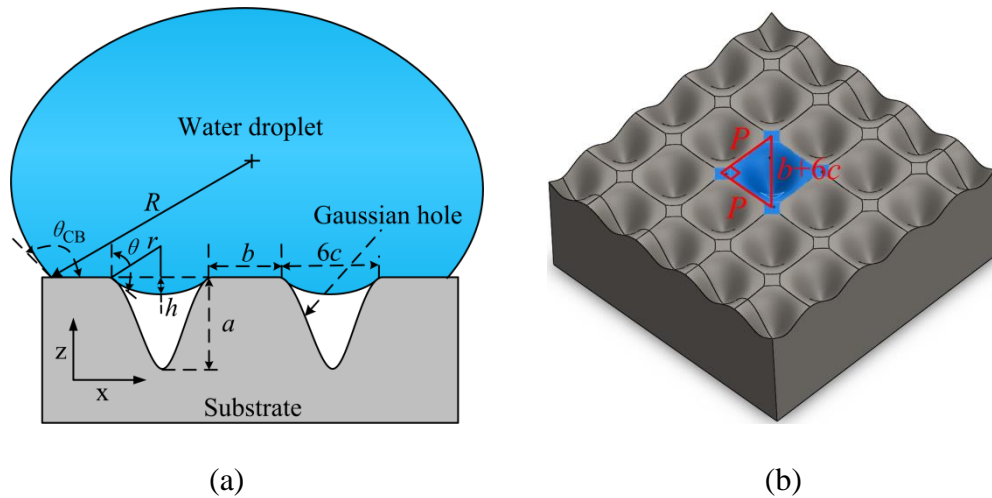


Figure 3.3 Geometrical model of laser ablated Gaussian holes at Cassie-Baxter state: (a) 2D geometric model; (b) 3D topography.

For the water droplet in the Cassie-Baxter state, the surface contact angle can be expressed as [16]:

$$\cos\theta_{CB} = -1 + f(1 + \cos\theta) \quad (3-3)$$

where f is the fraction of solid surface area wet by the liquid and can be described as:

$$f = \frac{\text{actual solid and liquid contact area}}{\text{planar area}} = \frac{b^2}{2(\frac{b}{2} + 3c)^2} \quad (3-4)$$

From Equations 3-3 and 3-4, it can be seen that f is inversely proportional to contact angle θ_{CB} . Hence, the minimum value of f will result in the contact angle θ_{CB} reaching its maximum value. So Equation 3-4 is the objective function of nonlinear programming.

In order to make the droplet maintain a stable Cassie-Baxter state on the surface, the structure should meet some geometric and physical constraints which are listed as follows.

First of all, the droplet cannot have contact with the bottom of the micro Gaussian hole, so the sag in height h should be smaller than a , which can be expressed as:

$$a > h = 3c\left(\frac{1 - \sin\theta}{-\cos\theta}\right) \quad (3-5)$$

Equation 3-5 can be further simplified as:

$$3c\left(\frac{1 - \sin\theta}{-\cos\theta}\right) - a \leq 0 \quad (3-6)$$

Secondly, the state of the droplet is affected by its weight in Newtons (W) and Laplace pressure (F_{LP}) force. The Laplace pressure is the pressure difference between the inside and the outside of a curved surface that forms the boundary between a gas region and a liquid region [201]. The pressure difference is caused by the surface tension of the interface between liquid and gas. Thus, the balance between weight and Laplace pressure is also a crucial condition for the Cassie-Baxter state. It means that

the Laplace pressure should be greater than the weight of the droplet. The average droplet weight for every hole and the Laplace pressure are shown in Equations 3-7 and 3-8. The constraint can be expressed by Equation 3-9. The pillar can be estimated to possess a rectangular shape with side length b .

$$W = \frac{\rho \left(\frac{4}{3} \pi R^3 g \right)}{\pi R^2 \sin^2 \theta} \left[2 \left(\frac{b}{2} + 3c \right)^2 - b^2 \right] \quad (3-7)$$

$$F_{LP} = 12\pi\gamma_{LG}c \left(\frac{1 - \sin\theta}{-\cos\theta} \right) \quad (3-8)$$

$$W - F_{LP} \leq 0 \quad (3-9)$$

where, γ_{LG} is the surface tension between liquid and gas in the unit of N/m.

Thirdly, the principle of the lowest energy is a general rule in nature. Since the mechanical system is trying to find a state of minimum surface free energy [202], the surface free energy of Cassie-Baxter state (E_{CB}) should be smaller than Wenzel state (E_W) [203]. The E_{CB} and E_W in the unit of J are calculated by Equations 3-10 and 3-11. Equation 3-12 is Young's equation [204]. The constraint about the principle of the lowest energy can be expressed by Equation 3-13. The pillar side area is processed as a frustum of a pyramid to calculate the area.

$$E_{CB} = \gamma_{LG} \left[\frac{18\pi c^2 (1 - \sin\theta)}{\cos^2 \theta} \right] + \gamma_{SL} b^2 + 4\gamma_{SG} \sqrt{a^2 + 9c^2} (b + 3c) \quad (3-10)$$

$$E_W = \gamma_{SL} [b^2 + 4\sqrt{a^2 + 9c^2} (b + 3c)] \quad (3-11)$$

$$\gamma_{SG} = \gamma_{LG} \cos\theta + \gamma_{SL} \quad (3-12)$$

$$E_{CB} - E_W \leq 0 \quad (3-13)$$

where γ_{SL} is the surface tension between solid and liquid, γ_{SG} is the surface tension between solid and gas.

Finally, there are some additional geometrical constraints, as shown in Figure 3.3 (b) according to the Pythagorean theorem, the relationship of b , c and P can be expressed as:

$$b + 6c = \sqrt{2}P \quad (3-14)$$

For every specimen, the depth of microhole is also limited by actual depth. As an extension of R_a (arithmetical mean height of a line) to a surface, S_a is often used to evaluate surface roughness in an area. It represents the difference in the height of each point compared to the arithmetical mean of the surface, so it cannot wholly reflect the size of peak and valley on the periodic surface. On the other hand, the maximum height S_z is a surface characterisation parameter to evaluate the absolute highest and lowest points found on the surface, which is the sum of the maximum peak height (S_p) and the maximum valley depth (S_v) within the defined area. For this reason, S_z can reflect the depth information of the specimen better than S_a . The depth of the hole should be smaller than S_z :

$$a \leq S_z \quad (3-15)$$

In this optimisation problem, Equations 3-6, 3-14 and 3-15 are linear constraints while Equations 3-9 and 3-13 are nonlinear constraints. MATLAB Optimisation Toolbox was used to solve the above optimisation problems and the initial conditions in this study are listed in Table 3.2. The value of θ is obtained from the contact angle of water droplet on smooth AISI 316L stainless steel, the radius of 5 μL water droplet is around 1.06mm.

Table 3.2 Initial conditions used in the optimisation process.

θ (°)	R (mm)	γ_{LG} (N/m)
105	1.06	0.073

The predicted dimensions of a , b and c under six different pitches and the corresponding predicted maximum contact angles are shown in Table 3.3. Specifically, P is the abbreviation of pitch of Gaussian holes, P050 means the specimen with a pitch of 50 μm . All these dimensions are the values that can realise the maximal contact angle and satisfy the constraint conditions simultaneously to ensure the Cassie-Baxter state of the water droplet. With the increase of pitch from 50 μm to 150 μm , the predicted width of pillar b increase from 13.8 μm to 58.3 μm . The ratio of b and $6c$ increased from 0.242 to 0.379, which means that the water droplet requires more solid part on the surface to sustain the water droplet to satisfy the constrained conditions, the droplet has a stable Cassie-Baxter state on the specimen surface. However, the increasing ratio of b and $6c$ also results in a decrease in the predicted maximum contact angle from 160.5 $^\circ$ to 152.6 $^\circ$.

Table 3.3 Predicted dimensions of Gaussian hole and its contact angle.

Pitch (μm)		P050	P070	P090	P110	P130	P150
Predicted dimensions (μm)	a	51.7	69	76.4	86	99.6	110.9
	b	13.8	20.6	31	40.8	49.1	58.3
	c	9.5	13.1	16	19.1	22.4	25.6
	$b/6c$	0.242	0.262	0.323	0.356	0.364	0.379
Predicted value of contact angle ($^\circ$)	θ_{CB}	160.5	159.4	155.7	153.8	153.4	152.6

3.3 CFD simulation: method and setup

Section 3.2 obtained the best dimensions for a Gaussian hole to maximise superhydrophobicity under different pitches. However, the above design results are only based on theoretical and geometrical analysis. In this section, the CFD simulation will be conducted to predict the contact angles of different substrates. Furthermore, the

dynamic behaviour of the water droplet that impacts the textured surface is critical to understand the underlying mechanism of hydrophobicity and directly influences its applications. However, it is extremely difficult to reveal the dynamic behaviour experimentally due to unfavourable optical measurement conditions and short impacting time. This section, therefore, adopts the Volume of Fluid (VOF) method to ultimately reveal the dynamic impacting behaviour and the wetting transition regime of water droplets on smooth and designed substrates with different Gaussian hole dimensions.

3.3.1 Mathematical model of the VOF method

The VOF method can be applied on two or more immiscible fluids by solving a series of momentum equations and by tracking the volume fraction for every fluid throughout the domain [205]. In the superhydrophobic phenomenon, solid phase (AISI 316L stainless steel), liquid phase (water) and gas phase (air) are three immiscible fluids. Thus, the VOF method can be employed to simulate the impacting behaviour of water droplets on smooth and textured substrates to explore the underlying physics of the superhydrophobic phenomenon.

In this study, the water droplet impacting process is considered to take place at room temperature, and the process is adiabatic. ANSYS-CFD solver was employed in the simulation. The general form of the mass conservation equation is shown in Equation 3-16, which is valid for both incompressible and compressible flows.

$$\frac{\partial \rho}{\partial t} + \nabla \cdot (\rho \vec{v}) = S_m \quad (3-16)$$

where ρ is density, t is time, and \vec{v} is fluid velocity. S_m represents the source item, which means the mass added to the continuous phase from another phase or other phase. S_m is zero in this research.

G. K. Batchelor et al. described the conservation of momentum as [206]:

$$\frac{\partial}{\partial t}(\rho\vec{v}) + \nabla \cdot (\rho\vec{v}\vec{v}) = -\nabla p + \nabla \cdot (\bar{\tau}) + \rho g + \vec{F} \quad (3-17)$$

where p is the static pressure, $\bar{\tau}$ is the stress tensor and expressed in Equation 3-18. g is the acceleration of gravity, \vec{F} is the external body force.

$$\bar{\tau} = \mu[(\nabla\vec{v} + \nabla\vec{v}^T) - \frac{2}{3}\nabla \cdot \vec{v}I] \quad (3-18)$$

where μ is the molecular viscosity, I is the unit tensor, and the second term on the right side is the effect of volume dilation.

For a single water droplet, the surface tension has a significant effect on its impacting behaviour. The continuum surface force (CSF) model developed by Brackbill [207] et al. was used in this research to consider the surface tension effect. In the CSF model, the volume force (F_{vol}) of surface tension to the VOF numerical is a source term \vec{F} in the Equation 3-17. For two phase numerical calculation, the phases are represented by the subscripts 1 and 2. The volume force (F_{vol}) can be expressed by Equation 3-19. k_1 is the curvature of the first phase and can be expressed by Equation 3-20. \hat{n}_1 is the unit normal as described in Equation 3-21.

$$F_{vol} = \gamma_{12} \frac{\rho k_1 \nabla \alpha_1}{\frac{1}{2}(\rho_1 + \rho_2)} \quad (3-19)$$

$$k_1 = \nabla \cdot \hat{n}_1 \quad (3-20)$$

$$\hat{n}_1 = \frac{\nabla \alpha_1}{|\nabla \alpha_1|} \quad (3-21)$$

where, γ_{12} is the surface tension coefficient between the two phases, and α_1 is the volume fraction of the first phase.

The intrinsic contact angle (θ) provides information about the wettability of an ideal smooth surface. Typically, it comes from the test results. In the VOF simulation, θ is not imposed on the wall itself, but it is used to adjust the surface normal in cells near the wall [207]. Hence, it results in the adjustment of the curvature of the surface near the wall. The surface unit normal at the live cell next to the wall is represented as:

$$\hat{n} = \hat{n}_{wall} \cos \theta + \hat{t}_{wall} \sin \theta \quad (3-22)$$

where \hat{n}_{wall} and \hat{t}_{wall} are the unit vectors normal and tangential to the wall, respectively.

The Weber number (We), often used in analysing fluid flows of an interface between two different fluids, is a dimensionless parameter. It represents the ratio of the inertial force to the surface tension force. The Weber number (We) is given by Equation 3-23.

$$We = \frac{\rho v^2 l}{\sigma} \quad (3-23)$$

where l is its characteristic length, typically the diameter of the droplet.

3.3.2 Geometrical model and simulation parameter setup

The 3D geometry models used in the VOF simulation are based on the designed results of Section 3.2.1. The optimised dimensions of P110 (optimised) and P150 (optimised) in Table 3.3 are used for the simulation to make a comparison with the theoretical value. In addition, smooth surface and P150 (revised) are employed to simulate the impacting behaviour of water droplets on a smooth surface and structure without the optimised dimensions.

Various efforts have been focused on droplet impact on surfaces with higher impacting velocity. However, it is difficult to predict the final contact angle under higher impacting velocity due to the longer impacting time needed to establish an equilibrium state. In this research, the simulation was conducted with low and high Weber numbers. The simulation at low Weber number ($We = 0.026$) shows the quasi-static process of water droplets, and it can be used to predict the contact angle because the small Weber number takes a short time to reach the equilibrium state. However, the simulation at a high Weber number ($We = 7.26$) can display the impacting process of water droplets on substrates. The dimensions and initial conditions of the Gaussian hole model for the VOF simulation are shown in Table 3.4. Specifically, P150 (revised) has a smaller depth a and width of microhole $6c$ than P150 (optimised), and it has a larger pitch if compared with P110 (optimised). Thus, the effect of depth and width on the droplet impacting behaviour and the final apparent contact angle and microstructures can be investigated from the comparison between P150 (revised) and P110 (optimised). And the effect of Gaussian hole's pitch can be investigated from the comparison between P150 (revised) and P110 (optimised). According to the results displayed in Table 2.5, Table 2.6 and Table 2.7, the volume of water droplet used for contact angle test are varied from 1 to 15 μL , most of research used a water droplet with volume about 5 μL . Thus water droplets with volume of 5 μL (2.12mm in diameter) were applied in the simulation and experiments. As shown in Table 2.4, previous studies used the impact velocities of water droplet are varies from 0.001 to 3.2 m/s. Based on the above analysis, the water droplet with a diameter of 2.12 mm (5 μL) has impact velocity of 0.03 m/s ($We = 0.026$) and 0.5 m/s ($We = 7.26$) are used in this study.

Table 3.4 Dimensions and initial conditions of Gaussian hole model for VOF simulation.

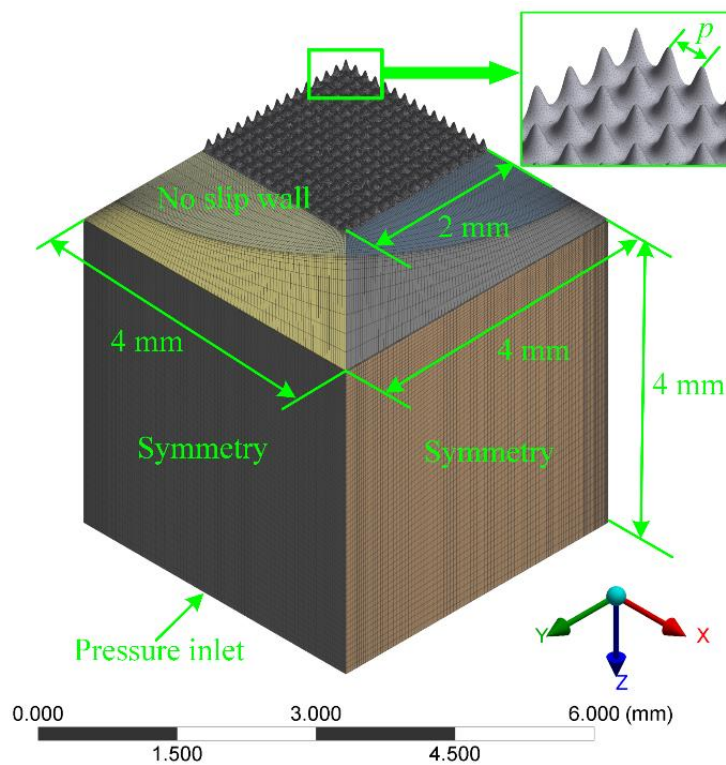
Case run	Name	Surface pattern	P (μm)	a (μm)	$6c$ (μm)	Impacting velocity (m/s)	We
1	Smooth	Smooth	0	0	0	0.03	0.026
2	P150 (revised)	Gaussian hole arrays	150	86	114.6	0.03	0.026
3	P150 (optimised)	Gaussian hole arrays	150	110.9	153.6	0.03	0.026
4	P110 (optimised)	Gaussian hole arrays	110	86	114.6	0.03	0.026
5	P150 (revised)	Gaussian hole arrays	150	86	114.6	0.5	7.26
6	P150 (optimised)	Gaussian hole arrays	150	110.9	153.6	0.5	7.26
7	P110 (optimised)	Gaussian hole arrays	110	86	114.6	0.5	7.26

The computational setup in the VOF simulation is shown in Table 3.5. The solid substrate material is steel. The wall adhesion angle is same as the initial contact angle on the smooth surface.

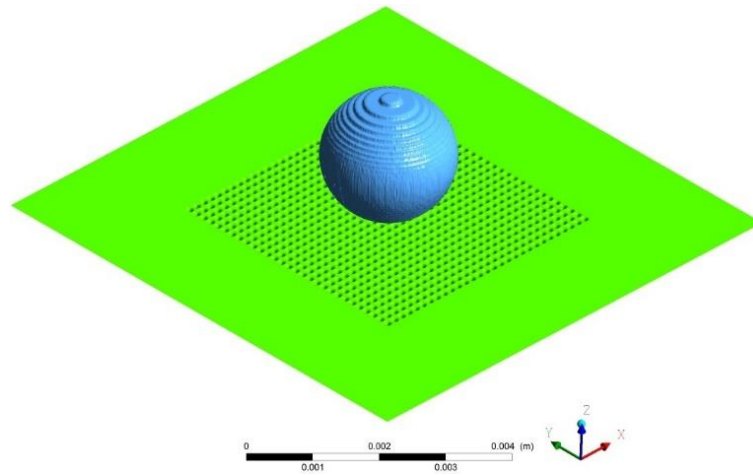
Table 3.5 VOF simulation parameters.

Parameter	Setting/Value
Primary phase	Air
Second phase	Water
Solid	Steel
Calculation type	Transient model
Calculation model	Volume of fluid
Diameter of water droplet (D_0)	2.12 mm (5 μL)
Surface tension	0.073 N/m
Wall adhesion angle	105 $^\circ$
Time step	2.5×10^{-5} s

Since the Gaussian hole model and the water droplet are symmetric, a one-quarter symmetric model was used in this research. Contact angle is the most common quantitative measure of the wettability of a solid by a water droplet. In order to make comparison with contact angle test results and simulate dynamic behaviours of water droplet, a water droplet is defined above the substrate and impacting on the substrate in this study. The 3D computational domain and boundary conditions of the Gaussian hole model are illustrated in Figure 3.4 (a). The dimension of the computational domain is $4 \times 4 \times 4 \text{ mm}^3$. All the side walls are set as a symmetry boundary condition. A rigid no-slip wall boundary condition with a static contact angle 105° is imposed at the structured surface. The initial state of the water droplet is shown in Figure 3.4 (b).



(a)



(b)

Figure 3.4 (a) 3D geometrical model of fluid domain based on Gaussian characters; (b) initial state of a water droplet.

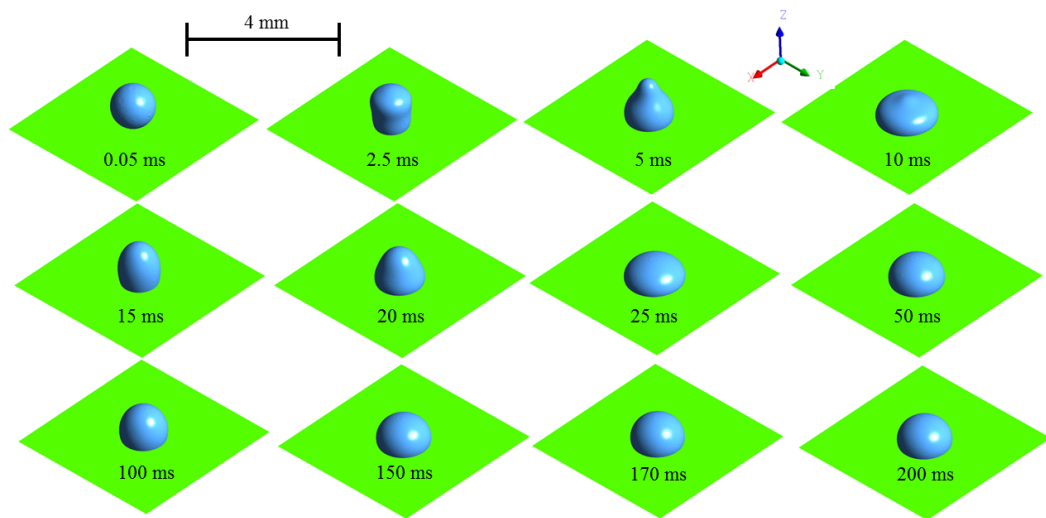
3.4 CFD simulation: results and discussions

3.4.1 *Dynamic behaviour of the water droplet on varied substrates at a Weber number of 0.026*

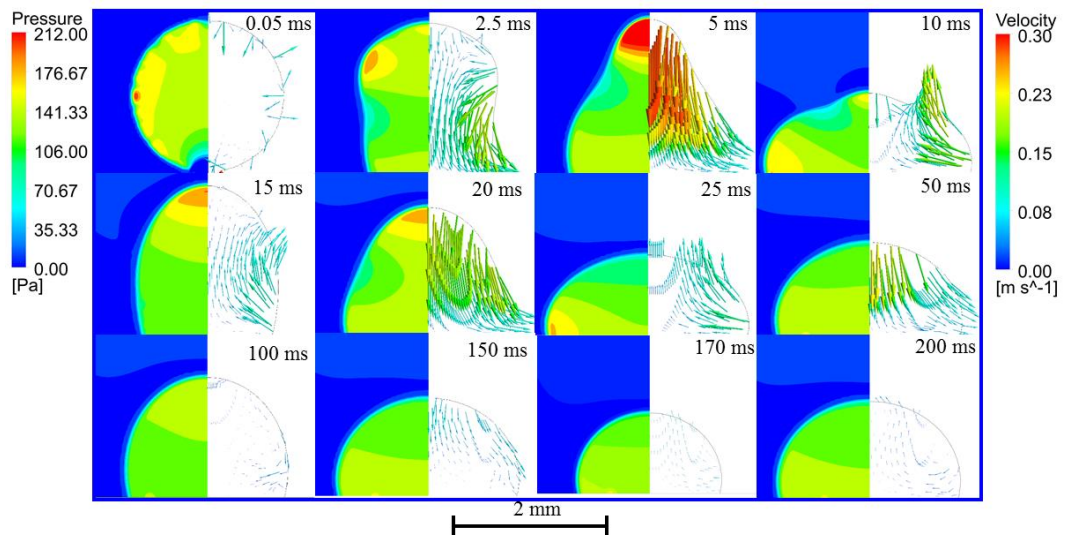
In this section, a low impacting velocity of 0.03 m/s is employed as the initial condition to impact the different substrates to predict the static contact angle in the equilibrium state.

In general, when the water droplet impacts a solid surface, two stages, spreading and retracting, are cyclically observed until realising an equilibrium state. As shown in Figure 3.5 (a) and (b), the droplet expanded rapidly in the radial direction from 0.05 ms to 10 ms, and the water droplet height decreased continuously until the vertical velocity component was reduced to 0, which is called the spreading stage. The retracting stage started at 10 ms and lasted until 15 ms, and the droplet moved upward due to the surface tension effect. Figure 3.5 (b) shows the variations in pressure and

velocity vector. During the spreading stage, the water droplet's velocity vectors moved downward and to the outside. Inversely, the velocity vectors at the retracting stage moved upward and to the inside. After multiple oscillations, the water droplet reached an equilibrium state at 200 ms. Figure 3.5 (c) shows that the water droplet's pressure distribution at 200 ms complied with the law of pressure variation in a static fluid, which states that pressure increases with depth. Furthermore, the velocity vector was lower than 0.05 m/s at 200 ms, which is negligible and can be regarded as an equilibrium state.



(a)



(b)

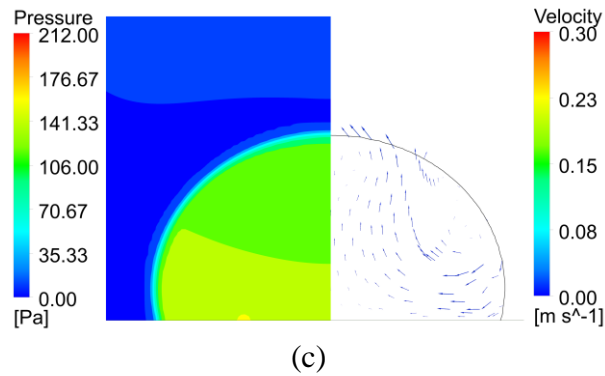
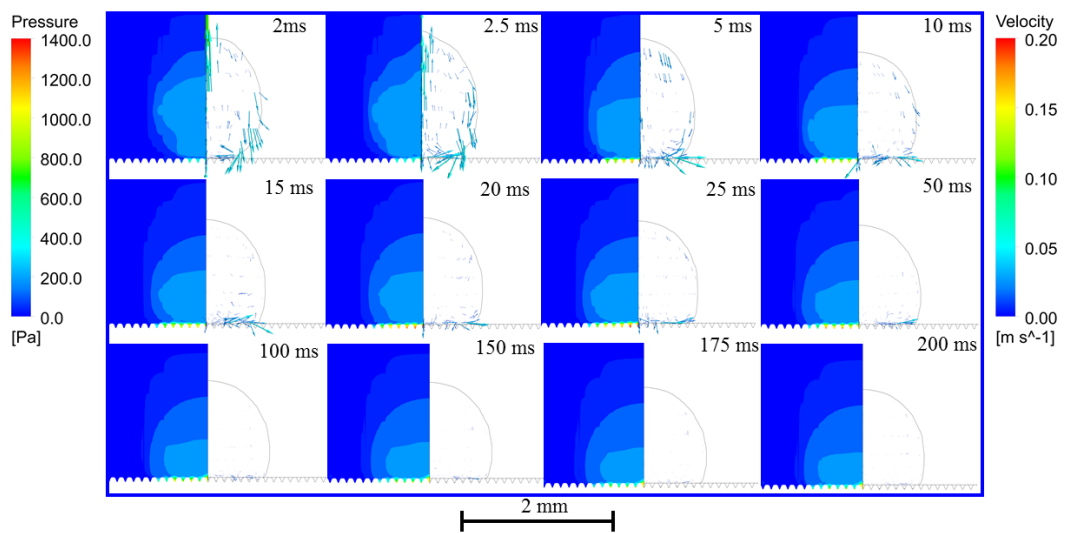
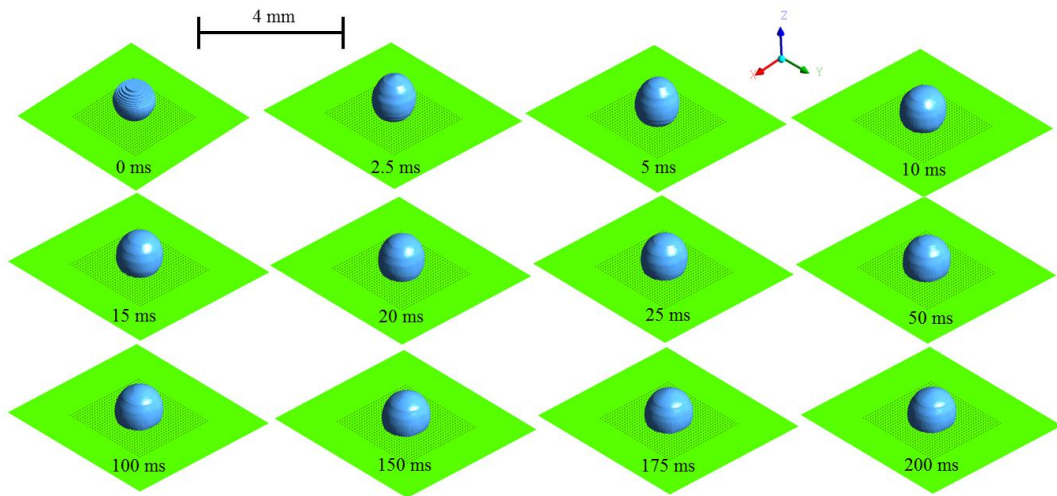
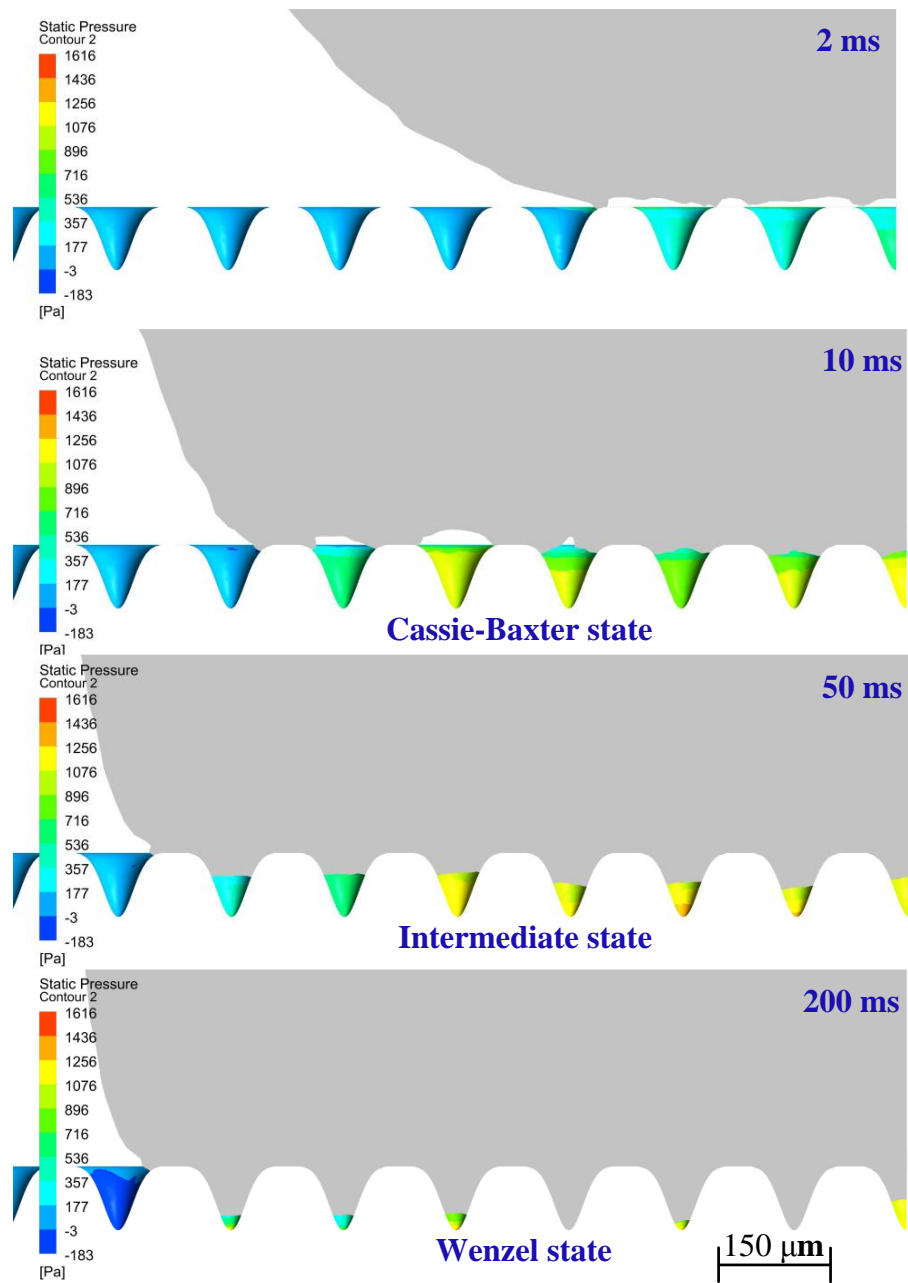


Figure 3.5 A series of images of a water droplet impact on the specimen with a smooth surface at a low impact velocity of 0.03 m/s ($We = 0.026$, Case 1): (a) shape of the water droplet, (b) static pressure and velocity vector and (c) static pressure and velocity vector at 200 ms.

The dynamic droplet shape and its cloud map of pressure-velocity vector for the P150 (revised) specimen at We 0.026 are shown in Figure 3.6. When the water droplet started to contact the smooth surface, there was only one rebound process, between 0 ms and 5 ms, as shown in Figure 3.6 (a) and (b). Then, the water droplet's height decreased gradually. More details of the Cassie-Wenzel transition process are shown in Figure 3.6 (c). When the water droplet started to contact the substrate, the water droplet was in a metastable Cassie-Baxter state, between 0 ms to 10 ms. The static pressure shows an increasing trend due to the air pocket formed under the water droplet. After 10 ms, the velocity vector is distributed at the bottom of the water droplet (Figure 3.6 (b)), which means the transition from a Cassie-Baxter state to a Wenzel state. The intermediate state at 50 ms proves this inference (Figure 3.6 (c)). From 50 ms to 200 ms, with the decrease of the velocity vector, the water penetrated the Gaussian hole and reached an equilibrium state. The water almost entirely penetrated the structures, and the wetting transition finished at 200 ms, even though a negligible

amount of air was still trapped at the bottom of the structures. Therefore, the water droplet was impaled on the microstructures and showed a Wenzel state at 200 ms.



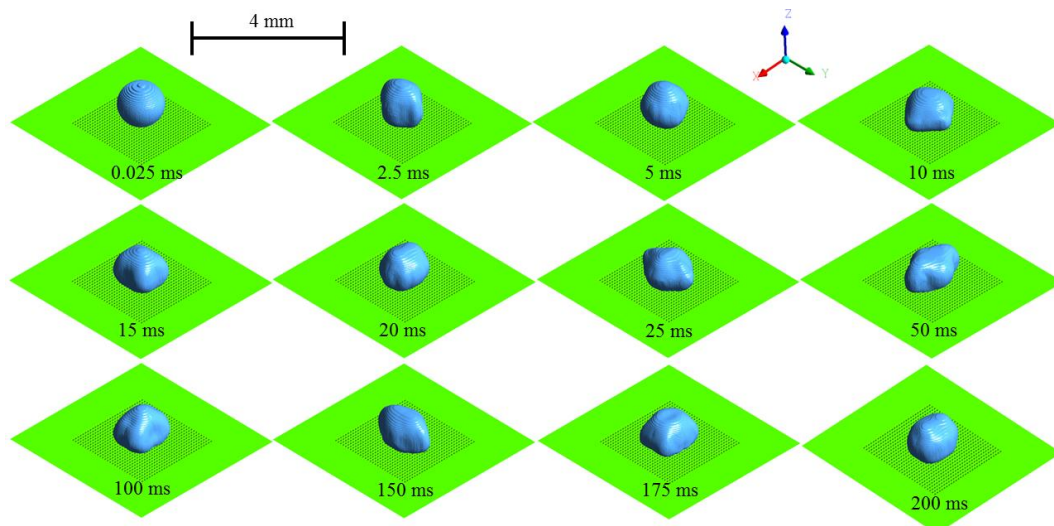


(c)

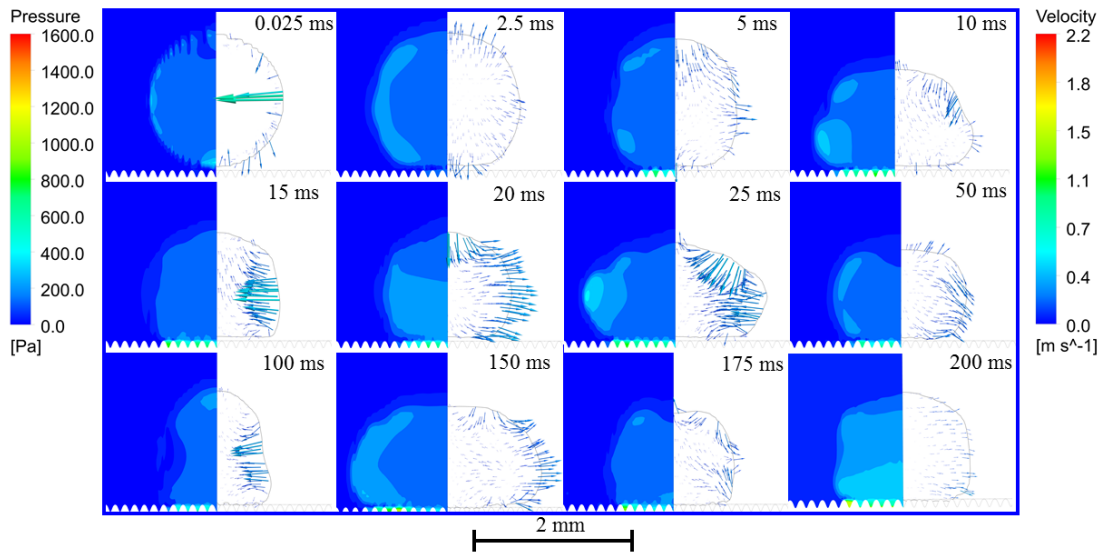
Figure 3.6 A series of images of a water droplet impact on a specimen with Gaussian hole arrays P150 (revised) at a low impact velocity of 0.03m/s ($We = 0.026$, Case 2): (a) shape of water droplet, (b) static pressure and velocity vector and (c) Cassie-Wenzel transition process and pressure distribution of Gaussian holes.

The dynamic droplet shapes and its cloud map of pressure-velocity vector for the P150 (optimised) specimen at We 0.026 are shown in Figure 3.7. The P150 (optimised) substrate has optimised dimensions, that produce superhydrophobicity with a predicted contact angle of 152.6° , according to the designed results. As shown in Figure 3.7 (a) and (b), the water droplet had both horizontal and vertical shape deformation in the spreading process. Furthermore, after 10 ms, the radial velocity vectors were more pronounced when compared with the vertical direction. The water droplet shape significantly changed in a radial direction due to the water being unable to penetrate the microstructures.

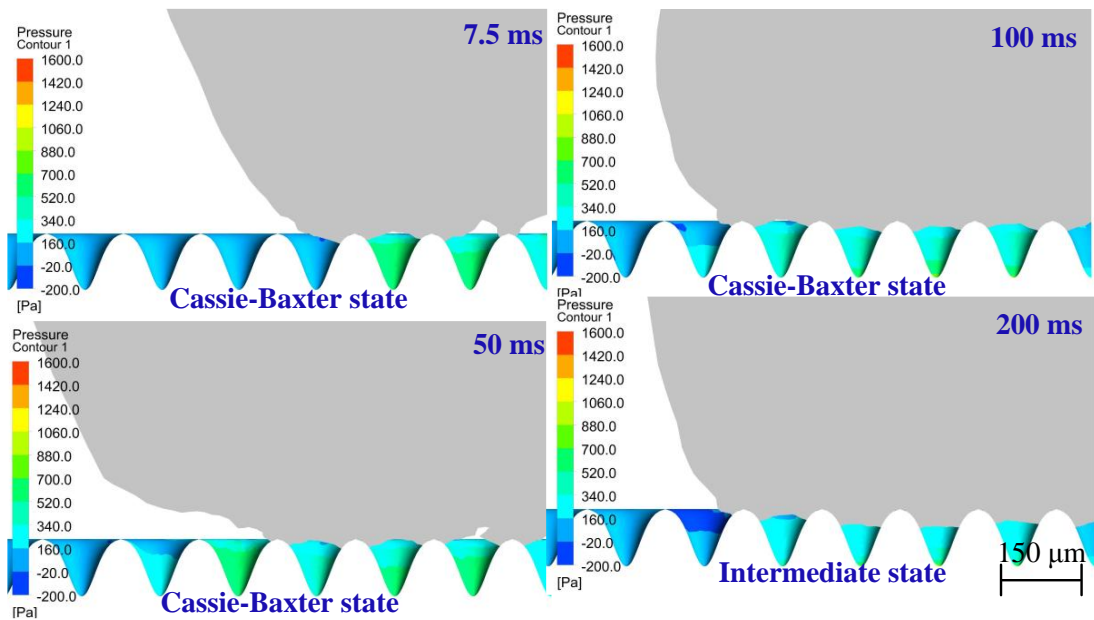
More details of the water droplet state and air pocket pressure are shown in Figure 3.7 (c). A large volume of air was trapped at the bottom of the structures, resulting in lower adhesion force and making the water droplet stay in a Cassie-Baxter state before 100 ms. However, the water droplet penetrates the Gaussian holes until realising the balance among weight, Laplace pressure and air pocket pressure between 100 ms and 200 ms. Furthermore, the water droplet shows an intermediate state of Cassie-Baxter and Wenzel state on P150 (optimised) at 200 ms.



(a)



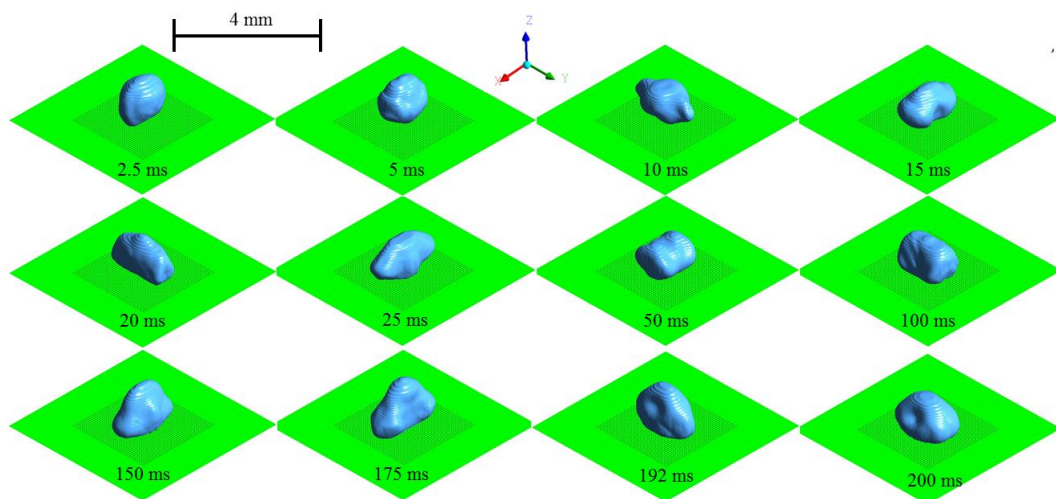
(b)



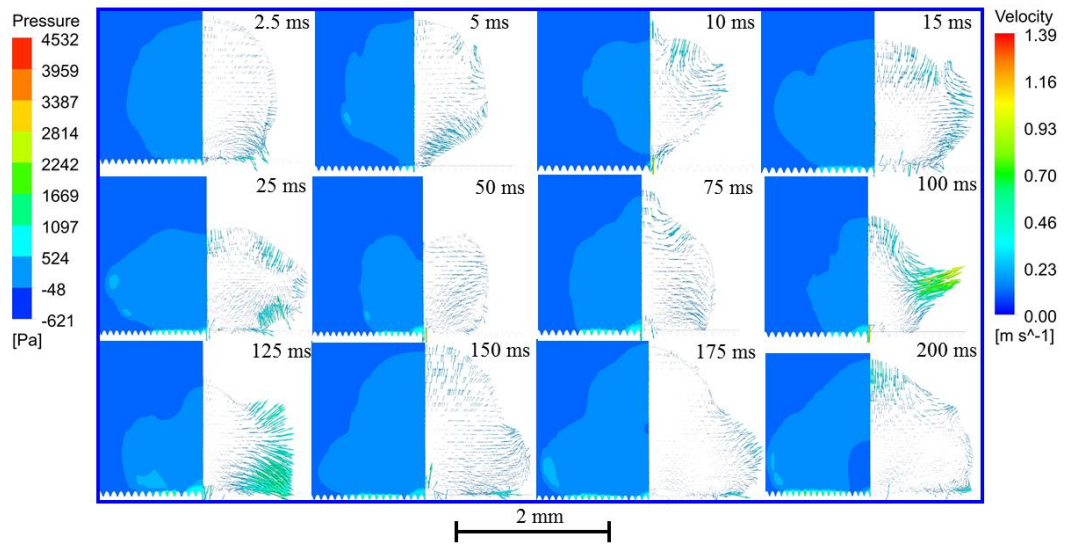
(c)

Figure 3.7. A series of images of a water droplet impact on the specimen with Gaussian hole arrays P150 (optimised) at a low impact velocity of 0.03m/s ($We = 0.026$, Case 3): (a) shape of water droplet, (b) static pressure and velocity vector and (c) Cassie-Wenzel transition process and pressure distribution of Gaussian holes.

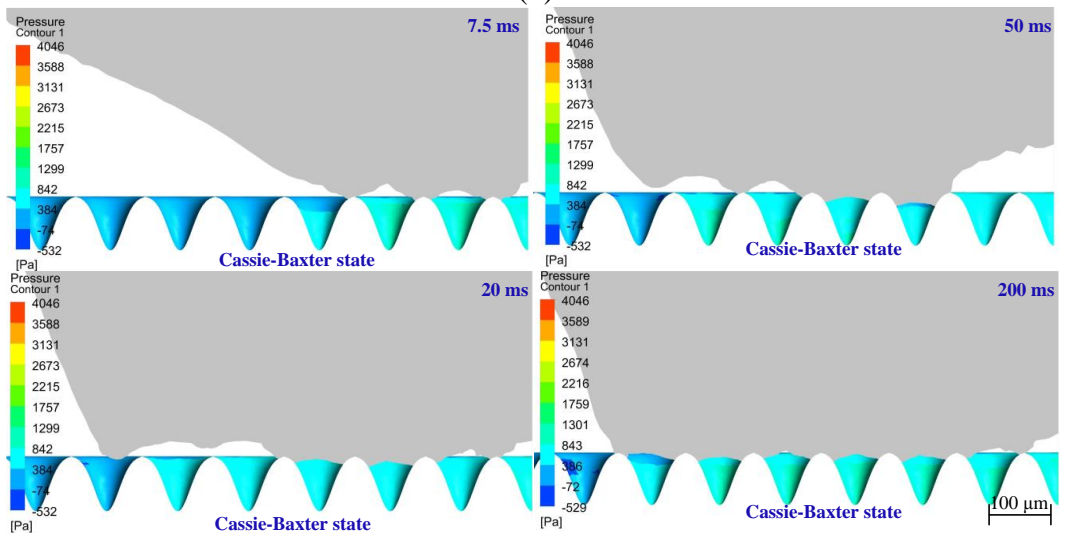
The dynamic droplet shape and its cloud map of pressure-velocity vector for the P110 (optimised) specimen at a Weber number of 0.026 are shown in Figure 3.8. The P110 (optimised) substrate has optimised dimensions, that produce superhydrophobicity with a predicted contact angle of 153.8° , according to the designed results. Similar to P150 (optimised), the water droplet had both horizontal and vertical shape deformations in the spreading process. Furthermore, after 10 ms, the radial velocity vectors were more notable when compared with the vertical direction. Thus, the water droplet shape significantly changed in a radial direction due to the water droplet being unable to wet the Gaussian holes. More details of the water droplet state and air pocket pressure are shown in Figure 3.8 (c). A large volume of air was trapped at the bottom of the structures, which resulted in the water droplet having a Cassie-Baxter state on the substrate.



(a)



(b)



(c)

Figure 3.8 A series of images of a water droplet impact on the specimen with Gaussian hole arrays P110 (optimised) at a low impact velocity of 0.03 m/s ($We = 0.026$, Case 4): (a) shape of water droplet, (b) static pressure and velocity vector and (c) Cassie-Wenzel transition process and pressure distribution of Gaussian holes.

In the impacting process of the water droplets on the substrates, the droplet's shape varied with time in both horizontal and vertical directions. Thus, two dimensionless coefficients (i.e. dimensionless diameter D^* and dimensionless height

h^*) were defined to quantitatively evaluate the impacting process of a water droplet on the substrates as follows:

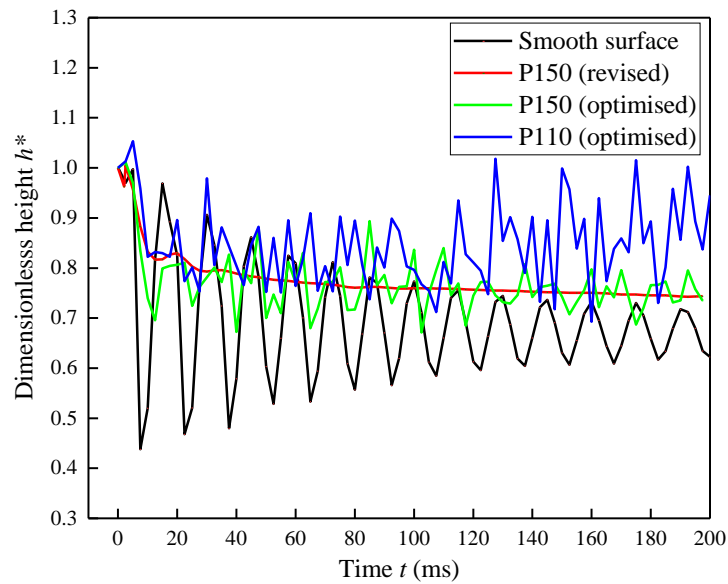
$$D^* = \frac{D}{D_0} \quad (3-24)$$

$$h^* = \frac{h}{D_0} \quad (3-25)$$

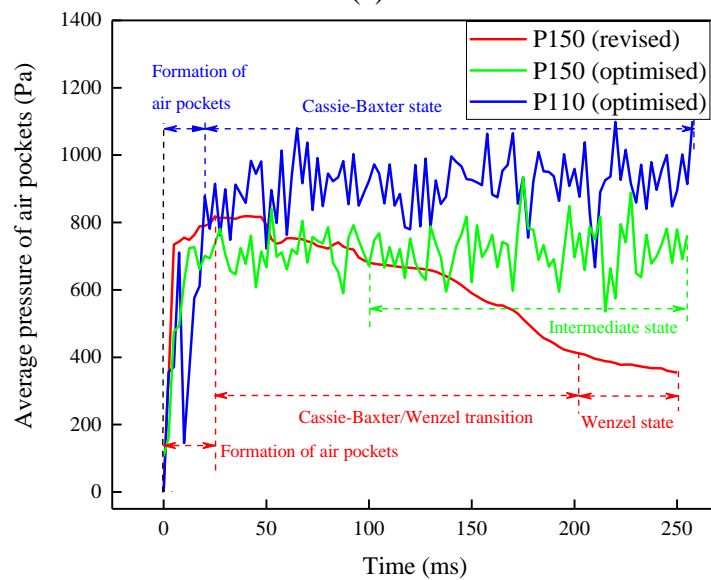
where D_0 is the initial diameter of the water droplet (2.12mm for a 5 μ L water droplet), D is the instantaneous maximum diameter of the water droplet and h is the instantaneous maximum height of water droplet, which is the distance from the top of the water droplet to the solid substrate.

Figure 3.9 (a) presents the dimensionless height h^* of the droplet for four cases at We 0.026 to explore the hydrophobic and superhydrophobic phenomenon. At a low Weber number, h^* can reflect the water droplet's wetting state and dynamic behaviour. For a smooth surface, the droplet's oscillation exhibited a form of damping vibration, and a decreasing trend of oscillation amplitude was observed. For specimen P150 (revised), there was no distinct vibration, and h^* was decreased gradually with the wetting process. However, for superhydrophobic substrates P150 (optimised) and P110 (optimised), h^* was larger than the other two cases because the water could not wet the structures. Knowledge of the average pressure of the air pockets underneath the droplet during its interaction helps reveal the root mechanism behind different wetting states (Figure 3.9 (b)). For both substrates, the average air pockets' pressure shows an increasing trend in the initial formation stage due to air being gradually trapped in the structures. However, the air pockets for P150 (revised) are metastable, and the average pressure of the air pockets remains constant for an extremely short time and then starts decreasing with the wetting transition process from the Cassie-

Baxter state to the Wenzel state. For P150 (optimised) and P110 (optimised), the air pockets' pressure increases at first and then remains stable, which helps prevent the water from penetrating the micro Gaussian holes. However, the stable pressure of P150 (optimised) is smaller than that of P110 (optimised); thus this demonstrates an intermediate state and not a Cassie-Baxter state, like the one found with P110 (optimised).



(a)



(b)

Figure 3.9 (a) Time evolution of h^* of water drops ($We = 0.026$); (b) variations of average air pockets' pressure ($We = 0.026$).

Furthermore, the variations in the water droplet's mechanical energy are highly related to the practical applications of a superhydrophobic surface. For example, the self-cleaning property is highly associated with the water droplet's kinetic energy (E_k), and gravitational potential energy (E_g) can reflect the wetting state. Simulation results are used to calculate the kinetic energy and gravitational potential energy. The water droplet's gravitational potential energy (E_g) and kinetic energy (E_k) can be calculated by summing all the related elements, which can be expressed as:

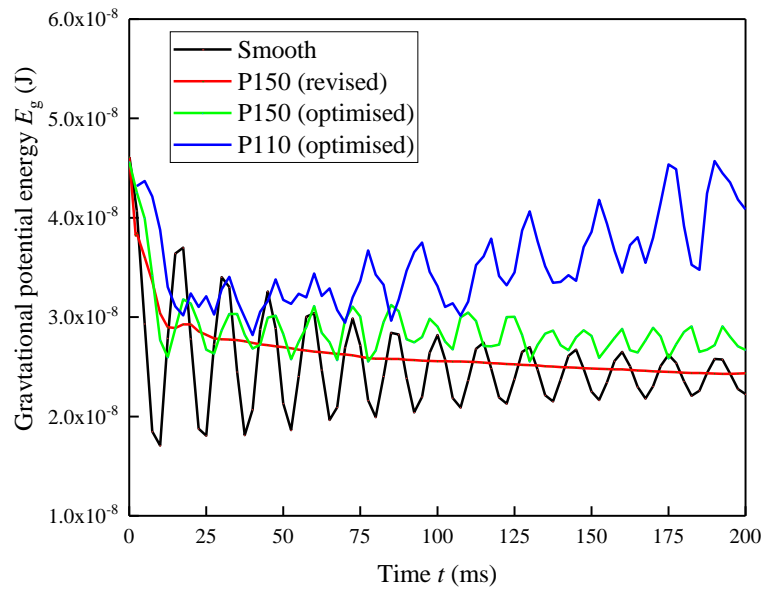
$$E_g = \sum_1^n (\rho_w V_{\text{element}} \alpha_2) g h_{\text{element}} \quad (3-26)$$

$$E_k = \sum_1^n \frac{1}{2} (\rho_w V_{\text{element}} \alpha_2) \vec{v}^2 \quad (3-27)$$

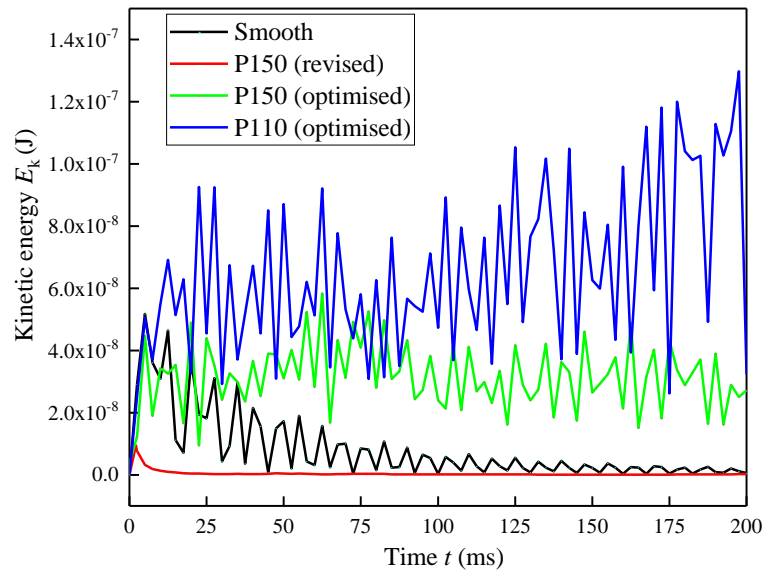
where n is the total number of the element that contains the water phase, ρ_w is the density of water, V_{element} is the volume of the element, α_2 is the volume fraction of the water phase, g is the gravitational acceleration equal to 9.81 m/s^2 , h_{element} is the height of every element and \vec{v} is the water velocity in every element.

The simulation results of potential energy and kinetic energy at We 0.026 are shown in Figure 3.10. At the initial time, the water droplet had maximum gravitational potential energy in all cases (Figure 3.10 (a)) due to the water droplet being in the highest position and having no contact with the substrate. With increased time, the gravitational potential energy is converted to kinetic energy; thus, the kinetic energy had a significant increase at the initial moment accompanied with the falling and spreading of the water droplet (Figure 3.10 (b)). The potential and kinetic energies showed declining trends and no oscillation in the gradual wetting process in the hydrophobic substrate P150 (revised). The water droplet penetrated the

microstructure; hence, the initial kinetic energy and potential energy transferred to surface energy due to the increased solid-liquid contact area of the water droplet's Wenzel state on P150 (revised). For P150 (optimised), the water droplet cannot fully penetrate the microstructure and shows an intermediate wetting state, and the initial kinetic energy and potential energy of the water droplet is difficult to transfer to surface energy, which results in the water droplet having higher kinetic energy and potential energy. The superhydrophobic substrate (P110 (optimised)) had the maximum potential energy and kinetic energy in the whole impacting process due to the water droplet having a Cassie-Baxter state on the substrate, which has the smallest solid-liquid contact area.



(a)



(b)

Figure 3.10 The variations in the water droplet's (a) gravitational potential energy (E_g) and (b) kinetic energy (E_k).

Figure 3.11 shows the simulated contact angles of a water droplet at 200 ms, based on image analysis software (Digimizer), to evaluate the hydrophobic property of four different substrates. The average contact angles were 105.6° for the smooth surface and 130.95° for the P150 (revised) substrate. The measured apparent contact angle for the P150 (optimised) and the P110 (optimised) substrates were 151.1° and $157.6^\circ (> 150^\circ)$ respectively, which classifies them as superhydrophobic surfaces. Furthermore, stable air pockets can be observed under the bottom of a water droplet in both. As shown in Figure 3.12, there are minor errors between the simulation results and the theoretically predicted result of the contact angle. Thus, the simulation results have a good agreement with the designed value.

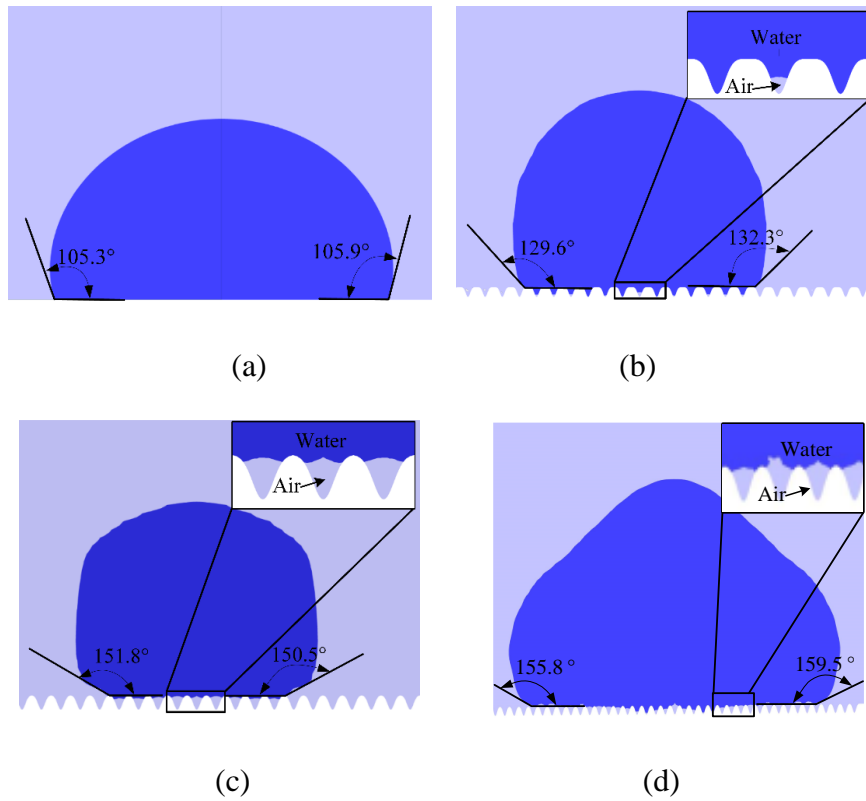


Figure 3.11 Simulated contact angle of water droplet at 200 ms for (a) smooth surface, (b) P150 (revised), (c) P150 (optimised) and (d) P110 (optimised).

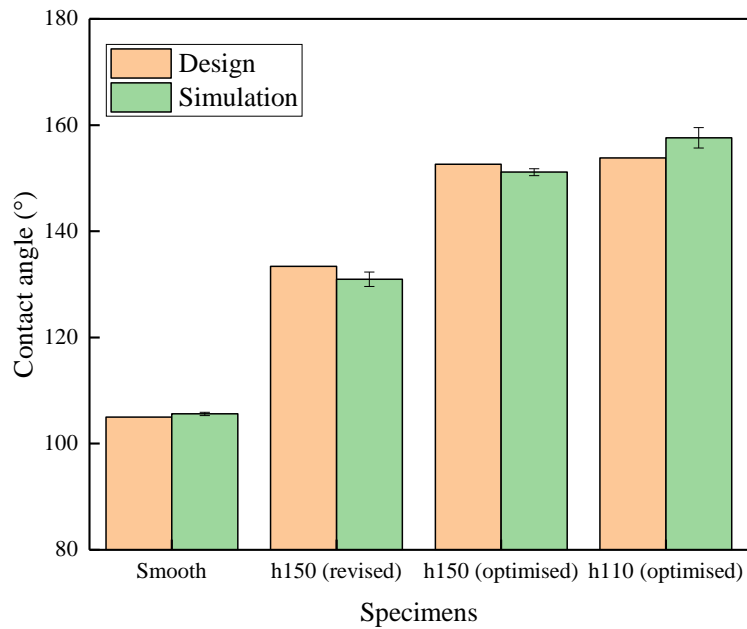
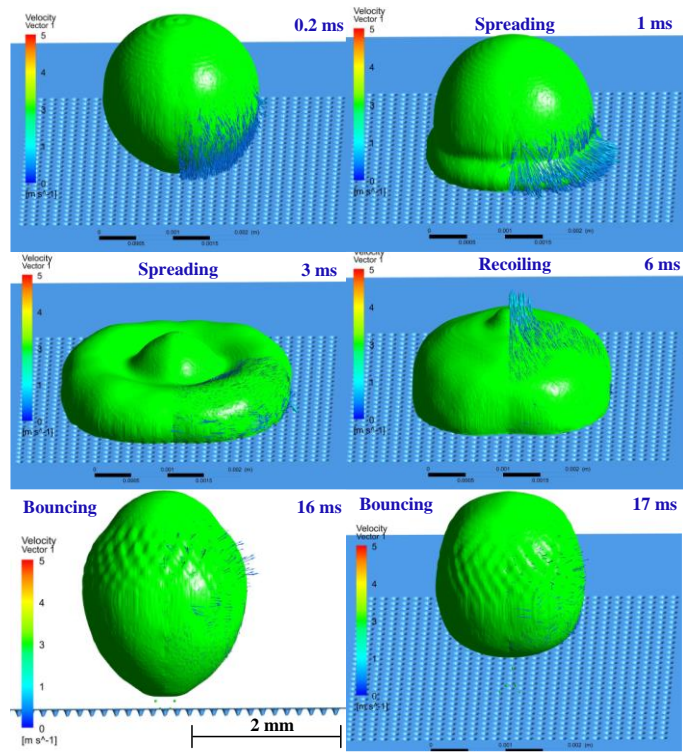


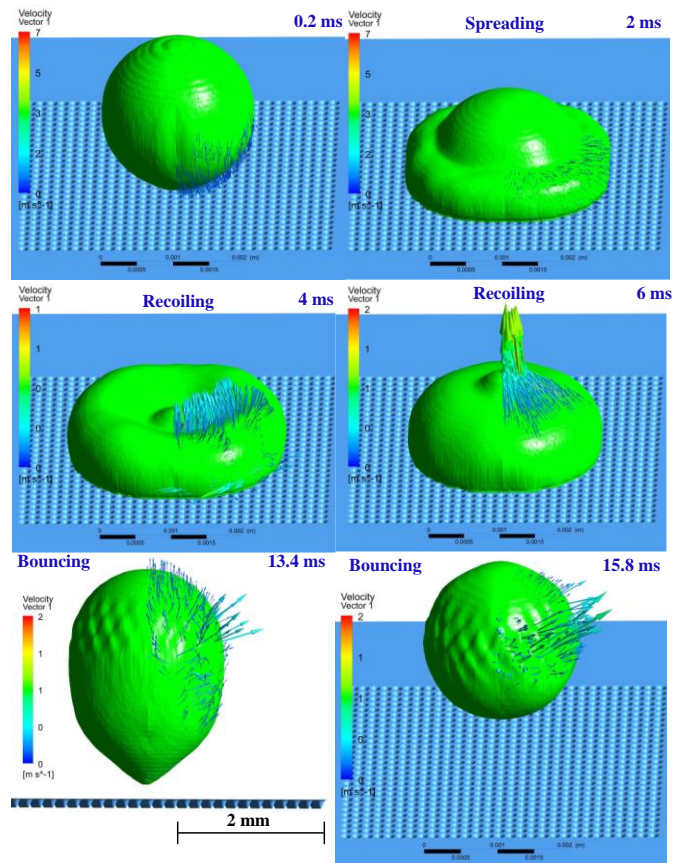
Figure 3.12 Comparison between simulation and the theoretical predicted value of contact angle.

3.4.2 Impacting behaviour of water droplet on varied substrates at Weber number of 7.26

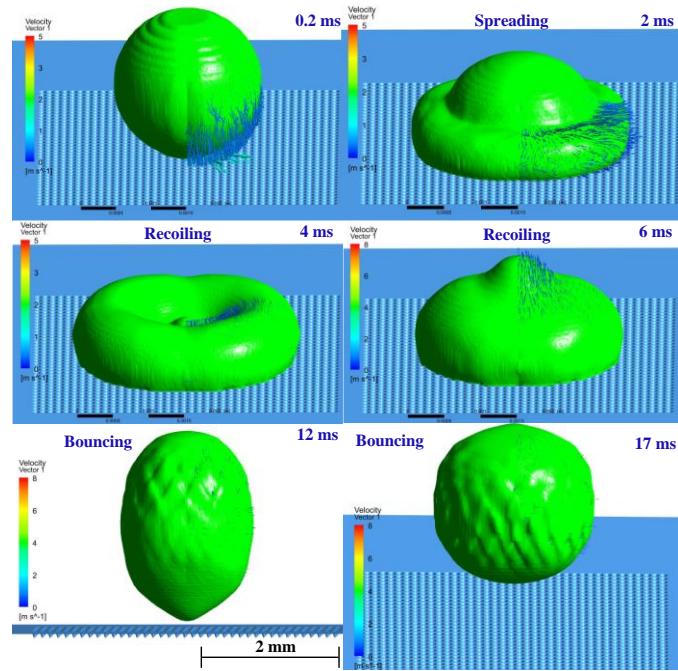
Section 3.4.1 explored the underlying mechanism of a water droplet during a quasi-static impacting process. In this section, a medium impacting velocity of 0.5m/s is applied to explore the dynamic rebounding behaviour of water droplets on different substrates. After the droplets impact the substrates, four stages of spreading, recoiling, rebounding and falling are performed until the energy is dissipated. Figure 3.13 displays the 3D shapes and velocity vectors of a water droplet on various substrates at different times. In the spreading stage, the water droplet moves downward, which results in water flowing outward along the radial direction. At 2 ms, the water droplet has a maximum velocity of 0.89 m/s on substrate P150 (revised), and of 0.64 m/s and 0.72 m/s on P150 (optimised) and P110 (optimised), respectively. As shown in Figure 3.13 (a), with further increased time, the water droplet has an increased diameter; however, the transverse velocity at the edge of the droplet gradually decreases. Then, the centre of the water droplet keeps going down, as shown at 3ms, due to the impact of inertia force. However, the water droplet's edge has an upward velocity due to the extrusion force from the water at the centre and lower position. As shown in the shape of the water droplet at 6 ms, the water at the central axis has a vertical upward velocity at the recoiling stage. As shown in Figure 3.13 (b) and (c), the water droplet shows similar behaviour on P150 (optimised) and P110 (optimised) substrates. However, for substrate P150 (revised), the water detaches from the substrate at 16 ms, while for P150 (optimised) and P110 (optimised), the water droplet requires just 13.4 ms and 12 ms, respectively, to detach from the surface.



(a)



(b)



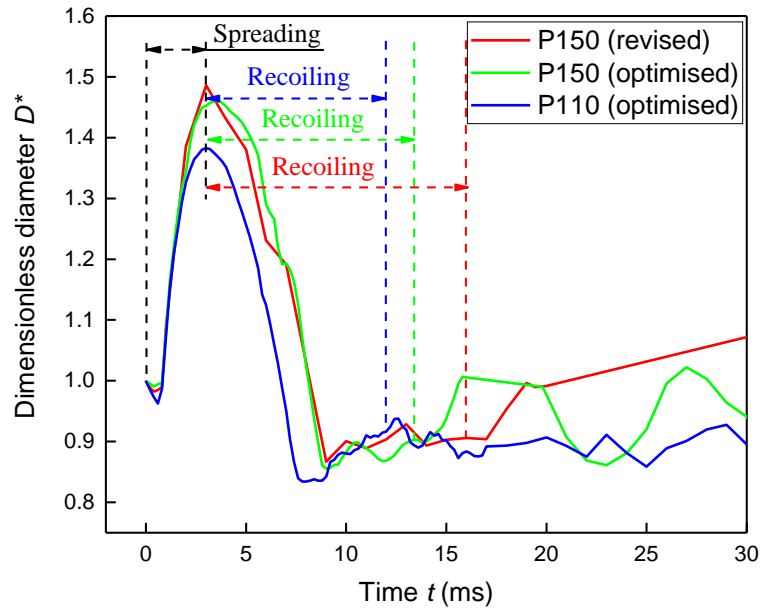
(c)

Figure 3.13 Time evolution of water drops with impacting velocity 0.5 m/s at (a) P150 (revised; $We = 7.26$, Case 5), (b) P150 (optimised; $We = 7.26$, Case 6) and (c) P110 (optimised; $We = 7.26$, Case 7).

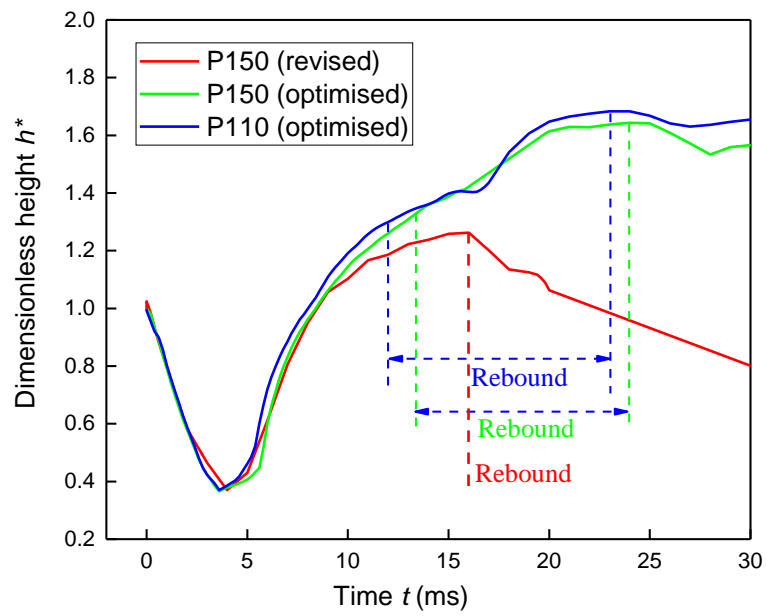
Figure 3.14 presents the D^* and h^* of the droplet for three textured substrates at $We = 7.26$ to quantitatively analyse the water droplet's dynamic behaviour. D^* can reflect the water droplet's spreading and compressing during the impacting process. As shown in Figure 3.14 (a), the water droplet on the P150 (revised) substrate has the maximum value of D^* (1.49) at 3 ms, which means the water droplet has the maximum spreading diameter at that moment. However, the P150 (optimised) and P110 (optimised) substrates have a smaller peak value of D^* compared with the P150 (revised), which are 1.46 and 1.38, respectively. In the recoiling stage, the water droplet starts retracting from the moment of possessing maximum D^* until detachment from the surface and entering the rebound stage. The adhesion force between the water

drop and the substrate is the “pull-off” force when the water drop separates from the surface [208]. Figure 3.14 (a) shows that P110 (optimised) has the shortest recoiling stage, which means the superhydrophobic surface has less adhesion force; hence, the water droplet can retract quickly. As shown in Figure 3.14 (b), h^* was displayed to reflect the water droplet’s rebound behaviour in the impacting process. In the rebound stage, the h^* value shows a steady increasing trend until the water droplet reaches the highest point. Thus, the point with the maximum h^* value represents the end of the rising stage. The water droplet on P150 (revised) substrate has an extremely short (less than 1 ms) rising stage. However, the rebound time for the P150 (optimised) and P110 (optimised) is approximately 11 ms. Thus, the simulation results proved that water droplets on the superhydrophobic substrates have shorter recoiling time and longer rebounding time than on the hydrophobic substrate.

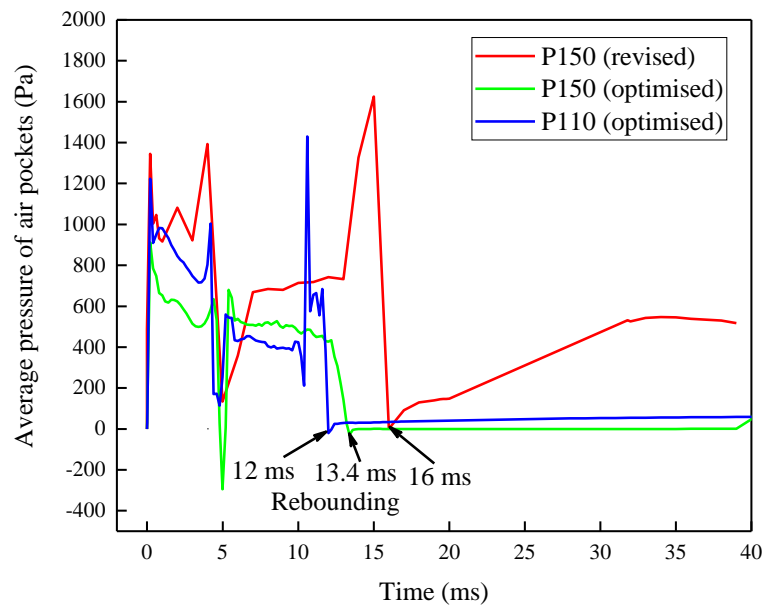
The rebound stage’s starting point can also be reflected in the variations of the air pockets’ average pressure at We 7.26, as shown in Figure 3.14 (c). The average pressure of the centre Gaussian hole in Figure 3.4 (b) was employed to represent the air pressure pocket due to the dynamic impacting process resulting in a varied area of the substrate being affected by the water droplet. The average air pressure is about zero (ambient pressure) due to the water droplet detachment from the surface during the rebound stage.



(a)



(b)



(c)

Figure 3.14 Time evolution of (a) D^* , (b) h^* and (c) average pressure of air pocket (We 7.26).

3.5 Summary

In this chapter, a geometrical model for laser machined Gaussian micro holes, together with the theoretical constraints for a stable Cassie-Baxter state, were established for the first time to provide a good understanding of the superhydrophobic mechanism and to optimise the Gaussian hole dimensions. Then, CFD simulation was conducted to predict the hydrophobicity of the designed structures, and the conclusions are as follows:

1. The design results prove that all the substrates (with the pitch varying from 50–150 μm) can have predicted contact angles higher than 150° under a water droplet of 5 μL to realise superhydrophobicity. Furthermore, the maximum contact angle shows a decreasing trend with an increase in the microstructures' pitch.

2. In a quasi-static impacting process ($We = 0.026$), the water droplet on the smooth surface acted as a damping vibration, and the air pockets' pressure shows a declining trend with the transition from a Cassie-Baxter state to a Wenzel state for hydrophobic substrate P150 (revised). However, the superhydrophobic substrates P150 (optimised) and P110 (optimised) trapped a large volume of air with a high pressure at the bottom of structures resulting in a stable intermediate state and a Cassie-Baxter state, respectively. Furthermore, the superhydrophobic substrate has the maximum potential energy and kinetic energy, which helps explain its low adhesion and self-cleaning properties.

3. In the impacting process at a Weber number of 7.26, all the water droplets have experienced four stages of spreading, recoiling, rebounding and falling with viscous energy dissipation. With the increase of the three specimens' hydrophobicity, the water droplet detachment occurs earlier, varying from 16 ms to 12 ms. Good hydrophobicity results in a smaller dimensionless diameter, and a larger dimensionless height. The simulation results also proved that water droplets on the superhydrophobic substrates have a shorter recoiling time and a longer rebound time than on the hydrophobic substrate.

4. The minor errors between the simulation and the theoretical results of contact angles prove the VOF simulation is a practical approach to predict the wetting state and the apparent contact angle at an equilibrium state.

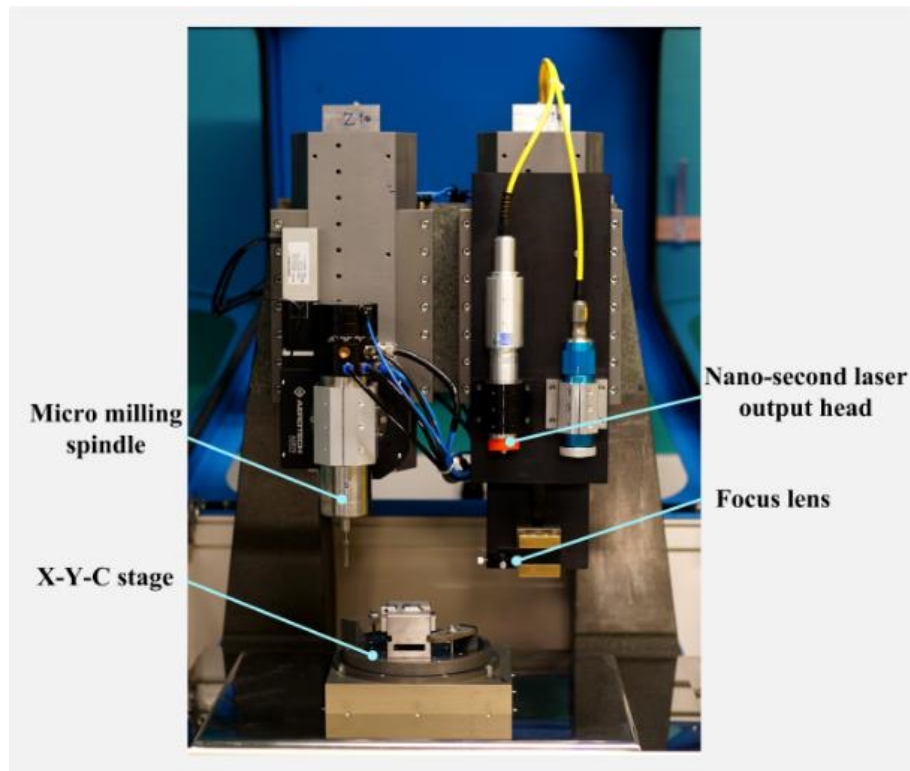
Chapter 4 Experimental Validation

4.1 Introduction

Chapter 3 presented the design approach and the CFD simulation results of the superhydrophobic surface with an array of Gaussian holes. However, an experimental investigation is still necessary to verify the design and simulation results. This chapter presents the experimental setup and methodology for the laser processing and characterisation of a superhydrophobic surface as well as the experimental validation results.

4.2 Laser processing experiment hardware

All the laser processing experiments were carried out on a hybrid ultra-precision machine, as shown in Figure 4.1 (a). It is equipped with a nanosecond pulsed fibre laser which has a central emission wavelength of 1064 nm as shown in Figure 4.1 (b). The laser source has a nominal average output power of 20 W and its maximum pulse repetition rate is 200 kHz. At a pulse repetition rate of 20 kHz, the average pulse duration is 100 ns and the pulse energy is 1 mJ. An achromatic doublet with a focal length of 26.054 mm was used to focus the laser beam. The achieved spot size is about 15 μm in diameter. More detail information about laser parameters can be found in Table 3.1. During the laser processing operation, the laser beam passes through a lens and is focused on the specimen surface which is mounted on a precision X-Y-C stage. All the experiments are conducted in the ambient air environment.



(a)



(b)

Figure 4.1 Experimental setup for laser ablation trials: (a) hybrid ultra-precision machine; (b) IPG fibre laser.

4.3 Laser processing parameters

4.3.1 Laser power (P_{ave})

In the nanosecond pulsed laser ablation process, the absorbed energy from the laser pulse melts the stainless steel and heats it to a temperature at which the atoms gain sufficient energy to enter into a gaseous state. Due to the vapour and plasma pressure, the molten material is partially ejected from the cavity and forms surface debris. At the end of a pulse, the heat quickly dissipates into the bulk of the work material and recast layers are formed. The relationship between laser power, pulse repetition rate and peak power can be expressed as:

$$E_p = \frac{P_{ave}}{f_p} \quad (4-1)$$

$$P_{peak} = \frac{E_p}{\Delta\tau} \quad (4-2)$$

where P_{ave} is laser average power, f_p is pulse repetition rate, E_p is the energy of a single pulse, P_{peak} is the peak power of laser and $\Delta\tau$ is the pulse duration, respectively.

4.3.2 Exposure time (t_e)

For a substrate with periodic Gaussian holes generated by the laser ablation process, the exposure time t_e means the machining time for a single Gaussian hole, which determines the number of laser pulses that irradiated the surface. It has a significant effect on the dimension and morphology of Gaussian holes. As shown in Figure 4.2, the relationship between the number of irradiated pulses, N , and exposure time, t_e , can be expressed as:

$$N = \frac{t_e}{T} \quad (4-3)$$

where T is the pulse period.

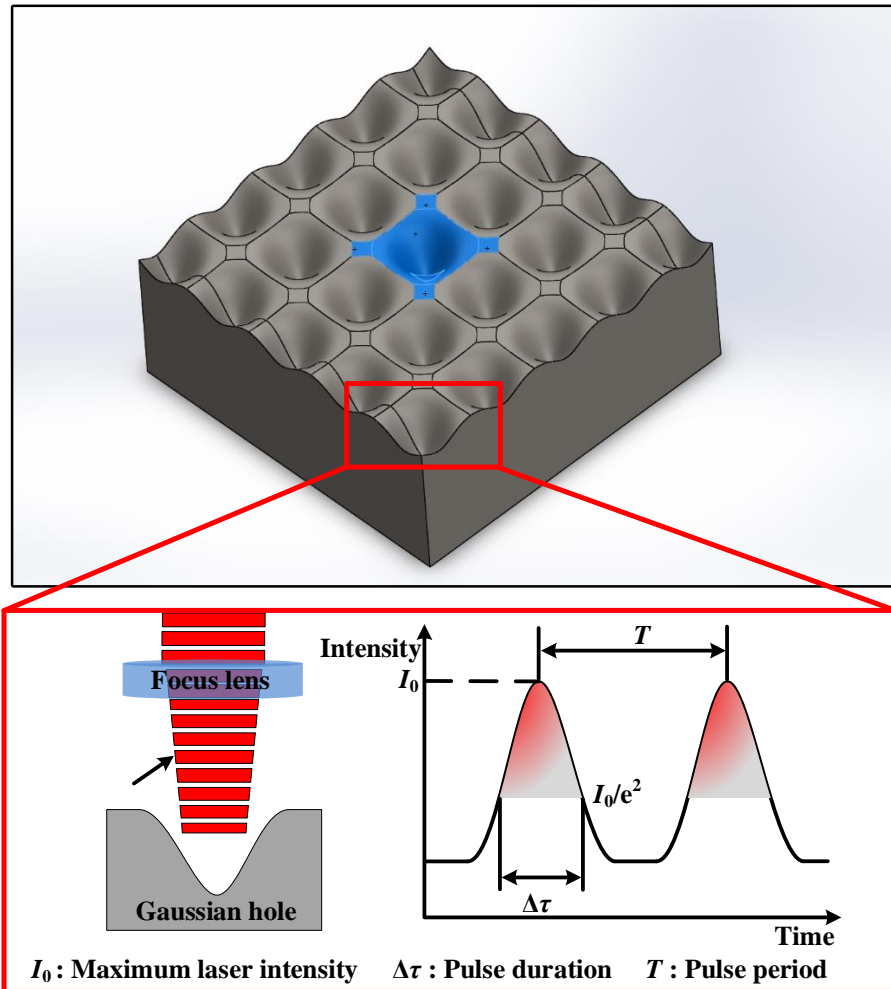


Figure 4.2 Schematic of periodic Gaussian holes machined by laser ablation.

4.4 Surface preprocessing, post-processing and characterisation

AISI 316L stainless steel (Goodfellow Ltd.) specimens were used in this research. Each specimen has a dimension of 10 mm × 10 mm × 2 mm. Before laser machining, all the specimens were machined by using a 6 mm diameter end mill to ensure the surfaces are smooth. The machined surface roughness S_a and S_z are 0.2 μm and 2.1 μm respectively after the planar milling operations.

Figure 4.3 shows the schematic of the methodology of laser ablated superhydrophobic surface. After the geometry model design and laser ablation process, the specimens were rinsed with deionised water in ultrasonic cleaning equipment for half an hour to remove the molten slags on the surface. Then, these specimens were degreased in an ultrasonic bath for 30 minutes in acetone and ethanol respectively. Finally, these specimens were dried in an oven. Before measuring the contact angle, these specimens were silanized in a vacuum oven using silane reagent (1H, 1H, 2H, 2H-Perfluorooctyltriethoxysilane, 97%, Alfa Aesar Ltd), at 100 °C for 12 hours to reduce their surface free energies. Figure 4.4 illustrates the chemical reaction mechanism for the reaction in the silanization process. The interfacial condensation and polymerisation reactions occur between the hydroxyl groups of sample and ethoxy groups, transforming the Si–OCH₂CH₃ bonds into Si–O bonds. Thus, the treated surfaces exhibit the low surface energy because of the strong covalency and small polarizability of the C-F bond.

The morphology of the laser structured surface was measured by a scanning electron microscope (SEM). Surface topography was measured by optical 3D surface measurement devices (i.e. Alicona G4 and Keyence VK-250). The contact angle was measured by a drop shape analyser DSA25B (Kruss Ltd.) after the silanization process. The selected water droplet volume was 5 µL. For each specimen, the apparent contact angle of the water droplet was measured three times and the average value was adopted.

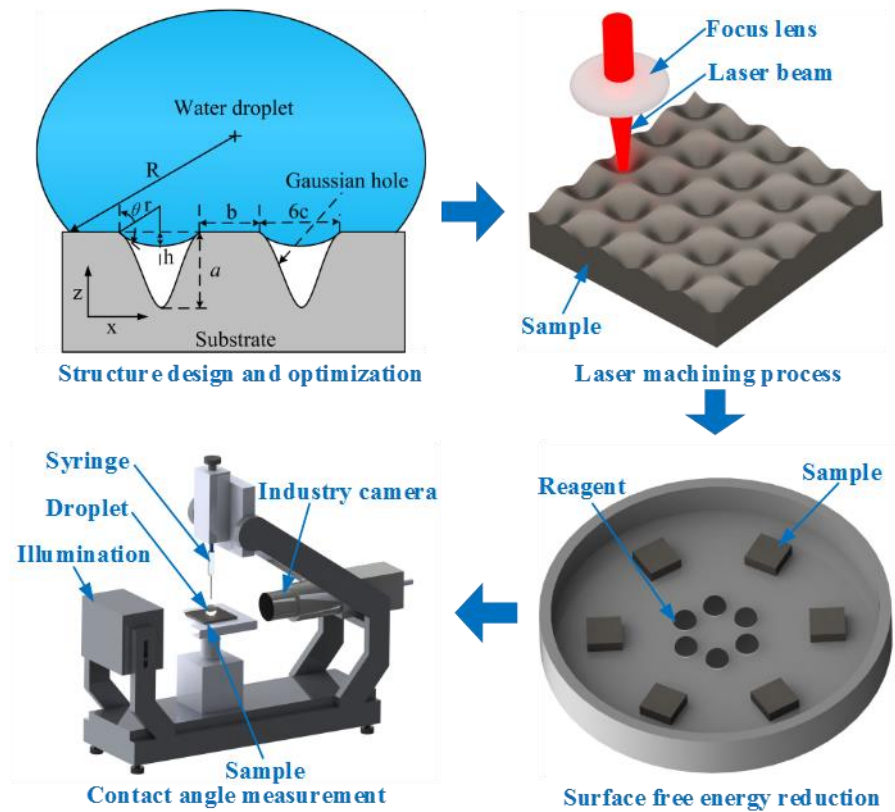


Figure 4.3 Schematic of preparation of laser ablated superhydrophobic surface.

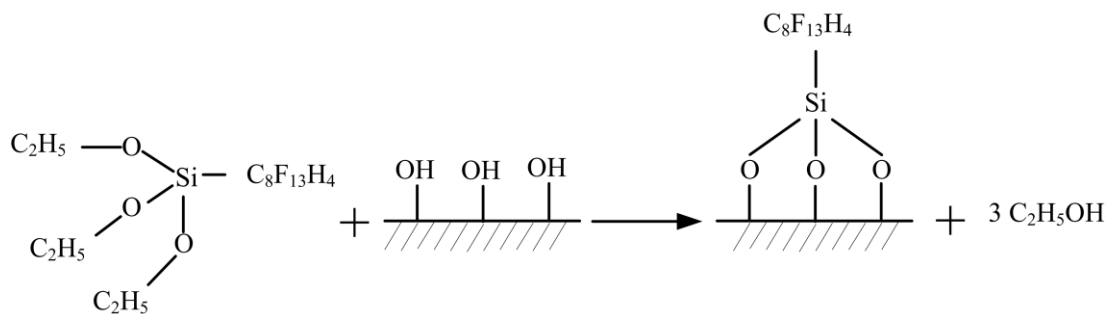


Figure 4.4 Schematic of the silanization procedure.

4.5 Dynamic impacting test of water droplets by a high-speed camera

As shown in Figure 4.5, a high-speed camera (Phantom v2012) was used to capture images of the dynamic impacting process of water droplets on smooth and superhydrophobic substrates. The frame rate was set at 1000 fps in this test. As shown in Table 4.1, the water droplet with a volume of 5 μL was released from certain

distances to the surface to achieve contact impacting velocities of 0.5 m/s and 1 m/s respectively.



Figure 4.5 Phantom v2012 high-speed camera.

Table 4.1 Conditions of high-speed camera test.

Volume of water droplet (μL)	Distance (mm)	Impacting velocity (m/s)	Weber number
5	12.7	0.5	7.26
5	51	1	29

4.6 Experimental validation results

This section presents the experimental results to validate the design and simulation results. Moreover, the influences of processing laser power and pitch of the microstructures on the topography of the machined surface were investigated through laser ablation experiments. Subsequently, the water droplet contact angle was measured to evaluate the hydrophobicity of different specimens. The laser ablation parameters are listed in Table 4.2. The average laser power varies from 4 W to 14 W. The laser processing route for Gaussian holes is shown in Figure 4.6. The laser pulse exposure 0.4 s to form the first Gaussian hole A, then the laser shutdown and moved

to position B with a feed rate of 200 mm/min. The pitch P means the distance between the two adjacent holes.

Table 4.2 The laser ablation parameters in the experiments.

Laser power (W)	Pulse repetition rate (kHz)	Feed rate (mm/min)	Exposure time (s)
4, 6, 10, 14	100	200	0.4

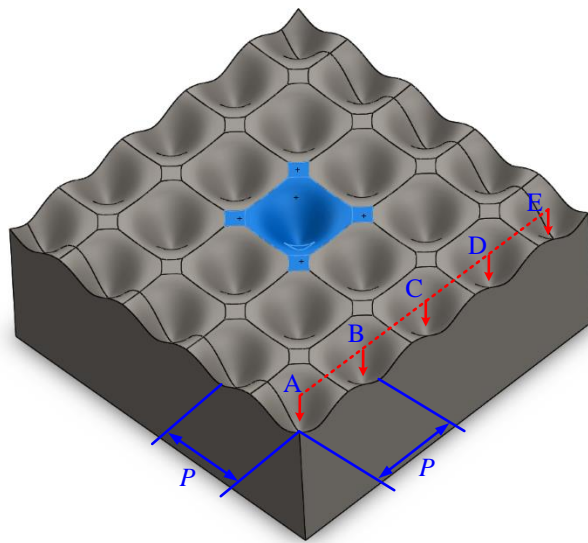


Figure 4.6 Schematic for laser processing route.

4.6.1 Analysis of surface morphology

The surface topography and dimensions of the machined structures vary with the laser power and the designed pitch. The SEM images of the surface topography of P110 series specimens (with pitch 110 μm) are shown in Figure 4.7. It can be seen that the micro holes are well separated when the laser power is 4W. With the increase of laser power, a large amount of material was vapoured and melted, the wall thickness between adjacent holes reduced gradually. Then, the recast layers formed on the circumference of the micro holes. The micro holes partially overlapped each other as

the wall material melted and evaporated gradually to form the pillars. Moreover, the pillar width decreases with increasing laser power.

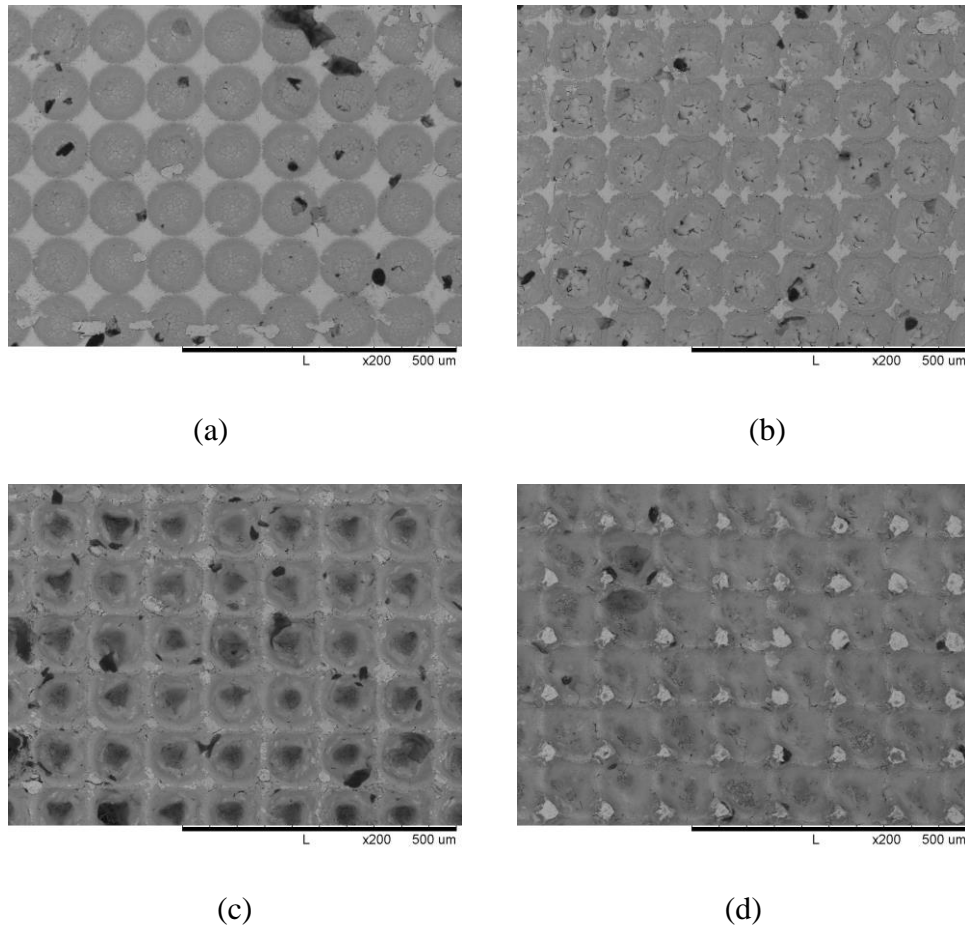


Figure 4.7 SEM images of P110 specimens at different laser power: (a) 4 W, (b) 6 W, (c) 10 W and (d) 14 W.

The SEM images of specimens machined using a laser power of 14 W with micro holes of different pitches are shown in Figure 4.8. For a small pitch of 50 μm, the whole surface was ablated (as shown in Figure 4.8 (a)) due to the large proportion of the overlapping area. As the pitch is increased, the proportion of un-ablated surface increases and the surface starts to show rectangle pillars between the holes gradually, as shown in Figure 4.8 (b), (c) and (d).

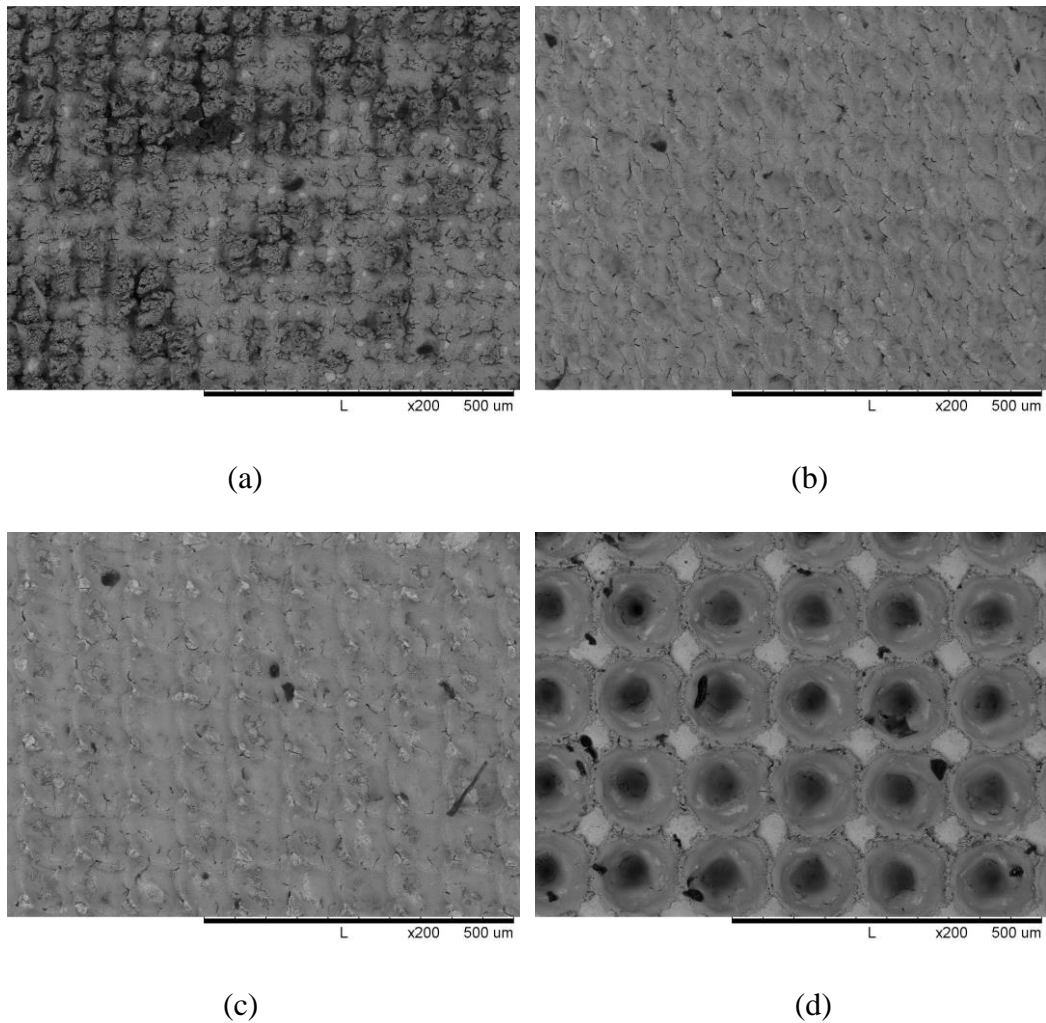


Figure 4.8 SEM images of specimens ablated under laser power of 14 W with different pitches (a) 50 μm , (b) 70 μm , (c) 90 μm and (d) 150 μm .

Figure 4.9 shows the 3D surface morphologies of machined surfaces with a pitch of 130 μm . It can be seen that only a few materials are redeposited around the micro holes when using small laser powers of 4 W and 6 W. But some materials are deposited at the centre of holes due to weak evaporations. With the increase of laser power, the depth and diameter of the holes increase significantly, and more molten materials are deposited on the surface between the micro holes. Particularly, when laser power reaches 14 W, as shown in Figure 4.9 (d), the large volume of molten materials almost

cover the whole surface between micro holes, which results in a rough surface and periodic pillar structures.

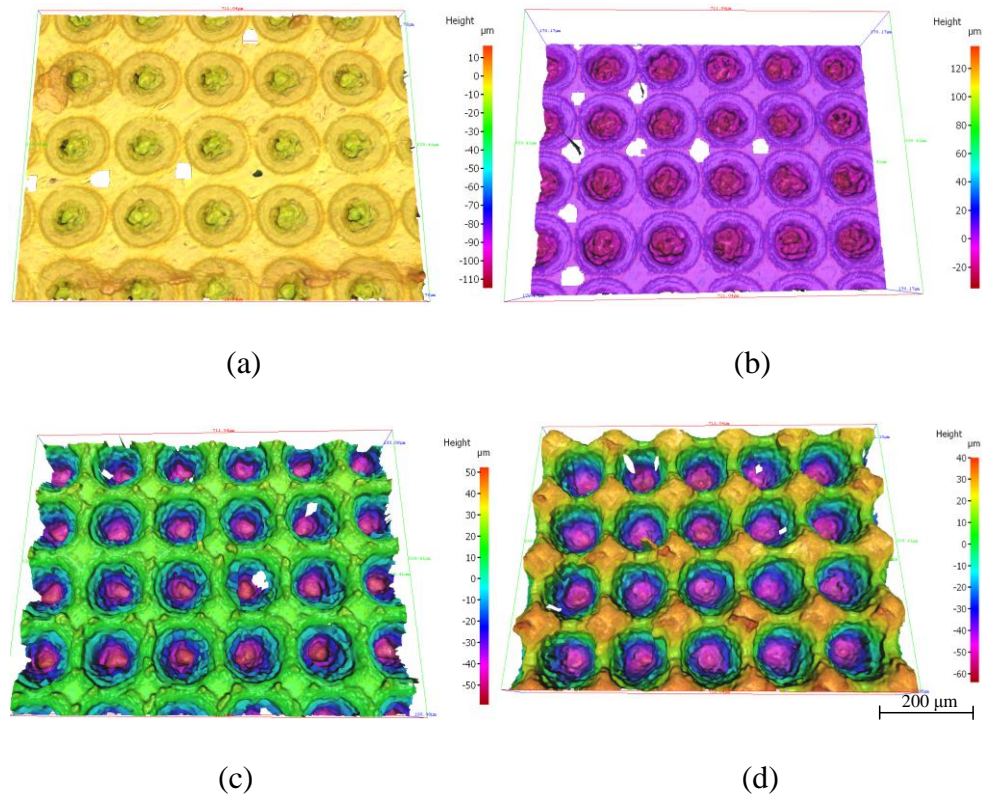


Figure 4.9 Surface morphologies under different laser powers for microstructures with a pitch of 130 μm (P130): (a) 4 W, (b) 6 W, (c) 10 W and (d) 14 W.

4.6.2 Analysis of surface hydrophobicity

In this section, static contact angles of water droplets were measured using the sessile drop method to characterise the hydrophobicity of the specimen surfaces, including a smoothly milled surface as a benchmark. A 5 μL droplet of deionised water was dropped on the smoothly milled specimen at atmospheric condition. A drop shape analyser DSA25B (Kruss Ltd.) captured the side view and the contact angles are calculated by image processing software on a PC. As shown in Figure 4.10, the contact

angle θ is 86° for the smooth milled surface before silanization. After the silanization process, the contact angle θ is measured as 105° .

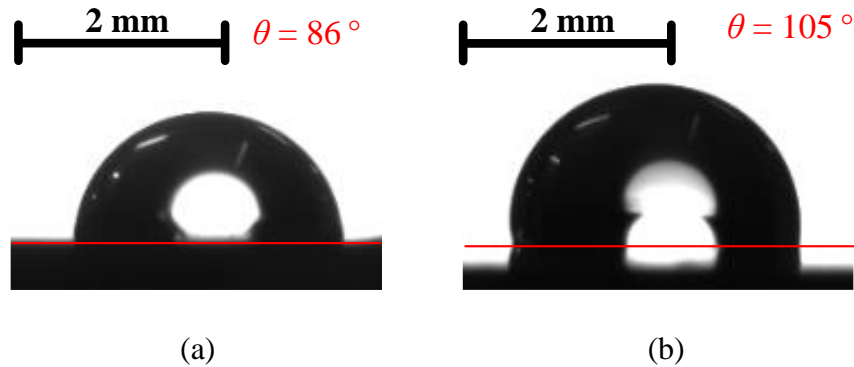
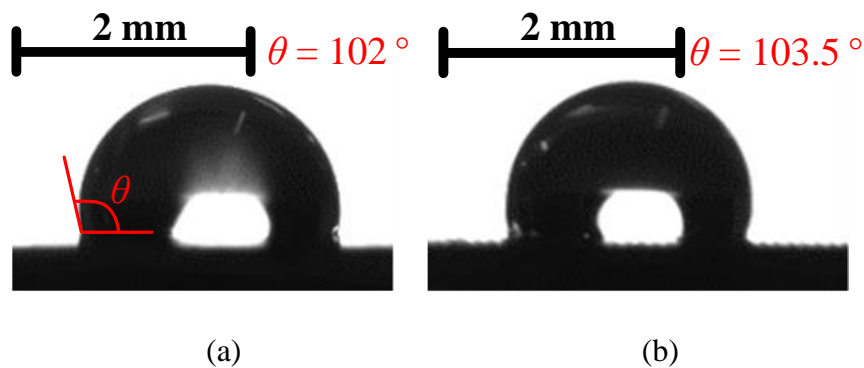


Figure 4.10 Water droplet on the smooth milled surface (a) before and after (b) silanization.

4.6.2.1 Effect of laser power and pitch of structure on surface hydrophobicity

Figure 4.11 shows the captured images of the droplets in the contact angle measurements. As shown in Figure 4.11 (d), (e) and (f), the three specimens, P110-14 W (i.e. pitch of $110\ \mu\text{m}$ under laser power of 14 W), P090-10 W and P050-6 W show the larger contact angles. As a comparison, the contact angle of the smooth surface with chemical treatments is only 105° in Figure 4.10. It is the laser textured microstructures that further improved the contact angle to 153.2° , which can be classified as superhydrophobic surface.



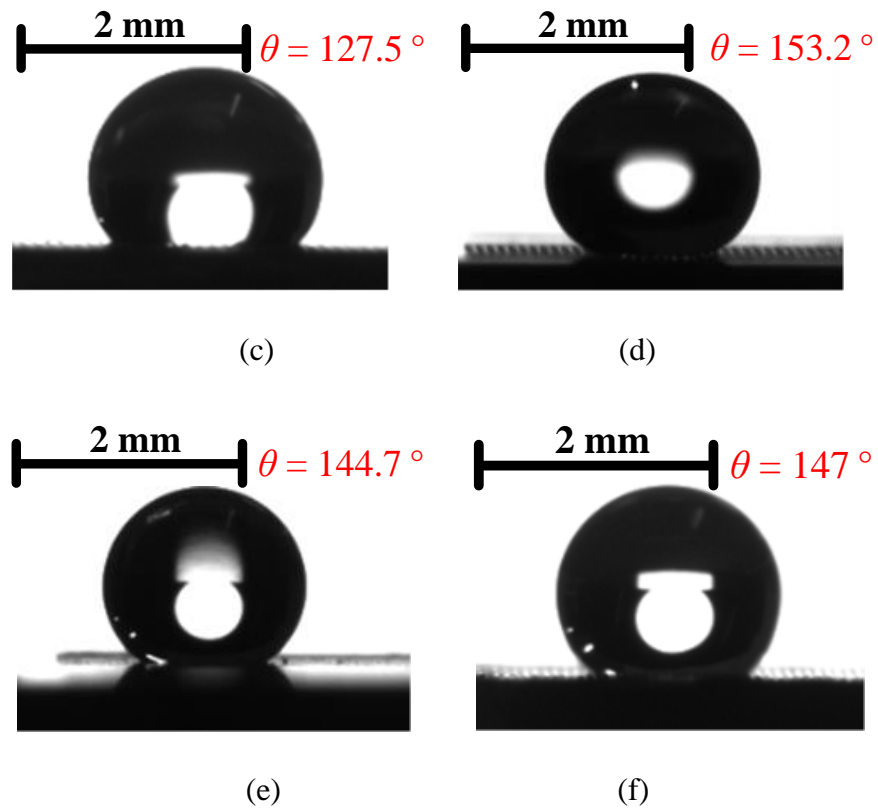


Figure 4.11 Water droplet shapes for different specimens: (a) P110-4 W, (b) P110-6 W, (c) P110-10 W, (d) P110-14 W, (e) P050-6 W and (f) P090-10 W.

As shown in Figure 4.12, the water droplet falls from the height of 2 mm (the distance between the bottom of water droplet and specimen) onto the specimen P110-14 W at a tilt angle of 3.5° . The water droplet is easy running off from the surface, which proved the low adhesion property of laser ablated superhydrophobic surface.

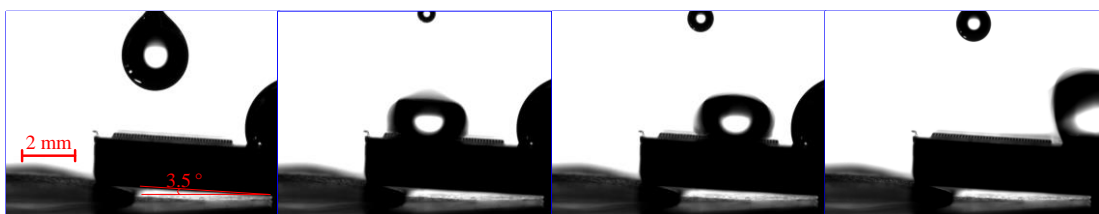


Figure 4.12 Water droplet fall on specimen P110-14 W at a tilt angle of 3.5° .

Figure 4.13 shows the variations of water contact angle of the microstructured surfaces as a function of pitch and processing laser power. The error bar in the graph represents the minimum and maximum contact angle in three measurements for each specimen.

The microstructured surface machined at 4W has the same level of surface contact angle as a smooth milled surface of 105° . As shown in Figure 4.7 (a) and Figure 4.9 (a), there are few materials removed from specimens at the laser power of 4W. So the water droplet entirely wets the structures and results in a homogeneous liquid-solid interface as described in the Wenzel model. Besides, the surface contact angle decreases slightly when the pitch is chosen as $130\ \mu\text{m}$ or $150\ \mu\text{m}$ because the Wenzel state becomes dominant.

For the specimens machined using a laser power of 6 W, the contact angle shows a gradually decreasing trend. For the specimens machined using laser powers of 10 W and 14 W, the variations of the surface contact angles are very similar. With increasing pitch, the contact angle rises to a peak value and then gradually decreases. Moreover, with increasing laser power, the pitch of the specimen with a maximal contact angle increases gradually. In particular, for the series with laser power of 6 W, the maximum contact angle is 144.7° when the pitch is $50\ \mu\text{m}$. For laser power of 10 W, the maximum contact angle is 145.2° when the pitch is $90\ \mu\text{m}$. P110-14 W specimen shows superhydrophobicity among all specimens with a contact angle of 153.2° . The above phenomenon can be explained as follows. With a laser power of 6 W, less material was removed from the specimen than at 10 W and 14 W. Thus, with the increase in the laser power, the width of microhole, $6c$, also increases because more

materials are removed from the specimen. Therefore, the surface contact angle is not only affected by the laser power, but also the pitch of microstructure.

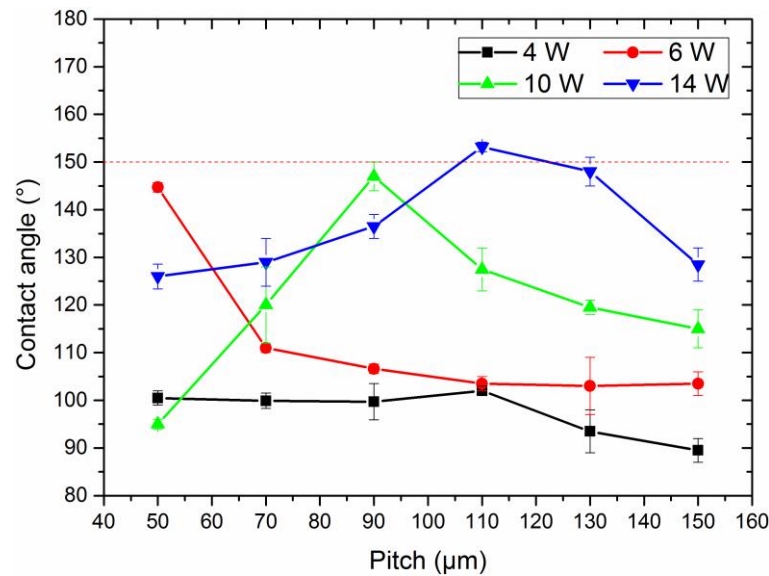


Figure 4.13 Effect of laser power and pitch on the hydrophobicity of laser ablated specimens.

4.6.2.2 Effect of surface roughness on surface hydrophobicity

The above analysis suggests that both the processing laser power and pitch of microstructure have significant influences on the hydrophobicity of AISI 316L stainless steel specimens. The influence of laser power on the contact angle is reflected from the surface roughness (S_z). As shown in Figure 4.14, the increase of surface roughness S_z leads to increasing contact angles under all pitches. The reason can be explained as follows: the droplet can touch the bottom of the hole and exhibits the Wenzel state when S_z has a small value. Moreover, for the specimen with small S_z , the droplet can remain in the Cassie-Baxter state, due to minor spaces for air pockets beneath the water droplet. The Cassie-Baxter state is metastable and is easily transformed to the Wenzel state. However, with the increase of S_z , the depth from peak to valley increases, so there are more spaces for droplet sag. The droplet will not

contact the bottom of microholes. Thus, large S_z is an essential condition to form a stable and robust Cassie–Baxter state.

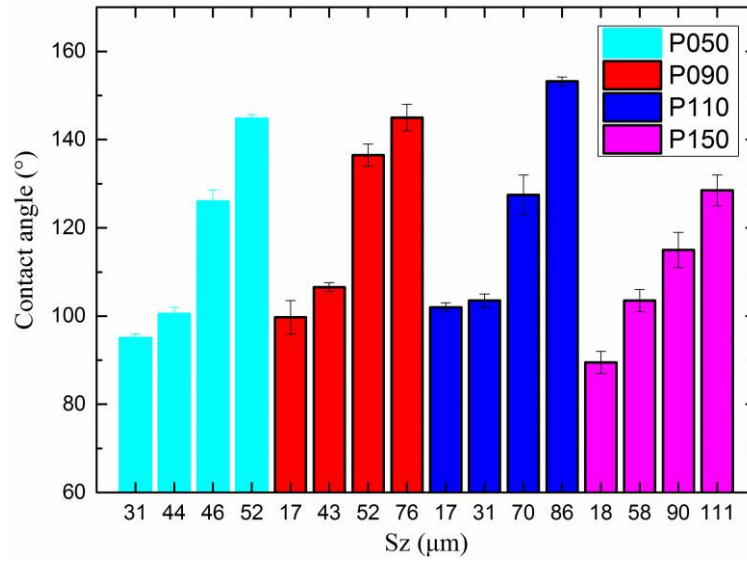
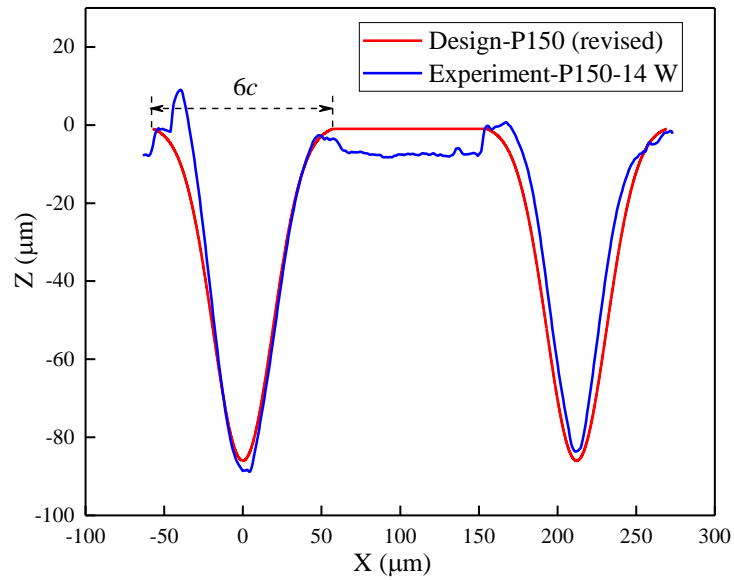


Figure 4.14 Influence of surface roughness on contact angles.

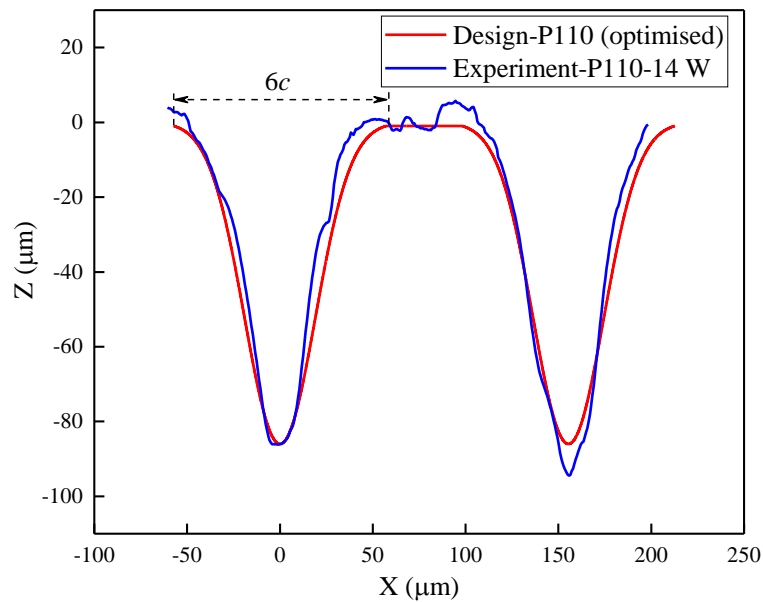
4.6.3 Results comparison

Figure 4.15 shows a comparison between the experimental and designed microstructure profiles. The specimen P150-14 W has a similar size with the designed specimen P150 (revised). Figure 4.16 shows the comparison of the predicted value of the contact angle with the measured value. For specimen P150 (revised), the actual width of the Gaussian hole is smaller than the optimised value $6c$, as shown in Figure 4.15 (a), which results in an increased fraction of solid-liquid contact area (f). Consequently, the actual contact angle is smaller than the predicted value, as shown in Figure 4.16. The specimen P110-14 W has a similar profile with the designed specimen P110 (optimised), as shown in Figure 4.15 (b). Hence, the actual contact angle 153.2° is also extremely close to the predicted value of 153.8° .

However, there are no specimens that have similar dimensions to P150 (optimised). Hence, not all the designed profiles can be obtained in the experiments. The relationship between process parameters and superhydrophobicity must be explored to control the hydrophobicity according to the technical requirement.



(a)



(b)

Figure 4.15 Comparison of design profile and experiments for specimens with pitches of (a) 150 μm and (b) 110 μm .

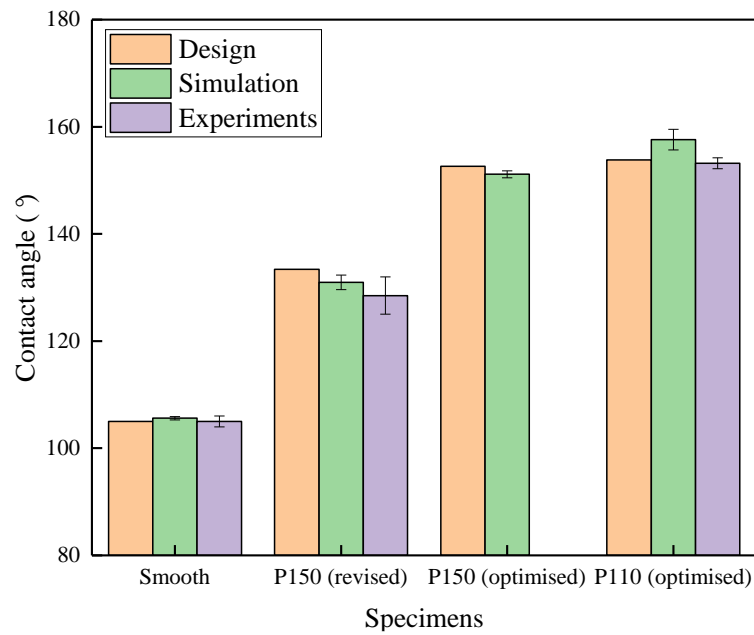


Figure 4.16 Comparison between the predicted, simulated and measured contact angles.

4.6.4 High-speed camera test

The sequential images of a simulated water droplet with a Weber number of 7.26 impacting on the P150 (revised) specimen were compared with the test results of a high-speed camera on specimen P150-14 W. As presented in Figure 4.17, there is a good visual agreement between the water droplet's simulated and real shapes during the spreading and initial recoiling stages (0–6 ms) due to inertia dominating the motion. However, unlike the simulation results, the water droplet in the experiment did not detach from the substrate at 16 ms. The actual laser ablated specimen is rougher than the 3D geometry model due to the existing slags and recast layers on the surface, as shown in Figure 4.15 (a), which results in larger solid-liquid contact area than the simulation. In the impacting process, the kinetic energy was gradually dissipated by the adhesion force between the solid and liquid and by the viscous force during the

recoiling stage. Hence, more kinetic energy is dissipated in the recoiling process and there is insufficient kinetic energy to raise the water droplet from the substrate in the experiments.

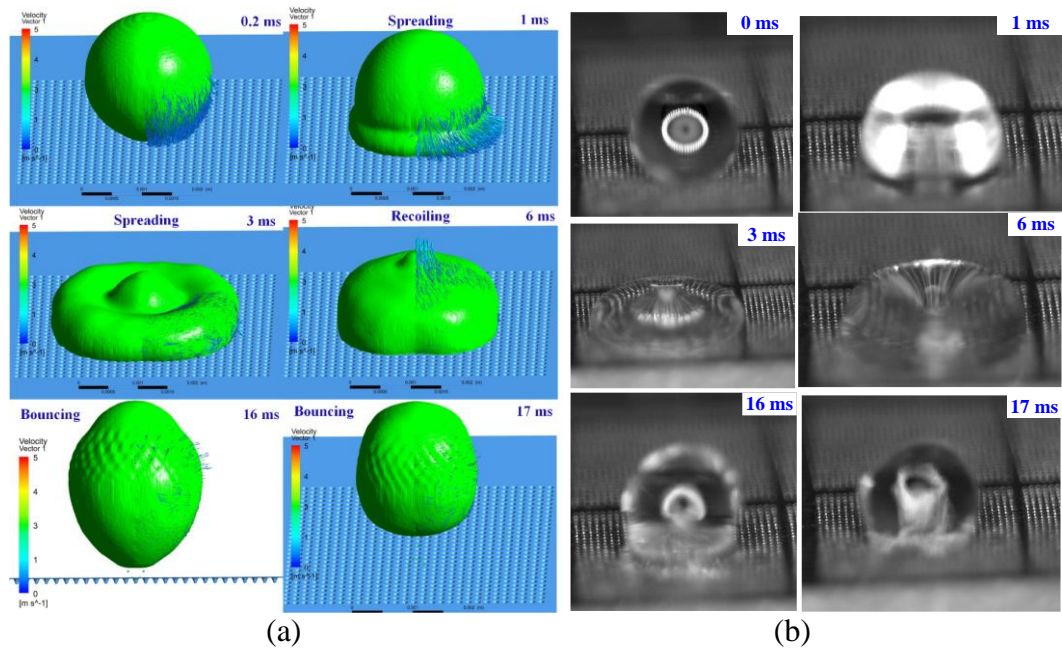
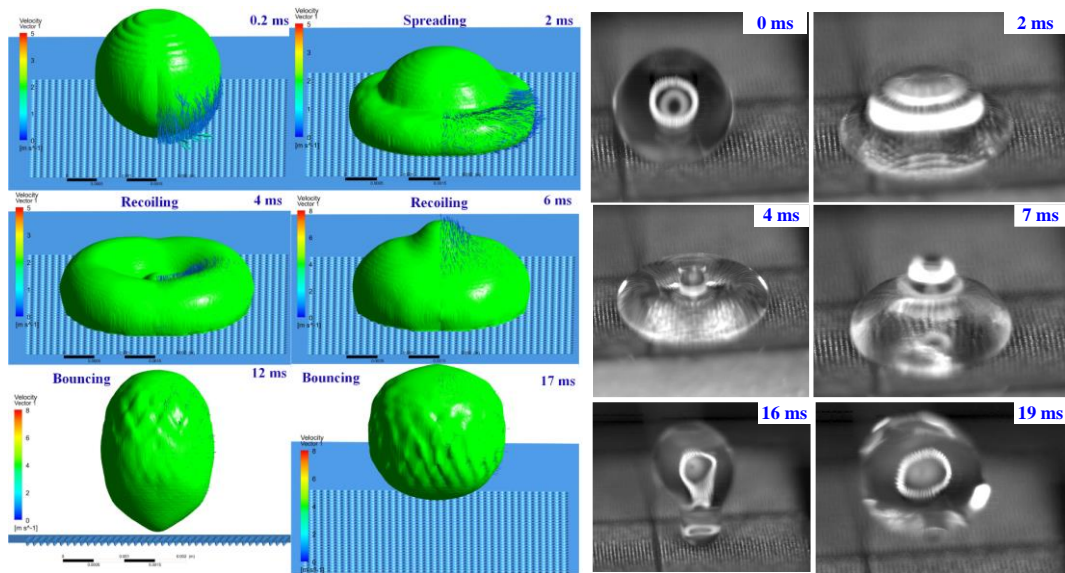


Figure 4.17 Time evolution of water drops with impacting velocity 0.5 m/s: (a) simulation results of P150 (revised) and (b) captured images of P150-14 W.

Similarly, the simulated and experimental images of a water droplet with a Weber number of 7.26 impacting the P110 (optimised) specimen are presented in Figure 4.18. The results also show good agreement in the spreading and recoiling stages. Regarding the simulation results, it was predicted that the water droplet would rebound from the substrate at 12 ms. However, the high-speed camera experiment shows that the time of detachment is 16ms. This minor error resulted from the morphology difference between the laser ablation experiment and the ideal geometry model.

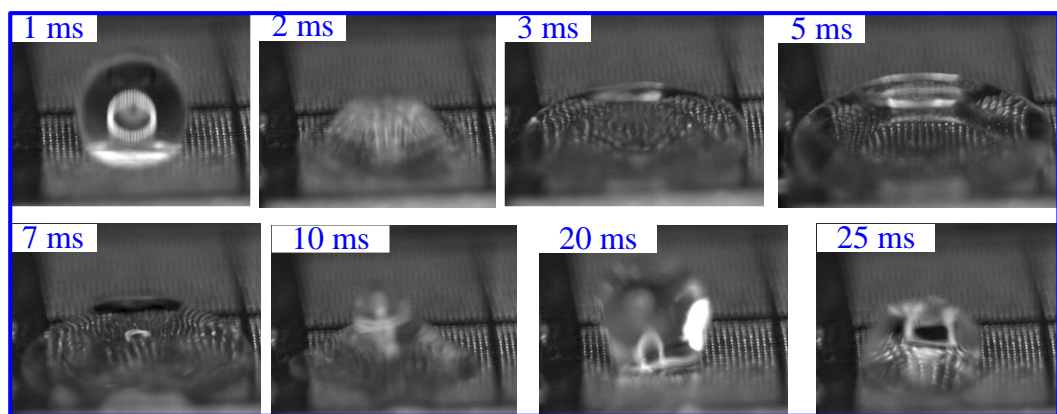


(a)

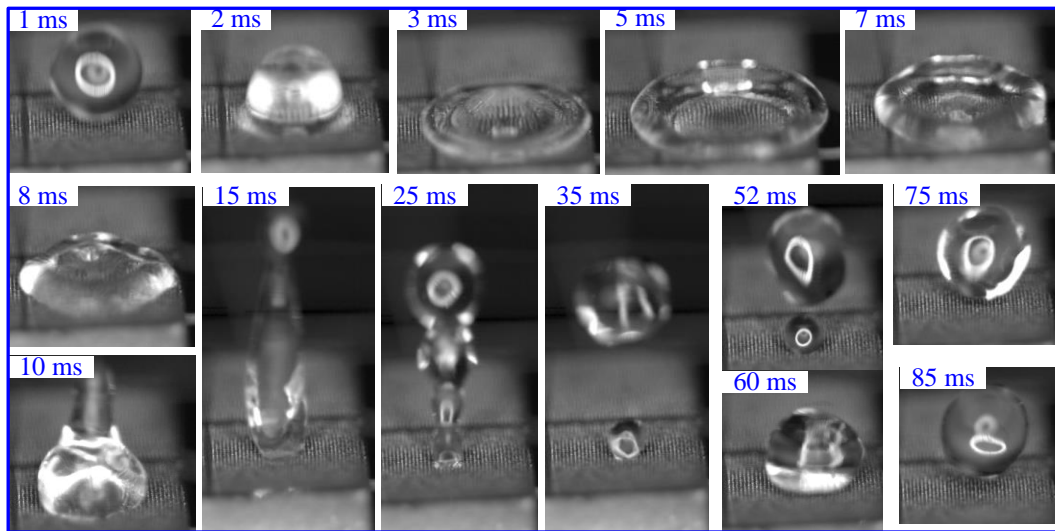
(b)

Figure 4.18 Time evolution of water drops with impacting velocity 0.5 m/s: (a) simulation results of P110 (optimised) and (b) captured images of P110-14 W.

According to Table 4.1, to show the low adhesion property of a water droplet on the superhydrophobic substrate, a higher impacting velocity of 1 m/s ($We = 29$) was conducted on the P150-14 W (hydrophobic substrate) and the P110-14 W (superhydrophobic substrate) as shown in Figure 4.19. The results show that the water droplet did not detach from P150-14 W; however, the droplet rebounded from the P110-14 W at 35 ms and 75 ms.



(a)



(b)

Figure 4.19 High-speed camera captured images under impacting velocity 1 m/s of (a) P150-14 W and (b) P110-14 W.

Therefore, the laser ablated superhydrophobic surface has a low adhesion force to the water droplet, which will enable this technology to be used in practical applications.

4.7 Summary

This chapter presented the details of the experimental setup, the methodology and the validation results for the proposed design method and simulation models. The conclusions are as follows:

1. The contact angle is not only affected by the laser power, but also the microstructure's pitch. Furthermore, for microstructures of the same pitch, the increase of surface roughness S_z leads to the increase of contact angle.

2. The designed and simulated contact angles are in very good agreement with the experimental values, as the machined specimens P150-14 W and P110-14 W have similar dimensions to the designed profiles.

3. The experimental results also show that not all of the designed profile can be obtained in the experiments. There are no machined specimens that have a similar profile with P150 (optimised). Therefore, further exploration of the relationship between process parameters and hydrophobicity is needed to accurately control the superhydrophobicity of the AISI 316L stainless steel.

4. The dynamic impact behaviour of a water droplet at a Weber number of 7.26 proved that the simulation results have good agreement with high-speed camera test results, and the minor deviation was due to the laser ablated specimens being rougher than the simulation model.

5. The high-speed camera test of a water droplet at a Weber number of 29 showed that the water droplet did not detach from P150-14 W; however, the droplet rebounded from P110-14 W at 35 ms and 75 ms. This proves that the laser ablated superhydrophobic surface (P110-14 W) has a lower adhesion force than the hydrophobic surface (P150-14 W).

Chapter 5 Process and Product Fingerprints for a Laser Ablated Superhydrophobic Surface

5.1 Introduction

The literature review indicates that the laser machining parameters would significantly affect the specimen's hydrophobicity, and the surface topography is a crucial factor in determining the specimen's superhydrophobicity. However, there has been little systematic research exploring the correlation between surface topography and a specimen's hydrophobicity.

Furthermore, according to the results of Chapter 4, not all the designed profile can be obtained in the experiments. Therefore, further exploration of the relationship between process parameters and hydrophobicity is needed to accurately control the superhydrophobicity of the AISI 316L stainless steel.

To address these challenges, one must determine the most effective process and surface characterisation parameters for these microstructures that are sensitive to the hydrophobicity of substrates. This chapter proposes the concepts of process and product fingerprints as critical measurable characteristics for determining the required surface topography and process parameters for a superhydrophobic surface. Therefore, process and product fingerprints are expected to provide a solution to the so-called inverse problem in manufacturing, which means the laser machining parameters and surface characterisation parameters can be determined according to the required hydrophobicity (i.e. contact angle).

First, an analysis of the potential process and product fingerprint candidates is conducted. Then, the most appropriate product fingerprint is determined from

Spearman and Kendall rank correlation coefficients, according to the experimental results. Third, a new process parameter is chosen as the best process fingerprint. Finally, the correlation between process fingerprint and functional performance (i.e. contact angle) is explored.

5.2 Definition of process and product fingerprints

The concept of “product fingerprint” refers to those unique measurable characteristics (e.g. surface characterisation parameters) on the laser ablated specimen that, if kept under control and within specifications, will ensure that the specimen possesses superhydrophobicity as required. The product fingerprint must also be sensitive to the variations of the process parameters. Hence it can be well-controlled by process parameters. For the laser ablation process, since the surface characterisation parameters are highly related to laser machining parameters, the “Process fingerprint” is defined as a specific process parameter to be controlled in order to maintain the manufacture of the specimen within the specified surface characterisation parameters. The product and process fingerprints can be used as an objective function within an optimisation tool to assist in determining the required surface topography and process parameters for the superhydrophobic surface.

Figure 5.1 illustrates the concept of process and product fingerprints in the laser ablation process for obtaining the superhydrophobic surface with an array of Gaussian holes of designed geometry. The comparison of all the potential candidates of process and product fingerprints will be discussed in detail later. Most of the research performed to date has focused on correlation A (i.e. the effect of laser machining parameters on the contact angle of specimens). However, correlation A is composed of correlation B and C. Correlation B refers to the relationship between contact angle

and product fingerprint, which is used to explain the underlying mechanism of effect of surface topography on hydrophobicity. Correlation C can describe the relationship between the process fingerprint and product fingerprint, to explore how the process parameters affect the surface topography. Thus, product fingerprint is a bridge to connect between the process parameters and the functional performances (e.g. contact angle).

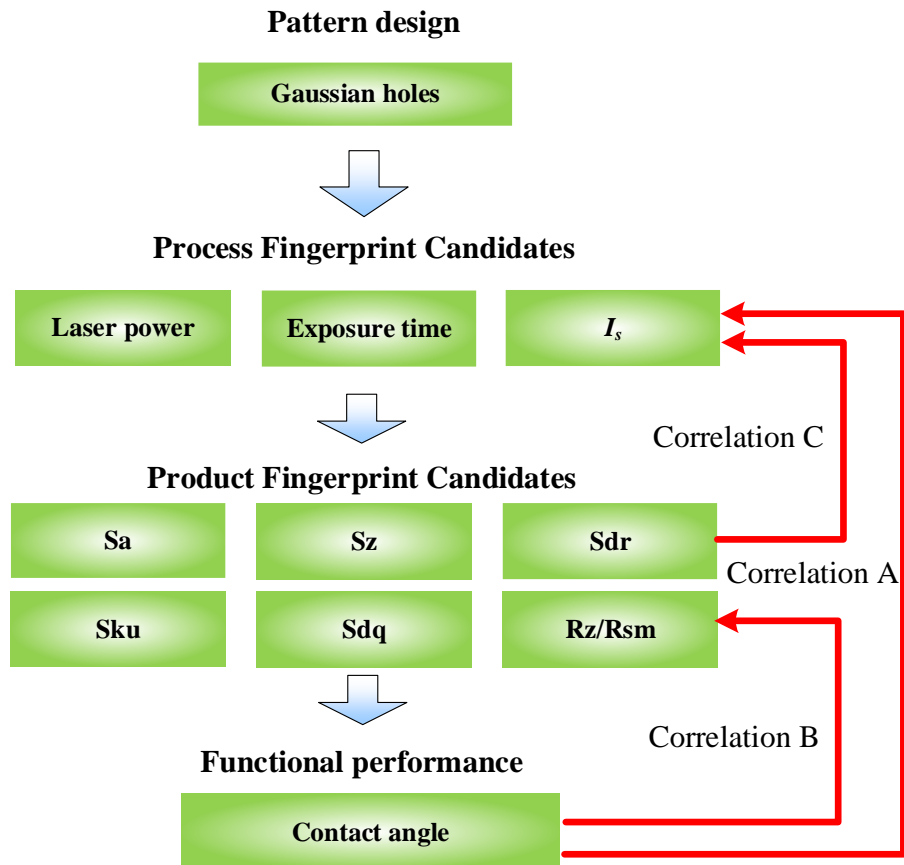


Figure 5.1 Concept of the process and product fingerprints in the laser ablation of the superhydrophobic surface.

5.2.1 Analysis of process fingerprint candidates

According to the analysis in section 4.3, the laser power is a good candidate for the process fingerprint as it determines the laser fluence which directly affects the

formation of Gaussian holes. Moreover, exposure time t_e determines the number of laser pulses that irradiated the surface. It also has a significant effect on the dimension and morphology of Gaussian holes.

I_s means the average laser pulse energy irradiated on a unit area of the specimen. This parameter depends on pulse repetition rate f_p and exposure time t_e . It can be expressed as:

$$I_s = \frac{t_e * f_p * E_p (\frac{L}{P})^2}{L^2} \quad (5-1)$$

where P is the pitch of Gaussian holes, and L is the length of the specimen.

According to Equation 4-1, $f_p * E_p = P_{ave}$, hence Equation 5-1 can be simplified as:

$$I_s = \frac{t_e * P_{ave}}{P^2} \quad (5-2)$$

Thus, the candidates of the process fingerprint include the laser power, exposure time, laser pulse energy per unit area of the specimen.

5.2.2 Analysis of product fingerprint candidates

In literature, two typical models (i.e. the Wenzel and Cassie-Baxter models) have been developed to describe the behaviour of a droplet on rough surfaces [16,17]. According to the Wenzel model, the water droplet maintains contact with the structures and penetrates the asperities, and the surface contact area is increased. Alternatively, according to the Cassie-Baxter model, the droplet is not able to penetrate the microstructure spaces. However, in order to ensure that the droplet does not connect with the bottom of the microstructures, the sag in height of water droplet between microstructures should be smaller than the depth of microstructures. Moreover, deep

microstructures will help form stable air pockets under the water droplet. Stable air pockets underneath the water droplet promote the formation of superhydrophobicity with strong resistance against the transition to the Wenzel state.

The above analysis proves that the contact angles obtained in both Wenzel and Cassie-Baxter states are highly related to the vertical and horizontal features of the surface topography. Six surface characterisation parameters that most probably correlated with the hydrophobicity of specimens are listed in Table 5.1. S_a , S_z and S_{ku} are roughness parameters to characterise the height of the surface. S_{dr} , S_{dq} , R_{hy} are hybrid parameters which determined from both height and horizontal parameters of the surface. For a rough surface, S_{dr} means the additional surface area contributed by the texture as compared to the planar definition area. Therefore, $1+S_{dr}$ has the same meaning as the roughness factor r in the Wenzel state.

Theoretical analysis proved that microstructures should have a high aspect ratio to provide a larger surface area and a smaller separation distance which will improve the stabilisation of the solid-liquid-air composite interface [47]. However, the present functional parameters cannot reflect the aspect ratio of surface asperities. Hence, R_{hy} is proposed for the first time as a dimensionless functional parameter in this research and is defined as the average ratio of R_z to R_{sm} . The subscript “hy” is the short abbreviation of hydrophobicity. The R_{hy} is calculated from the average value of 60 lines that evenly distributed on the structured surface horizontally and vertically. A surface with large R_{hy} can be obtained from a large R_z or smaller R_{sm} , which means the features of the surface should have a large depth or small separation distance (i. e. high density) in the horizontal direction.

Table 5.1 Product fingerprint candidates.

Name	Symbol	Meaning
Arithmetical mean height	Sa	The difference in height of each point compared to the arithmetical mean of the surface.
Maximum height	Sz	The sum of the largest peak height value and the largest pit depth value within the defined area.
Kurtosis	Sku	A measure of the sharpness of the roughness profile. Sku < 3: Height distribution is skewed above the mean plane. Sku = 3: Height distribution is normal. (Sharp portions and indented portions co-exist). Sku > 3: Height distribution is spiked.
Developed interfacial area ratio	Sdr	The percentage of the definition area's additional surface area contributed by the texture as compared to the planar definition area.
Root mean square gradient	Sdq	Root mean square of slopes at all points in the definition area. When a surface has any slope, its Sdq value becomes larger.
Average ratio of Rz to Rsm	R _{hy}	Average ratio of the maximum height of profile (Rz) and mean width of the profile elements (Rsm)

5.2.3 Laser ablation experiments

Laser ablation experiments were carried out on AISI 316L stainless steel by varying the process parameters to identify the best product and process fingerprints as listed in Table 5.2 and Table 5.3.

Table 5.2 The laser ablation parameters with varied laser power and pitch.

Pitch (µm)	Laser Power (W)	Pulse Repetition Rate (KHz)	Feed Rate (mm/min)	Exposure Time (s)	Pattern Types
90	4,6,10,14,20	100	200	0.4	Gaussian holes
110	4,6,10,14,20	100	200	0.4	Gaussian holes
130	4,6,10,14,20	100	200	0.4	Gaussian holes
150	4,6,10,14,20	100	200	0.4	Gaussian holes

Table 5.3 The laser ablation parameters with varied exposure time and pitch.

Pitch (μm)	Laser Power (W)	Pulse Repetition Rate (KHz)	Feed Rate (mm/min)	Exposure Time (s)	Pattern types
70	20	100	200	0.2,0.4,0.6,1	Gaussian holes
90	20	100	200	0.2,0.4,0.6,1	Gaussian holes
110	20	100	200	0.2,0.4,0.6,1	Gaussian holes
130	20	100	200	0.2,0.4,0.6,1	Gaussian holes
150	20	100	200	0.2,0.4,0.6,1	Gaussian holes

5.3 Product fingerprint

The investigation of experimental results was carried out to identify the product fingerprint from six candidates related to surface topography. The product fingerprint is the indicator that has the highest level of correlation to contact angle. In this research, the Spearman rank correlation coefficient and Kendall rank correlation coefficient were employed to determine the product fingerprint. Spearman rank correlation coefficient evaluates how strong a monotonic function can define the correlation between two variables. It measures the strength and direction of the monotonic association between two variables, a perfect Spearman correlation of +1 or -1 occurs when each variable is a perfect monotone function of the other [209]. A positive Spearman correlation coefficient corresponds to an increasing monotonic trend between two variables, while a negative value means a decreasing monotonic trend. Besides, the Spearman rank correlation coefficient is appropriate for data that is not normally distributed. It can be used to identify a non-linear correlation between the two variables. Kendall rank correlation coefficient is a statistic used to measure the ordinal association between two variables [210]. However, unlike the Spearman coefficient, Kendall rank correlation coefficient only considers directional agreement while does not consider the difference between ranks. Therefore, this coefficient is

more appropriate for discrete data. This coefficient returns a value of -1 to 1 , where 0 is no correlation, 1 is a perfect positive correlation, and -1 is a perfect negative correlation.

In most cases, the interpretations of Spearman and Kendall rank correlation coefficients are very similar and thus invariably lead to the same inferences. The above two coefficients were combined to determine the product fingerprint that has the maximum absolute value. The strength of the correlation between the variables can be evaluated by the absolute value of coefficients, as shown in Table 5.4.

Table 5.4 Interpretation of the strength of the correlation coefficient.

Value of Coefficient	Correlation Type
1	Perfect correlation
0.81–0.99	Strong correlation
0.71–0.80	Good correlation
0.51–0.70	Weak correlation
0.01–0.50	Poor correlation
0	No correlation

Figure 5.2 shows scatter plots between the contact angle and the six candidates of product fingerprint. With the increase of S_a , S_z , S_{dr} , S_{dq} and R_{hy} , the contact angle shows an increasing trend. It should be noted that a significant linear relationship appears between S_z and contact angle. However, it can be observed that there is no apparent correlation between S_{ku} and contact angle (Figure 5.2 (c)). The increasing S_{dr} from 0.02 to 4.1 leads to contact angle increase rapidly from 89.5° to 159° , but it has minor impact on the contact angle when S_{dr} was further increased from 4.1 to 9.8 as shown in Figure 5.2 (d). Besides, Figure 5.2 (f) indicates that the contact angle

increases gradually from 89.5° to 164° with the value of R_{hy} increasing from 0.06 to 0.94.

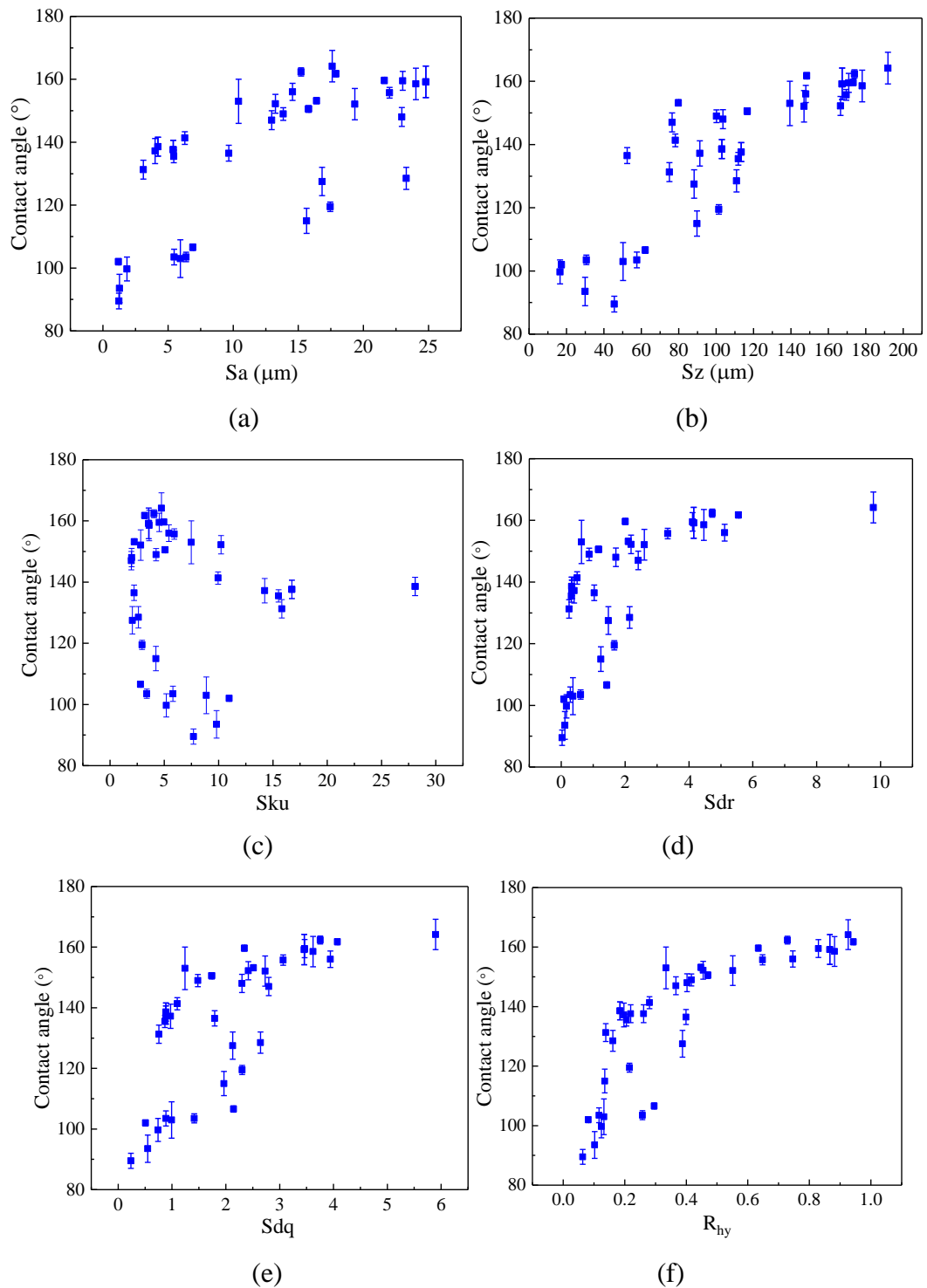


Figure 5.2 Influences of the product fingerprint candidates on the contact angle for Gaussian hole pattern: (a) Sa, (b) Sz, (c) Sku, (d) Sdr, (e) Sdq and (f) R_{hy} .

Figure 5.3 shows the variations of Spearman and Kendall rank correlation coefficient between contact angle and candidates of product fingerprint. According to the criterion in Table 5.4, Sz and R_{hy} both have a strong correlation with the contact angle; the Spearman rank correlation coefficients are 0.89 and 0.92 respectively. The Kendall rank correlation coefficients of Sz-contact angle and R_{hy}-contact angle are 0.74 and 0.76, respectively. Thus, Figure 5.3 suggests that R_{hy} should be determined as the best product fingerprint as it has the maximum Spearman and Kendall rank correlation coefficients.

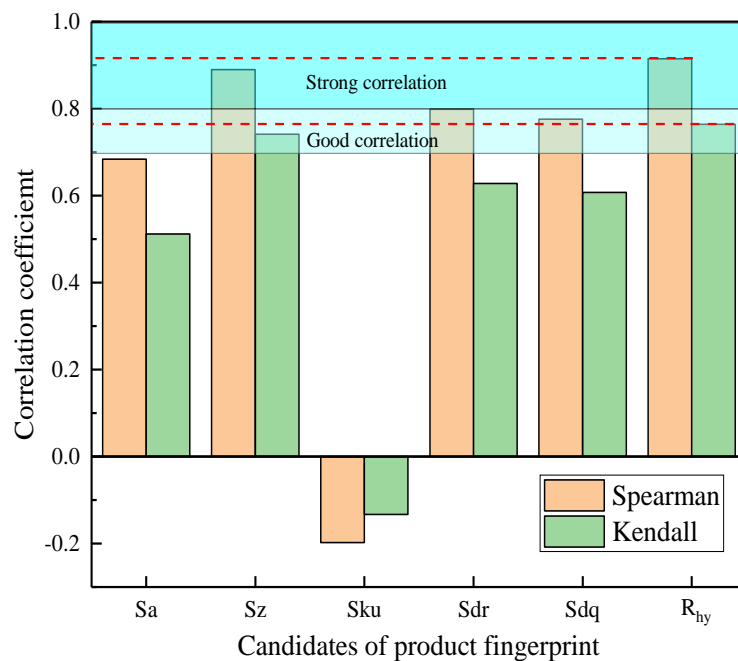


Figure 5.3 Spearman and Kendall rank correlation coefficient between the contact angle and six candidates of product fingerprint.

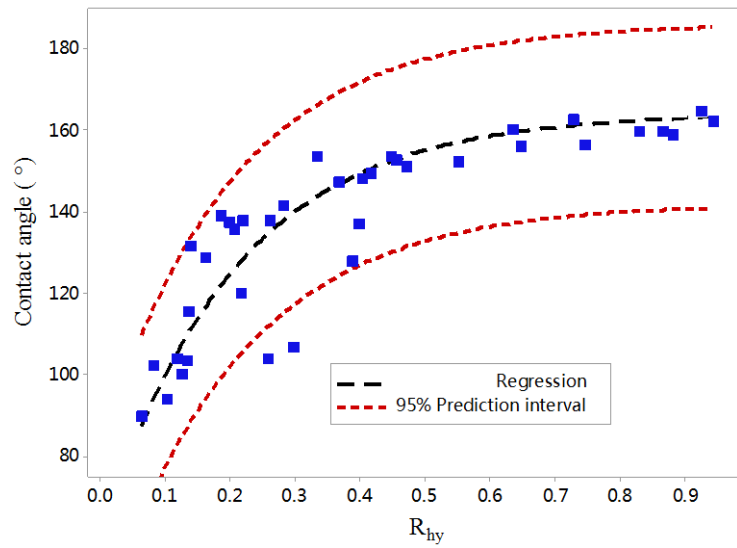
According to the results in Figure 5.2 (f), an empirical equation was deduced to correlate the experimental R_{hy} and contact angle. The equation is expressed as:

$$\theta = X_1 - X_2 * e^{X_3 * R_{hy}} \quad (5-3)$$

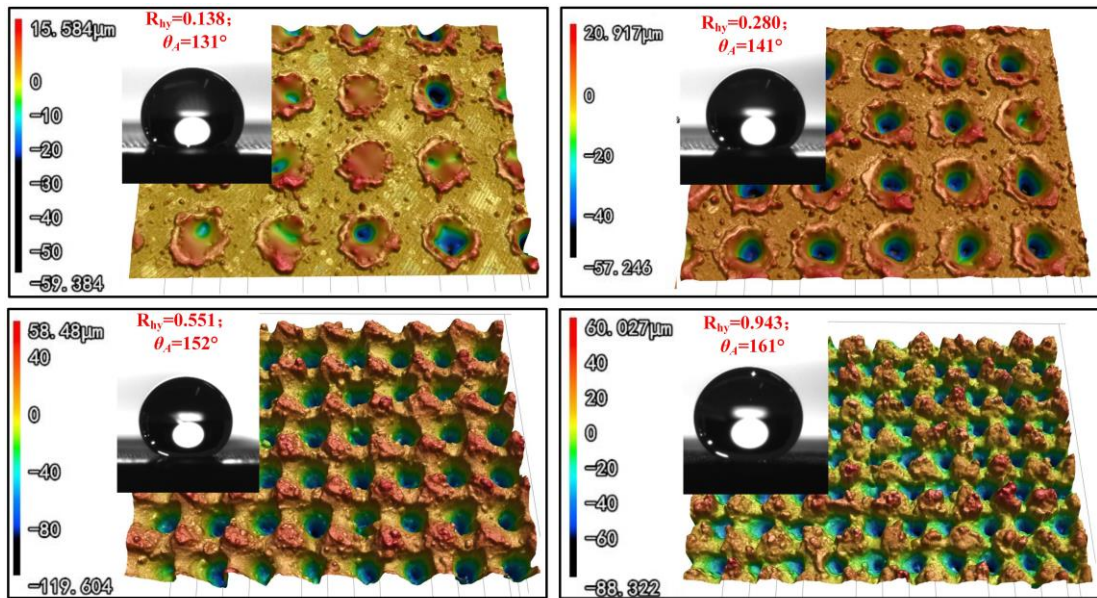
where θ is the apparent contact angle of the specimen; X_1 , X_2 and X_3 are coefficients equal to 164, 105 and -4.9 respectively.

As shown in Figure 5.4 (a), the regression curve has excellent accuracy for simulating the experimental data. It was found that the coefficient “ X_1 ” is the maximum contact angle (164° in this research), the value of “ X_2 ” is equal to the initial contact angle (105°) of AISI 316L stainless steel after chemical modification. Thus, the contact angle of the specimen is highly related to its maximum contact angle, initial contact angle on a smooth surface and hydrophobicity functional parameter R_{hy} . According to Equation 5-3, the value of R_{hy} is 0.41 when $\theta = 150^\circ$. Thus, 0.41 can be regarded as the threshold value of R_{hy} that ensure water contact angle of the specimen higher than 150° .

The dimensionless ratio R_{hy} is the most sensitive candidate parameter for the contact angle of the specimen, which can, therefore, be regarded as product fingerprint. In literature, many studies proved that a high density of microstructures and smaller period of microstructure help decrease solid-liquid contact area and increase its hydrophobicity [211,212]. With the increase of R_{hy} from 0.138 to 0.943 (Figure 5.4 (b)), R_{sm} decrease from $137.0\ \mu\text{m}$ to $81.8\ \mu\text{m}$. Therefore, the density of peaks shows a significant increasing trend. Moreover, the depth of microstructures shows an increasing trend, due to average R_z increased from $18.9\ \mu\text{m}$ to $77.2\ \mu\text{m}$. Therefore, it can be concluded that the superhydrophobicity will benefit from the increase of R_{hy} .



(a)



(b)

Figure 5.4 (a) Fitted line by exponential function between R_{hy} and contact angle; (b) surface morphology and shape of water drops on specimens with a different value of R_{hy} .

5.4 Process fingerprints

The above section proves that R_{hy} is the most appropriate product fingerprint to the laser ablated superhydrophobic structures on AISI 316L stainless steel. In this section, further analysis of the experimental results will be performed to identify which process fingerprint candidate (i.e. P_{ave} , t_e and I_s) has the strongest correlation with R_{hy} . The control of process fingerprints helps to choose appropriate process parameters to obtain a surface with R_{hy} greater than the threshold value ($R_{hy} > 0.41$). The correlation among laser power, the pitch of Gaussian hole and R_{hy} is shown in Figure 5.5. It shows that higher laser power and smaller pitch lead to a higher value of R_{hy} . Laser power and pitch of structures have combined effects on the value of R_{hy} .

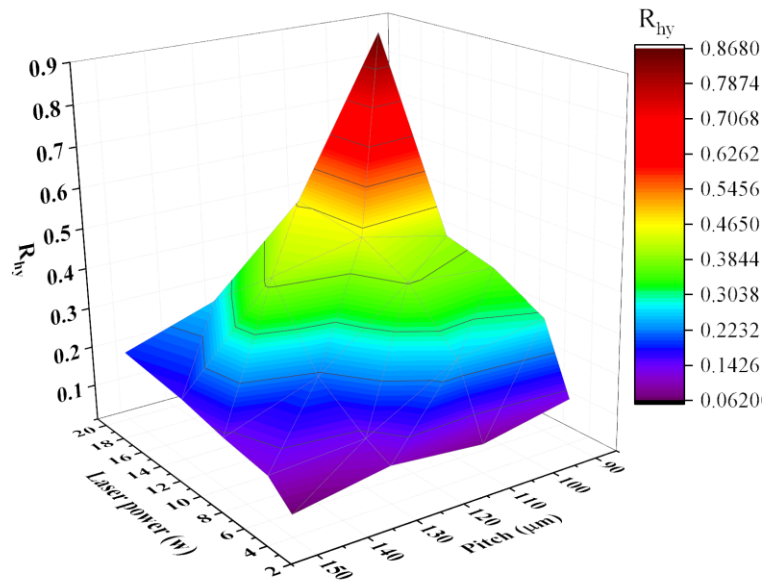


Figure 5.5 3D colourmap of the product fingerprint (R_{hy}) as a function of laser power and pitch of Gaussian hole.

The effect of exposure time and pitch of Gaussian holes on the value of R_{hy} is presented in Figure 5.6. There is no significant linear correlation between exposure time and R_{hy} , but this does not mean the exposure time has no effect on R_{hy} . As a

whole, it can be found that the value of R_{hy} shows a significantly increasing trend with the reduction of the pitch from 150 μm to 70 μm .

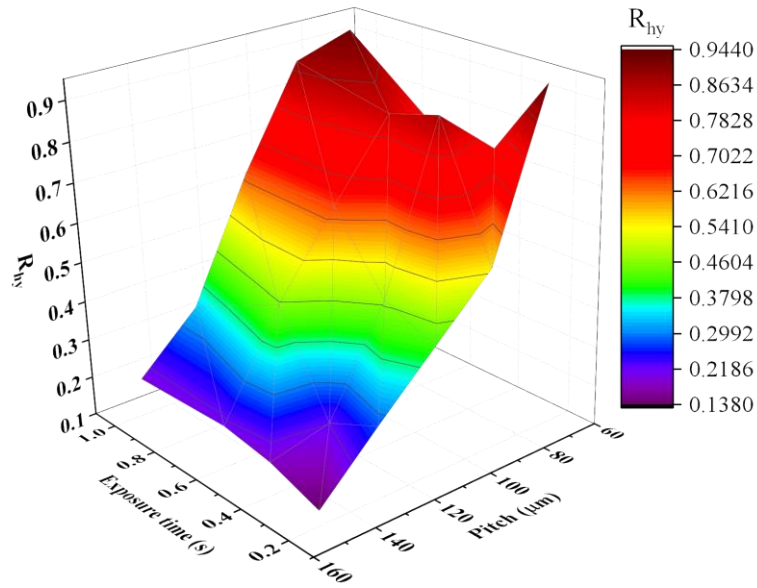


Figure 5.6 3D colourmap of the product fingerprint (R_{hy}) as a function of exposure time and pitch of Gaussian holes.

The above analysis shows that laser power, pitch and exposure time have a collective influence on R_{hy} . Focusing on one of them and ignoring the other two would lead to a situation that the determined correlation is only valid in certain partial conditions. For instance, the R_{hy} will increase with laser power, but this is only valid at a precondition of constant pitch and exposure time. Therefore, a comprehensive factor I_s was designed to represent the combined influence of laser power, pitch and exposure time. I_s means the energy intensity that irradiated on the unit area of the specimen and can be calculated by Equation 5-2. I_s is proportional to the laser power P_{ave} and the exposure time t_e , but inversely proportional to the square of the pitch of the microstructures. Figure 5.7 reveals that the increasing I_s leads R_{hy} to increase rapidly at first, and then level off to become asymptotic to the upper limit. The presence of the upper limit means that further increases in laser power, exposure time and

smaller pitch cannot lead to a further increase in R_{hy} . The correlation between I_s and R_{hy} can be expressed as Equation 5-4. According to the calculation result, I_s should be greater than 536 J/mm^2 to ensure that R_{hy} is greater than 0.41. Hence the contact angle of the specimen will be larger than 150° .

$$R_{hy} = 0.895 - 0.898 * 0.9985^{I_s} \quad (5-4)$$

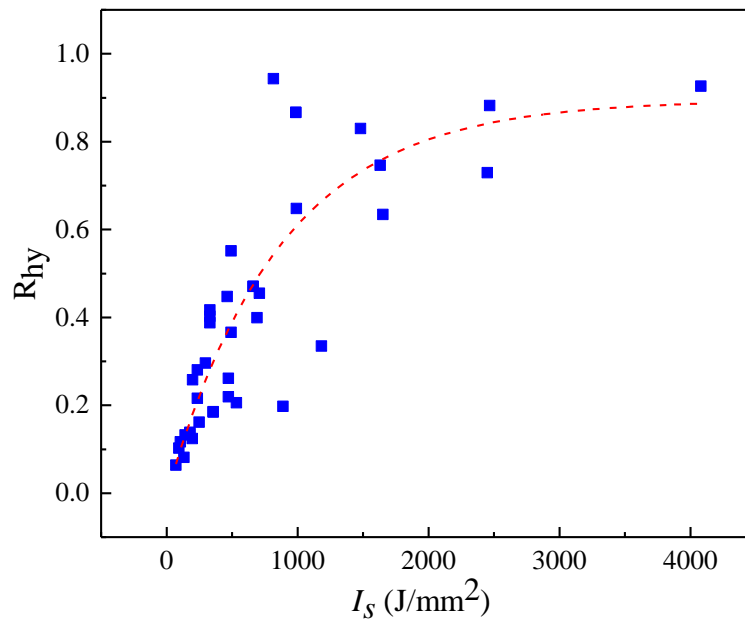


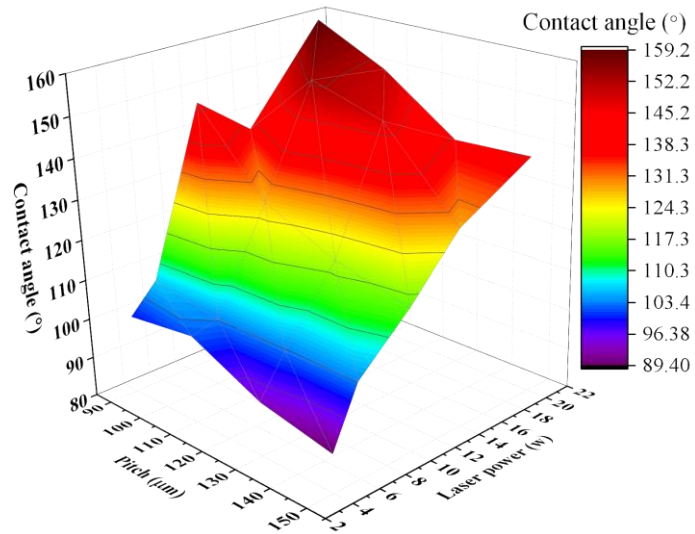
Figure 5.7 Scatter plots and fitted curve of R_{hy} and I_s .

Therefore, the increased I_s leads to increase of R_{hy} rapidly; the exponential function can describe the correlation between I_s and R_{hy} . I_s is the most sensitive parameters among the investigated three process fingerprint candidates, so it is the best process fingerprint that can be used to control surface morphology, especially the product fingerprint R_{hy} .

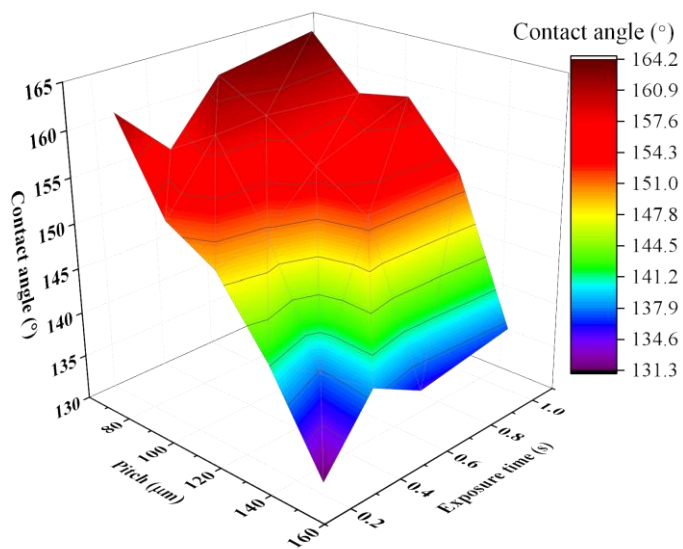
5.5 Correlation between laser ablation parameters and contact angle

As shown in Figure 5.8, 3D colourmaps are used to display the relationship between laser power, exposure time, the pitch of structures and contact angle. To sum

up, the higher contact angle benefits from larger laser power and smaller pitch of microstructures except for some outliers.



(a)



(b)

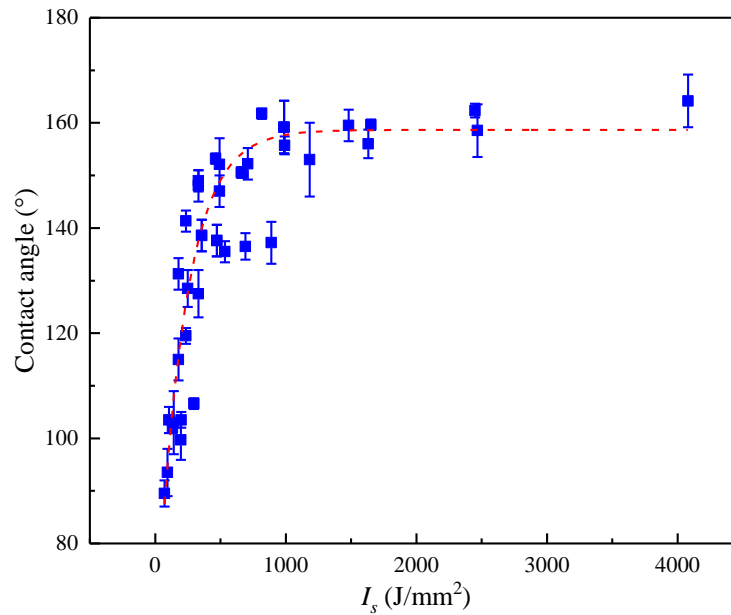
Figure 5.8 (a) 3D colourmap of the contact angle as a function of laser power and pitch of microstructures; (b) 3D colourmap of the contact angle as a function of exposure time and pitch of microstructures.

Figure 5.9 (a) shows the scatter diagram and fitted curve between contact angle and I_s . The increasing I_s results in a rapid increase of contact angle at first, and then level off to become asymptotic to the upper limit when I_s greater than 1000 J/mm². The empirical correlation between contact angle and I_s can be expressed by Equation 5-5. When the value of R_{hy} equals to the threshold value of 0.41, the corresponding I_s 516.6 J/mm², which is very close to the value of 536 J/mm² obtain from Equation 5-4. Therefore, I_s should be greater than 536 J/mm² in the laser ablation process, which help ensure the contact angle larger than 150 °.

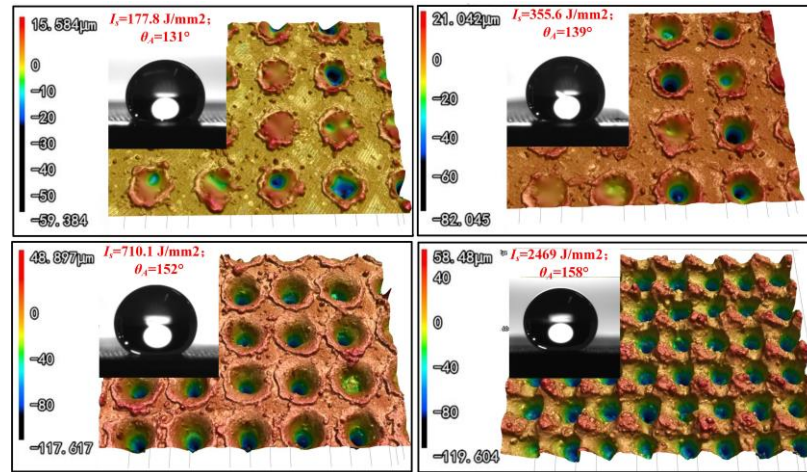
$$\theta = X_1 - X_2 * e^{X_4 * I_s} \quad (5-5)$$

where, $X_1 = 164$, $X_2 = 105$, $X_4 = -0.0039$. Coefficients of X_1 and X_2 have the same meaning as Equation 5-3.

The surface morphology and shape of water drops on specimens with different values of I_s are shown in Figure 5.9 (b). With the increase of I_s , the depth and density of structures show a significant increasing trend. Thus, the surface topography and contact angle can be well controlled by choosing the appropriate process parameter I_s .



(a)



(b)

Figure 5.9 (a) Scatter plot and fitted curve between contact angle and I_s ; (b) surface morphology and shape of water drops on specimens with a different value of I_s .

5.6 Summary

In this chapter, the concepts of process and product fingerprints were proposed for the first time to reveal the correlations among process parameters, surface topography and functional performance (i.e. the contact angle of laser ablated superhydrophobic surface on AISI 316L stainless steel). Spearman and Kendall rank correlation coefficients determined the most appropriate product fingerprint. Then, the candidate that was most sensitive to the product fingerprint was determined the best process fingerprint. Finally, the correlation between the process fingerprint and functional performance was developed. The conclusions are as follows:

1. The dimensionless surface functional characterisation parameter R_{hy} (i.e. the average ratio of R_z to R_{sm}) is the most sensitive parameter to the specimen's contact angle, which can be regarded as the product fingerprint.

2. Laser pulse energy per unit area on the specimen (I_s) represents the combined effects of laser power, exposure time and structure pitch on surface topography, and it is the best process fingerprint that can be used to control the product fingerprint R_{hy} .

3. Increasing I_s leads to the R_{hy} value increasing rapidly at first and then levelling off to become asymptotic to the upper limit. A similar trend can also be found between I_s -contact angle and R_{hy} -contact angle. The threshold values of R_{hy} and I_s are 0.41 and 536 J/mm², respectively, ensuring the specimen's superhydrophobicity (contact angle larger than 150 °) in the laser ablation process.

Chapter 6 A Sequential Process for Manufacturing

Nature-inspired Anisotropic Superhydrophobic Structures

6.1 Introduction

Surfaces with anisotropic superhydrophobicity have great potential applications in drug delivery and microfluidic devices due to their unique properties of drag reduction and unidirectional fluid transportation. Observations of natural biological surfaces have proven that directional microstructures are indispensable for realising anisotropic superhydrophobicity. However, current lithography-based manufacturing approaches have limited scalability for real-world industrial applications. This chapter proposes a sequential process of laser ablation and chemical etching (LA-CE), for the first time, to manufacture ratchet-like microstructures on AISI 316L stainless steel by harvesting the advantages of both processes. The laser ablation will form the undesired oxide and recast layers, which often result in short service life and poor surface quality. These layers can be easily removed in the chemical etching process, then the periodic ratchet-like microstructures can be obtained simultaneously. Evaluation experiments will be conducted to test the performance of the fabricated microstructure surfaces.

6.2 Work principle of LA-CE and experimental setup

6.2.1 Work principle of LA-CE

The schematic of the LA-CE process is illustrated in Figure 6.1. The laser pulses are firstly focused on the specimen by an objective lens, inducing microchannels on the specimen. The laser pulses will be obliquely irradiated on the

specimen surface due to the resultant motion of the work stage in the feed and pulsed directions and result in asymmetric ratchet-like recast layers. The laser ablated specimen is then treated by an aqueous solution of ferric chloride hexahydrate (32g $\text{FeCl}_3 \cdot 6\text{H}_2\text{O}$, 3 ml of 37% HCl, 3 ml of 85% H_3PO_4 , 120 ml H_2O) to remove the oxide layer and laser-induced recast layers and to obtain periodic ratchet-like laminar structures. Lastly, the same post-process with section 4.3 was employed to reduce surface free energy and achieve its superhydrophobicity. Furthermore, Figure 6.1 also shows the images of the specimen by the laser ablation and LA-CE processes, respectively. The specimen of laser ablation shows a black colour due to the oxide layer laser formed in the laser ablation process, and this was confirmed using X-ray diffraction patterns (XRD) as shown in Figure 6.4. However, the specimen prepared by LA-CE process shows a similar colour to the unprocessed surface.

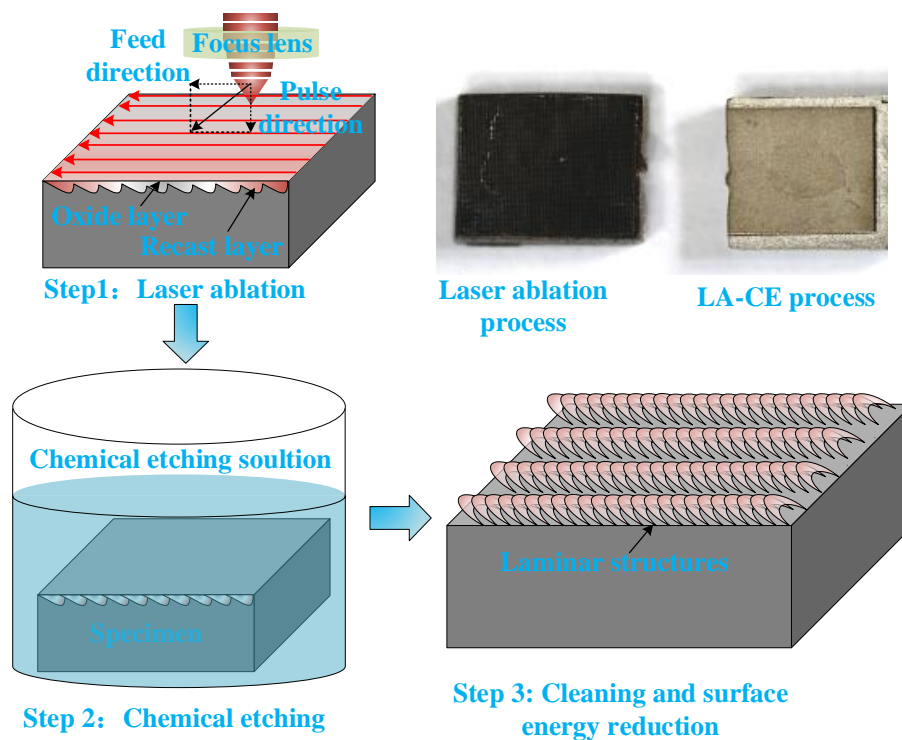


Figure 6.1 Schematic illustration of the manufacturing process (LA-CE) of superhydrophobic ratchet structures.

6.2.2 Materials and experimental setup

AISI 316L stainless steel was used as the experimental material in this experiment. Identically to section 4.3, the stainless steel plates were machining by a flat end mill (with a diameter of 6 mm). The details of the operational conditions for the experiments are shown in Table 6.1. The fourth group in Table 6.1 is chosen as the control group to display the relationship between the direction of laser beam feed and microstructures. The schematics of unidirectional and bidirectional feed directions are shown in Figure 6.2.

Table 6.1 Operational conditions for experiments.

Number	Pitch (μm)	Laser power (W)	Frequency (KHz)	Feed rate (mm/min)	Feed direction
1	25	10	20	30	Unidirectional
2	25	15	20	30	Unidirectional
3	25	20	20	30	Unidirectional
4	25	20	20	30	Bidirectional
5	50	10	20	30	Unidirectional
6	50	15	20	30	Unidirectional
7	50	20	20	30	Unidirectional

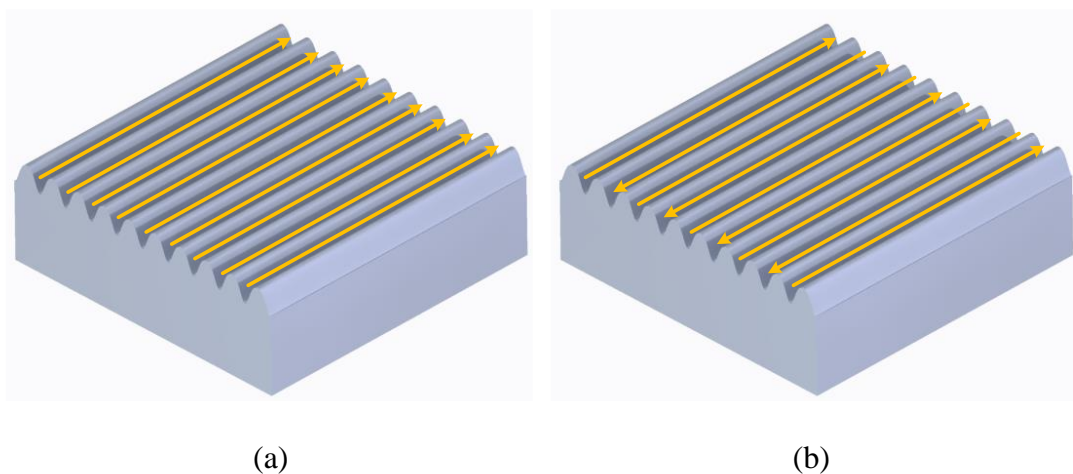


Figure 6.2 Schematic of feed directions: (a) unidirectional and (b) bidirectional.

6.3 Experimental results and discussion

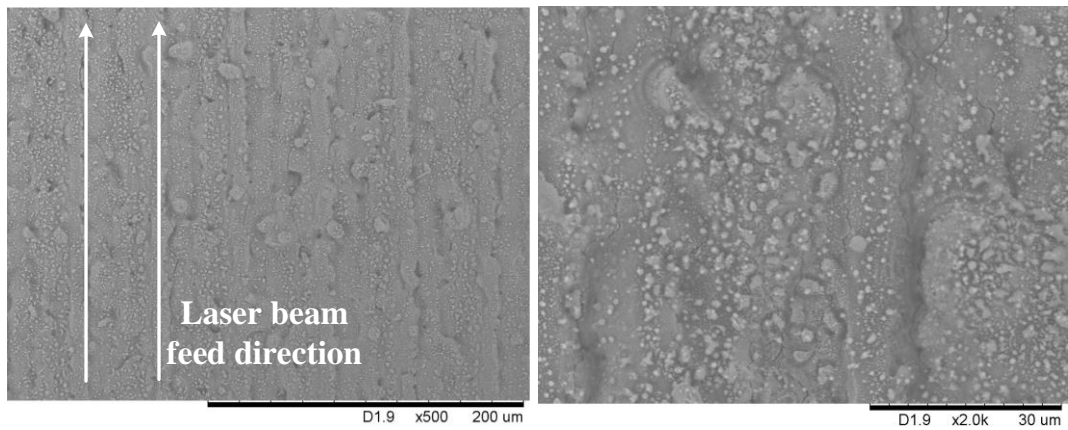
6.3.1 Surface morphologies and composition

The morphologies of specimens prepared by LA-CE process are presented in Figure 6.3. In the laser ablation process, the molten materials are partially ejected from the cavity and form surface debris. Meanwhile, the oxidation reaction can occur with the molten materials. At the end of a pulse, the heat quickly dissipates into the bulk of the work material and the oxide layers and recast layers are formed as shown in Figure 6.3 (a).

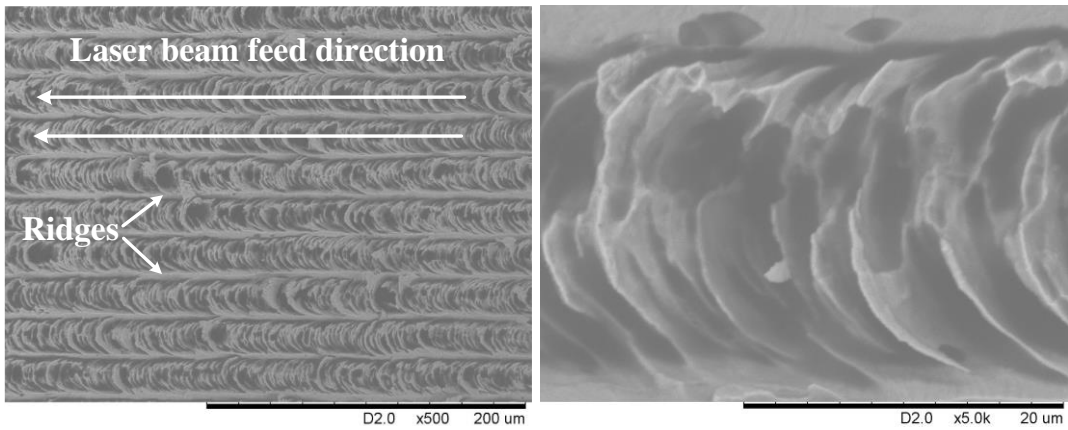
During the chemical etching process, the oxide layers and recast layers were removed from the surface, and the laminar microstructures were formed. As shown in Figure 6.3 (b), (c), (d), (f), (g), (h), the direction of the tilted microstructures is towards the laser beam feed direction. To verify the above phenomena, the specimen 4 was processed by employing bidirectional laser beam feed. As expected, bidirectional microstructures were formed as shown in Figure 6.3 (e). Therefore, it can conclude that the direction of microstructures can be well-controlled by the laser beam feed direction.

At the laser power of 10 W (Figure 6.3 (b)), the surface morphologies are laminar periodic microstructures with clear boundaries between the adjacent rows and well-separated by ridges. However, the adjacent rows of microstructures are connected when the laser power is further increased to 15 W and 20 W, and no ridges are observed after the chemical etching process. This is because the increased laser power results in thicker recast layers. Both the depth and width of the etched microstructures increase with increasing laser power. At a larger pitch of 50 μm , the width and depth of

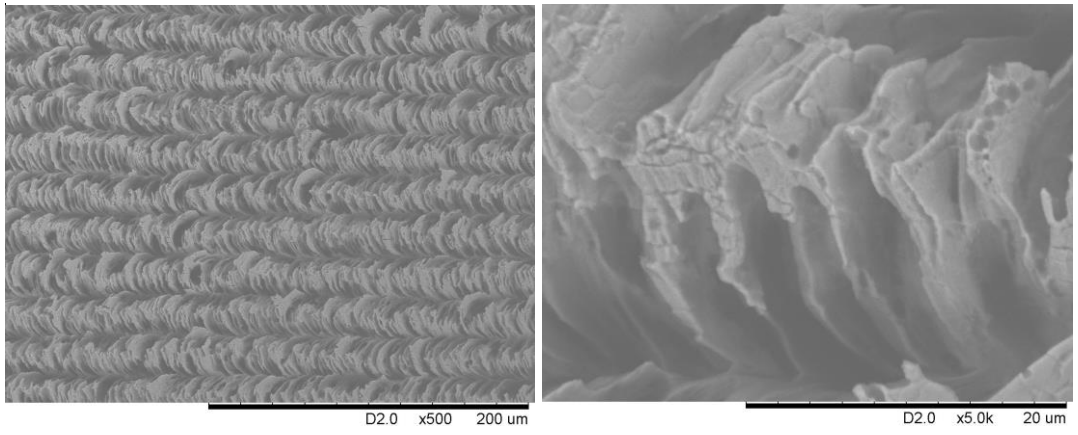
microstructures show a similar increasing trend with laser power increase, as shown in Figure 6.3 (f), (g), (h). Furthermore, it can be observed that the depth of microstructures shows an increasing trend with increasing laser power. Thus, the width and depth of microstructures are determined by both the pitch of microstructures and the laser power.



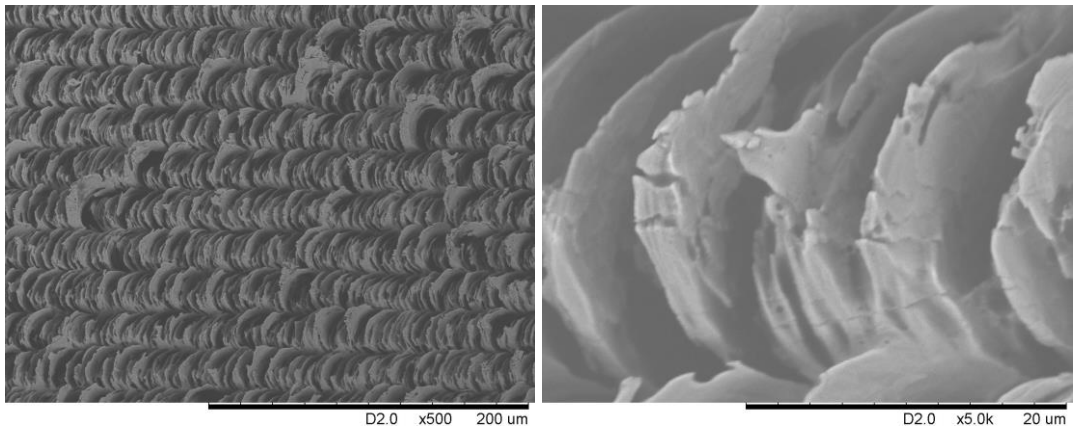
(a)



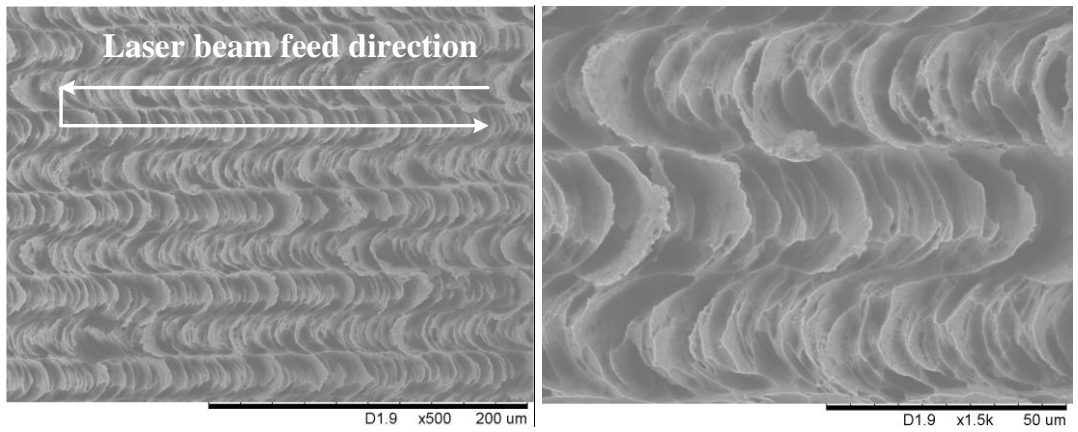
(b)



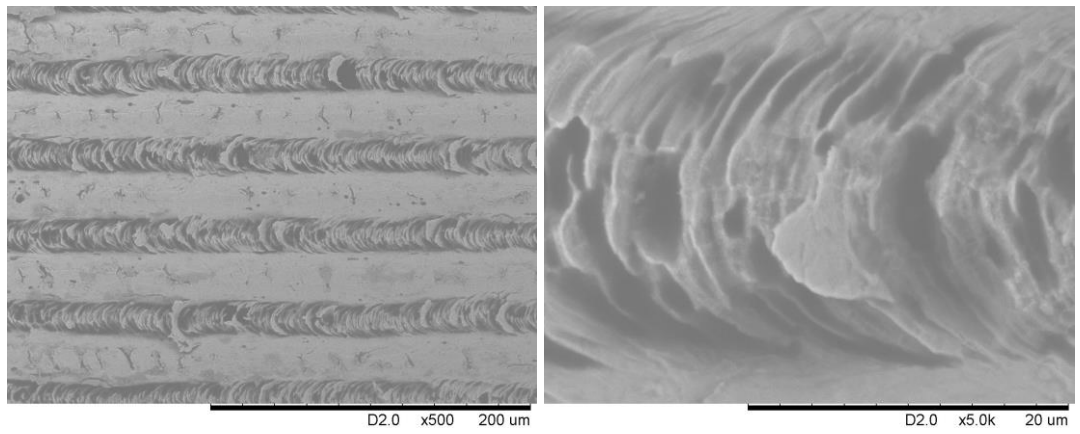
(c)



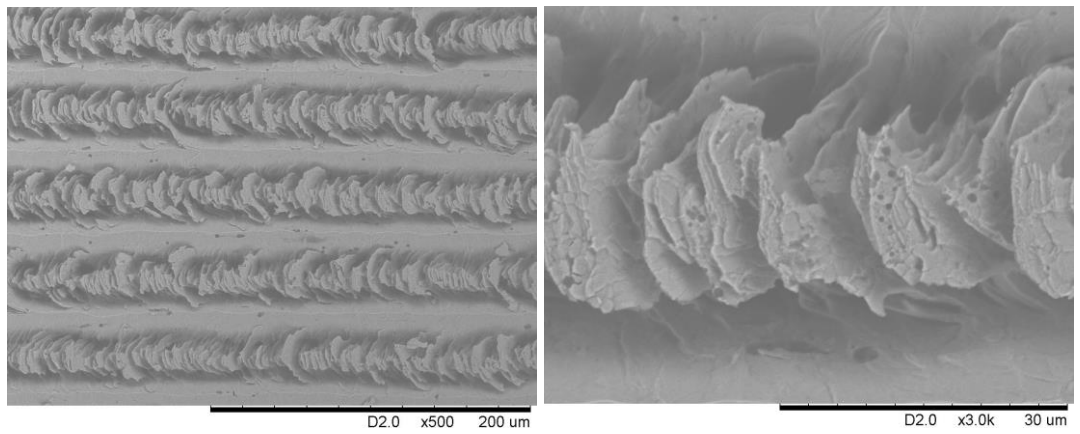
(d)



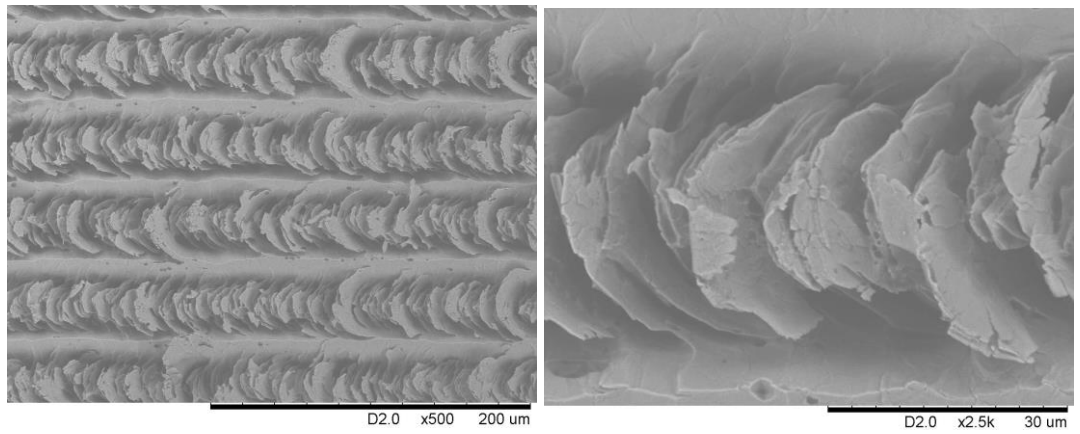
(e)



(f)



(g)



(h)

Figure 6.3 SEM images (left) and high-magnification images (right) of Specimens: (a) Specimen 1 with a pitch of 25 μm after laser ablation; (b),(c),(d),(e),(f),(g),(h) surface morphologies of specimens 1 to 7 manufactured by LA-CE process.

Figure 6.4 shows the XRD of smooth surface, laser ablated surface and surface fabricated by hybrid laser ablation and chemical etching process of AISI 316L stainless steel. In Figure 6.4 (a), four sharp diffraction peaks correspond to the XRD pattern of austenite and one peak for ferrite. For the laser-ablated surface, it was found that austenite, Fe_3O_4 and Fe_2O_3 were recognised on the XRD pattern (Figure 6.4 (b)). Figure 6.4 (c) shows that there is no iron oxide on the surface machined by the hybrid laser ablation and chemical etching process.

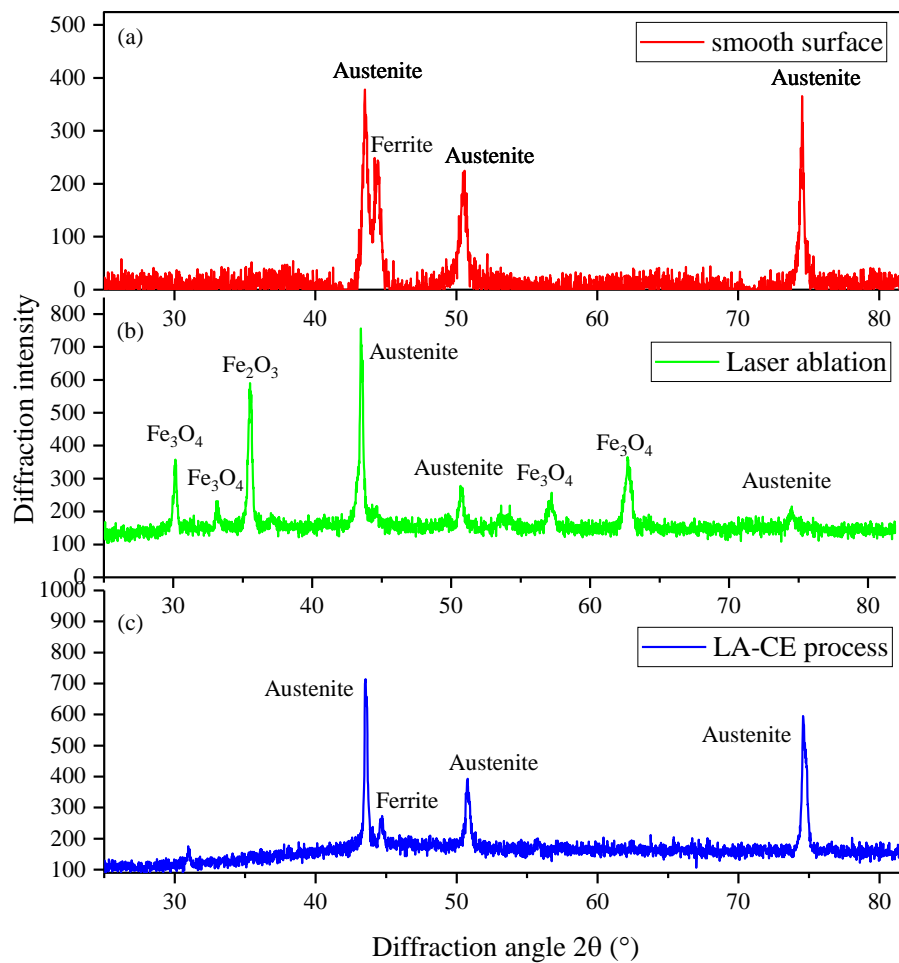
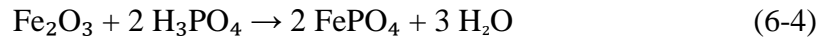
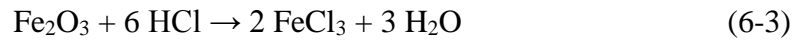


Figure 6.4 X-ray diffraction pattern of AISI 316L stainless steel at different process: (a) smooth surface, (b) laser ablation and (c) LA-CE process.

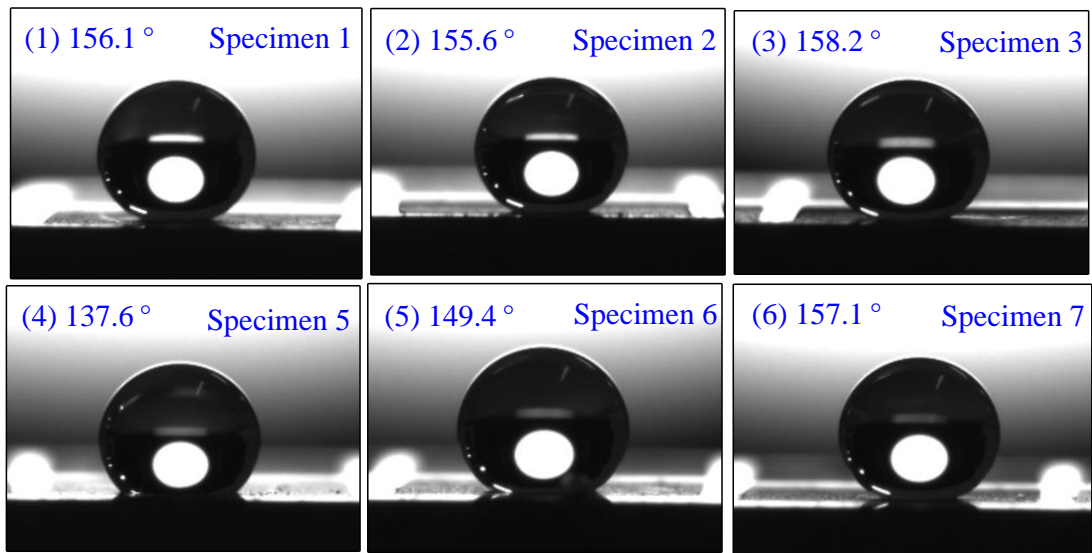
The above results proved that the main components of the oxide layer are Fe₃O₄ and Fe₂O₃ on the specimen. Hence, the details of the chemical reaction can be expressed as:



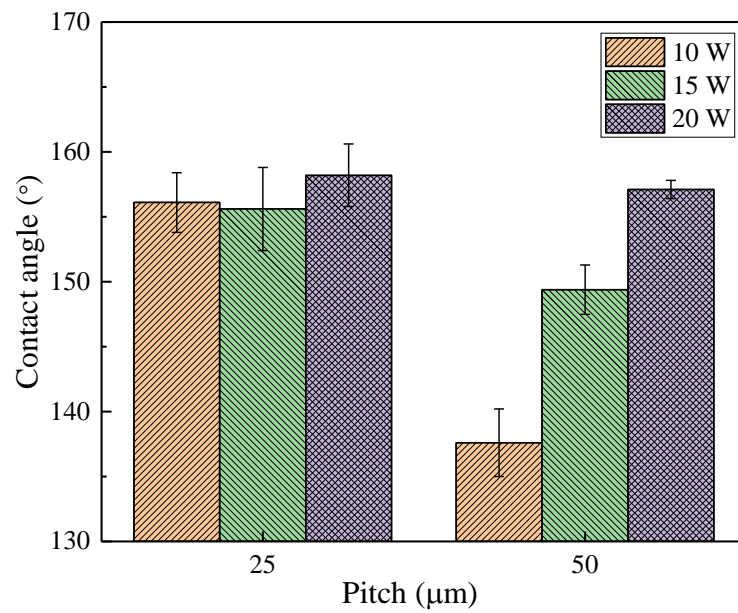
As shown in the above chemical equations, the oxide layer will react with acid to form the corresponding salt and water. And the iron will react with ferric chloride to produce iron (II) chloride simultaneously.

6.3.2 Anisotropic superhydrophobicity of specimens

Figure 6.5 (a) shows the captured images of water droplets on different specimens. Figure 6.5 (b) shows the variations of the contact angle of the machined surfaces versus pitches obtained under different laser power. The contact angles for the specimens with the pitch of 25 μm are similar when the average laser power increased from 10 W to 20 W, which are 156.1 °, 155.6 °, 158.2 ° respectively. However, increasing laser power will cause the contact angle to increase significantly from 137.6 ° to 157.1 ° for specimens with a larger pitch of 50 μm. The larger laser power results in a larger laser ablation area and smaller unstructured region. Moreover, it further leads to a smaller solid-liquid contact area, which is beneficial to the hydrophobicity of the specimen.



(a)



(b)

Figure 6.5 (a) Captured images of water droplets; (b) variations of contact angle versus pitches for different laser power.

Figure 6.6 shows the anisotropic superhydrophobicity of Specimen 3. A $5 \mu\text{L}$ drop has a rolling-off angle of 7° when the dip direction of the specimen is the same

as the laser beam feed direction. However, the water droplet shows a pinning state in the opposite direction, due to exist of the taper-ratchet structures.

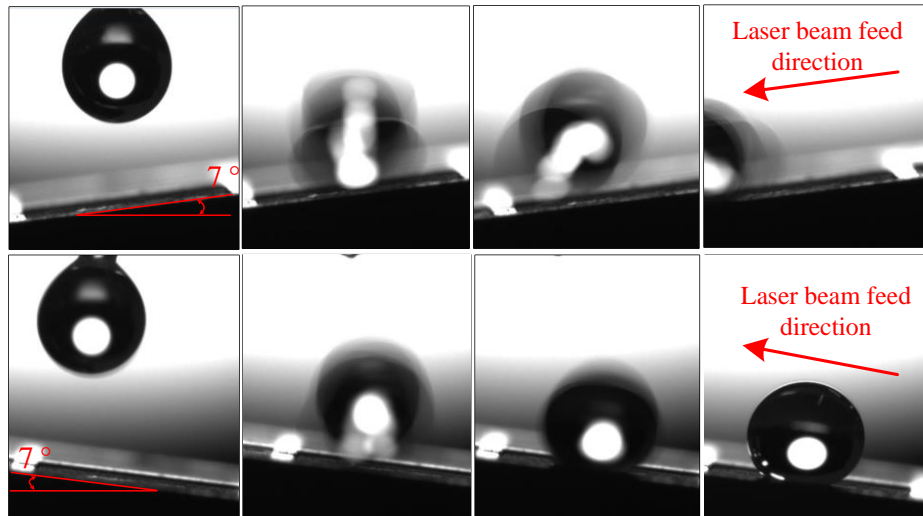


Figure 6.6 Anisotropic superhydrophobicity of specimen 3 (pitch 25 μ m at laser power of 20W).

The phenomenon of the directional move of water droplet along the tilt orientation of microstructures have been found and theoretically explained in some research [213–215]. C.W. Extrand found that liquid drops tend to move preferentially in the direction of dip on asymmetric sawtooth surfaces [213]. The theoretical analysis results suggest that the increasing feature asymmetry will result in an increase in the difference between the retention force in one direction versus the other [213].

Figure 6.7 (a) shows the wetting state of a water droplet for different dip directions. For a given tilt angle α , there is a downslope gravitational force F_d on the water droplet:

$$F_d = F_g \sin \alpha = \rho_w g V \sin \alpha \quad (6-6)$$

where F_g is the gravity of water droplet, ρ_w is the density of water, g is the gravitational acceleration and V is the drop volume.

The retention force of the substrate to water droplet in two directions are F_1 and F_2 , which is the consequence of contact angle hysteresis and causes droplets to adhere to surfaces [214].

F_1 is the retention force when the downslope gravitational force F_d is opposite to the laser beam feed direction. F_2 is the retention force when the downslope gravitational force F_d is in the same direction as the laser beam feed.

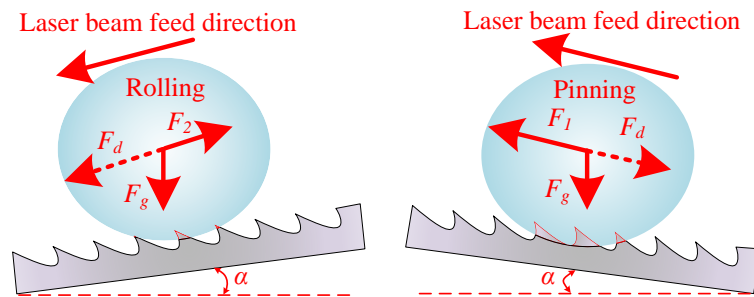
For a given tilt angle α , the downslope gravitational force F_d is greater than the retention force F_1 or F_2 is an essential condition for rolling off from the substrate of the water droplet. Figure 6.7 (b) illustrated the asymmetric feature with rising angles of ω_1 and ω_2 . The ratio of retention force F_1 and F_2 can be expressed as [213,214]:

$$F_1/F_2 \sim \frac{\sin(\omega_1 + \frac{1}{2}\Delta\theta)}{\sin(\omega_2 + \frac{1}{2}\Delta\theta)} \quad (6-7)$$

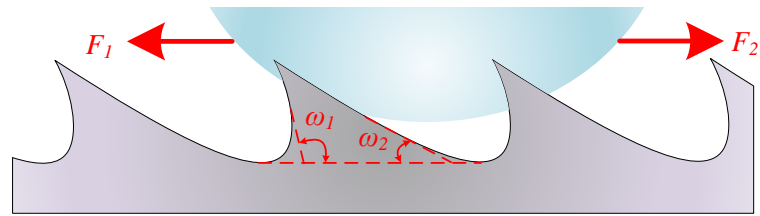
$$\Delta\theta = \theta_{ADV} - \theta_{REC} \quad (6-8)$$

where $\Delta\theta$ is the differential of the advancing angle θ_{ADV} and receding angle θ_{REC} .

As shown in Figure 6.7 (b), ω_1 is greater than ω_2 ; hence, the retention force F_1 is larger than F_2 . The downslope gravitational force F_d is easier to overcome the retention force F_2 than F_1 . Hence, the water droplet easily rolling off the surface when F_d is in the same direction as the laser beam feed.



(a)



(b)

Figure 6.7 (a) Wetting states of a water droplet at different dip directions; (b) retention force of asymmetric feature with rising angles of ω_1 and ω_2 .

6.4 Summary

In this chapter, the LA-CE process was developed to generate anisotropic superhydrophobic structures on AISI 316L stainless steel. The conclusions are as follows:

1. The direction of microstructures is the same as the laser beam feed direction.
2. The width and depth of microstructures increase with increasing laser power, which results in the disappearance of ridges. This is because the large laser power results in a large influence zone. However, increasing the pitch of microstructures will cause the ridges to reappear.
3. The specimen with a pitch of 25 μm machined at a laser power of 20 W has a maximum contact angle of 158.2°. Furthermore, with a dip angle of 7°, this specimen shows anisotropic superhydrophobicity, as the droplet easily rolls off the surface in the laser beam feed direction; however, it is pinned tightly in the opposite direction.

Chapter 7 A Single-step Fabrication Approach for the Development of Antimicrobial Surfaces

7.1 Introduction

In recent years, the increasing incidence of healthcare-associated infections and antibiotics overuse has led to the high demand for antimicrobial-coated medical devices. Silver nanoparticles (AgNPs) have attracted tremendous attention as the subject of investigation due to their well-known antimicrobial properties. However, current physical and chemical synthesis methods for AgNPs are costly, time-consuming and not eco-friendly.

In this chapter, an innovative StruCoat approach is proposed for the preparation of antimicrobial microstructures with AgNPs coatings through a single-step process. The approach is a hybrid fabrication process that combines laser ablation technology for micro-structuring and laser-assisted thermal decomposition and deposition for synthesising and coating AgNPs from silver nitrate (AgNO_3) solution simultaneously. The StruCoat approach offers advantages for the synthesis of “green” AgNPs. There is no requirement for reducing and stabilising agents to be involved in the chemical reaction; thus, the need for this type of chemical reagent is reduced. More importantly, the approach offers durable silver-coated microstructured antimicrobial surfaces. This chapter will explore the StruCoat mechanism and the effects of laser power and silver nitrate molarity on the morphology of microstructures and the size of AgNPs. The chapter will also evaluate the antimicrobial performance of specimens prepared using StruCoat.

7.2 The working mechanism of StruCoat and experimental setup

7.2.1 Working principle of StruCoat

The schematic of StruCoat is illustrated in Figure 7.1. In this work, an ultrasonic atomiser was used to produce micro/nano drops of AgNO_3 from liquid based on vibrating piezo crystal due to its robustness and capability of working at low pressure [216]. As shown in Figure 7.1, micro liquid drops of aqueous solutions of AgNO_3 emerging from the ultrasonic atomiser are transported to the nanosecond pulsed laser ablation zone. Laser heating will cause the melting and even gasification of stainless steel. The vapour and plasma pressure will result in the partial ejection of the molten materials from the cavity and formation of surface debris. The recast layers are formed as the thermal energy rapidly dissipates into the internal material [217]. During the laser-material interaction, the laser ablation zone is in a high-temperature state, so the adherent AgNO_3 drops are thermally decomposed to AgNPs and deposited on the surface continuously.

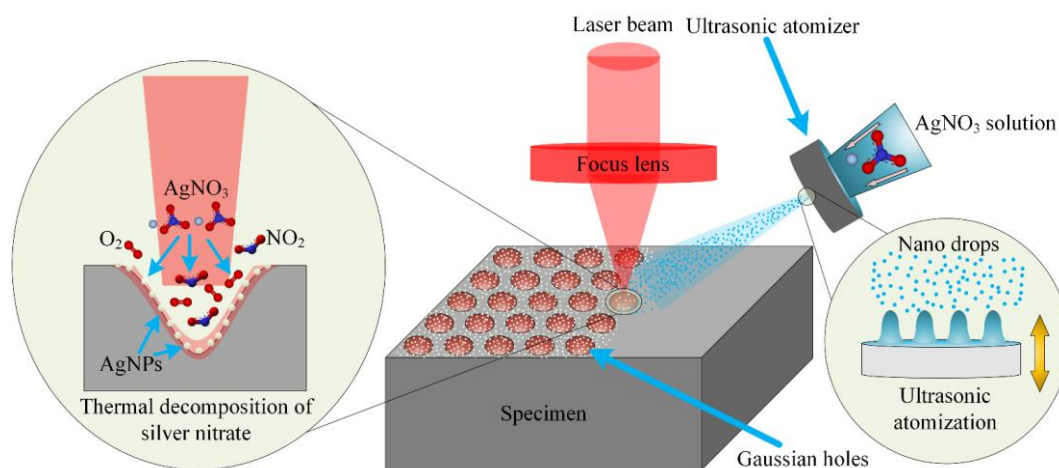
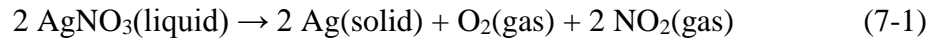


Figure 7.1 Schematic illustration of StruCoat approach.

7.2.2 Mechanism of decomposition and deposition of AgNPs

Heating will result in decomposition of most metallic nitrates into their corresponding oxides. However, the decomposition product of silver nitrate is elemental silver as silver oxide has a lower decomposition temperature than silver nitrate. Qualitatively, decomposition of silver nitrate is negligible under the melting point, but it is becoming increasingly apparent at about 250 °C, while total decomposition will take place at 440 °C [218]. The chemical decomposition equation of silver nitrate is described as:



In this research, an ultrasonic atomiser with a diameter of 20 mm and frequency of (f_{atomiser}) 113 KHz was employed in the experiments. In the process of ultrasonic atomization, a square wave pattern would be formed on the surface of the liquid when approaching resonance frequency of atomiser. Micro drops were ejected from square waves crests. Thus, its diameters were strongly correlated to the wavelength [219]. The wavelength λ is expressed as:

$$\lambda = \left(\frac{16\pi\gamma}{\rho_L f_{\text{atomiser}}^2} \right)^{\frac{1}{3}} \quad (7-2)$$

where γ is the surface tension of the liquid, ρ_L is the density of the liquid, and f_{atomiser} is the frequency of atomiser.

The most probable diameter of drops, D_L , can be calculated by [220]:

$$D_L = C^{-1}\lambda \quad (7-3)$$

where C is an experimentally determined coefficient [221]. According to the recommendation by Šarkovic and Babovic [220], $C = 4$ is used in this research. Thus, the probability diameter of drops D_L is 8.2 μm , when $\gamma = 0.073 \text{ N/m}$, $\rho_L = 1000 \text{ Kg/m}^3$.

Then, the most probable diameter of silver particle D_{Ag} can be calculated by:

$$D_{Ag} = \frac{1}{4} \left[\left(\frac{2\pi\gamma C_{Ag} M_{Ag}}{\rho_L \rho_{Ag} f_{atomiser}^2} \right) \right]^{\frac{1}{3}} \quad (7-4)$$

where, C_{Ag} is the molarity of silver ions, which is equal to the molarity of silver nitrate solution. M_{Ag} is the molar mass of silver, which is 107.8682 g/mol, and ρ_{Ag} is the density of silver, which is 10530 kg/m³. The calculation results are shown in Figure 7.8.

Figure 7.2 illustrates the whole chemical reaction processes. The water starts to evaporate when drops of silver nitrate solution make contact with the high-temperature molten layer. Solid silver nitrate crystals are formed on the surface, but they start to decompose to silver oxide and silver when the temperature is higher than 250 °C and decomposes completely when the temperature is above 440 °C [218]. In addition, the silver oxide is continuously decomposed to silver if the temperature is still higher than 300 °C. In the laser machining process, the absorption of laser energy leads to a rapid increase of local temperature. The maximum temperature realised 3500-14500 K [222], which is higher than the vapour temperature (3135 K for iron) of stainless steel. This temperature is much higher than the decomposition temperature of silver nitrate; so, there is sufficient thermal energy to finish the decomposition reaction as shown in Figure 7.2. Then, the AgNPs are deposited on the surface during the solidification of the molten materials in the laser ablation zone.

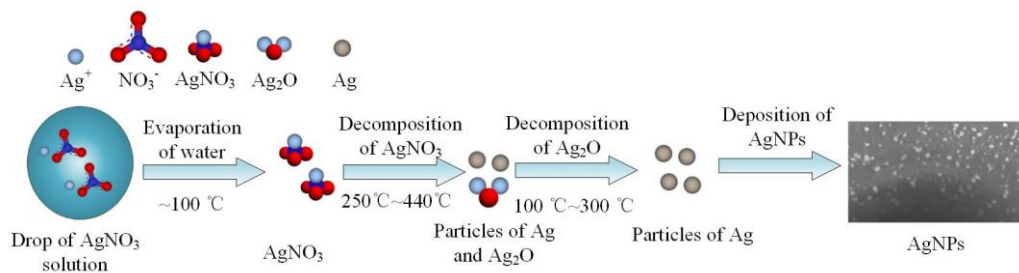


Figure 7.2 Schematic of chemical reaction process of AgNPs.

7.2.3 Materials and experimental setup

The AISI 316L stainless steel plates (6 mm × 6 mm × 2 mm) were used as the experimental specimens in this research. Same with section 4.3, the stainless steel plates were machined by a flat end mill (with a diameter of 6 mm). Silver nitrate (Alfa Aesar) and deionised water were used to prepare chemical solutions with different molarities of 25 to 200 mmol/L. The experiments are also conducted by the hybrid ultra-precision machine as shown in Figure 4.1. An ultrasonic atomiser was employed to generate micro liquid drops as shown in Figure 7.3. This research will investigate the effect of laser power and molarity of AgNO₃ on the surface topography and the size of AgNPs. Details of the operational conditions for the two experiments are shown in Table 7.1 and Table 7.2.



Figure 7.3 Ultrasonic atomiser used to generate micro drops.

Table 7.1 Operational conditions used to evaluate the effect of laser power on the synthesis of AgNPs.

Laser power (W)	Pulse repetition rate (Hz)	Feed rate (mm/min)	Duration time (s)	Pitch (µm)	Molarity of AgNO ₃ (mmol/L)
2, 8, 14, 20	100K	200	0.4	90	50

Table 7.2 Operational conditions used to evaluate the effect of molarity of silver nitrate on the synthesis of AgNPs.

Laser power (W)	Pulse repetition rate (kHz)	Feed rate (mm/min)	Duration time (s)	Pitch (μm)	Molarity of AgNO_3 (mmol/L)
14	100	200	0.4	90	25, 50, 100, 200

7.2.4 Post-processing and characterization

All specimens were cleaned ultrasonically with deionised water, acetone and ethanol for 10 minutes to remove any organic compounds on the surface before and after the experiments. Then, these specimens were dried in an oven at 100 °C for 20 minutes. The surface chemistry and the morphology of laser structured Gaussian holes and deposited AgNPs were characterised by scanning electron microscopy (SEM) and X-ray diffraction (XRD).

7.3 Experiments with StruCoat technology

In the laser ablation process, the material was removed from the substrate surface because high peak power results in a thermal energy that is higher than the breakdown thresholds of material which would lead to material melting, ablation and vapour generation. The thermal energy also helped to form the high-temperature zone around the laser radiation area. The thermal decomposition of silver nitrate to silver particles relied on the heat generated in the laser ablation process. Thus, the size of microstructure and AgNPs could be tightly controlled by the laser power and molarity of silver nitrate. This section will analyse the influences of the above factors.

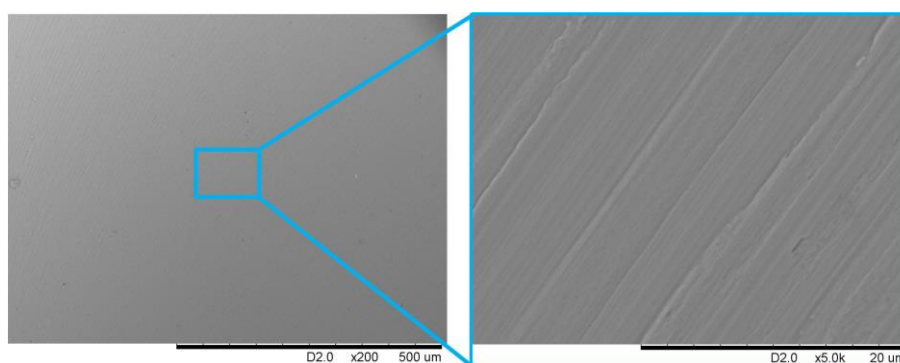
7.3.1 The effect of laser power on the morphology of AgNPs and microstructures

Figure 7.4 shows the SEM images of the smooth surface and laser-ablated microstructures obtained using different laser powers, but at constant molarity of silver nitrate of 50 mmol/L. The increasing size of laser ablated microstructures was observed with the increase of laser power. The increased diameter of laser ablated holes and the thickness of casting layers is the result of molten metal flow driven by surface tension and recoil pressure formed by the evaporation [223]. Figure 7.4 (b) to (e), shows all specimens contained a certain amount of silver particles deposited on the surfaces. The presence of silver nanoparticles was further confirmed by XRD analysis results shown in Figure 7.5.

When the laser power is 2W, the heat dissipates quickly, so micro drops of silver nitrate have a very short period to decompose to AgNPs. The theoretical diameter of liquid drops calculated by Equation 7-3 is around 8.2 μm . However, the obtained maximum diameter of the microstructures in the experiment was approximately 20 μm at the laser power of 2 W. This indicated that the droplets have a smaller probability of falling within the laser ablated high-temperature area. When the laser power is increased to 8 W, the maximum diameter of microstructure reached 50 μm . Some AgNPs were also formed on microstructures due to the high temperature of the molten layer. Figure 7.4 (c) and Figure 7.4 (d) show that more AgNPs were formed at a laser power of 14 W than 8 W. The diameter and depth of the melt pool increased with the increase of laser power as more energy was transferred into the heat-affected zone (HAZ). The sputtering area was formed at 14 W due to the vertical movement of liquid during irradiation caused by the vapour flow that expands in the Gaussian hole. As a result, AgNPs were deposited on both the spatter area and

Gaussian holes. However, the flake-like silver started to form on the microstructures when laser power was further increased to 20 W.

The thermal stress accumulation increased with the increase of laser power. This explained the increased quantity of AgNPs from lower to high laser powers. At the low laser power of 4 W, not enough accumulated thermal stress and physical space was generated for the silver nitrate to finish the decomposition process. However, when the laser power increased to 20 W, the laser ablated area was overheated. The excess heat energy led to a longer cooling time, so much more silver drops participated in the chemical reduction. These silver particles accumulated and formed silver particles with large dimensions. On the other hand, the evaporation and sputtering phenomenon would be enhanced significantly under high laser power, which had a negative effect on the deposition of AgNPs. Therefore, overheating would not be beneficial for growing more AgNPs on the laser-ablated structures. Suitable thermal energy would be necessary for the deposition of AgNPs. It is also known that the uniform distribution of AgNPs is beneficial to antimicrobial properties [224]. As such, specimens processed at the laser power 14 W had the most homogeneous size distribution of the AgNPs, and thus it was deemed the best result for deposition of AgNPs on the laser ablation zone.



(a)

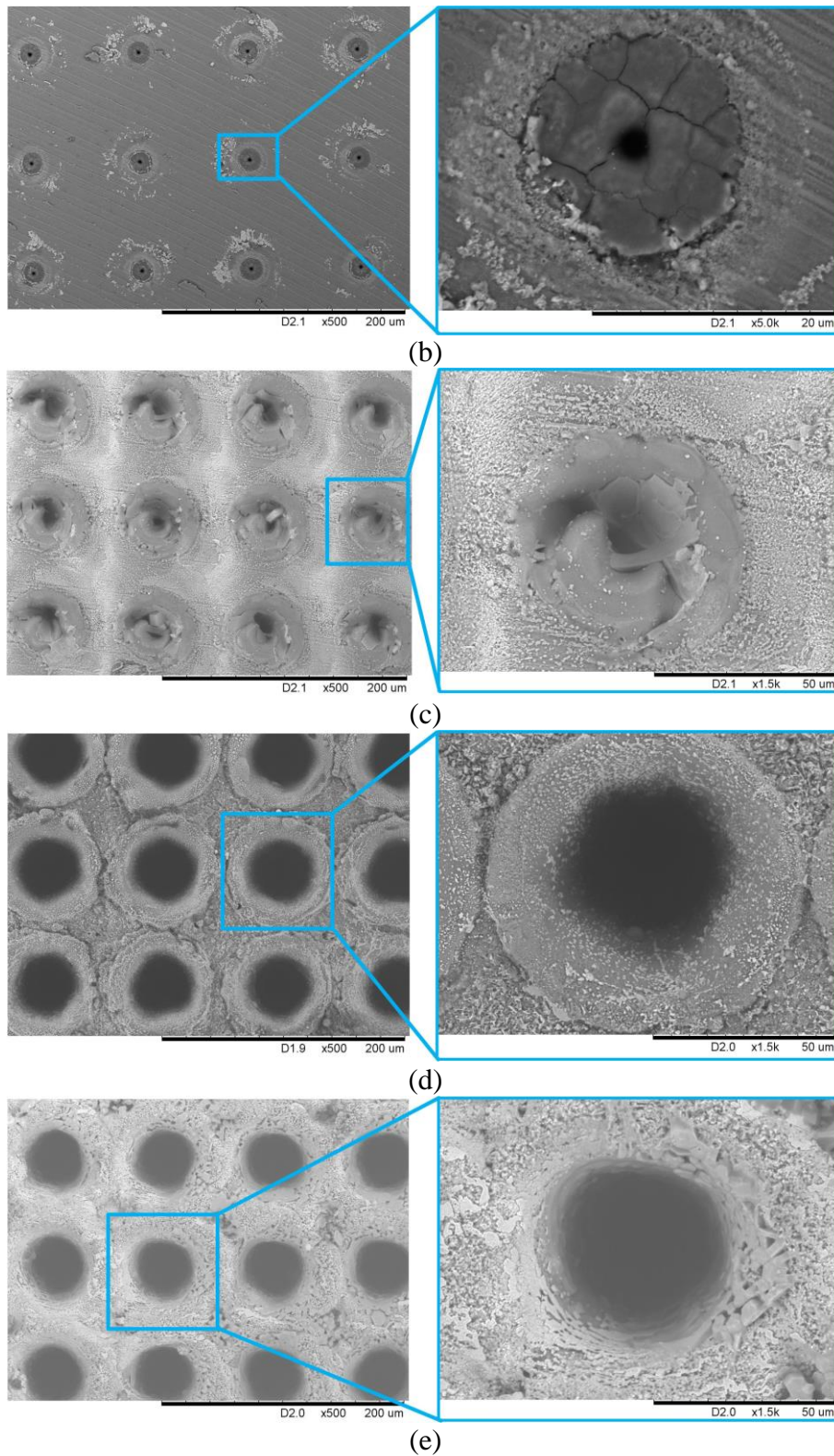


Figure 7.4 SEM image (left) and high-magnification image (right) of Specimens manufactured by StruCoat under different laser powers: (a) smooth and machined at laser powers of (b) 2 W; (c) 8 W; (d) 14 W; (e) 20 W.

Figure 7.5 displays the XRD patterns of the smooth surface, laser-machined surface and StruCoat surface of AISI 316L stainless steel. In Figure 7.5 (a), three sharp diffraction peaks correspond to the XRD pattern of austenite and one peak for ferrite. For the laser-machined surface, as shown in Figure 7.5 (b), it was found that austenite, Fe_3O_4 and Fe_2O_3 were recognised on the XRD pattern. In Figure 7.5 (c), the presence of pure silver is confirmed by the diffraction peaks at $2\theta = 38.2^\circ$, 44.4° , 64.6° and 77.5° on StruCoat surface, which correspond to scattering from (111), (200), (220) and (311) planes of pure silver. Thus, the XRD pattern in Figure 7.5 (c) proves the existence of AgNPs.

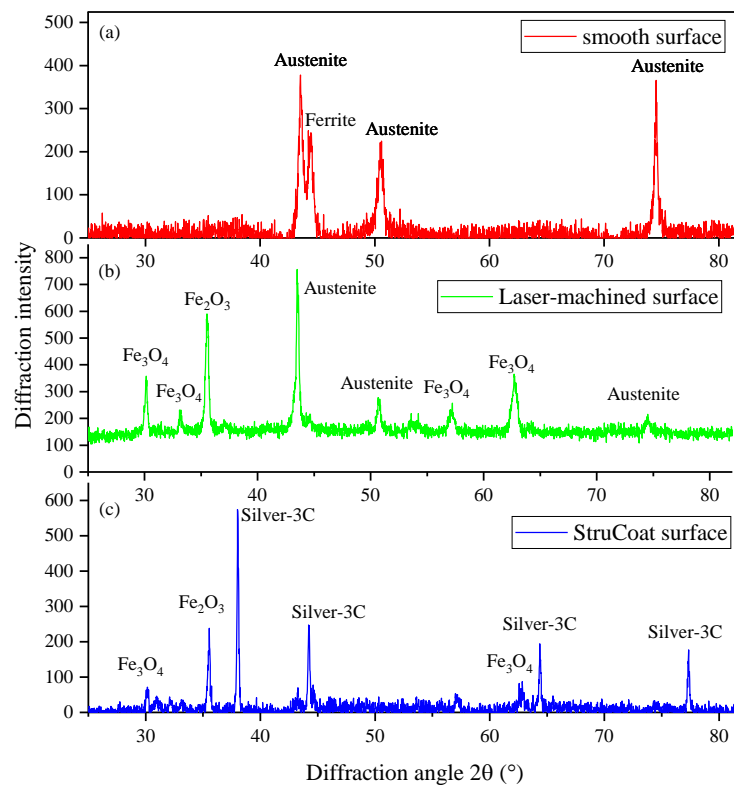


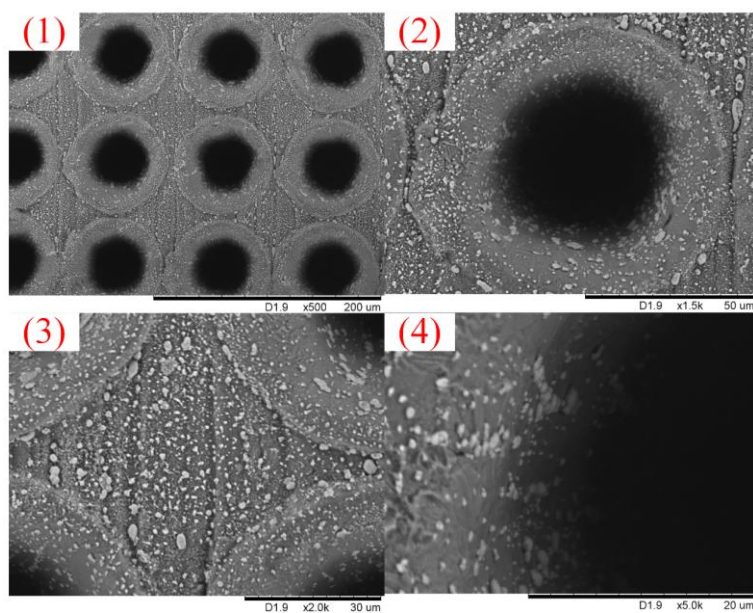
Figure 7.5 X-ray diffraction pattern of AISI 316L stainless steel: (a) smooth surface, (b) laser-machined surface and (c) StruCoat surface.

7.3.2 The effect of silver nitrate molarity on the synthesis of AgNPs

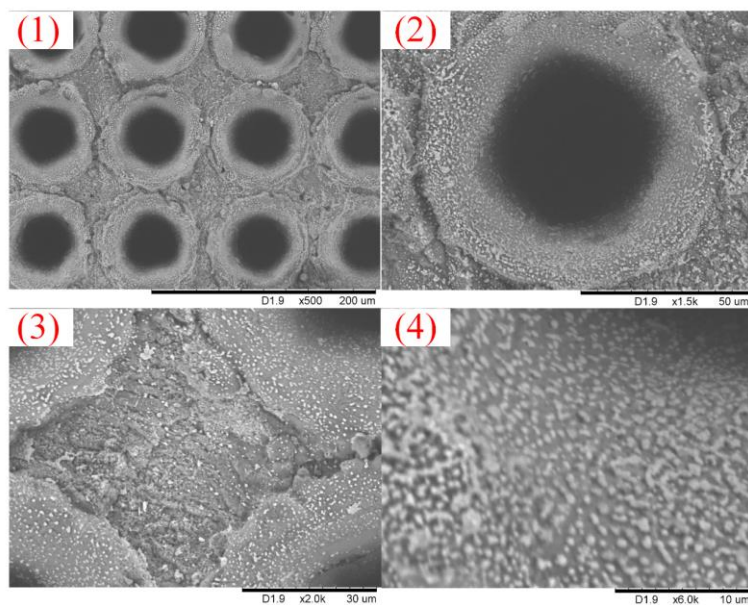
The molarity of silver nitrate is another critical processing parameter in StruCoat for deposition of AgNPs. In this section, different molarities of silver nitrate, as listed in Table 7.2, were employed to experiment.

Figure 7.6 shows the morphologies of microstructured surfaces processed by StruCoat at different molarities of silver nitrate solutions varying from 25 mmol to 200 mmol, while the laser power was fixed at 14 W. For the specimens which employed 25 mmol, 50 mmol and 100 mmol silver nitrate solutions, the AgNPs could be observed. The distribution density of AgNPs was significantly higher while the molarity of the silver nitrate solution was 50 mmol. The number of silver ions increased with the increase of molarity of silver nitrate solution. Low molarity of silver ions required less thermal energy in the chemical reduction process. Thus, the excess heat leads to AgNPs being evaporated further. This explains the increase in distribution density of AgNPs while the molarity of silver nitrate solution was increased from 25 mmol to 50 mmol. However, when the molarity of silver nitrate solution was increased to 100 mmol, aggregation and clumping of the AgNPs were observed. Some adjacent AgNPs started to weld together, with some silver bars starting to appear on the microstructure. There are several reasons which could explain these observations. Firstly, the silver nitrate solution of higher molarity required more energy to complete the thermal decomposition reaction, resulting in insufficient heat energy for the evaporation of the silver particles. Secondly, the surface tension and density of drops of silver nitrate increased with the increase of molarity of silver nitrate. Thus the adjacent drops were more possibly connected when they were deposited on the microstructure and formed larger drops. Thirdly, the high molarity of silver ions in

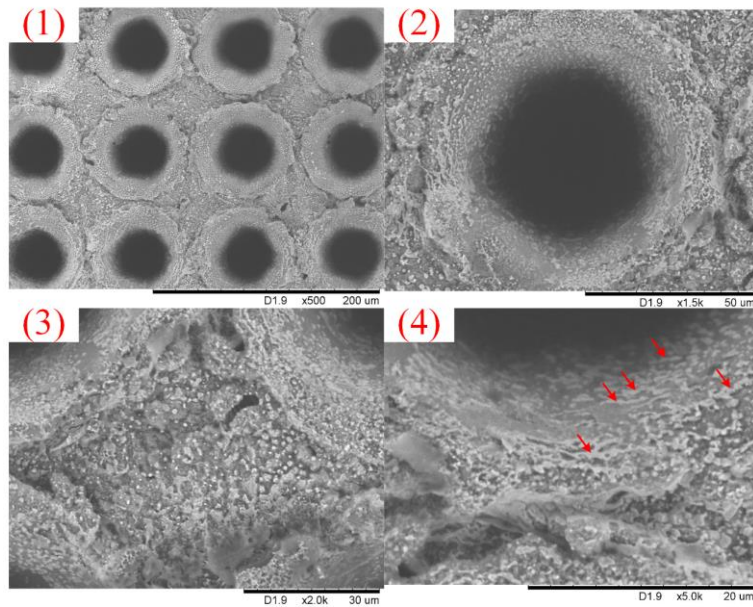
every drop could have resulted in more silver being deposited on the substrates. As shown in Figure 7.6 (d), the aggregation and clumping of the AgNPs became more significant when the molarity of silver nitrate solution increased to 200 mmol.



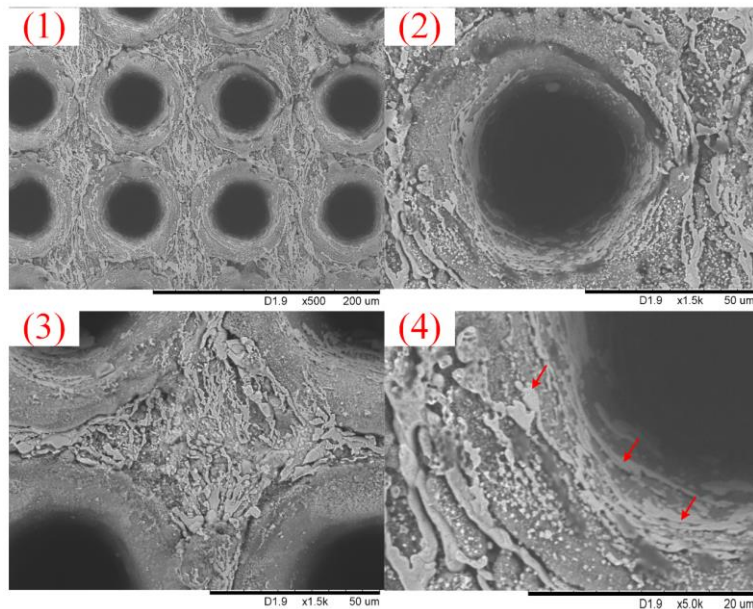
(a)



(b)



(c)



(d)

Figure 7.6 Low and high magnification SEM images of StruCoat processed microstructured surfaces with different molarities of silver nitrate: (a) 25 mmol; (b) 50 mmol; (c) 100 mmol; (d) 200 mmol. Images labelled (1) were low magnification ($\times 500$), and (2)-(4) were high magnification ($\times 1.5$ - 6.0 k). Arrows on images indicate the silver particles.

AgNPs have a large surface-to-volume ratio, so it exhibits unique and dramatically different physical, chemical, and biological properties relative to bulk materials [225]. Some research proved that smallest-sized AgNPs demonstrated a better antibacterial activity against bacterial as compared to the triangular and larger spherical shaped AgNPs [225,226]. In this study, the histogram and probability density function of AgNPs is shown in Figure 7.7. The length of 100 particles with a clear profile was measured manually by image processing software (Nano Measurer 1.2.5) based on the SEM image (4) in Figure 7.6. The size of AgNPs was found to be dependent on the molarity of the silver nitrate solution. At low molarity (25 mmol and 50 mmol), the mean particle size of microspheres was 400-600 nm. At high molarity (100 mmol and 200 mmol), the mean particle size reached micron level. Nevertheless, the particle size of 500 nm had the maximum proportion for all the specimens. Besides, a low standard deviation indicated that the data points tended to close to the mean value, while a high standard deviation indicated that the data points were spread out over a broader range of values. Thus, the best molarity was 50 mmol as it allowed specimens with a minimum mean particle size of 480 nm and the minimum standard deviation of 224 nm. This indicated that too high a molarity was not beneficial for growing more nanoscale silver particles on the laser-ablated structures, and a suitable molarity of silver nitrate solution would be necessary for the generation of AgNPs with uniform distribution in the average size.

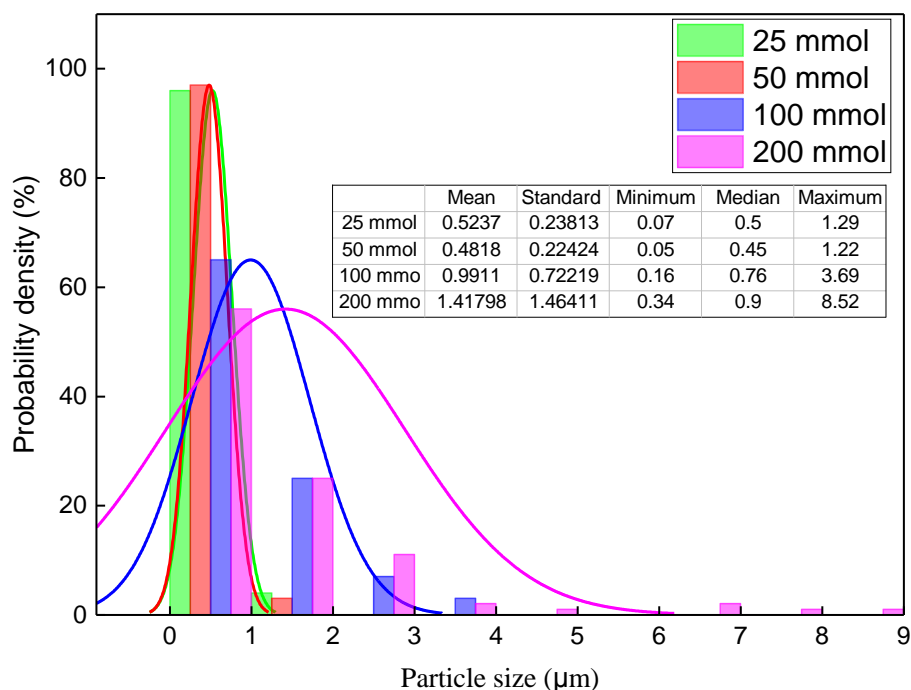


Figure 7.7 Histogram and probability density function of AgNPs.

Comparison between the predicted and measured diameter of silver particles is shown in Figure 7.8. The predicted value was closer to the measured median value than the average value. In theory, with the increase of molarity of silver nitrate, the predicted particle size increased gradually due to the increased silver included in the micro drops. The experimental results showed the same tendency except at 50 mmol. It obtained similar particle sizes of approximately 500 nm at molarities of 25 and 50 mmol in experiments. Thus, the theoretical and experimental results indicated that it was not necessary to employ silver solutions with high molarity as it could lead to the increased size of deposited particles. When the molarity is 200 mmol, the measured average size of AgNPs is 36% larger than the predicted value. The reason is that the high molarity of silver nitrate solution result in aggregation and clumping of the adjacent silver nitrate drops as shown in Figure 7.6 (d).

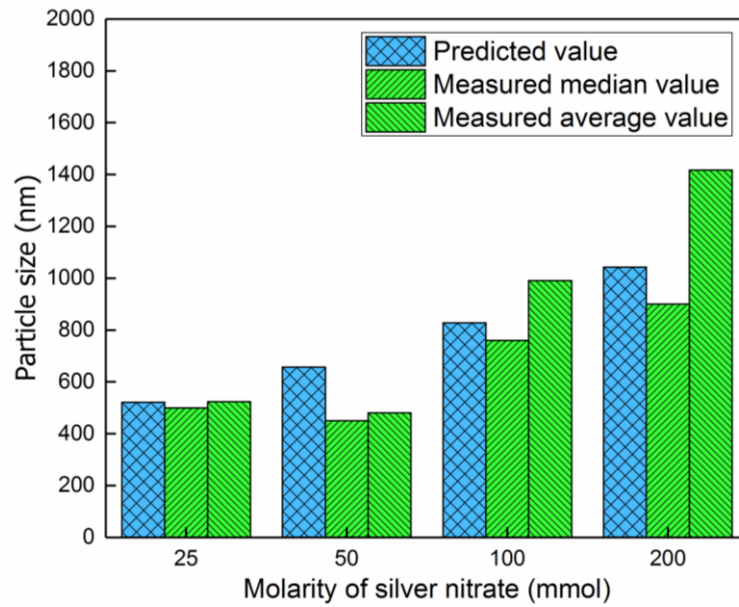


Figure 7.8 Comparison between predicted and measured particles size.

Focused Ion Beam (FIB) milling was used to make a cross-section on the StruCoat processed surfaces to observe the interface between AgNPs and the substrates of stainless steel. Figure 7.9 shows SEM images of the subsurface topography. It could be observed that the AgNPs were firmly connected with the stainless steel after the welding effect in the laser ablation process, and this helps to attain the high strength of interfacial bonding.

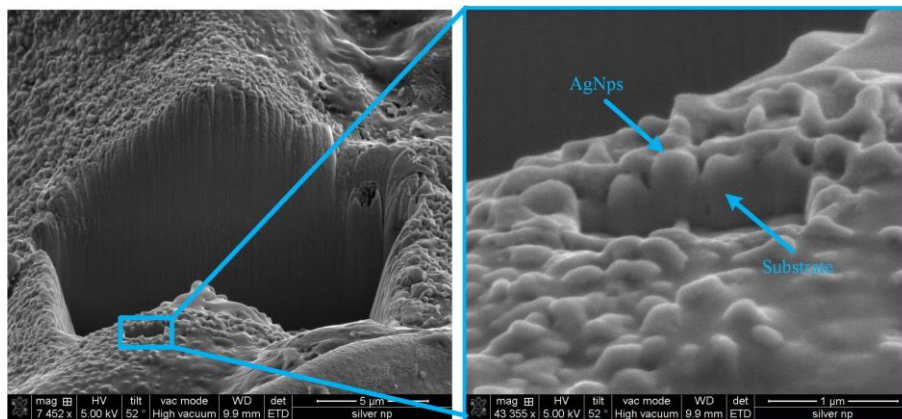


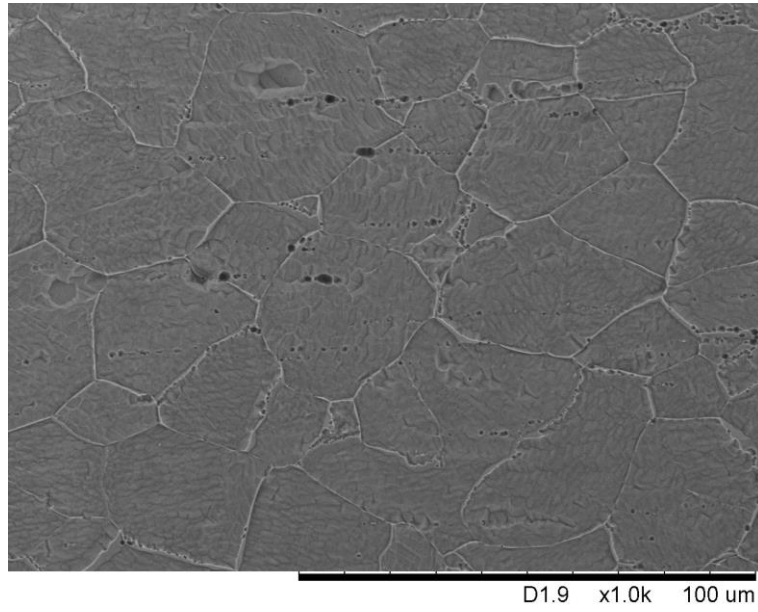
Figure 7.9 Whole image of FIB processed areas (Left) and magnified image of the cross-section (Right).

7.3.3 *Material microstructures of StruCoat processed substrates*

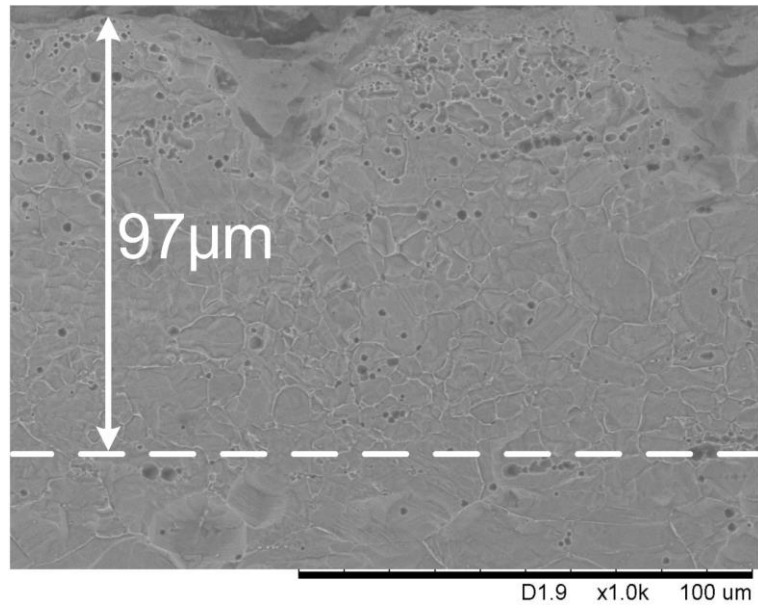
During the laser machining process, the rapid heating and cooling lead to modification of material microstructure. The laser machining heat affected zone is defined as the area that has not melted, but has undergone thermally induced microstructural modification by laser pulses [227]. This section will investigate the cross-sectional material microstructure of HAZ of AISI 316L austenitic stainless steel in the traditional laser machining process and the StruCoat process. Metallographic methods were used to polish and etch cross-sections of specimens in order to evaluate the changes in substrate structures.

SEM images of the metallographic structure of stainless steel surfaces (unprocessed, processed by laser machining, and processed by StruCoat) are shown in Figure 7.10. The linear line intercept method was employed to measure grain size. The average grain sizes after laser machining process and StruCoat were about 9.3 μm and 4.5 μm , while the average size of the original grain in the as-received AISI 316L stainless steel was about 24.6 μm . The significant grain size refinement was due to the laser reversion annealing through the intense heat input during the laser machining process. As a result, the grain refinement effect would lead to an increase in both material strength and fracture toughness. More importantly, the specimen had even higher cooling rates in StruCoat than in laser machining due to the evaporation of the aqueous solution, which resulted in a further decrease of grain size (81% reduction).

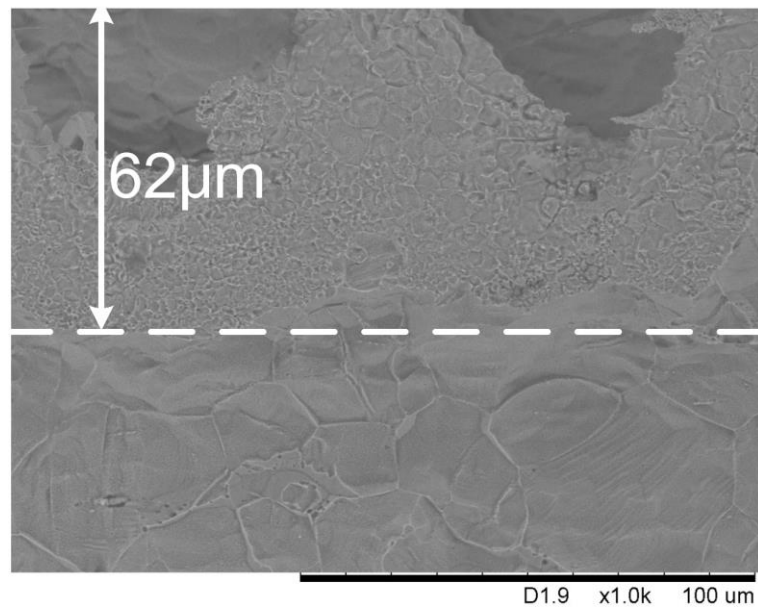
In addition, it could be clearly seen from Figure 7.10 (b) that the depth of the HAZ subjected to the laser machining process was about 97 μm , while the depth of HAZ in the StruCoat was about 62 μm as shown in Figure 7.10 (c). The reduced depth of HAZ in StruCoat was also due to the increased cooling rate in StruCoat.



(a)



(b)



(c)

Figure 7.10 SEM images ($\times 1.0k$) of cross-sections of stainless steel surfaces: (a) unprocessed, (b) processed by laser machining and (c) processed by StruCoat.

7.4 Antimicrobial test and results

7.4.1 Antimicrobial activity testing

Antimicrobial experiments were implemented to assess the susceptibility of three different kinds of specimens to bacterial attachment and biofilm growth: (i) smooth, (ii) laser ablated and (iii) specimens fabricated by StruCoat. Samples were cleaned before each experiment using 70% ethanol to remove any contaminant bacteria already on their surface.

The bacteria used in all experiments was *Staphylococcus aureus* (NCTC 4135) and were selected as they are widely associated with commonly contracted medical device-related infections [228]. *S. aureus* was cultured in 100 ml nutrient solution (Oxoid Ltd, UK) for 18 hours at 37 °C with a rotational speed of 120 rpm. Post-

incubation, the bacterial culture was centrifuged at 3939 ×g and the pellet resuspended in phosphate buffered saline (PBS; Oxoid Ltd, UK), before being serially diluted to a concentration of 10⁴ CFU/ml for experimental use.

Stainless steel specimens were immersed in 5 mL 10⁴ CFU/mL bacterial suspension in multiwell culture plates and incubated at 37 °C for 24 hours to permit attachment and subsequent biofilm formation [229]. Following incubation, the samples were rinsed in sterile phosphate buffered saline (PBS) solution to remove any excess planktonic bacteria not attached to the biofilm. The samples were then placed into 9 mL PBS, and the surface-attached bacteria were physically removed from the surfaces using the following methodology: 10 seconds manual agitation followed by 300 seconds in an ultrasonic bath followed by a further 10 seconds manual agitation. This process facilitated the release of the attached bacteria from the surface into the PBS ‘capture fluid’, with this fluid then being serially diluted and samples spread plated onto nutrient agar (Oxoid Ltd, UK) (n=3). Plates were incubated at 37 °C for 24 hours, and results enumerated as CFU/mL.

7.4.2 Antimicrobial evaluation of StruCoat

In this section, the antimicrobial capabilities of the two stainless steel specimens processed by laser ablation and StruCoat were evaluated after 24 h cultivation with bacterial contamination. A smooth stainless steel specimen with no surface modifications was included as a comparative control. Results showed that specimens machined by laser ablation and StruCoat both demonstrated reductions in bacterial attachment and biofilm formation compared to the unmodified control, as shown in Figure 7.11. Specimens processed by StruCoat exhibited a significantly

greater reduction in bacterial attachment than laser ablated specimens with a total decrease in the bacterial count of 86.2% compared to the unmodified material. Thus, the coating of AgNPs was critical for enhancing the antimicrobial capabilities of specimens manufactured by StruCoat. The slight antimicrobial activity evidenced by the laser-ablated specimens without AgNPs (9.6% reduction in surface contamination) can likely be attributed to the generation of iron oxide during the laser ablation process; an effect which was documented in a study by Fazio et al. (2016) [230].

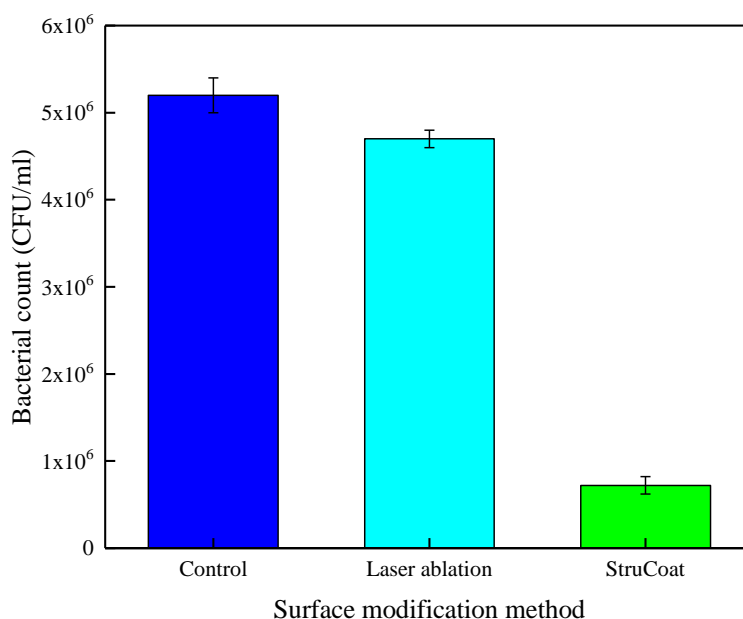


Figure 7.11 Bacterial attachment and biofilm formation on StruCoat modified stainless steel surfaces. Results on smooth and laser ablated surfaces are included as a comparison ($n=3 \pm$ standard deviation).

Jia et al. (2016) explored the synergistic effect of AgNPs and microstructures, and proved that microstructures had a special antimicrobial mode named “trap & kill” [196]. Figure 7.12 illustrates the possible sterilise modes engaged in the antimicrobial process. First, the released silver ions from AgNPs killed some bacteria before they contact with the surface, termed ‘release killing’. After the silver ion treatment, the

bacterial membrane interacted with silver ions and resulted in cytoplasmic membrane shrinking and damage [231]. Secondly, some bacterial kill can be attributed to direct contact with silver particles, termed ‘contact killing’. The accumulation of AgNPs in the bacterial membrane led to a significant increase in permeability, which results in the death of bacteria [232]. More importantly, bacterial cells with a negative charge would be introduced into the microstructures of the surfaces, causing binding with AgNPs via electrostatic attraction, and these were then killed through the contact killing mechanism. In addition, the microstructures could act simultaneously as storage pockets of AgNPs to attain sustainable release of silver ions, protecting AgNPs from friction-induced particle detachment. In terms of the significant antimicrobial effects observed in the present study, further work is required to determine the exact mechanism of action, and correlate with that of other studies using AgNPs such as that of Jia et al. (2016) [196].

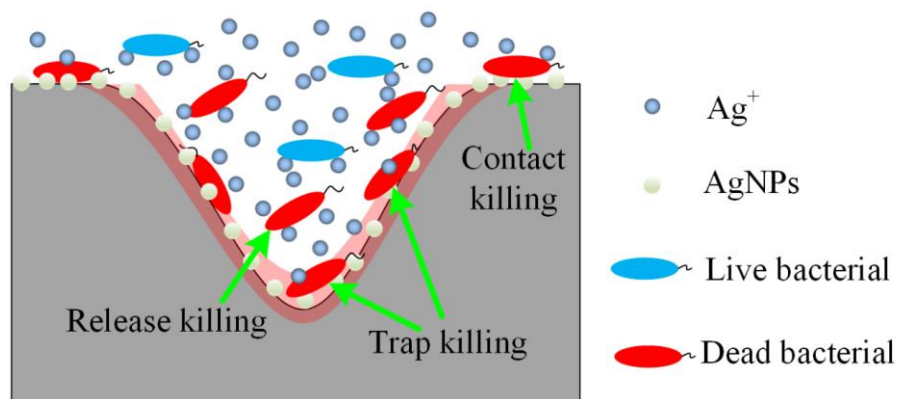


Figure 7.12 Antimicrobial mechanism of structured specimens coated with AgNPs.

7.5 Summary

A single-step fabrication approach named StruCoat was proposed for the first time in this work to generate antimicrobial microstructures coated with AgNPs on AISI 316L stainless steel. StruCoat laser ablation was used to generate microstructures,

while micro drops of silver nitrate solution were delivered to the laser ablation zone to decompose and coat AgNPs onto microstructures by using the thermal energy generated in the laser ablation process. The laser power and the silver nitrate molarity were identified as the major control parameters for StruCoat. Experimental studies show that silver nitrate with a molarity of 50 mmol at the laser power of 14 W, which resulted in AgNPs with a mean size of 480 nm, was the best processing condition for the chemical decomposition of silver nitrate micro drops in this study.

StruCoat is an eco-friendly process due to not requiring reducing and stabiliser agents, and only silver nitrate is required in the decomposition process. Furthermore, the microstructures can store AgNPs to attain the sustainable release of silver ions. AgNPs would mostly be distributed along the inner area of the microstructures. Thus, microstructures could provide protection for the AgNPs to avoid friction-induced particle detachment. In addition, StruCoat would help increase the cooling rate of the substrate in the laser machining process, resulting in a significant decrease in material grain size (by 81%). Decreasing grain size will increase the material strength and fracture toughness. Antimicrobial efficacy testing also demonstrated the enhanced antimicrobial properties of StruCoat, with an 86.2% antimicrobial rate against *Staphylococcus aureus*, compared to unmodified samples, in the present study.

Chapter 8 Conclusions and Future Works

8.1 Conclusions

This PhD thesis investigated the design method and underlying mechanism of superhydrophobicity on a laser ablated AISI 316L stainless steel surface based on simulation and experimental studies. The concepts of process and product fingerprints were proposed as critical measurable characteristics for determining the required surface topography and process parameters for a superhydrophobic surface. Furthermore, anisotropic superhydrophobic structures and antimicrobial surfaces with AgNPs were developed through two different laser-based hybrid manufacturing processes. The main conclusions from the research can be summarised as follows:

1. The proposed deterministic design approach, including a geometrical model for laser ablated Gaussian micro holes, and the theoretical constraints for a stable Cassie-Baxter state, can accurately design microstructures for maximising surface hydrophobicity. The design results prove that all the substrates (with pitches from 50–150 μm) have contact angles greater than 150° to realise superhydrophobicity. Furthermore, the maximum contact angle shows a decreasing trend with increasing microstructure pitch.

2. The CFD simulated contact angle has good agreement with the designed value, which also proves the VOF simulation is an effective approach to predict the wetting state and the apparent contact angle at an equilibrium state at Weber number 0.026. The simulated water droplet behaviour on the smooth surface acts as a damping vibration. For the hydrophobic substrate P150 (revised), the air pocket's pressure shows a declining trend with the transition from a Cassie-Baxter state to a Wenzel state. However, the superhydrophobic substrates P150 (optimised) and P110

(optimised) trapped a large volume of air with high pressure at the bottom of structures, resulting in a stable intermediate state and a Cassie-Baxter state, respectively. Furthermore, the superhydrophobic substrate has the maximum potential energy and kinetic energy, which helps explain its low adhesion and self-cleaning properties.

In the impacting process at a Weber number of 7.26, all the water droplets experienced four stages of spreading, recoiling, rebounding and falling with viscous energy dissipation. With the increased hydrophobicity of the three specimens, the water droplet detachment occurred earlier, varying from 16 ms to 12 ms. The simulation results also proved that water droplets on the superhydrophobic substrates have shorter recoiling time and longer rebound time than on the hydrophobic substrate.

3. The laser ablation experiments show that the measured contact angle has a minor deviation from the designed and simulated values because the machined specimens P150-14 W and P110-14 W having similar dimensions with the designed profile. The water droplet's dynamic impacting behaviour at a Weber number of 7.26 also proves that the simulation results have good agreement with high-speed camera test results, and the minor error major was caused due to the laser ablated specimens being rougher than the simulation model. Furthermore, the high-speed camera test at a Weber number of 29 showed that the superhydrophobic substrate has a low-adhesion property with water when compared with a hydrophobic substrate.

4. The dimensionless surface functional characterisation parameter R_{hy} (i.e. the average ratio of R_z to R_{sm}) is the most sensitive parameter to the specimen's contact angle, which can be regarded as the product fingerprint. The laser pulse energy per unit area on the specimen (I_s) represents the combined effects of laser power, exposure time and structure pitch on surface topography, and it is the best process fingerprint

that can be used to control the product fingerprint R_{hy} . The threshold values of R_{hy} and I_s are 0.41 and 536 J/mm², respectively, which ensure the specimen's superhydrophobicity (contact angle larger than 150 °) in the laser ablation process. The maximum contact angle of a laser ablated specimen in this research is 164 °.

5. The experimental results for the sequential process of laser ablation and chemical etching (LA-CE) showed that the direction of ratchet-like microstructures is the same as the laser beam feed direction. With the increase of laser power, the width and the depth of microstructures showed an increasing trend, which resulted in the disappearance of ridges. The above phenomenon is caused by fact that the large laser power has a large influence zone. However, increasing the pitch causes the ridges to reappear. Specimen 3, with a pitch of 25 μm machined at a laser power of 20 W, has a maximum contact angle of 158.2 °. Furthermore, with a dip angle of 7 °, specimen 3 shows anisotropic superhydrophobicity, as the droplet easily rolled off along the laser beam feed direction; however, it was pinned tightly in the opposite direction.

6. A single-step fabrication approach (StruCoat) for the development of antimicrobial surfaces based on laser ablation technology has been successfully developed to generate antimicrobial microstructures coated with AgNPs on AISI 316L stainless steel for the first time. The experimental results showed that silver nitrate with a molarity of 50 mmol at the laser power of 14 W, which resulted in AgNPs with a mean size of 480 nm, was the best processing condition for the chemical decomposition of silver nitrate micro drops in this research. In addition, StruCoat can help increase the cooling rate of the substrate in the laser machining process, resulting in the significant decrease of material grain size (by 81%). Antimicrobial efficacy testing also demonstrated the enhanced antimicrobial properties of StruCoat, with an

86.2% antimicrobial rate against *Staphylococcus aureus*, compared to unmodified samples, in the present study.

The optimal technological parameters and key performance indicators for fabricating functional surface on AISI 316L stainless steel are summarised in Table 8.1.

Table 8.1 The optimal technological parameters and key performance indicators for fabricating functional surfaces on AISI 316L stainless steel.

Type of functional surfaces	Methodology	Surface characteristics	Processing parameters	Key performance indicators
Superhydrophobic surface	Laser ablation and silanization.	Gaussian hole pattern	$P = 70 \mu\text{m}$, $P_{\text{ave}}=20 \text{ W}$, $t_e = 1 \text{ s}$, $f_p = 100 \text{ KHz}$, feed rate 200 mm/min.	Contact angle 164 °
Anisotropic superhydrophobic surface	Laser ablation, chemical etching and silanization.	Ratchet-like microstructures	$P = 25 \mu\text{m}$, $P_{\text{ave}} = 20 \text{ W}$, $f_p = 20 \text{ KHz}$, feed rate 30 mm/min, unidirectional feed, aqueous solution of ferric chloride hexahydrate (32g FeCl ₃ 6H ₂ O, 3ml of 37% HCl, 3ml of 85% H ₃ PO ₄ , 120ml H ₂ O).	Contact angle 158 °, for a dip angle of 7 °, the specimen shows anisotropic superhydrophobicity.
Antimicrobial surface	StruCoat	Gaussian hole pattern and AgNPs.	$P = 90 \mu\text{m}$, $P_{\text{ave}}=14 \text{ W}$, $t_e = 0.4 \text{ s}$, $f_p = 100 \text{ KHz}$. Feed rate 200 mm/min, 50 mmol AgNO ₃ solution.	Size of AgNPs 480 nm, 86.2% antimicrobial ate

8.2 Contributions to knowledge

The contributions to knowledge in this dissertation can be listed as follows:

1. Developed a deterministic design method to design the dimensions of microstructures to be fabricated by laser ablation to maximise superhydrophobicity.

2. Validated the concepts of process and product fingerprints as critical measurable characteristics to determine the required surface topography and process parameters for a laser ablated superhydrophobic surface.

3. Created an innovative process to prepare ratchet-like microstructures on AISI 316L stainless steel that possess anisotropic superhydrophobicity. Different from the normal laser ablation process, the undesired oxide layers and recast layers, which result in short service life, poor surface quality and appearance, will be removed through the hybrid process. This new process has great potential to be scaled-up for practical industrial applications.

4. Created a single-step fabrication approach for the development of antimicrobial surfaces that combines laser ablation technology for micro-structuring and laser-assisted thermal decomposition and deposition for synthesising and coating AgNPs from silver nitrate (AgNO_3) solution simultaneously. The approach offers advantages for the synthesis of “green” AgNPs. There is no requirement for reducing and stabilising agents in the chemical reaction. Through the hybridisation of the subtractive laser ablation and additive chemical deposition processes, the new manufacturing approach has promising applications for providing antimicrobial micro-structured silver coatings for medical devices such as surgical tools and implants.

8.3 Recommendations for future works

The research presented in this thesis provides a solid foundation for the development of functional surfaces on surgical tools and implants. However, there are still some challenges that must be addressed for practical application. The recommendations for further research are:

1. Service life is still the main issue for most superhydrophobic surfaces; thus, future research should focus on obtaining a superhydrophobic substrate with a long-term service life or on using efficient and straightforward remanufacturing techniques to make the substrate achieve the superhydrophobicity conveniently. Furthermore, in some cases, the superhydrophobic surface will work in an extreme environment; therefore, the effect of the testing condition on hydrophobicity is also an interesting topic.

2. Currently, most superhydrophobic coating or microstructures are manufactured on planar surfaces. However, most surgical tools (e.g. scalpels, needles and retractors) have curved surfaces. Hence, the further exploration of laser ablation on curved superhydrophobic surfaces would be beneficial to the industrial popularisation of this technology.

3. The StruCoat approach was advanced for the first time in this thesis. Therefore, the further exploration of this approach's mechanism, process stability (using a long-term antimicrobial test) and more widespread application is required.

References

- [1] V. Jokinen, E. Kankuri, S. Hoshian, S. Franssila, R.H.A. Ras, Superhydrophobic blood-repellent surfaces, *Adv. Mater.* 30 (2018). doi:10.1002/adma.201705104.
- [2] S. Movafaghi, V. Leszczak, W. Wang, J.A. Sorkin, L.P. Dasi, K.C. Popat, A.K. Kota, Hemocompatibility of superhemophobic titania surfaces, *Adv. Healthc. Mater.* 6 (2017). doi:10.1002/adhm.201600717.
- [3] C.J. Nonckreman, S. Fleith, P.G. Rouxhet, C.C. Dupont-Gillain, Competitive adsorption of fibrinogen and albumin and blood platelet adhesion on surfaces modified with nanoparticles and/or PEO, *Colloids Surfaces B Biointerfaces.* 77 (2010) 139–149. doi:10.1016/j.colsurfb.2010.01.014.
- [4] Global antimicrobial resistance surveillance system (GLASS), (2018). doi:10.17226/6121.
- [5] J.R. Catterall, *Streptococcus pneumoniae*, *Thorax.* 54 (1999) 929–937. doi:10.1136/thx.54.10.929.
- [6] E.A. Ameh, S.E. Cox, A. Nasir, Surgical site infection, (2014). <https://www.cdc.gov/HAI/ssi/ssi.html>.
- [7] D.J. Leaper, C.E. Edmiston, World Health Organization: global guidelines for the prevention of surgical site infection, *J. Hosp. Infect.* 95 (2017) 135–136. doi:10.1016/j.jhin.2016.12.016.
- [8] B. Bhushan, Y.C. Jung, A. Niemietz, K. Koch, Lotus-like biomimetic hierarchical structures developed by the self-assembly of tubular plant waxes, *Langmuir.* 25 (2009) 1659–1666. doi:10.1021/la802491k.
- [9] L. Feng, S. Li, Y. Li, H. Li, L. Zhang, J. Zhai, Y. Song, B. Liu, L. Jiang, D. Zhu,

- Super-hydrophobic surfaces: from natural to artificial, *Adv. Mater.* 14 (2002) 1857–1860. doi:10.1002/adma.200290020.
- [10] Y. Zheng, X. Gao, L. Jiang, Directional adhesion of superhydrophobic butterfly wings, *Soft Matter*. 3 (2007) 178–182. doi:10.1039/b612667g.
- [11] X. Gao, L. Jiang, Water-repellent legs of water striders, *Nature*. 432 (2004) 36–36. doi:10.1038/432036a.
- [12] Wikipedia contributors, Laser ablation, Wikipedia. (2019). https://en.wikipedia.org/w/index.php?title=Laser_ablation&oldid=877482249 (accessed July 4, 2019).
- [13] Global fiber laser market by type and application - global opportunity analysis and industry forecast, 2018-2025, (2018). <https://www.reportlinker.com/p05563977/Global-Fiber-Laser-Market-by-Type-and-Application-Global-Opportunity-Analysis-and-Industry-Forecast.html> (accessed February 15, 2019).
- [14] O.J. Guy, K.A.D. Walker, Graphene functionalization for biosensor applications, Second Edi, Elsevier Inc., 2016. doi:10.1016/B978-0-12-802993-0.00004-6.
- [15] T. Young, An essay on the cohesion of fluids, *Philos. Trans. R. Soc. London*. 95 (1805) 65–87.
- [16] A.B.D. Cassie, S. Baxter, Wettability of porous surfaces, *Trans. Faraday Soc.* 40 (1944) 546–551. doi:10.1039/tf9444000546.
- [17] R.N. Wenzel, Resistance of solid surfaces to wetting by water, *Ind. Eng. Chem.* 28 (1936) 988–994. doi:10.1021/ie50320a024.
- [18] T. Darmanin, F. Guittard, Superhydrophobic and superoleophobic properties in

- nature, *Mater. Today*. 18 (2015) 273–285. doi:10.1016/j.mattod.2015.01.001.
- [19] K. Koch, B. Bhushan, W. Barthlott, Multifunctional surface structures of plants: An inspiration for biomimetics, *Prog. Mater. Sci.* 54 (2009) 137–178. doi:10.1016/j.pmatsci.2008.07.003.
- [20] Z. Guo, W. Liu, B.L. Su, Superhydrophobic surfaces: from natural to biomimetic to functional, *J. Colloid Interface Sci.* 353 (2011) 335–355. doi:10.1016/j.jcis.2010.08.047.
- [21] Z. Guo, W. Liu, Biomimic from the superhydrophobic plant leaves in nature: binary structure and unitary structure, *Plant Sci.* 172 (2007) 1103–1112. doi:10.1016/j.plantsci.2007.03.005.
- [22] J. Ma, Y. Sun, K. Gleichauf, J. Lou, Q. Li, Nanostructure on taro leaves resists fouling by colloids and bacteria under submerged conditions, *Langmuir*. 27 (2011) 10035–10040. doi:10.1021/la2010024.
- [23] J.B.K. Law, A.M.H. Ng, A.Y. He, H.Y. Low, Bioinspired ultrahigh water pinning nanostructures, *Langmuir*. 30 (2014) 325–331. doi:10.1021/la4034996.
- [24] Y. Yoon, D. Kim, J.-B. Lee, Hierarchical micro/nano structures for superhydrophobic surfaces and super-lyophobic surface against liquid metal, *Micro Nano Syst. Lett.* 2 (2014) 1–18. doi:10.1186/s40486-014-0003-x.
- [25] L. Feng, Y. Zhang, J. Xi, Y. Zhu, N. Wang, F. Xia, L. Jiang, Petal effect: A superhydrophobic state with high adhesive force, *Langmuir*. 24 (2008) 4114–4119. doi:10.1021/la703821h.
- [26] Y.T. Cheng, D.E. Rodak, C.A. Wong, C.A. Hayden, Effects of micro- and nano-structures on the self-cleaning behaviour of lotus leaves, (2006). doi:10.1088/0957-4484/17/5/032.

- [27] H.J. Ensikat, P. Ditsche-kuru, C. Neinhuis, W. Barthlott, Superhydrophobicity in perfection: the outstanding properties of the lotus leaf, *Beilstein J. Nanotechnol.* (2011) 152–161. doi:10.3762/bjnano.2.19.
- [28] G.D. Bixler, B. Bhushan, Bioinspired rice leaf and butterfly wing surface structures combining shark skin and lotus effects, *Soft Matter*. 8 (2012) 11271–11284. doi:10.1039/c2sm26655e.
- [29] T. Wagner, C. Neinhuis, W. Barthlott, Wettability and contaminability of insect wings as a function of their surface sculptures, *Acta Zool.* 77 (2010) 213–225. doi:10.1111/j.1463-6395.1996.tb01265.x.
- [30] D. Byun, J. Hong, Saputra, J.H. Ko, Y.J. Lee, H.C. Park, B.K. Byun, J.R. Lukes, Wetting characteristics of insect wing surfaces, *J. Bionic Eng.* 6 (2009) 63–70. doi:10.1016/S1672-6529(08)60092-X.
- [31] G.D. Bixler, B. Bhushan, Fluid drag reduction and efficient self-cleaning with rice leaf and butterfly wing bioinspired surfaces, *Nanoscale*. 5 (2013) 7685–7710. doi:10.1039/c3nr01710a.
- [32] H. Mei, D. Luo, P. Guo, C. Song, C. Liu, Y. Zheng, L. Jiang, Multi-level micro-/nanostructures of butterfly wings adapt at low temperature to water repellency, *Soft Matter*. 7 (2011) 10569–10573. doi:10.1039/c1sm06347b.
- [33] W. Peng, X. Hu, D. Zhang, Bioinspired fabrication of magneto-optic hierarchical architecture by hydrothermal process from butterfly wing, *J. Magn. Mater.* 323 (2011) 2064–2069. doi:10.1016/j.jmmm.2011.03.015.
- [34] C. Liu, J. Ju, Y. Zheng, L. Jiang, Asymmetric ratchet effect for directional transport of fog drops on static and dynamic butterfly wings, *ACS Nano*. 8 (2014) 1321–1329. doi:10.1021/nn404761q.

- [35] Y. Cui, D. Li, H. Bai, Bioinspired smart materials for directional liquid transport, *Ind. Eng. Chem. Res.* 56 (2017) 4887–4897. doi:10.1021/acs.iecr.7b00583.
- [36] P. Guo, Y. Zheng, C. Liu, J. Ju, L. Jiang, Directional shedding-off of water on natural/bio-mimetic taper-ratchet array surfaces, *Soft Matter*. 8 (2012) 1770–1775. doi:10.1039/c1sm06631e.
- [37] W. Tong, D. Xiong, N. Wang, C. Yan, T. Tian, Green and timesaving fabrication of a superhydrophobic surface and its application to anti-icing, self-cleaning and oil-water separation, *Surf. Coatings Technol.* 352 (2018) 609–618. doi:10.1016/j.surfcoat.2018.08.035.
- [38] S. Li, K. Page, S. Sathasivam, F. Heale, G. He, Y. Lu, Y. Lai, G. Chen, C.J. Carmalt, I.P. Parkin, Efficiently texturing hierarchical superhydrophobic fluoride-free translucent films by AACVD with excellent durability and self-cleaning ability, *J. Mater. Chem. A*. 6 (2018) 17633–17641. doi:10.1039/c8ta05402a.
- [39] C. Anitha, S. Syed Azim, S. Mayavan, Influence of particle size in fluorine free corrosion resistance superhydrophobic coating - optimization and stabilization of interface by multiscale roughness, *J. Alloys Compd.* 765 (2018) 677–684. doi:10.1016/j.jallcom.2018.06.214.
- [40] A. Rastegari, R. Akhavan, The common mechanism of turbulent skin-friction drag reduction with superhydrophobic longitudinal microgrooves and riblets, *J. Fluid Mech.* 838 (2018) 68–104. doi:10.1017/jfm.2017.865.
- [41] X. Xie, Q. Weng, Z. Luo, J. Long, X. Wei, Thermal performance of the flat micro-heat pipe with the wettability gradient surface by laser fabrication, *Int. J.*

Heat Mass Transf. 125 (2018) 658–669.
doi:10.1016/j.ijheatmasstransfer.2018.04.110.

- [42] U. Trdan, M. Hočevár, P. Gregorčič, Transition from superhydrophilic to superhydrophobic state of laser textured stainless steel surface and its effect on corrosion resistance, *Corros. Sci.* 123 (2017) 21–26.
doi:10.1016/j.corsci.2017.04.005.
- [43] M. Karlsson, P. Forsberg, F. Nikolajeff, From hydrophilic to superhydrophobic: fabrication of micrometer-sized nail-head-shaped pillars in diamond, *Langmuir*. 26 (2010) 889–893. doi:10.1021/la902361c.
- [44] T. Nishino, M. Meguro, K. Nakamae, M. Matsushita, Y. Ueda, The lowest surface free energy based on $-CF_3$ alignment, *Langmuir*. 15 (2002) 4321–4323. doi:10.1021/la981727s.
- [45] M.S. Bell, A. Shahraz, K.A. Fichthorn, A. Borhan, Effects of hierarchical surface roughness on droplet contact angle, *Langmuir*. 31 (2015) 6752–6762. doi:10.1021/acs.langmuir.5b01051.
- [46] M. Nosonovsky, B. Bhushan, Roughness-induced superhydrophobicity: a way to design non-adhesive surfaces, *J. Phys. Condens. Matter*. 20 (2008). doi:10.1088/0953-8984/20/22/225009.
- [47] M. Nosonovsky, B. Bhushan, Hierarchical roughness optimization for biomimetic superhydrophobic surfaces, *Ultramicroscopy*. 107 (2007) 969–979. doi:10.1016/j.ultramic.2007.04.011.
- [48] S. Herminghaus, Roughness-induced non-wetting, *Europhys. Lett.* 52 (2000) 165–170. doi:10.1209/epl/i2000-00418-8.
- [49] J.L. Liu, X.Q. Feng, G. Wang, S.W. Yu, Mechanisms of superhydrophobicity

- on hydrophilic substrates, *J. Phys. Condens. Matter.* 19 (2007).
doi:10.1088/0953-8984/19/35/356002.
- [50] A. Sarkar, A.M. Kietzig, Design of a robust superhydrophobic surface: thermodynamic and kinetic analysis, *Soft Matter.* 11 (2015) 1998–2007.
doi:10.1039/c4sm02787f.
- [51] B. Bhushan, Y. Chae Jung, Wetting study of patterned surfaces for superhydrophobicity, *Ultramicroscopy.* 107 (2007) 1033–1041.
doi:10.1016/j.ultramic.2007.05.002.
- [52] A. Telecka, T. Li, S. Ndoni, R. Taboryski, Nanotextured Si surfaces derived from block-copolymer self-assembly with superhydrophobic, superhydrophilic, or superamphiphobic properties, *RSC Adv.* 8 (2018) 4204–4213.
doi:10.1039/c8ra00414e.
- [53] B. Bhushan, K. Koch, Y.C. Jung, Nanostructures for superhydrophobicity and low adhesion, *Soft Matter.* 4 (2008) 1799–1804. doi:10.1039/b808146h.
- [54] M.A. Sarshar, Y. Jiang, W. Xu, C.H. Choi, Depinning force of a receding droplet on pillared superhydrophobic surfaces: analytical models, *J. Colloid Interface Sci.* 543 (2019) 122–129. doi:10.1016/j.jcis.2019.02.042.
- [55] Y.B. Park, M. Im, H. Im, Y.K. Choi, Superhydrophobic cylindrical nanoshell array, *Langmuir.* 26 (2010) 7661–7664. doi:10.1021/la100911s.
- [56] F. Gentile, M.L. Coluccio, T. Limongi, G. Perozziello, P. Candeloro, E. Di Fabrizio, The five Ws (and one H) of super-hydrophobic surfaces in medicine, *Micromachines.* 5 (2014) 239–262. doi:10.3390/mi5020239.
- [57] G. Marinaro, A. Accardo, F. De Angelis, T. Dane, B. Weinhausen, M. Burghammer, C. Riekkel, A superhydrophobic chip based on SU-8 photoresist

- pillars suspended on a silicon nitride membrane, *Lab Chip*. 14 (2014) 3705–3709. doi:10.1039/c4lc00750f.
- [58] R. Narhe, Water condensation on ultrahydrophobic flexible micro pillar surface, *Epl*. 114 (2016). doi:10.1209/0295-5075/114/36002.
- [59] S.F. Toosi, S. Moradi, S. Kamal, S.G. Hatzikiriakos, Superhydrophobic laser ablated PTFE substrates, *Appl. Surf. Sci.* 349 (2015) 715–723. doi:10.1016/j.apsusc.2015.05.026.
- [60] Y.H. Yeong, A. Milionis, E. Loth, I.S. Bayer, Microscopic receding contact line dynamics on pillar and irregular superhydrophobic surfaces, *Sci. Rep.* 5 (2015) 1–10. doi:10.1038/srep08384.
- [61] P. Wang, T. Hayashi, Q. Meng, Q. Wang, H. Liu, K. Hashimoto, L. Jiang, Highly boosted oxygen reduction reaction activity by tuning the underwater wetting state of the superhydrophobic electrode, *Small*. 13 (2017) 1–7. doi:10.1002/sml.201601250.
- [62] M. Jung, T. Kim, H. Kim, R. Shin, J. Lee, J. Lee, J. Lee, S. Kang, Design and fabrication of a large-area superhydrophobic metal surface with anti-icing properties engineered using a top-down approach, *Appl. Surf. Sci.* 351 (2015) 920–926. doi:10.1016/j.apsusc.2015.06.024.
- [63] L. He, W. Liang, Z. Wang, B. Yang, Z. Duan, Y. Chen, 3-D thermodynamic analysis on wetting behavior of superhydrophobic surfaces, *Colloids Surfaces A Physicochem. Eng. Asp.* 504 (2016) 201–209. doi:10.1016/j.colsurfa.2016.05.070.
- [64] C. Liu, H. Zhan, J. Yu, R. Liu, Q. Zhang, Y. Liu, X. Li, Design of superhydrophobic pillars with robustness, *Surf. Coatings Technol.* 361 (2019)

342–348. doi:10.1016/j.surfcoat.2019.01.041.

- [65] J. Han, M. Cai, Y. Lin, W. Liu, X. Luo, H. Zhang, K. Wang, M. Zhong, Comprehensively durable superhydrophobic metallic hierarchical surfaces Via tunable micro-cone design to protect functional nanostructures, *RSC Adv.* 8 (2018) 6733–6744. doi:10.1039/c7ra13496g.
- [66] Y. Jin, A. Qamar, Y. Shi, P. Wang, Preferential water condensation on superhydrophobic nano-cones array, *Appl. Phys. Lett.* 113 (2018). doi:10.1063/1.5053697.
- [67] M. Wang, Q. Liu, H. Zhang, C. Wang, L. Wang, B. Xiang, Y. Fan, C.F. Guo, S. Ruan, Laser direct writing of tree-shaped hierarchical cones on a superhydrophobic film for high-Efficiency water collection, *ACS Appl. Mater. Interfaces.* 9 (2017) 29248–29254. doi:10.1021/acsami.7b08116.
- [68] S.Q. Cai, A. Bhunia, Superhydrophobic condensation enhanced by conical hierarchical structures, *J. Phys. Chem. C.* 121 (2017) 10047–10052. doi:10.1021/acs.jpcc.7b02554.
- [69] C.V. Ngo, G. Davaasuren, H.S. Oh, D.M. Chun, Transparency and superhydrophobicity of cone-shaped micropillar array textured polydimethylsiloxane, *Int. J. Precis. Eng. Manuf.* 16 (2015) 1347–1353. doi:10.1007/s12541-015-0177-z.
- [70] J. Ge, J. Zhang, F. Wang, Z. Li, J. Yu, B. Ding, Superhydrophilic and underwater superoleophobic nanofibrous membrane with hierarchical structured skin for effective oil-in-water emulsion separation, *J. Mater. Chem. A.* 5 (2017) 497–502. doi:10.1039/c6ta07652a.
- [71] N. Wang, Y. Yuan, Y. Wu, T. Hang, M. Li, Wetting transition of the caterpillar-

- Like superhydrophobic Cu/Ni-Co hierarchical structure by heat treatment, *Langmuir*. 31 (2015) 10807–10812. doi:10.1021/acs.langmuir.5b02535.
- [72] X. Hu, C. Tang, Z. He, H. Shao, K. Xu, J. Mei, W.M. Lau, Highly stretchable superhydrophobic composite coating based on self-adaptive deformation of hierarchical structures, *Small*. 13 (2017) 1–10. doi:10.1002/smll.201602353.
- [73] J. Wu, J. Xia, W. Lei, B. Wang, Superhydrophobic surface based on a coral-like hierarchical structure of ZnO, *PLoS One*. 5 (2010). doi:10.1371/journal.pone.0014475.
- [74] P. Wang, T. Zhao, R. Bian, G. Wang, H. Liu, Robust superhydrophobic carbon nanotube film with Lotus Leaf mimetic multiscale hierarchical structures, *ACS Nano*. 11 (2017) 12385–12391. doi:10.1021/acsnano.7b06371.
- [75] J. Yong, Q. Yang, F. Chen, D. Zhang, H. Bian, Y. Ou, J. Si, G. Du, X. Hou, Stable superhydrophobic surface with hierarchical mesh-porous structure fabricated by a femtosecond laser, *Appl. Phys. A Mater. Sci. Process*. 111 (2013) 243–249. doi:10.1007/s00339-013-7572-z.
- [76] Z. Xue, Z. Sun, Y. Cao, Y. Chen, L. Tao, K. Li, L. Feng, Q. Fu, Y. Wei, Superoleophilic and superhydrophobic biodegradable material with porous structures for oil absorption and oil-water separation, *RSC Adv*. 3 (2013) 23432–23437. doi:10.1039/c3ra41902a.
- [77] O.C. Aktas, S. Schröder, S. Veziroglu, M.Z. Ghori, A. Haidar, O. Polonskyi, T. Strunskus, K. Gleason, F. Faupel, Superhydrophobic 3d porous PTFE/TiO₂ hybrid structures, *Adv. Mater. Interfaces*. 6 (2019) 2–6. doi:10.1002/admi.201801967.
- [78] Y. Li, Z. Zhang, B. Ge, X. Men, Q. Xue, One-pot, template-free synthesis of a

- robust superhydrophobic polymer monolith with an adjustable hierarchical porous structure, *Green Chem.* 18 (2016) 5266–5272. doi:10.1039/c6gc01171c.
- [79] B. Liu, W. Wang, G. Jiang, X. Mei, K. Wang, J. Wang, Formation of porous structure with subspot size under the irradiation of picosecond laser pulses, *J. Nanomater.* 2013 (2013) 1–9. doi:10.1155/2013/301301.
- [80] W.Z. Yuan, L.Z. Zhang, Lattice Boltzmann simulation of droplets impacting on superhydrophobic surfaces with randomly distributed rough structures, *Langmuir.* 33 (2017) 820–829. doi:10.1021/acs.langmuir.6b04041.
- [81] J. Yan, K. Yang, X. Zhang, J. Zhao, Analysis of impact phenomenon on superhydrophobic surfaces based on molecular dynamics simulation, *Comput. Mater. Sci.* 134 (2017) 8–16. doi:10.1016/j.commatsci.2017.03.013.
- [82] S. Khan, J.K. Singh, Wetting transition of nanodroplets of water on textured surfaces: a molecular dynamics study, *Mol. Simul.* 40 (2014) 458–468. doi:10.1080/08927022.2013.819578.
- [83] W. Xu, Z. Lan, B.L. Peng, R.F. Wen, X.H. Ma, Effect of surface free energies on the heterogeneous nucleation of water droplet: a molecular dynamics simulation approach, *J. Chem. Phys.* 142 (2015) 054701. doi:10.1063/1.4906877.
- [84] K. Connington, T. Lee, Lattice Boltzmann simulations of forced wetting transitions of drops on superhydrophobic surfaces, *J. Comput. Phys.* 250 (2013) 601–615. doi:10.1016/j.jcp.2013.05.012.
- [85] L.Z. Zhang, W.Z. Yuan, A lattice Boltzmann simulation of coalescence-induced droplet jumping on superhydrophobic surfaces with randomly distributed structures, *Appl. Surf. Sci.* 436 (2018) 172–182.

doi:10.1016/j.apsusc.2017.11.200.

- [86] C. Antonini, A. Amirfazli, M. Marengo, Drop impact and wettability: From hydrophilic to superhydrophobic surfaces, *Phys. Fluids*. 24 (2012). doi:10.1063/1.4757122.
- [87] Z. Ke, J. Shi, B. Zhang, C.L. Chen, Numerical investigation of condensation on microstructured surface with wettability patterns, *Int. J. Heat Mass Transf.* 115 (2017) 1161–1172. doi:10.1016/j.ijheatmasstransfer.2017.08.121.
- [88] M. Tembely, R. Attarzadeh, A. Dolatabadi, On the numerical modeling of supercooled micro-droplet impact and freezing on superhydrophobic surfaces, *Int. J. Heat Mass Transf.* 127 (2018) 193–202. doi:10.1016/j.ijheatmasstransfer.2018.06.104.
- [89] W. Zhang, R. run Zhang, C. gang Jiang, C. wei Wu, Effect of pillar height on the wettability of micro-textured surface: Volume-of-fluid simulations, *Int. J. Adhes. Adhes.* 74 (2017) 64–69. doi:10.1016/j.ijadhadh.2016.12.011.
- [90] C. Liu, L. Zhu, W. Bu, Y. Liang, Superhydrophobic surfaces: from nature to biomimetic through VOF simulation, *Micron*. 107 (2018) 94–100. doi:10.1016/j.micron.2018.01.013.
- [91] S. Yun, Bouncing of an ellipsoidal drop on a superhydrophobic surface, *Sci. Rep.* 7 (2017) 1–9. doi:10.1038/s41598-017-18017-2.
- [92] Y. Quan, L.Z. Zhang, Numerical and analytical study of the impinging and bouncing phenomena of droplets on superhydrophobic surfaces with microtextured structures, *Langmuir*. 30 (2014) 11640–11649. doi:10.1021/la502836p.
- [93] K. Murugadoss, P. Dhar, S.K. Das, Role and significance of wetting pressures

- during droplet impact on structured superhydrophobic surfaces, *Eur. Phys. J. E.* 40 (2017) 1–10. doi:10.1140/epje/i2017-11491-x.
- [94] R.M.M. Hasan, X. Luo, Promising lithography techniques for next-generation logic devices, *Nanomanufacturing Metrol.* 1 (2018) 67–81. doi:10.1007/s41871-018-0016-9.
- [95] J. Feng, M.T. Tuominen, J.P. Rothstein, Hierarchical superhydrophobic surfaces fabricated by dual-scale electron-beam-lithography with well-ordered secondary nanostructures, *Adv. Funct. Mater.* 21 (2011) 3715–3722. doi:10.1002/adfm.201100665.
- [96] F. Wang, S. Li, L. Wang, Fabrication of artificial super-hydrophobic lotus-leaf-like bamboo surfaces through soft lithography, *Colloids Surfaces A Physicochem. Eng. Asp.* 513 (2017) 389–395. doi:10.1016/j.colsurfa.2016.11.001.
- [97] P. Kothary, X. Dou, Y. Fang, Z. Gu, S.Y. Leo, P. Jiang, Superhydrophobic hierarchical arrays fabricated by a scalable colloidal lithography approach, *J. Colloid Interface Sci.* 487 (2017) 484–492. doi:10.1016/j.jcis.2016.10.081.
- [98] J. Zhu, Y. Tian, X. Liu, C. Yang, Lithography-induced hydrophobic surfaces of silicon wafers with excellent anisotropic wetting properties, *Microsyst. Technol.* 25 (2019) 735–745. doi:10.1007/s00542-018-4010-3.
- [99] C.L. Cheung, R.J. Nikolić, C.E. Reinhardt, T.F. Wang, Fabrication of nanopillars by nanosphere lithography, *Nanotechnology.* 17 (2006) 1339–1343. doi:10.1088/0957-4484/17/5/028.
- [100] B. Liu, Y. He, Y. Fan, X. Wang, Fabricating super-hydrophobic lotus-leaf-like surfaces through soft-lithographic imprinting, *Macromol. Rapid Commun.* 27

(2006) 1859–1864. doi:10.1002/marc.200600492.

- [101] Y.H. Sung, Y.D. Kim, H.J. Choi, R. Shin, S. Kang, H. Lee, Fabrication of superhydrophobic surfaces with nano-in-micro structures using UV-nanoimprint lithography and thermal shrinkage films, *Appl. Surf. Sci.* 349 (2015) 169–173. doi:10.1016/j.apsusc.2015.04.141.
- [102] H.J. Choi, S. Choo, J.H. Shin, K.I. Kim, H. Lee, Fabrication of superhydrophobic and oleophobic surfaces with overhang structure by reverse nanoimprint lithography, *J. Phys. Chem. C.* 117 (2013) 24354–24359. doi:10.1021/jp4070399.
- [103] S.H. Kang, T.Y. Tai, T.H. Fang, Replication of butterfly wing microstructures using molding lithography, *Curr. Appl. Phys.* 10 (2010) 625–630. doi:10.1016/j.cap.2009.08.007.
- [104] A. Pozzato, S.D. Zilio, G. Fois, D. Vendramin, G. Mistura, M. Belotti, Y. Chen, M. Natali, Superhydrophobic surfaces fabricated by nanoimprint lithography, *Microelectron. Eng.* 83 (2006) 884–888. doi:10.1016/j.mee.2006.01.012.
- [105] Y. Lai, C. Lin, H. Wang, J. Huang, H. Zhuang, L. Sun, Superhydrophilic-superhydrophobic micropattern on TiO₂ nanotube films by photocatalytic lithography, *Electrochem. Commun.* 10 (2008) 387–391. doi:10.1016/j.elecom.2007.12.020.
- [106] Y. Li, J. Zhang, S. Zhu, H. Dong, F. Jia, Z. Wang, Y. Tang, L. Zhang, S. Zhang, B. Yang, Bioinspired silica surfaces with near-infrared improved transmittance and superhydrophobicity by colloidal lithography, *Langmuir.* 26 (2010) 9842–9847. doi:10.1021/la100183y.
- [107] Y. Liu, S. Li, J. Zhang, J. Liu, Z. Han, L. Ren, Corrosion inhibition of

- biomimetic super-hydrophobic electrodeposition coatings on copper substrate, *Corros. Sci.* 94 (2015) 190–196. doi:10.1016/j.corsci.2015.02.009.
- [108] P. Liu, L. Cao, W. Zhao, Y. Xia, W. Huang, Z. Li, Insights into the superhydrophobicity of metallic surfaces prepared by electrodeposition involving spontaneous adsorption of airborne hydrocarbons, *Appl. Surf. Sci.* 324 (2015) 576–583. doi:10.1016/j.apsusc.2014.10.170.
- [109] Q. Liu, D. Chen, Z. Kang, One-Step electrodeposition process to fabricate corrosion-resistant superhydrophobic surface on magnesium alloy, *ACS Appl. Mater. Interfaces.* 7 (2015) 1859–1867. doi:10.1021/am507586u.
- [110] N. Xu, D.K. Sarkar, X.G. Chen, W.P. Tong, Corrosion performance of superhydrophobic nickel stearate/nickel hydroxide thin films on aluminum alloy by a simple one-step electrodeposition process, *Surf. Coatings Technol.* 302 (2016) 173–184. doi:10.1016/j.surfcoat.2016.05.050.
- [111] D. Kumar, X. Wu, Q. Fu, J.W.C. Ho, P.D. Kanhere, L. Li, Z. Chen, Hydrophobic sol-gel coatings based on polydimethylsiloxane for self-cleaning applications, *Mater. Des.* 86 (2015) 855–862. doi:10.1016/j.matdes.2015.07.174.
- [112] S. Liu, X. Liu, S.S. Lathe, L. Gao, S. An, S.S. Yoon, B. Liu, R. Xing, Self-cleaning transparent superhydrophobic coatings through simple sol-gel processing of fluoroalkylsilane, *Appl. Surf. Sci.* 351 (2015) 897–903. doi:10.1016/j.apsusc.2015.06.016.
- [113] Z. Jiang, S. Fang, C. Wang, H. Wang, C. Ji, Durable polyorganosiloxane superhydrophobic films with a hierarchical structure by sol-gel and heat treatment method, *Appl. Surf. Sci.* 390 (2016) 993–1001.

doi:10.1016/j.apsusc.2016.08.152.

- [114] J.W. Lee, W. Hwang, Exploiting the silicon content of aluminum alloys to create a superhydrophobic surface using the sol-gel process, *Mater. Lett.* 168 (2016) 83–85. doi:10.1016/j.matlet.2015.12.137.
- [115] M. Raimondo, F. Veronesi, G. Boveri, G. Guarini, A. Motta, R. Zanoni, Superhydrophobic properties induced by sol-gel routes on copper surfaces, *Appl. Surf. Sci.* 422 (2017) 1022–1029. doi:10.1016/j.apsusc.2017.05.257.
- [116] X. Chen, Y. Chen, T. Jin, L. He, Y. Zeng, Q. Ma, N. Li, Fabrication of superhydrophobic coating from non-fluorine siloxanes via a one-pot sol-gel method, *J. Mater. Sci.* 53 (2018) 11253–11264. doi:10.1007/s10853-018-2348-7.
- [117] M. Yang, W. Liu, C. Jiang, S. He, Y. Xie, Z. Wang, Fabrication of superhydrophobic cotton fabric with fluorinated TiO₂ sol by a green and one-step sol-gel process, *Carbohydr. Polym.* 197 (2018) 75–82. doi:10.1016/j.carbpol.2018.05.075.
- [118] C. Jiang, W. Liu, M. Yang, S. He, Y. Xie, Z. Wang, Synthesis of superhydrophobic fluoro-containing silica sol coatings for cotton textile by one-step sol-gel process, *J. Sol-Gel Sci. Technol.* 87 (2018) 455–463. doi:10.1007/s10971-018-4750-7.
- [119] C. Jiang, W. Liu, Y. Sun, C. Liu, M. Yang, Z. Wang, Fabrication of durable superhydrophobic and superoleophilic cotton fabric with fluorinated silica sol via sol-gel process, *J. Appl. Polym. Sci.* 136 (2019) 1–9. doi:10.1002/app.47005.
- [120] M. Ma, Y. Mao, M. Gupta, K.K. Gleason, G.C. Rutledge, Superhydrophobic

- fabrics produced by electrospinning and chemical vapor deposition, *Macromolecules*. 38 (2005) 9742–9748. doi:10.1021/ma0511189.
- [121] C. Su, Y. Li, Y. Dai, F. Gao, K. Tang, H. Cao, Fabrication of three-dimensional superhydrophobic membranes with high porosity via simultaneous electrospinning and electrospinning, *Mater. Lett.* 170 (2016) 67–71. doi:10.1016/j.matlet.2016.01.133.
- [122] Z. Liu, H. Wang, E. Wang, X. Zhang, R. Yuan, Y. Zhu, Superhydrophobic poly(vinylidene fluoride) membranes with controllable structure and tunable wettability prepared by one-step electrospinning, *Polymer (Guildf)*. 82 (2016) 105–113. doi:10.1016/j.polymer.2015.11.045.
- [123] A.B. Radwan, A.M.A. Mohamed, A.M. Abdullah, M.A. Al-Maadeed, Corrosion protection of electrospun PVDF-ZnO superhydrophobic coating, *Surf. Coatings Technol.* 289 (2016) 136–143. doi:10.1016/j.surfcoat.2015.12.087.
- [124] A. Bahgat Radwan, A. Abdullah, A. Mohamed, M. Al-Maadeed, New electrospun polystyrene/Al₂O₃ nanocomposite superhydrophobic coatings; synthesis, characterization, and application, *Coatings*. 8 (2018) 65. doi:10.3390/coatings8020065.
- [125] K.K. Yan, L. Jiao, S. Lin, X. Ji, Y. Lu, L. Zhang, Superhydrophobic electrospun nanofiber membrane coated by carbon nanotubes network for membrane distillation, *Desalination*. 437 (2018) 26–33. doi:10.1016/j.desal.2018.02.020.
- [126] A. Kumar, B. Gogoi, Development of durable self-cleaning superhydrophobic coatings for aluminium surfaces via chemical etching method, *Tribol. Int.* 122 (2018) 114–118. doi:10.1016/j.triboint.2018.02.032.

- [127] K. Li, X. Zeng, H. Li, X. Lai, A study on the fabrication of superhydrophobic iron surfaces by chemical etching and galvanic replacement methods and their anti-icing properties, *Appl. Surf. Sci.* 346 (2015) 458–463. doi:10.1016/j.apsusc.2015.03.130.
- [128] X. Gao, W. Tong, X. Ouyang, X. Wang, Facile fabrication of a superhydrophobic titanium surface with mechanical durability by chemical etching, *RSC Adv.* 5 (2015) 84666–84672. doi:10.1039/c5ra15293c.
- [129] A. Ganne, V.O. Lebed, A.I. Gavrillov, Combined wet chemical etching and anodic oxidation for obtaining the superhydrophobic meshes with anti-icing performance, *Colloids Surfaces A Physicochem. Eng. Asp.* 499 (2016) 150–155. doi:10.1016/j.colsurfa.2016.04.019.
- [130] H. Jie, Q. Xu, L. Wei, Y.L. Min, Etching and heating treatment combined approach for superhydrophobic surface on brass substrates and the consequent corrosion resistance, *Corros. Sci.* 102 (2016) 251–258. doi:10.1016/j.corsci.2015.10.013.
- [131] J.H. Kim, A. Mirzaei, H.W. Kim, S.S. Kim, Facile fabrication of superhydrophobic surfaces from austenitic stainless steel (AISI 304) by chemical etching, *Appl. Surf. Sci.* 439 (2018) 598–604. doi:10.1016/j.apsusc.2017.12.211.
- [132] Y. Huang, D.K. Sarkar, X. Grant Chen, Superhydrophobic aluminum alloy surfaces prepared by chemical etching process and their corrosion resistance properties, *Appl. Surf. Sci.* 356 (2015) 1012–1024. doi:10.1016/j.apsusc.2015.08.166.
- [133] C. Zhang, P. Li, B. Cao, Fabrication of superhydrophobic-superoleophilic

- fabrics by an etching and dip-coating two-step method for oil-water separation, *Ind. Eng. Chem. Res.* 55 (2016) 5030–5035. doi:10.1021/acs.iecr.6b00206.
- [134] H.J. Choi, J.H. Shin, S. Choo, S.W. Ryu, Y.D. Kim, H. Lee, Fabrication of superhydrophobic and oleophobic Al surfaces by chemical etching and surface fluorination, *Thin Solid Films.* 585 (2015) 76–80. doi:10.1016/j.tsf.2015.03.046.
- [135] P. Varshney, S.S. Mohapatra, A. Kumar, Superhydrophobic coatings for aluminium surfaces synthesized by chemical etching process, *Int. J. Smart Nano Mater.* 7 (2016) 248–264. doi:10.1080/19475411.2016.1272502.
- [136] Z. He, Y. Chen, J. Yang, C. Tang, J. Lv, Y. Liu, J. Mei, W. ming Lau, D. Hui, Fabrication of polydimethylsiloxane films with special surface wettability by 3D printing, *Compos. Part B Eng.* 129 (2017) 58–65. doi:10.1016/j.compositesb.2017.07.025.
- [137] J. Lv, Z. Gong, Z. He, J. Yang, Y. Chen, C. Tang, Y. Liu, M. Fan, W.M. Lau, 3D printing of a mechanically durable superhydrophobic porous membrane for oil-water separation, *J. Mater. Chem. A.* 5 (2017) 12435–12444. doi:10.1039/c7ta02202f.
- [138] Y. Yang, X. Li, X. Zheng, Z. Chen, Q. Zhou, Y. Chen, 3d-printed biomimetic super-hydrophobic structure for microdroplet manipulation and oil/water separation, *Adv. Mater.* 30 (2018) 1704912. doi:10.1002/adma.201704912.
- [139] S. Yuan, D. Strobbe, J.P. Kruth, P. Van Puyvelde, B. Van Der Bruggen, Superhydrophobic 3D printed polysulfone membranes with a switchable wettability by self-assembled candle soot for efficient gravity-driven oil/water separation, *J. Mater. Chem. A.* 5 (2017) 25401–25409. doi:10.1039/c7ta08836a.

- [140] G. Graeber, O.B.M. Kieliger, T.M. Schutzius, D. Poulikakos, 3d-printed surface architecture enhancing superhydrophobicity and viscous droplet repellency, *ACS Appl. Mater. Interfaces.* 10 (2018) 43275–43281. doi:10.1021/acsami.8b16893.
- [141] K.M. Lee, H. Park, J. Kim, D.M. Chun, Fabrication of a superhydrophobic surface using a fused deposition modeling (FDM) 3d printer with poly lactic acid (PLA) filament and dip coating with silica nanoparticles, *Appl. Surf. Sci.* 467–468 (2019) 979–991. doi:10.1016/j.apsusc.2018.10.205.
- [142] T. Baldacchini, J.E. Carey, M. Zhou, E. Mazur, Superhydrophobic surfaces prepared by microstructuring of silicon using a femtosecond laser, *Langmuir.* 22 (2006) 4917–4919. doi:10.1021/la053374k.
- [143] D. Zhang, F. Chen, Q. Yang, J. Yong, H. Bian, Y. Ou, J. Si, X. Meng, X. Hou, A simple way to achieve pattern-dependent tunable adhesion in superhydrophobic surfaces by a femtosecond laser, *ACS Appl. Mater. Interfaces.* 4 (2012) 4905–4912. doi:10.1021/am3012388.
- [144] M.S. Ahsan, F. Dewanda, M.S. Lee, H. Sekita, T. Sumiyoshi, Formation of superhydrophobic soda-lime glass surface using femtosecond laser pulses, *Appl. Surf. Sci.* 265 (2013) 784–789. doi:10.1016/j.apsusc.2012.11.112.
- [145] D. Gong, J. Long, D. Jiang, P. Fan, H. Zhang, L. Li, M. Zhong, Robust and stable transparent superhydrophobic polydimethylsiloxane films by duplicating via a femtosecond laser-ablated template, *ACS Appl. Mater. Interfaces.* 8 (2016) 17511–17518. doi:10.1021/acsami.6b03424.
- [146] J. Yong, F. Chen, Q. Yang, D. Zhang, G. Du, J. Si, F. Yun, X. Hou, Femtosecond laser weaving superhydrophobic patterned PDMS surfaces with

- tunable adhesion, *J. Phys. Chem. C.* 117 (2013) 24907–24912.
doi:10.1021/jp408863u.
- [147] B. Wu, M. Zhou, J. Li, X. Ye, G. Li, L. Cai, Superhydrophobic surfaces fabricated by microstructuring of stainless steel using a femtosecond laser, *Appl. Surf. Sci.* 256 (2009) 61–66. doi:10.1016/j.apsusc.2009.07.061.
- [148] E. Fadeeva, V.K. Truong, M. Stiesch, B.N. Chichkov, R.J. Crawford, J. Wang, E.P. Ivanova, Bacterial retention on superhydrophobic titanium surfaces fabricated by femtosecond laser ablation, *Langmuir.* 27 (2011) 3012–3019. doi:10.1021/la104607g.
- [149] L.B. Boinovich, A.G. Domantovskiy, A.M. Emelyanenko, A.S. Pashinin, A.A. Ionin, S.I. Kudryashov, P.N. Saltuganov, Femtosecond laser treatment for the design of electro-insulating superhydrophobic coatings with enhanced wear resistance on glass, *ACS Appl. Mater. Interfaces.* 6 (2014) 2080–2085. doi:10.1021/am4051603.
- [150] M. V. Rukosuyev, J. Lee, S.J. Cho, G. Lim, M.B.G. Jun, One-step fabrication of superhydrophobic hierarchical structures by femtosecond laser ablation, *Appl. Surf. Sci.* 313 (2014) 411–417. doi:10.1016/j.apsusc.2014.05.224.
- [151] D.H. Kam, S. Bhattacharya, J. Mazumder, Control of the wetting properties of an AISI 316L stainless steel surface by femtosecond laser-induced surface modification, *J. Micromechanics Microengineering.* 22 (2012). doi:10.1088/0960-1317/22/10/105019.
- [152] S. Moradi, S. Kamal, P. Englezos, S.G. Hatzikiriakos, Femtosecond laser irradiation of metallic surfaces: effects of laser parameters on superhydrophobicity, *Nanotechnology.* 24 (2013). doi:10.1088/0957-

4484/24/41/415302.

- [153] A.Y. Vorobyev, C. Guo, Multifunctional surfaces produced by femtosecond laser pulses, *J. Appl. Phys.* 117 (2015). doi:10.1063/1.4905616.
- [154] J. Yong, F. Chen, Q. Yang, Y. Fang, J. Huo, X. Hou, Femtosecond laser induced hierarchical ZnO superhydrophobic surfaces with switchable wettability, *Chem. Commun.* 51 (2015) 9813–9816. doi:10.1039/c5cc02939b.
- [155] J. Long, P. Fan, D. Gong, D. Jiang, H. Zhang, L. Li, M. Zhong, Superhydrophobic surfaces fabricated by femtosecond laser with tunable water adhesion: from lotus leaf to rose petal, *ACS Appl. Mater. Interfaces.* 7 (2015) 9858–9865. doi:10.1021/acsami.5b01870.
- [156] R. Jagdheesh, B. Pathiraj, E. Karatay, G.R.B.E. Römer, A.J. Huis In't Veld, Laser-induced nanoscale superhydrophobic structures on metal surfaces, *Langmuir.* 27 (2011) 8464–8469. doi:10.1021/la2011088.
- [157] T. Jiang, J. Koch, C. Unger, E. Fadeeva, A. Koroleva, Q. Zhao, B.N. Chichkov, Ultrashort picosecond laser processing of micro-molds for fabricating plastic parts with superhydrophobic surfaces, *Appl. Phys. A Mater. Sci. Process.* 108 (2012) 863–869. doi:10.1007/s00339-012-6985-4.
- [158] J. Long, P. Fan, M. Zhong, H. Zhang, Y. Xie, C. Lin, Superhydrophobic and colorful copper surfaces fabricated by picosecond laser induced periodic nanostructures, *Appl. Surf. Sci.* 311 (2014) 461–467. doi:10.1016/j.apsusc.2014.05.090.
- [159] X.C. Wang, B. Wang, H. Xie, H.Y. Zheng, Y.C. Lam, Picosecond laser micro/nano surface texturing of nickel for superhydrophobicity, *J. Phys. D: Appl. Phys.* 51 (2018) 115305. doi:10.1088/1361-6463/aaad24.

- [160] S. Faas, U. Bielke, R. Weber, T. Graf, Scaling the productivity of laser structuring processes using picosecond laser pulses at average powers of up to 420 W to produce superhydrophobic surfaces on stainless steel AISI 316L, *Sci. Rep.* 9 (2019) 1933. doi:10.1038/s41598-018-37867-y.
- [161] J. Long, M. Zhong, H. Zhang, P. Fan, Superhydrophilicity to superhydrophobicity transition of picosecond laser microstructured aluminum in ambient air, *J. Colloid Interface Sci.* 441 (2015) 1–9. doi:10.1016/j.jcis.2014.11.015.
- [162] B. Zheng, G. Jiang, W. Wang, X. Mei, Fabrication of superhydrophilic or superhydrophobic self-cleaning metal surfaces using picosecond laser pulses and chemical fluorination, *Radiat. Eff. Defects Solids.* 171 (2016) 461–473. doi:10.1080/10420150.2016.1211658.
- [163] R. Jagdheesh, Fabrication of a superhydrophobic Al₂O₃ surface using picosecond laser pulses, *Langmuir.* 30 (2014) 12067–12073. doi:10.1021/la5033527.
- [164] K. Sun, H. Yang, W. Xue, A. He, D. Zhu, W. Liu, K. Adeyemi, Y. Cao, Antibiofouling superhydrophobic surface fabricated by picosecond laser texturing of stainless steel, *Appl. Surf. Sci.* 436 (2018) 263–267. doi:10.1016/j.apsusc.2017.12.012.
- [165] F.H. Rajab, Z. Liu, L. Li, Long term superhydrophobic and hybrid superhydrophobic/superhydrophilic surfaces produced by laser surface micro/nano surface structuring, *Appl. Surf. Sci.* 466 (2019) 808–821. doi:10.1016/j.apsusc.2018.10.099.
- [166] P. Gregorčič, B. Šetina-Batič, M. Hočevar, Controlling the stainless steel

- surface wettability by nanosecond direct laser texturing at high fluences, *Appl. Phys. A Mater. Sci. Process.* 123 (2017) 1–8. doi:10.1007/s00339-017-1392-5.
- [167] Z. Yang, X. Liu, Y. Tian, Insights into the wettability transition of nanosecond laser ablated surface under ambient air exposure, *J. Colloid Interface Sci.* 533 (2019) 268–277. doi:10.1016/j.jcis.2018.08.082.
- [168] V.D. Ta, A. Dunn, T.J. Wasley, J. Li, R.W. Kay, J. Stringer, P.J. Smith, E. Esenturk, C. Connaughton, J.D. Shephard, Laser textured superhydrophobic surfaces and their applications for homogeneous spot deposition, *Appl. Surf. Sci.* 365 (2016) 153–159. doi:10.1016/j.apsusc.2016.01.019.
- [169] V.D. Ta, A. Dunn, T.J. Wasley, J. Li, R.W. Kay, J. Stringer, P.J. Smith, E. Esenturk, C. Connaughton, J.D. Shephard, Laser textured surface gradients, *Appl. Surf. Sci.* 371 (2016) 583–589. doi:10.1016/j.apsusc.2016.03.054.
- [170] Z. Yang, Y. Tian, Y. Zhao, C. Yang, Study on the fabrication of superhydrophobic surface on inconel alloy via nanosecond laser ablation, *Materials (Basel)*. 12 (2019) 278. doi:10.3390/ma12020278.
- [171] D. V. Ta, A. Dunn, T.J. Wasley, R.W. Kay, J. Stringer, P.J. Smith, C. Connaughton, J.D. Shephard, Nanosecond laser textured superhydrophobic metallic surfaces and their chemical sensing applications, *Appl. Surf. Sci.* 357 (2015) 248–254. doi:10.1016/j.apsusc.2015.09.027.
- [172] T.-H. Dinh, C.-V. Ngo, D.-M. Chun, Controlling the wetting properties of superhydrophobic titanium surface fabricated by UV nanosecond-pulsed laser and heat treatment, *Nanomaterials*. 8 (2018) 766. doi:10.3390/nano8100766.
- [173] C.V. Ngo, D.M. Chun, Effect of heat treatment temperature on the wettability transition from hydrophilic to superhydrophobic on laser-ablated metallic

- surfaces, *Adv. Eng. Mater.* 20 (2018) 1–11. doi:10.1002/adem.201701086.
- [174] D.M. Chun, C.V. Ngo, K.M. Lee, Fast fabrication of superhydrophobic metallic surface using nanosecond laser texturing and low-temperature annealing, *CIRP Ann. - Manuf. Technol.* 65 (2016) 519–522. doi:10.1016/j.cirp.2016.04.019.
- [175] C.V. Ngo, D.M. Chun, Fast wettability transition from hydrophilic to superhydrophobic laser-textured stainless steel surfaces under low-temperature annealing, *Appl. Surf. Sci.* 409 (2017) 232–240. doi:10.1016/j.apsusc.2017.03.038.
- [176] Y. Wan, C. Xi, H. Yu, Fabrication of self-cleaning superhydrophobic surface on stainless steel by nanosecond laser, *Mater. Res. Express.* 5 (2018). doi:10.1088/2053-1591/aadbf2.
- [177] D. Patil, S. Aravindan, M. Kaushal Wasson, V. P., P. V. Rao, Fast fabrication of superhydrophobic titanium alloy as antibacterial surface using nanosecond laser texturing, *J. Micro Nano-Manufacturing.* 6 (2017) 011002. doi:10.1115/1.4038093.
- [178] A. He, W. Liu, W. Xue, H. Yang, Y. Cao, Nanosecond laser ablated copper superhydrophobic surface with tunable ultrahigh adhesion and its renewability with low temperature annealing, *Appl. Surf. Sci.* 434 (2018) 120–125. doi:10.1016/j.apsusc.2017.10.143.
- [179] Q. Ma, Z. Tong, W. Wang, G. Dong, Fabricating robust and repairable superhydrophobic surface on carbon steel by nanosecond laser texturing for corrosion protection, *Appl. Surf. Sci.* 455 (2018) 748–757. doi:10.1016/j.apsusc.2018.06.033.
- [180] L. Hu, L. Zhang, D. Wang, X. Lin, Y. Chen, Fabrication of biomimetic

- superhydrophobic surface based on nanosecond laser-treated titanium alloy surface and organic polysilazane composite coating, *Colloids Surfaces A Physicochem. Eng. Asp.* 555 (2018) 515–524. doi:10.1016/j.colsurfa.2018.07.029.
- [181] J. Song, D. Wang, L. Hu, X. Huang, Y. Chen, Superhydrophobic surface fabricated by nanosecond laser and perhydropolysilazane, *Appl. Surf. Sci.* 455 (2018) 771–779. doi:10.1016/j.apsusc.2018.05.227.
- [182] J. Long, Z. He, C. Zhou, X. Xie, Z. Cao, P. Zhou, Y. Zhu, W. Hong, Z. Zhou, Hierarchical micro- and nanostructures induced by nanosecond laser on copper for superhydrophobicity, ultralow water adhesion and frost resistance, *Mater. Des.* 155 (2018) 185–193. doi:10.1016/j.matdes.2018.05.069.
- [183] Z. Lei, Z. Tian, X. Chen, Y. Chen, J. Bi, S. Wu, H. Sun, Large spot diameter nanosecond laser treatment of aluminum alloy sheets for high-speed superhydrophobic hierarchical micro- and nanostructured surface preparation, *Surf. Coatings Technol.* 361 (2019) 249–254. doi:10.1016/j.surfcoat.2019.01.020.
- [184] M. Conradi, A. Drnovšek, P. Gregorčič, Wettability and friction control of a stainless steel surface by combining nanosecond laser texturing and adsorption of superhydrophobic nanosilica particles, *Sci. Rep.* 8 (2018) 2–10. doi:10.1038/s41598-018-25850-6.
- [185] J. Long, Z. Cao, C. Lin, C. Zhou, Z. He, X. Xie, Formation mechanism of hierarchical micro- and nanostructures on copper induced by low-cost nanosecond lasers, *Appl. Surf. Sci.* 464 (2019) 412–421. doi:10.1016/j.apsusc.2018.09.055.

- [186] I. Roca, M. Akova, F. Baquero, J. Carlet, M. Cavaleri, S. Coenen, J. Cohen, D. Findlay, I. Gyssens, O.E. Heure, G. Kahlmeter, H. Kruse, R. Laxminarayan, E. Li đbana, L. L ópez-Cerero, A. MacGowan, M. Martins, J. Rodr uez-Ba o, J.M. Rolain, C. Segovia, B. Sigauque, E. Taconelli, E. Wellington, J. Vila, The global threat of antimicrobial resistance: Science for intervention, *New Microbes New Infect.* 6 (2015) 22–29. doi:10.1016/j.nmni.2015.02.007.
- [187] W.R. Li, X.B. Xie, Q.S. Shi, H.Y. Zeng, Y.S. Ou-Yang, Y. Ben Chen, Antibacterial activity and mechanism of silver nanoparticles on *Escherichia coli*, *Appl. Microbiol. Biotechnol.* 85 (2010) 1115–1122. doi:10.1007/s00253-009-2159-5.
- [188] E. De Giglio, D. Cafagna, S. Cometa, A. Allegretta, A. Pedico, L.C. Giannossa, L. Sabbatini, M. Mattioli-Belmonte, R. Iatta, An innovative, easily fabricated, silver nanoparticle-based titanium implant coating: development and analytical characterization, *Anal. Bioanal. Chem.* 405 (2013) 805–816. doi:10.1007/s00216-012-6293-z.
- [189] H. Cao, X. Liu, F. Meng, P.K. Chu, Biological actions of silver nanoparticles embedded in titanium controlled by micro-galvanic effects, *Biomaterials.* 32 (2011) 693–705. doi:10.1016/j.biomaterials.2010.09.066.
- [190] F.G. Echeverrigaray, S. Echeverrigaray, A.P.L. Delamare, C.H. Wanke, C.A. Figueroa, I.J.R. Baumvol, C. Aguzzoli, Antibacterial properties obtained by low-energy silver implantation in stainless steel surfaces, *Surf. Coatings Technol.* 307 (2016) 345–351. doi:10.1016/j.surfcoat.2016.09.005.
- [191] M. Ferraris, S. Perero, S. Ferraris, M. Miola, E. Vern S. Skoglund, E. Blomberg, I. Odnevall Wallinder, Antibacterial silver nanocluster/silica

- composite coatings on stainless steel, *Appl. Surf. Sci.* 396 (2017) 1546–1555.
doi:10.1016/j.apsusc.2016.11.207.
- [192] Y. Inoue, M. Uota, T. Torikai, T. Watari, I. Noda, T. Hotokebuchi, M. Yada, Antibacterial properties of nanostructured silver titanate thin films formed on a titanium plate, *J. Biomed. Mater. Res. - Part A.* 92 (2010) 1171–1180.
doi:10.1002/jbm.a.32456.
- [193] M. Soloviev, A. Gedanken, Coating a stainless steel plate with silver nanoparticles by the sonochemical method, *Ultrason. Sonochem.* 18 (2011) 356–362. doi:10.1016/j.ultsonch.2010.06.015.
- [194] M. Diantoro, R. Fitrianiingsih, N. Mufti, A. Fuad, Synthesis of silver nanoparticles by chemical reduction at various fraction of MSA and their structure characterization, *AIP Conf. Proc.* 1589 (2014) 257–261.
doi:10.1063/1.4868795.
- [195] S. Heinonen, E. Huttunen-Saarivirta, J.P. Nikkanen, M. Raulio, O. Priha, J. Laakso, E. Storgårds, E. Levänen, Antibacterial properties and chemical stability of superhydrophobic silver-containing surface produced by sol-gel route, *Colloids Surfaces A Physicochem. Eng. Asp.* 453 (2014) 149–161.
doi:10.1016/j.colsurfa.2014.04.037.
- [196] Z. Jia, P. Xiu, M. Li, X. Xu, Y. Shi, Y. Cheng, S. Wei, Y. Zheng, T. Xi, H. Cai, Z. Liu, Bioinspired anchoring AgNPs onto micro-nanoporous TiO₂ orthopedic coatings: trap-killing of bacteria, surface-regulated osteoblast functions and host responses, *Biomaterials.* 75 (2016) 203–222.
doi:10.1016/j.biomaterials.2015.10.035.
- [197] M. Moreno-Couranjou, R. Mauchauffé S. Bonot, C. Detrembleur, P. Choquet,

- Anti-biofouling and antibacterial surfaces: via a multicomponent coating deposited from an up-scalable atmospheric-pressure plasma-assisted CVD process, *J. Mater. Chem. B.* 6 (2018) 614–623. doi:10.1039/c7tb02473h.
- [198] P. Cao, X. He, J. Xiao, C. Yuan, X. Bai, Covalent bonding of AgNPs to 304 stainless steel by reduction in situ for antifouling applications, *Appl. Surf. Sci.* 452 (2018) 201–209. doi:10.1016/j.apsusc.2018.04.227.
- [199] S. Ferraris, F. Warchomicka, C. Ramskogler, M. Tortello, A. Cochis, A. Scalia, G. Gautier di Confiengo, J. Keckes, L. Rimondini, S. Spriano, Surface structuring by electron beam for improved soft tissues adhesion and reduced bacterial contamination on Ti-grade 2, *J. Mater. Process. Technol.* 266 (2019) 518–529. doi:10.1016/j.jmatprotec.2018.11.026.
- [200] S.H. Park, E.H. Cho, J. Sohn, P. Theilmann, K. Chu, S. Lee, Y. Sohn, D. Kim, B. Kim, Design of multi-functional dual hole patterned carbon nanotube composites with superhydrophobicity and durability, *Nano Res.* 6 (2013) 389–398. doi:10.1007/s12274-013-0316-8.
- [201] S.B. Sant, *Physics and Chemistry of Interfaces*, John Wiley & Sons, 2013. doi:10.1080/10426914.2013.840916.
- [202] Surface tension, (2019). https://en.wikipedia.org/wiki/Surface_tension#cite_note-s_z-7 (accessed July 8, 2019).
- [203] A. Mall, P.R. Jelia, A. Agrawal, R.K. Singh, S.S. Joshi, Design of arrayed micro-structures to get super-hydrophobic surface for single droplet and bulk flow conditions, in: *COMSOL Conf. 2009 Bangalore*, 2009.
- [204] T. Young, III. An essay on the cohesion of fluids, *Philos. Trans. R. Soc. London.*

- 95 (1805) 65–87. doi:10.1098/rstl.1805.0005.
- [205] Overview and limitations of the VOF model, Fluent Inc. (2006).
<http://cdlab2.fluid.tuwien.ac.at/LEHRE/TURB/Fluent.Inc/fluent6.3.26/help/html/ug/node881.htm>.
- [206] F. Ursell, An introduction to fluid dynamis, *J. Fluid Mech.* 5 (1959) 493–494.
doi:10.1017/S0022112059220333.
- [207] J.U. Brackbill, D.B. Kothe, C. Zemach, A continuum method for modeling surface tension, *J. Comput. Phys.* 100 (1992) 335–354. doi:10.1016/0021-9991(92)90240-Y.
- [208] B. Samuel, H. Zhao, K.Y. Law, Study of wetting and adhesion interactions between water and various polymer and superhydrophobic surfaces, *J. Phys. Chem. C.* 115 (2011) 14852–14861. doi:10.1021/jp2032466.
- [209] P. Sedgwick, Spearman’s rank correlation coefficient, *BMJ.* 349 (2014).
doi:10.1136/bmj.g7327.
- [210] Kendall rank correlation coefficient, *Concise Encycl. Stat.* (2008).
doi:10.1007/978-0-387-32833-1_211.
- [211] K.C. Park, H.J. Choi, C.H. Chang, R.E. Cohen, G.H. McKinley, G. Barbastathis, Nanotextured silica surfaces with robust superhydrophobicity and omnidirectional broadband supertransmissivity, *ACS Nano.* 6 (2012) 3789–3799. doi:10.1021/nm301112t.
- [212] E. Celia, T. Darmanin, E. Taffin de Givenchy, S. Amigoni, F. Guittard, Recent advances in designing superhydrophobic surfaces, *J. Colloid Interface Sci.* 402 (2013) 1–18. doi:10.1016/j.jcis.2013.03.041.
- [213] C.W. Extrand, Retention forces of a liquid slug in a rough capillary tube with

- symmetric or asymmetric features, *Langmuir*. 23 (2007) 1867–1871. doi:10.1021/la0625289.
- [214] N.A. Malvadkar, M.J. Hancock, K. Sekeroglu, W.J. Dressick, M.C. Demirel, An engineered anisotropic nanofilm with unidirectional wetting properties, *Nat. Mater.* 9 (2010) 1023–1028. doi:10.1038/nmat2864.
- [215] P. Guo, Y. Zheng, C. Liu, J. Ju, L. Jiang, Directional shedding-off of water on natural/bio-mimetic taper-ratchet array surfaces, *Soft Matter*. 8 (2012) 1770–1775. doi:10.1039/c1sm06631e.
- [216] L. Gaete-Garretón, D. Briceño-Gutiérrez, Y. Vargas-Hernández, C.I. Zanelli, Ultrasonic atomization of distilled water, *J. Acoust. Soc. Am.* 144 (2018) 222–227. doi:10.1121/1.5045558.
- [217] X. Wang, C. Ma, C. Li, M. Kang, K. Ehmann, Influence of pulse energy on machining characteristics in laser induced plasma micro-machining, *J. Mater. Process. Technol.* 262 (2018) 85–94. doi:10.1016/j.jmatprotec.2018.06.031.
- [218] K.H. Stern, High temperature properties and decomposition of inorganic salts part 3, nitrates and nitrites, *J. Phys. Chem. Ref. Data*. 1 (1972) 747–772. doi:10.1063/1.3253104.
- [219] M. Dobre, L. Bolle, Practical design of ultrasonic spray devices: experimental testing of several atomizer geometries, *Exp. Therm. Fluid Sci.* 26 (2002) 205–211. doi:10.1016/S0894-1777(02)00128-0.
- [220] D. Šarković, V. Babović, On the statistics of ultrasonically produced water droplets, *Zeitschrift Fur Naturforsch. A*. 60 (2005) 489–493. doi:10.1515/zna-2005-0704.
- [221] and K.S. Pohlman, Reimar, Investigation of the mechanism of ultrasonic

nebulisation of liquid surfaces with regard to technical applications, West German publisher, 1965.

- [222] T. Thorslund, F.J. Kahlen, A. Kar, Temperatures, pressures and stresses during laser shock processing, *Opt. Lasers Eng.* 39 (2003) 51–71. doi:10.1016/S0143-8166(02)00040-4.
- [223] J. Zhou, H. Shen, Y. Pan, X. Ding, Experimental study on laser microstructures using long pulse, *Opt. Lasers Eng.* 78 (2016) 113–120. doi:10.1016/j.optlaseng.2015.10.009.
- [224] S. Gurunathan, J.W. Han, D.N. Kwon, J.H. Kim, Enhanced antibacterial and anti-biofilm activities of silver nanoparticles against Gram-negative and Gram-positive bacteria, *Nanoscale Res. Lett.* 9 (2014) 1–17. doi:10.1186/1556-276X-9-373.
- [225] T. Takeshima, Y. Tada, N. Sakaguchi, F. Watari, B. Fugetsu, DNA/Ag Nanoparticles as Antibacterial Agents against Gram-Negative Bacteria, *Nanomaterials.* 5 (2015) 284–297. doi:10.3390/nano5010284.
- [226] M. Raza, Z. Kanwal, A. Rauf, A. Sabri, S. Riaz, S. Naseem, Size- and Shape-Dependent Antibacterial Studies of Silver Nanoparticles Synthesized by Wet Chemical Routes, *Nanomaterials.* 6 (2016) 74. doi:10.3390/nano6040074.
- [227] S.O. Al-Mashikhi, J. Powell, A. Kaplan, K.T. Voisey, Heat affected zones and oxidation marks in fiber laser–oxygen cutting of mild steel, *J. Laser Appl.* 23 (2011) 042003. doi:10.2351/1.3614404.
- [228] S.Y.C. Tong, J.S. Davis, E. Eichenberger, T.L. Holland, V.G. Fowler, Staphylococcus aureus infections: epidemiology, pathophysiology, clinical manifestations, and management., *Clin. Microbiol. Rev.* 28 (2015) 603–61.

doi:10.1128/CMR.00134-14.

- [229] T.L. Vollmerhausen, A. Conneely, C. Bennett, V.E. Wagner, J.C. Victor, C.P. O'Byrne, Visible and UVA light as a potential means of preventing *Escherichia coli* biofilm formation in urine and on materials used in urethral catheters, *J. Photochem. Photobiol. B Biol.* 170 (2017) 295–303. doi:10.1016/j.jphotobiol.2017.04.018.
- [230] E. Fazio, M. Santoro, G. Lentini, D. Franco, S.P.P. Guglielmino, F. Neri, Iron oxide nanoparticles prepared by laser ablation: synthesis, structural properties and antimicrobial activity, *Colloids Surfaces A Physicochem. Eng. Asp.* 490 (2016) 98–103. doi:10.1016/j.colsurfa.2015.11.034.
- [231] T.C. Dakal, A. Kumar, R.S. Majumdar, V. Yadav, Mechanistic basis of antimicrobial actions of silver nanoparticles, *Front. Microbiol.* 7 (2016) 1–17. doi:10.3389/fmicb.2016.01831.
- [232] I. Sondi, B. Salopek-Sondi, Silver nanoparticles as antimicrobial agent: a case study on *E. coli* as a model for Gram-negative bacteria, *J. Colloid Interface Sci.* 275 (2004) 177–182. doi:10.1016/j.jcis.2004.02.012.